



**Technische Universität München**  
Fakultät für Physik

---

# The self-monitoring precision calibration light source for the IceCube Upgrade

Felix Henningsen

---

Vollständiger Abdruck der von der Fakultät für Physik der Technischen Universität München zur Erlangung des akademischen Grades eines

**Doktors der Naturwissenschaften (Dr. rer. nat.)**

genehmigten Dissertation.

**Vorsitzender:**

apl. Prof. Dr. Norbert Kaiser

**Prüfer der Dissertation:**

1. Prof. Dr. Elisa Resconi
2. Prof. Dr. Stephan Paul

---

Die Dissertation wurde am **29.10.2021** bei der Technischen Universität München eingereicht und durch die Fakultät für Physik am **13.12.2021** angenommen.



## Abstract

---

Neutrino astronomy is one of the most promising fields for high-energy particle- and astrophysics. To measure these elusive particles, large-volume detectors and precise knowledge about the parameters of their media are necessary. With IceCube at the South Pole being the biggest operating neutrino telescope on the planet, the IceCube Upgrade aims to extend its scientific capabilities and improve its calibration with new instruments and methods. In the scope of this Upgrade, we developed the *Precision Optical Calibration Module* (POCAM), an isotropic, self-monitored calibration light source able to tackle existing optical detector systematics to high precision. In total 21 POCAMs are planned to be installed at the South Pole with the IceCube Upgrade. On the one hand, this thesis summarizes the simulation efforts to provide a proof of principle for calibration improvements in the IceCube detector using the POCAM and how this translates to oscillation physics sensitivities. On the other hand, it contains the baseline of the POCAM instrument for the IceCube Upgrade, including all mechanical, electrical and optical designs as well as several experimental setups for calibration and production. This new POCAM iteration presented here is developed for an application at the South Pole but also any other large-volume neutrino telescope.



## Zusammenfassung

---

Neutrino Astronomie ist eines der vielversprechendsten Forschungsfelder in der hochenergetischen Teilchen- und Astrophysik. Um diese schwer-messbaren Teilchen zu detektieren, werden Detektoren mit immensen Volumen und gut verstandenen optischen Eigenschaften benötigt. IceCube ist das größte operierende Neutrino Teleskop und befindet sich am Südpol. Mit neuen Instrumenten soll das geplante IceCube Upgrade dessen Sensitivität für niedrigere Energien erhöhen und seine Kalibration verbessern. Im Kontext des IceCube Upgrades wurde von uns das „Precision Optical Calibration Module“ (POCAM) entwickelt, welches eine isotrope, selbst-kalibrierende, nanosekunden-gepulste Lichtquelle darstellt. Diese soll es ermöglichen, die existierenden systematischen Unsicherheiten des antarktischen Eises in IceCube mit hoher Präzision zu kalibrieren. Insgesamt sollen 21 POCAMs im Upgrade Volumen installiert werden. Diese Dissertation beschreibt zum einen eine Simulationsstudie, die die Verbesserungen der IceCube Kalibrierung mithilfe der POCAMs untersucht. Zum anderen beschreibt es die detaillierte Entwicklung des Instruments in allen optischen, mechanischen und elektronischen Aspekten. Außerdem die Entwicklung von experimentellen Aufbauten für Kalibration und Produktion aller Instrumente für das Upgrade. Die POCAM-Version, die in dieser Dissertation beschrieben wird, ist für einen Einsatz am Südpol konzipiert, aber lässt sich durch ihr modulares Design auch in jedes andere Neutrino Teleskop integrieren.



## Acknowledgments

---

This thesis has been, without a doubt, one of the biggest projects that I have faced in my scientific life. With the scope and responsibility coming along with leading a larger project, it has been challenging at times and it would not have been possible without a great team of people. Here, I want to acknowledge their support.

**Elisa Resconi** I would like to thank you for this opportunity to lead my own project and all the valuable advice and support you have provided over the years. Your way of creating an effective and friendly group atmosphere has made pursuing science so much fun. I hope this can express how much I appreciate everything you have made available to me, be it travels, scientific development or personal growth. Your free way of guiding me towards my own ideas has been very rewarding.

**Michael Boehmer** I would like to thank you for countless discussions, companionship and valuable support throughout my years here at TUM. You have become a good friend and I am grateful to have had you and your experience as part of this project. Pet Bumble from me and I hope we continue to work together for a long time.

**Roman Gernhäuser** I want to express my gratitude to have had the chance to work with you on countless projects. Whether it was Siberia, the Pacific Ocean or the South Pole, your advice, be it professional or personal, has always been very helpful and allowed me to develop as a scientist and as a person.

**Christian Spannfellner** It is without a doubt that I can say you are among the best people and most dedicated scientists that I know. You drive projects and having you in the POCAM development team is part of the reason this project was successful in the end. Your support in both my professional and my personal life was invaluable and I am proud to call you a good friend. May our time together in science continue for a long time.

**Philipp Eller** I want to thank you for all the support you have offered me on all computational aspects of machine learning and analysis techniques. The countless discussion we had on neural nets and why things don't work have allowed me to get a grasp of machine learning within a year and eventually allowed me to produce also analysis output for my project.

**Tobias Pertl** All the work and effort you have put into the POCAM developments has been invaluable to the project and I am happy you stuck around after your Bachelor's and decided to join our team. I am very grateful for all the time you have invested into making this project thrive and I am confident that you taking over some responsibility in the future is the right way to go.

**Martin Rongen** It is always a pleasure to discuss and work with you on IceCube calibration and I want to thank you for always critically questioning everyone and everything. Your way of helping me understand my own problems in simulations, code, computations or analyses is what helped me to understand many things about IceCube in a lot more detail.

**Kilian Holzapfel** Visiting Siberia, discussing work and personal life or summitting countless mountain tops with you has been one of my favorite things about our group at TUM. Whether it is a discussion in your office or contemplating life under the stars on a mountain, I am happy to call you a dear colleague and friend.

**Jan-Henrik Schmidt-Dencker** I am happy to have met you in the group as you have become a good friend. Talking to you about work, career or life has always been a pleasure and you never failed to make me laugh. I wish you all the best in your (probably very successful) coming career.

**Laura Winter** From the time I advised your Bachelor's thesis to this day I am happy to say that I am proud to see you becoming the scientist and friend you are today. You always manage to make the group a very happy bunch and your natural way of making people enjoy what they are doing is something you should never lose.

**IceCube Collaboration** I want to thank the whole Collaboration and especially the calibration and tech-board working groups. Especially assistance with computational efforts and driving the improvements of simulation, analysis studies and hardware designs.

**ECP group at TUM** I am grateful for the group making work enjoyable in a friendly and familiar atmosphere. Many of you have become good friends over the years.

**Advisory Committee** I am very grateful for the support and valuable advice I received from my advisory committee including Prof. Elisa Resconi, Prof. Allen Caldwell and Dr. Roman Gernhäuser.

**Max Planck Institute for Physics** I appreciate the support from the Max Planck Institute for providing me with the means to pursue my doctoral career, the many opportunities and workshops, and all the friends I made this way.

Finally, I want to express my deepest appreciation for my family and friends. Especially, my mom Prisca, my brother Niklas, my aunt and uncle Lisa and Roger Paul with Eli, Kathi and Maxi, and my wonderful girlfriend Leonie. You all have been supportive through the best and toughest of times and helped me to develop to the person I am today, thank you.

Felix Henningsen

# Contents

---

<b>Abstract</b>	<b>iii</b>
<b>Acknowledgements</b>	<b>vii</b>
<b>1 Introduction</b>	<b>1</b>
<b>2 Neutrinos: Cosmic messengers</b>	<b>3</b>
2.1 Multi-messenger astronomy . . . . .	3
2.2 Cosmic rays & atmospheric neutrinos . . . . .	5
2.3 Astrophysical neutrinos . . . . .	7
<b>3 Neutrino mass, mixing and oscillations</b>	<b>13</b>
3.1 Neutrino oscillation in vacuum . . . . .	13
3.2 Matter effects . . . . .	15
3.3 Oscillation effects in astrophysics . . . . .	17
<b>4 Large-volume detectors, systematics and calibration</b>	<b>19</b>
4.1 Neutrino detection principles . . . . .	19
4.2 Large-volume neutrino experiments . . . . .	21
4.3 Detector systematics and calibration methods . . . . .	26
<b>5 The IceCube Neutrino Observatory</b>	<b>29</b>
5.1 Experimental design . . . . .	29
5.2 Systematic detector effects . . . . .	30
5.3 IceCube extensions . . . . .	34
<b>6 Precision Optical Calibration Module: simulation and sensitivity estimates</b>	<b>37</b>
6.1 Instrument concept . . . . .	37
6.2 Photon tracking simulation . . . . .	38
6.3 Machine learning approximation . . . . .	43
6.4 Data analysis methods . . . . .	52
6.5 POCAM emission and hole ice simulation . . . . .	58
6.6 Optical geometry calibration in water . . . . .	60
<b>7 POCAM development for the IceCube Upgrade</b>	<b>63</b>
7.1 Instrument overview . . . . .	63
7.2 Requirements for in-ice installation . . . . .	64
7.3 Measurement setups . . . . .	66
7.4 Mechanical and optical design . . . . .	72
7.5 Light pulsing and self-monitoring . . . . .	76
7.6 Digital and interface electronics . . . . .	87
7.7 Calibration procedures . . . . .	91
7.8 Instrument assembly and production . . . . .	94
<b>8 Conclusion</b>	<b>99</b>

<b>Appendix</b>	<b>101</b>
<b>A NN training</b>	<b>103</b>
<b>B MCMC implementation</b>	<b>107</b>
<b>C Schematics</b>	<b>111</b>
C.1 Dual-Kapustinsky driver . . . . .	111
C.2 LD-type driver . . . . .	112
C.3 Photodiode readout . . . . .	113
C.4 Silicon photomultiplier readout . . . . .	114
<b>D LED measurements</b>	<b>115</b>
<b>List of Figures</b>	<b>117</b>
<b>List of Tables</b>	<b>121</b>
<b>Bibliography</b>	<b>139</b>

With neutrino astronomy starting to become one of the most active fields in the multi-messenger era, the observations of large-volume neutrino telescopes become increasingly important to study the most violent objects in the universe. A promising example of such an observation was the first compelling evidence for a coincident neutrino and gamma ray point source of the blazar TXS 0506+056<sup>1,2</sup>. With these observations also the calibration precision of large-volume detectors becomes increasingly important. This is especially true for the IceCube detector at the South Pole which is subject to a number of systematic effects within the detection volume that limit the achievable physics precision.

In the scope of the IceCube Upgrade the IceCube detector will be extended with an additional set of seven strings targetting an extension towards lower energies and potentially aiming to provide competitive observations of neutrino oscillation parameters. Additionally, the installment of further strings also allows the inclusion of additional calibration hardware. As the recent years have shown, the calibration capabilities with the existing LED flashers within the IceCube detection modules are limited due to the poorly known intensity and pointing information of the LEDs. Thus, the chance to include new calibration instruments is one of the primary targets of the Upgrade. This includes the ice properties of the Antarctic ice volume within the detector as well as, for example, linearity and efficiency of the used detection modules and their electronics.

In this thesis a two-fold investigation of a novel calibration light source – called the *Precision Optical Calibration Module (POCAM)* – is discussed. First, a physical baseline for the device is investigated in order to verify that certain device characteristics eventually allow improvement of the IceCube systematics. For the example of an existing low-energy oscillation analysis and using novel machine learning techniques, these improved priors verify the improvement of physics sensitivities. The second part of the thesis then concentrates on the actual device development including simulation, design, testing, optimization, calibration and production for the IceCube Upgrade. The calibration and production aspects are of critical importance as around 30 instruments need to be developed for installment within the Upgrade volume and as such need to be streamlined as much as possible. Finally, the thesis contents are outlined as follows.

**Chapter 2** This chapter focuses on the field of multi-messenger astronomy and introduces the messenger particles and their properties. It further gives an overview of cosmic rays as well as known and hypothesized neutrino sources and their respective energy spectra.

<sup>1</sup> The IceCube Collaboration “Neutrino emission from the direction of the blazar TXS 0506+056 prior to the IceCube-170922A alert” (2018).

<sup>2</sup> The IceCube Collaboration “Multimessenger observations of a flaring blazar coincident with high-energy neutrino IceCube-170922A” (2018).

**Chapter 3** Focussing on neutrino oscillations, this chapter summarizes theoretical and experimental aspects of investigating the flavor-changing nature of neutrinos. It gives some level of detailed theory on both neutrino oscillations in vacuum and matter as well as describes some aspects of neutrino oscillations relevant within the field of astroparticle physics.

**Chapter 4** In this chapter the general concept of large-volume detectors is discussed. Hereby special focus is put on optical properties in water and ice and how the different media affect the telescope and its background in different ways. It further summarizes existing efforts of different large-volume experiments on the planet and discusses the importance and means of calibrating different aspects of these detectors.

**Chapter 5** With IceCube being a central aspect of this thesis, this chapter introduces the detector and its properties in detail. Especial focus is put on systematic effects within the detector as well as its general optical properties with respect to both the optical medium and sensor instrumentation. Additionally the planned IceCube extensions, namely the Upgrade and Gen2, are discussed.

**Chapter 6** In this chapter the simulation efforts for the POCAM are discussed which investigate the scientific potential of the device itself with respect to its IceCube Upgrade installation. In addition to simulation and machine learning efforts, the chapter presents fits on both simulated and experimental data of IceCube LED flashers using a machine learning approach which further provides the baseline of potential POCAM improvements. The chapter closes with a case study of improved IceCube systematics based on a simulated POCAM application and how this can improve results of an existing low-energy physics.

**Chapter 7** This chapter discusses the hardware development of the POCAM instrument from design over optimization towards instrument production for the Upgrade. This part focusses on mechanical, optical and electrical design of the device as well as light pulsing properties related to the increased instrument capabilities. In addition to investigations related to all major components of the instrument, this chapter also includes a variety of developed calibration measurement setups necessary to provide a streamlined calibration for all POCAMs which will eventually be deployed within the IceCube Upgrade. It closes with a summary of the instrument calibration and production plans for the coming months.

Finally, the thesis is concluded in chapter 8 and supplementary materials – for example important code snippets, hardware designs or schematics – are given in the appendix.

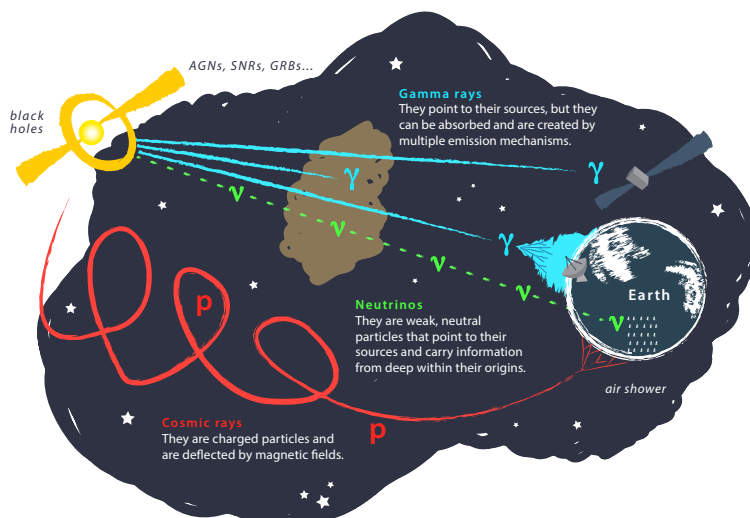
# 2

## Neutrinos: Cosmic messengers

Neutrinos, while known for decades, have recently opened a new observational window to the universe with the detection of both an astrophysical neutrino flux<sup>3</sup> and compelling evidence for the first neutrino point source coincident with observations in high-energy gamma rays<sup>1,2</sup>. Before focusing on detector requirements and calibration aspects of large volume telescopes, this first chapter introduces neutrinos, cosmic rays and the field of multi-messenger astronomy.

### 2.1 Multi-messenger astronomy

With the rise of large-volume telescopes detecting high-energy neutrinos, neutrinos complement the process of multi-messenger astronomy, that is, understanding astrophysical objects in the universe using multiple messenger particles. Most commonly, the field of multi-messenger astronomy comprises observations of photons ( $\gamma$ ), cosmic rays (CRs) and neutrinos ( $\nu$ ); a summary is depicted in fig. 2.1.



<sup>3</sup> Aartsen et al. “Evidence for High-Energy Extraterrestrial Neutrinos at the IceCube Detector” (2013).

**Figure 2.1:** Graphical depiction of different messenger particles. Shown are cosmic rays ( $p$ ) in red, gamma rays ( $\gamma$ ) in cyan and neutrinos ( $\nu$ ) in green color. Also included are graphical representations of the distinct particle paths from a potential source. Image courtesy of the IceCube Collaboration.

Cosmic rays are high-energy charged particles composed primarily of protons but also heavier nuclei<sup>4</sup> traversing the universe. Since they are charged, their paths are influenced heavily by intergalactic magnetic fields via the Lorentz force. Thus, using them to point back to sources is generally considered difficult but might be possible at the highest energies<sup>5</sup>. Nevertheless, the primary cosmic ray spectrum and its features give hints on different particle accelerating process within and outside our Galaxy. Although, the sources and processes responsible for the highest observed cosmic ray energies remain uncertain as of today. More details on cosmic rays are discussed in

<sup>4</sup> Aab et al. “Combined fit of spectrum and composition data as measured by the Pierre Auger Observatory” (2017).

<sup>5</sup> Sommers et al. “Cosmic ray astronomy” (2009).

section section 2.2.

Gamma rays, on the other hand, are not deflected by magnetic fields and as such are suited for pointing to potential sources. The drawback of photons is their interaction within interstellar medium via processes like Compton scattering which can attenuate and obscure potential source observations and thus can limit the observable distance of gamma ray sources. Nevertheless, with current means, high-energy gamma rays are a primary candidate for source detection and were the key counterpart in the coincident observation of the first potential neutrino point source, discussed in more detail in section 2.3.4.

Neutrinos are finally the messenger particles which are impacted the least by the environment along their path as they are neutral particles and only interact weakly. Weak interactions are mediated by the exchange of the heavy  $W^\pm$  and  $Z^0$  bosons which results in very low cross sections with respect to hadronic or electromagnetic processes. While that enables propagation from their potential source essentially undisturbed, it makes statistically significant detection on Earth extremely difficult; the latter is discussed in detail in chapter 4. However, the means of directly probing these violent astrophysical objects make neutrinos unique messengers to gain insight into the physics processes at their sources. Moreover, detecting neutrinos from a point source provides a strong hint towards hadronic processes happening at the source as neutrinos are mainly generated via charged meson decays, primarily pions<sup>6</sup>, via for example

$$\pi^+ \rightarrow \mu^+ + \nu_\mu \quad (2.1)$$

or similar processes. The pions themselves are believed to be generated by two main mechanisms, that is, inelastic proton-proton scattering or the resonant annihilation of proton and photon

$$p + p \rightarrow X + \pi^+ \quad (2.2)$$

$$p + \gamma \rightarrow \Delta^+ \rightarrow n + \pi^+ \quad (2.3)$$

The neutrino generation processes dominating at the source will further impact the emission ratios of the three known neutrino flavors  $\nu_e$ ,  $\nu_\mu$  and  $\nu_\tau$  which in turn provide a potential handle to understand the physics processes involved<sup>7,8</sup>. As such, it is a current task of neutrino observatories to disentangle the observed flavor ratios in order to potentially probe the processes inside cosmic accelerators which, however, is a complicated task.

Summarizing, the means of complementing observations with the different messengers provides the grounds for multi-messenger astronomy. Here, the recent addition of neutrino observations by large-volume detectors provides promising grounds for this new type of astronomy as further advancements in detector hardware and calibration are made. Nevertheless, it should be noted that the future might also include the coincident observation of gravitational waves as, for example, observations by the LIGO observatory<sup>9</sup>. The inclusion of gravitational waves will further extend the importance of this new multi-messenger era and potentially boost our understanding of astrophysical processes in the universe.

<sup>6</sup> Anchordoqui et al. “Cosmic neutrino pevatrons: A brand new pathway to astronomy, astrophysics, and particle physics” (2014).

<sup>7</sup> Pakvasa “Neutrino Flavor Geometry by High Energy Astrophysical Beams” (2008).

<sup>8</sup> Anchordoqui et al. “Neutrinos as a diagnostic of high energy astrophysical processes” (2005).

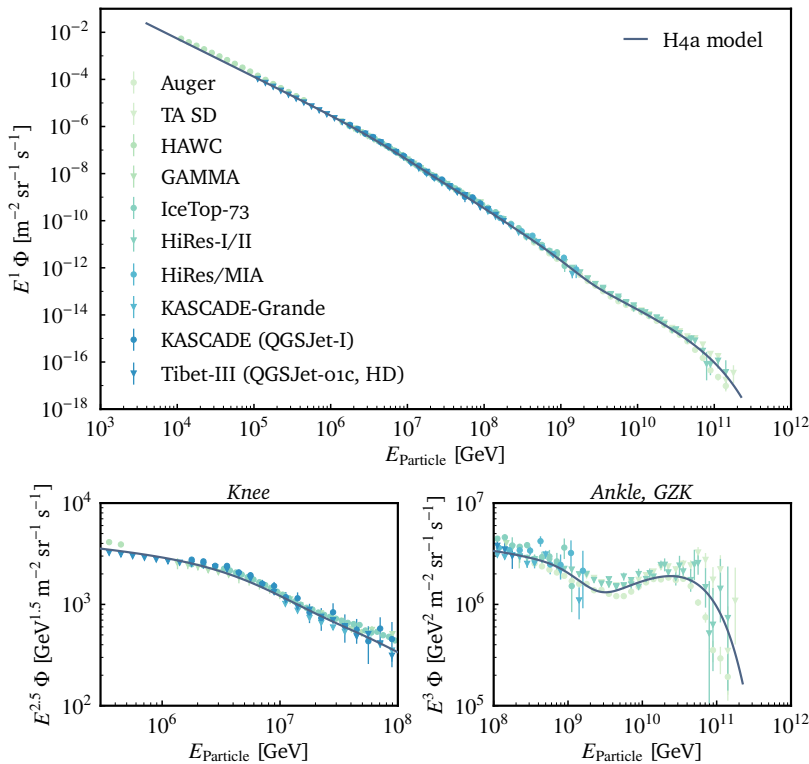
<sup>9</sup> Abbott et al. “GW170817: Observation of Gravitational Waves from a Binary Neutron Star Inspiral” (2017).

## 2.2 Cosmic rays & atmospheric neutrinos

Highly energetic charged particles, such as protons or heavier ionized atomic nuclei, propagating through the universe are commonly referred to as cosmic rays. First measured by Victor Hess in 1912<sup>10</sup>, the observation of cosmic rays and their properties has been an extensive field of study in astroparticle physics<sup>11,12</sup>. Over many orders of magnitude, the shape of the cosmic ray energy spectrum arriving at Earth can be described by an inverse *power-law* of the form<sup>12</sup>

$$\frac{d\phi}{dE} = \frac{d^4N}{dE dA d\Omega dt} \sim E^{-\gamma} \quad (2.4)$$

with the particle flux  $\phi$  arriving at Earth per energy  $E$ , area  $A$ , solid angle  $\Omega$  and time  $t$  and the shape described by spectral index  $\gamma$ . The measured all-particle cosmic ray spectrum is shown in fig. 2.2; reprocessed based on<sup>13</sup> and data courtesy by the authors of<sup>12</sup>.



<sup>10</sup> Hess “Über Beobachtungen der durchdringenden Strahlung bei sieben Freiballonfahrten” (1912).

<sup>11</sup> Watson “High-energy cosmic rays and the Greisen-Zatsepin-Kuz’min effect” (2014).

<sup>12</sup> Gaisser, T., Engel, R. and Resconi, E. “Cosmic Rays and Particle Physics” (2016).

<sup>13</sup> Henningsen “Optical Characterization of the Deep Pacific Ocean: Development of an Optical Sensor Array for a Future Neutrino Telescope” (2019).

**Figure 2.2:** All-particle high-energy cosmic ray spectrum as a function of particle energy. The upper plot shows the full energy spectrum with data from various experiments. The lower plots show enhanced versions of the spectrum in the knee region (left) and the ankle region (right). In order to enhance features of the spectrum, the latter have been multiplied by  $E^{2.5}$  and  $E^3$ , respectively. Also included is a current high-energy model. Details on the spectrum, its features and references to used data are given in the text.

With a spectral index of  $\gamma = 2.7$  the spectrum can be well described from energies of 10 GeV up until around 3 PeV<sup>12</sup>. While the cosmic ray composition for lower energies is heavily influenced by solar modulations<sup>12,14</sup>, this intermediate energy regime already shows a first distinct feature known as the *knee*. The knee is believed to represent the decline of the population of cosmic ray energies originating from galactic accelerators such as supernova remnants<sup>12</sup>. The second part of the spectrum, up until roughly 1 EeV, can be described by a spectral index of  $\gamma = 3.1$  until the spectrum starts to flatten again at what is called the *ankle*. The ankle is postulated to arise from the end the galactic and the beginning of the extragalactic cosmic ray contribution<sup>12</sup>. For energies above the ankle, the spectrum can

<sup>14</sup> Spurio “Particles and Astrophysics: A Multi-Messenger Approach” (2017).

be described by a spectral index of  $\gamma = 2.6$  until an abrupt cutoff at around  $10^{20}$  eV. The reason for this cut-off is not clearly identified. It is possible to either reflect the maximum acceleration power in astrophysical objects<sup>12,15</sup> or a potential dampening of the cosmic ray flux due to an interaction resonance with photons from the cosmic microwave background (CMB). The latter was first postulated in 1966 by Greisen<sup>16</sup> as well as by Zatsepin and Kuzmin<sup>17</sup> to be the resonant pion production of protons with the CMB as

$$p + \gamma_{\text{CMB}} \rightarrow \Delta^+ \rightarrow \begin{cases} p + \pi^0 \\ n + \pi^+ \end{cases} \quad (2.5)$$

which can significantly reduce the cosmic ray flux above energies of around  $4 \times 10^{19}$  eV. While this particular resonance holds true for protons only, already early studies<sup>18,19</sup> have shown this cut-off energy remains similar also in the case of heavier nuclei comprising the highest-energy cosmic rays. Most importantly, the acceleration mechanisms for ultra-high-energy cosmic rays remain barely understood. It was Hillas in 1984 who generalized a potential maximum particle energy depending on conditions present at the accelerator<sup>15</sup>. A summary of such objects with respect to site conditions is shown in fig. 2.3; reprocessed based on<sup>20</sup> using data from<sup>12</sup>. Example objects of interest for the acceleration of ultra-high-energy cosmic rays are active galactic nuclei (AGNs), gamma-ray bursts (GRBs) and supernova remnants (SNRs) but also conventional stellar and galactic objects could provide appropriate environments.

<sup>15</sup> Hillas “The Origin of Ultra-High-Energy Cosmic Rays” (1984).

<sup>16</sup> Greisen “End to the Cosmic-Ray Spectrum?” (1966).

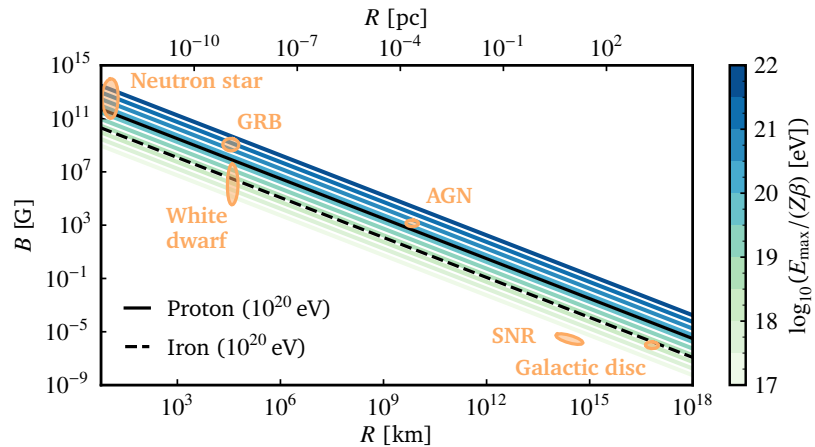
<sup>17</sup> Zatsepin et al. “Upper limit of the spectrum of cosmic rays” (1966).

<sup>18</sup> Hillas “The Effect of Intergalactic Propagation on the Energy Spectrum of Cosmic Ray Nuclei Above  $10^{15}$ -eV” (1975).

<sup>19</sup> Berezhinsky et al. “Metagalactic Nuclei of Ultrahigh-Energies” (1975).

<sup>20</sup> Huber “Multi-Messenger correlation study of Fermi-LAT blazars and high-energy neutrinos observed in IceCube” (2020).

**Figure 2.3:** Hillas plot showing high-energy cosmic accelerator conditions and resulting maximum particle energies. The color scale shows the maximum particle energy with respect to magnetic field strength ( $B$ ) and radius ( $R$ ) of the acceleration site as well as particle charge  $Z$ . Additionally included are the expected regions of known astrophysical objects. For details and references refer to the text.



Generally, there are two main detection principles for cosmic rays: direct detection in balloon- or space-born detectors and indirect detection using ground-based air-shower arrays. Eventhough the former only work in the low-energy regime due to detector size limitations, they allow precision measurements of the cosmic ray particle type and momentum up until roughly TeV-scales, as done for example in the PAMELA experiment<sup>21</sup>. At higher energies, these limited volumes do not allow a direct detection of cosmic rays anymore. However, in these energy ranges, cosmic rays can be detected indirectly via air showers induced in the atmosphere. Here, cosmic rays can inelastically scatter with present atoms and produce a cascade of secondary

<sup>21</sup> Galper et al. “The PAMELA experiment: a decade of Cosmic Ray Physics in space” (2017).

particles. These secondaries can iteratively induce the production of further particles by either decaying or interacting again with particles in the atmosphere. This cascade of particles continues until the initial energy deposition is depleted and is called an air shower; an example is depicted in fig. 2.4. Air-shower arrays make use of a multitude of detectors at ground level to detect these showers and thus indirectly observe cosmic rays. Prominent examples of such observatories are the Pierre Auger Observatory<sup>22</sup> or the Telescope Array<sup>23</sup>.

Naturally, also neutrinos are produced in air showers as the initially-produced mesons decay. These *atmospheric neutrinos* are commonly divided into two types: the *conventional* flux results from the decay of light mesons, such as pions or kaons, the *prompt* flux is the product of heavier meson or baryon decays with potential heavy-quark contributions. The conventional flux dominates the low-energy regime while the prompt flux becomes significant above energies of roughly  $10^6$  to  $10^7$  GeV<sup>24</sup> since these heavy intermediate hadrons have very short lifetimes and typically decay immediately, independent of energy. Thus, the spectrum of the prompt flux is expected to follow the primary spectrum. For the conventional flux, the hadronic secondaries traverse the atmosphere and, as such, their flux varies with energy and incident angle. Furthermore, the decay length for lighter mesons exceeds the interaction length at high energies, making the latter process more likely. Typically, the spectrum of atmospheric neutrinos is also described using an inverse power-law of the form eq. (2.4) with a spectral index similar to  $\gamma \sim 2.7$  for the prompt neutrino flux contribution at high energies<sup>25</sup>. Since interactions are dominant for the conventional secondaries, their spectrum is softer (that is larger in  $\gamma$ ) when compared to that of the decay-dominated heavier mesons. In fig. 2.5, a current model of the atmospheric neutrino flux<sup>24,26</sup> is shown together with data from selected experiments<sup>27–29</sup>.

### 2.3 Astrophysical neutrinos

In addition to atmospheric neutrinos, the universe hosts various astrophysical neutrino sources. These *astrophysical neutrinos* result from various processes and objects and hence cover a large range of neutrino energies. Prominent examples of low- to medium-energy neutrino production mechanisms are stellar fusion or supernovae but also violent environments, for instance AGNs or GRBs, or the interaction of ultra-high-energy cosmic rays with interstellar medium are expected to generate neutrinos, potentially with very high energies<sup>12,15</sup>.

The following paragraphs give a brief overview on the most common types of astrophysical neutrinos. A summary of various flux models and selected experimental results is shown in fig. 2.5; re-processed based on<sup>13</sup> with references for models and data given in section 2.2 as well as throughout sections 2.3.1 to 2.3.5 for atmospheric and all other contributions, respectively.

<sup>22</sup> Yamamoto “The first scientific results from the pierre auger observatory” (2006).

<sup>23</sup> Martens “The Telescope Array and its Low Energy Extension” (2007).

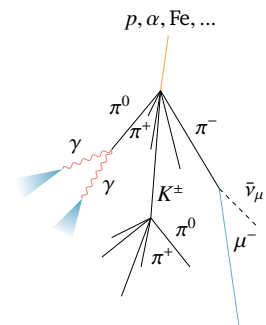


**Figure 2.4:** Illustration of an air shower induced by a primary cosmic ray. Graphic adapted from M. Nöthe (March 2021, [https://github.com/maxnoe/app\\_tikz\\_visualisations](https://github.com/maxnoe/app_tikz_visualisations))

<sup>24</sup> Fedynitch et al. “Calculation of conventional and prompt lepton fluxes at very high energy” (2015).

<sup>25</sup> Gaisser “Atmospheric Neutrinos” (2019).

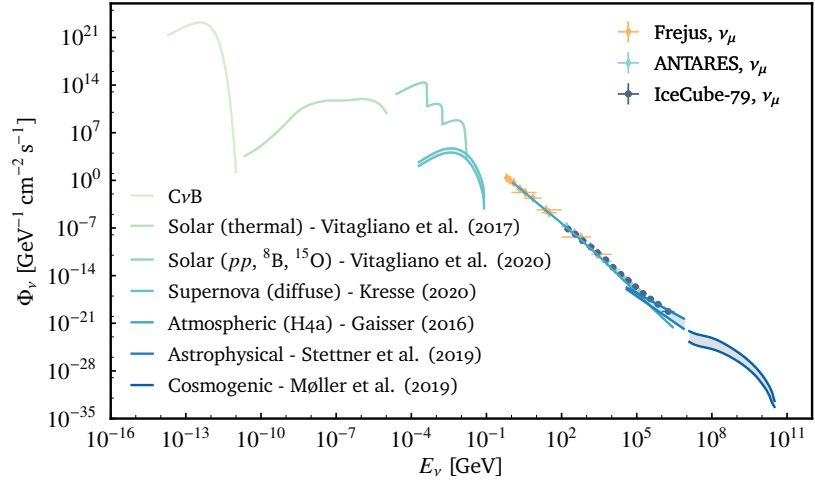
<sup>26</sup> Gaisser “Spectrum of cosmic-ray nucleons, kaon production, and the atmospheric muon charge ratio” (2012).

<sup>27</sup> Daum et al. “Determination of the atmospheric neutrino spectra with the Fréjus detector” (1995).

<sup>28</sup> ANTARES Collaboration et al. “Measurement of the atmospheric  $\nu_\mu$  energy spectrum from 100 GeV to 200 TeV with the ANTARES telescope” (2013).

<sup>29</sup> Aartsen et al. “Development of a General Analysis and Unfolding Scheme and its Application to Measure the Energy Spectrum of Atmospheric Neutrinos with Ice-Cube” (2015).

**Figure 2.5:** Neutrino flux models of various astrophysical origins as a function of energy including selected high-energy experimental results. If two lines are drawn for a specific contribution, they represent upper and lower bounds on the specific model. Details on the different contributions as well as references for the used models and data are given in the text.

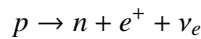


### 2.3.1 Relic neutrinos

One of the lowest-energy neutrino flux contributions is the thermal neutrino decoupling in the early universe. This *cosmic neutrino background* (or CvB) is expected from the plasma in the early universe cooling down enough so that neutrinos were able to decouple from the rest of the matter. This happened when the interaction length became larger than the observable universe at the time. It is estimated to have happened around 1 s after the Big Bang which corresponds to plasma temperatures of around  $k_B T \sim \text{MeV}$ . Due to the non-zero neutrino mass and the expansion and cooling of the universe, these neutrinos are expected to be at temperatures around 1.9 K today with a total neutrino density of around  $56 \text{ cm}^{-3}$  per neutrino flavor<sup>30</sup>. However, the weak nature of neutrinos and the extremely low energy makes this detection exceedingly difficult even though indirect searches<sup>31</sup> see first hints of the CvB.

### 2.3.2 Solar neutrinos

One of the closest neutrino sources to Earth is the Sun. As every active star, nuclear fusion in the Sun’s core upholds equilibrium against its own gravitational pressure. The governing process is the fusion of four protons to helium which includes the weak fusion of neutrons



via the release of electron neutrinos of intermediate energies in the range of a few to tens of MeV<sup>32</sup>. The two main helium fusion mechanisms are the *pp*-chain and the CNO-cycle with the dominant process depending on the mass of the star. These so-called *solar neutrinos* led the discovery of neutrino oscillations<sup>33</sup> due to a measured discrepancy between neutrino flavors, also known as the solar neutrino problem. The current scope of solar neutrino experiments is the precision determination of neutrino mixing parameters, as explained in more detail in chapter 3, as well as the further understanding of internal stellar processes in the Sun. For fig. 2.5, the fluxes from dominating contributions of the *pp*-chain and CNO-cycle<sup>34</sup> are drawn together

<sup>30</sup> Faessler et al. “Search for the Cosmic Neutrino Background” (2015).

<sup>31</sup> Follin et al. “First Detection of the Acoustic Oscillation Phase Shift Expected from the Cosmic Neutrino Background” (2015).

<sup>32</sup> Giunti et al. “Fundamentals of Neutrino Physics and Astrophysics” (2007).

<sup>33</sup> Ahmad et al. “Measurement of the rate of  $\nu_e + d \rightarrow p + p + e^-$  interactions produced by  $^8\text{B}$  solar neutrinos at the Sudbury Neutrino Observatory” (2001).

<sup>34</sup> Vitagliano et al. “Grand unified neutrino spectrum at Earth: Sources and spectral components” (2020).

with the flux of thermally-generated neutrinos from electromagnetic interactions in the Sun’s plasma <sup>35</sup>.

### 2.3.3 Supernova neutrinos

When stars run out of fusion material, they are not able to withstand their own gravitational pressure and collapse. Depending on the mass of the initial star, this can result in a violent explosion of the star known as a supernova. While there are different types of supernovae, for massive stars the core collapse supernova is believed to be the dominant mechanism. Here, the core of star – where matter is hottest and densest – eventually runs out of fusion material and the star collapses under its own gravitational pull. During the collapse, the core gets compressed immensely, fusing protons and electrons to neutrons and neutrinos and the resulting shock rips the star apart in a violent explosion. While the the exact hydrodynamics of supernovae are an active field of research, it is believed that neutrinos enable the explosion in the first place and carry away almost all of the released energy <sup>36,37</sup>. These neutrinos appear in all flavors and are postulated to reach energies of a few tens of MeV <sup>38</sup>. While only one distinct supernova – SN1987A – has been potentially observed by neutrino detectors <sup>39–41</sup>, the universe hosts so many stars that a diffuse, isotropic supernova neutrino background (DSNB) from the integral flux of all supernova explosions in the universe is expected. The detailed model calculations depend on many parameters including assumptions from cosmology. Figure 2.5 shows upper and lower bounds of one such potential model <sup>42</sup> representative of the DSNB.

### 2.3.4 High-energy astrophysical neutrinos

The observation of ultra-high-energy cosmic rays immediately suggests the presence of violent acceleration environments. With hadronic particles being part of these environments, it is natural to assume that high-energy neutrinos and gamma rays will be produced via intermediate meson states. One example is the creation of pions via the resonant interaction of hadrons with photons similar to eq. (2.5). Furthermore, the production of high-energy pions would not only result in high-energy neutrino but also coincident gamma-ray emission as pions provide weak and electromagnetic decay modes

$$\pi^0 \rightarrow \gamma\gamma \quad (2.6)$$

$$\pi^+ \rightarrow \mu^+ + \nu_\mu \rightarrow e^+ + \bar{\nu}_\mu + \nu_e + \nu_\mu \quad (2.7)$$

$$\pi^- \rightarrow \mu^- + \bar{\nu}_\mu \rightarrow e^- + \nu_\mu + \bar{\nu}_e + \bar{\nu}_\mu \quad (2.8)$$

which immediately suggest the prominent flavor ratio assumption for pion-dominated sources of  $(\nu_e : \nu_\mu : \nu_\tau) = (1 : 2 : 0)$ . This further reduces to flavor equipartition at Earth after averaging out neutrino oscillations <sup>43</sup>. However, depending the dominating process at the source, one expects a difference in the ratios of emitted neutrino (and anti-neutrino) flavors <sup>44</sup>. In addition to the prominent charged pion decay, typically considered are further the so-called muon-damped and neutron-decay scenarios <sup>45</sup>. In the former, strong magnetic fields

<sup>35</sup> Vitagliano et al. “Solar neutrinos at keV energies: thermal flux” (2017).

<sup>36</sup> Janka “Neutrino Emission from Supernovae” (2017).

<sup>37</sup> Müller “Hydrodynamics of core-collapse supernovae and their progenitors” (2020).

<sup>38</sup> Tamborra et al. “High-resolution supernova neutrino spectra represented by a simple fit” (2012).

<sup>39</sup> Bionta et al. “Observation of a neutrino burst in coincidence with supernova 1987A in the Large Magellanic Cloud” (1987).

<sup>40</sup> Alekseev et al. “Possible Detection of a Neutrino Signal on 23 February 1987 at the Baksan Underground Scintillation Telescope of the Institute of Nuclear Research” (1987).

<sup>41</sup> Hirata et al. “Observation of a Neutrino Burst from the Supernova SN 1987A” (1987).

<sup>42</sup> Kresse et al. “Stellar Collapse Diversity and the Diffuse Supernova Neutrino Background” (2020).

<sup>43</sup> Learned et al. “Detecting  $\nu_\tau$  oscillations at PeV energies” (1995).

<sup>44</sup> Kashti et al. “Astrophysical Neutrinos: Flavor Ratios Depend on Energy” (2005).

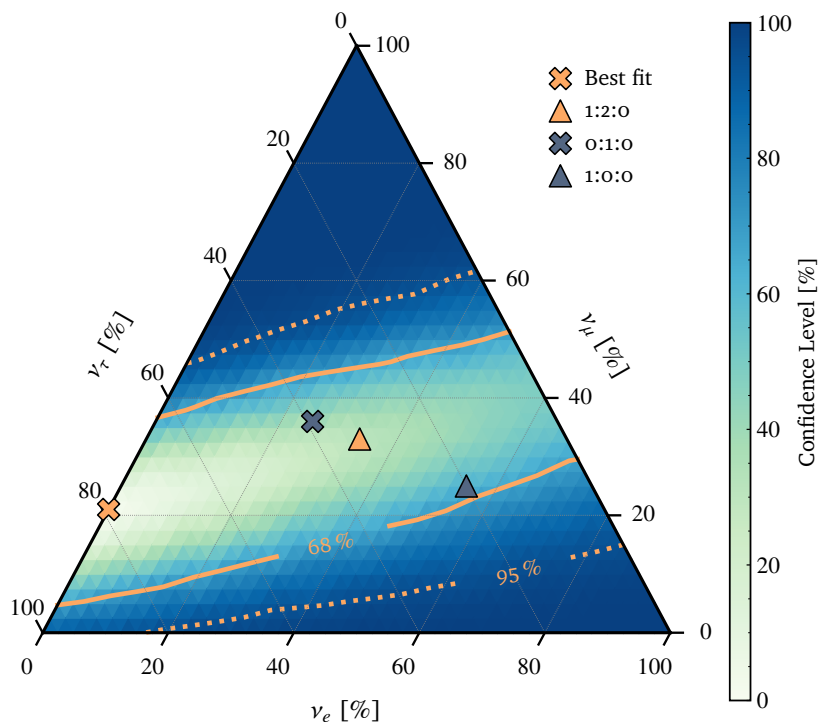
<sup>45</sup> Palladino “The flavor composition of astrophysical neutrinos after 8 years of IceCube: an indication of neutron decay scenario?” (2019).

present at the source result in significant muon energy losses prior to decay. This removes the secondary muon decay channel of eqs. (2.7) and (2.8) for high-energy neutrinos and thus results in a source flux flavor ratio of (0 : 1 : 0). Finally, the last scenario depicts the creation of neutrinos via the decay of neutrons which would remove the muon component of the neutrino flux and provide a source distribution of (1 : 0 : 0). Probing the flavor composition of the astrophysical neutrino flux is one possibility to assess the physics processes involved in cosmic accelerators, however, poses challenging as flavor differentiation of high-energy neutrino observations is difficult. A current high-energy flavor composition measurement by the IceCube experiment<sup>46</sup> is drawn<sup>47</sup> in fig. 2.6 including different source model predictions which, however, are all in agreement with the best fit.

<sup>46</sup> Aartsen et al. “Measurements using the inelasticity distribution of multi-TeV neutrino interactions in IceCube” (2019).

<sup>47</sup> Harper et al. “python-ternary: Ternary Plots in Python” (2021).

**Figure 2.6:** Flavor ratio measurement for high-energy astrophysical neutrinos detected by IceCube including different source models. The latter show the oscillation-averaged fluxes at Earth with different source emission flavor ratios of  $(\nu_e : \nu_\mu : \nu_\tau)$ . Here, the best fit agrees with all shown source models and can not distinguish between them. For references on the used data as well as details on model assumptions refer to the text.



Generally, the measurement of *astrophysical neutrinos* can be divided into *diffuse* and *point-source* observations. The former is – similar to the CνB for very low energies – an integral flux of all high-energy neutrino sources in the universe impinging on Earth. This diffuse astrophysical neutrino flux has been measured by IceCube and shows a spectral index of around  $\gamma \approx 2.3 - 2.7$  depending on the considered event selection<sup>48–50</sup>. In fig. 2.5, the ten-year IceCube diffuse astrophysical muon neutrino flux<sup>48</sup> is shown using its 99 % confidence interval. The point-source measurement of neutrino signals is considerably more difficult as current means limit the angular resolution with which neutrinos can be traced back to potential sources – refer to chapter 4 for an in-depth description of neutrino event topologies and detection limitations in large-volume detectors. However, for the first time, compelling evidence for a potential neutrino point source has been found. The object TXS0506+056 is a blazar – that is, an AGN with its jet pointing towards Earth – and was found to show coincident emission excesses of neutrinos and gamma rays<sup>1,2</sup>.

<sup>48</sup> Stettner “Measurement of the Diffuse Astrophysical Muon-Neutrino Spectrum with Ten Years of IceCube Data” (2019).

<sup>49</sup> Aartsen et al. “Characteristics of the Diffuse Astrophysical Electron and Tau Neutrino Flux with Six Years of IceCube High Energy Cascade Data” (2020).

<sup>50</sup> Abbasi et al. “The IceCube high-energy starting event sample: Description and flux characterization with 7.5 years of data” (2020).

These excesses were found in an archival data search triggered by a high-energy neutrino event detected in 2017. This first point-source observation marks the dawn of a new multi-messenger era.

### 2.3.5 *Cosmogenic neutrinos*

One of the highest-energy neutrino flux contributions is expected from the GZK-effect. Here, neutrinos result from the decay of mesons produced in cosmic ray interactions with photons from the CMB – example given for protons in eq. (2.5). While the detailed resonance behaviour depends on the chemical composition of cosmic rays, for both light and heavy nuclei dominating the cosmic ray composition at the highest energies, the production of ultra-high-energy neutrinos is expected<sup>51</sup>. Nevertheless, modeling of *cosmogenic neutrinos* depends on various parameters related to cosmic rays and their sources<sup>52,53</sup> and thus is an active research interest in the field. However, due to the low flux, a significant observation remains difficult<sup>54,55</sup>. In fig. 2.5, one potential flux estimate<sup>34,51</sup> is given using two distinct composition models for upper and lower bounds.

<sup>51</sup> Møller et al. “*Cosmogenic neutrinos through the GRAND lens unveil the nature of cosmic accelerators*” (2019).

<sup>52</sup> Ahlers et al. “*Minimal cosmogenic neutrinos*” (2012).

<sup>53</sup> Ahlers “*High-energy Cosmogenic Neutrinos*” (2015).

<sup>54</sup> Yacobi et al. “*Implication of the Non-detection of gzk Neutrinos*” (2016).

<sup>55</sup> Aartsen et al. “*Differential limit on the extremely-high-energy cosmic neutrino flux in the presence of astrophysical background from nine years of Ice-Cube data*” (2018).



# 3

## Neutrino mass, mixing and oscillations

In the Standard Model (SM) of particle physics neutrinos are neutral leptons without mass. Today it is a well-established experimental fact that neutrinos are massive, providing a first hint towards physics beyond the SM. In fact, it was as early as 1957 when Pontecorvo postulated the possibility of neutrinos oscillating between different states<sup>56</sup>. While his knowledge about neutrinos was limited at the time, it is clear today that neutrinos can in fact change between flavors when propagating. Nevertheless, it took almost forty years for this to be experimentally established. Around the turn of the millennium, two experiments pioneered in measuring the effect of neutrino oscillations: the *Super-Kamioka Neutrino Detection Experiment* (Super-K) reported oscillatory signatures of atmospheric neutrinos<sup>57</sup> and the *Sudbury Neutrino Observatory* (SNO) observed an excess of non-electron neutrinos in the solar neutrino flux<sup>58</sup> only explainable with neutrinos changing flavor on their way to Earth. These two observations were awarded the Nobel Prize in Physics in 2015. This chapter introduces the theory of neutrino oscillations in vacuum and matter, outlines experimental results representative of the efforts in the sector of neutrino mixing today and closes with a summary of the importance of oscillations on astrophysical neutrino observations.

<sup>56</sup> Pontecorvo “*Inverse beta processes and nonconservation of lepton charge*” (1957).

<sup>57</sup> Fukuda et al. “*Evidence for Oscillation of Atmospheric Neutrinos*” (1998).

<sup>58</sup> Ahmad et al. “*Direct Evidence for Neutrino Flavor Transformation from Neutral-Current Interactions in the Sudbury Neutrino Observatory*” (2002).

### 3.1 Neutrino oscillation in vacuum

Neutrinos in the SM can interact with other particles via the weak force in charged-current (CC) and neutral-current (NC) interactions. These interactions are mediated by the  $W^\pm$  or the  $Z^0$  boson, respectively. Following common literature e.g. <sup>32,59</sup>, the corresponding Lagrangians can be written as

$$\mathcal{L}_{\text{CC}} = -\frac{g}{2\sqrt{2}} j_\rho^{\text{CC}} W^\rho + \text{h.c.} \quad (3.1)$$

$$\mathcal{L}_{\text{NC}} = -\frac{g}{2\cos\theta_W} j_\rho^{\text{NC}} Z^\rho \quad (3.2)$$

with the gauge coupling constant  $g$  of the weak symmetry group  $\text{SU}(2)_L$ , the weak mixing angle  $\theta_W$  and the charged and neutral currents  $j_\rho$ . Due to symmetry, right-handed particles do not take part in weak SM interactions and so the currents

$$j_\rho^{\text{CC}} = 2 \sum_{\alpha=e,\mu,\tau} \overline{\nu_{\alpha L}} \gamma_\rho \ell_{\alpha L} + \dots \quad (3.3)$$

$$j_\rho^{\text{NC}} = 2 \sum_{\alpha=e,\mu,\tau} \overline{\nu_{\alpha L}} \gamma_\rho \ell_{\alpha L} + \dots \quad (3.4)$$

contain only left-handed neutrino fields  $\nu_{\alpha L}$  in addition to the leptonic

<sup>59</sup> Bilenky et al. “*Phenomenology of neutrino oscillations*” (1999).

fields  $\ell_\alpha$ . Note that in eqs. (3.3) and (3.4) only contributions with neutrino fields were written explicitly.

Now, if neutrinos are in fact massive, a neutrino with flavor  $\alpha$ , which was produced in some weak CC interaction, can be written as a superposition of neutrino mass states  $k$ , that is

$$|\nu_\alpha\rangle = \sum_k^n U_{\alpha k}^* |\nu_k\rangle \quad (\alpha = e, \mu, \tau) \quad (3.5)$$

with some matrix element  $U_{\alpha k}^*$  accounting for a potential tilt of the flavor basis with respect to the mass basis. Here, the unitary matrix  $U$  is commonly referred to as the Pontecorvo-Maki-Nakagawa-Sakata (PMNS) matrix, honoring contributions of pioneers in neutrino oscillation theory<sup>56,60</sup>. In three generations ( $n = 3$ ), this matrix can be written as

$$U = \begin{pmatrix} 1 & 0 & 0 \\ 0 & c_{23} & s_{23} \\ 0 & -s_{23} & c_{23} \end{pmatrix} \begin{pmatrix} c_{13} & 0 & s_{13}e^{-i\delta} \\ 0 & 1 & 0 \\ -s_{13}e^{-i\delta} & 0 & c_{13} \end{pmatrix} \begin{pmatrix} c_{12} & s_{12} & 0 \\ -s_{12} & c_{12} & 0 \\ 0 & 0 & 1 \end{pmatrix} \quad (3.6)$$

with the sine and cosine of the weak mixing angle  $\theta_{ij}$  denoted as  $s_{ij}$  and  $c_{ij}$ , respectively as well as a CP-violating phase  $\delta$ . While it is not yet known whether neutrinos are identical to their antiparticles (Majorana particles) or not (Dirac particles), in the case of the former the matrix  $U$  would have to be extended with two additional phases. However, since these phases do not alter observables of neutrino oscillations<sup>61</sup>, they will be omitted here. In general, unitarity of  $U$  would be broken in the three-generation case if there would exist additional neutrino states ( $n > 3$ ) that do not take part in weak interactions but contribute to neutrino mixing via non-zero matrix elements. Such particles are commonly referred to as *sterile neutrinos* and searching for hints of them is an active research topic in particle and astroparticle physics.

In any case, the propagation of neutrinos is governed by the free vacuum Hamiltonian. While the neutrino interactions occur in the flavor basis, the propagation is governed by the mass basis. In general, cosmology<sup>62</sup> and neutrino experiments<sup>63</sup> provide upper limits on the neutrino masses which, however, appear to be in the small (or even sub-) eV range. Thus, neutrinos are very light and can generally be viewed as ultra-relativistic. This justifies the approximation  $E_i = \sqrt{\vec{p}_i^2 + m_i^2} \approx E + m_i^2/2E$  with  $E \simeq |\vec{p}|^2$  and applying the Schrödinger equation for time evolution to eq. (3.5) eventually allows a formulation of the transition probability for an initial neutrino of flavor  $\alpha$  to be observed in flavor  $\beta$ , after propagating a length  $L = ct$ . In natural units it reads<sup>12</sup>

$$P_{\alpha \rightarrow \beta} = \delta_{\alpha\beta} - 4 \sum_{i>j} \Re(U_{\beta j}^* U_{\alpha j} U_{\beta i} U_{\alpha i}^*) \sin^2\left(\frac{\Delta m_{ij}^2 L}{4E}\right) + 2 \sum_{i>j} \Im(U_{\beta j}^* U_{\alpha j} U_{\beta i} U_{\alpha i}^*) \sin\left(\frac{\Delta m_{ij}^2 L}{2E}\right) \quad (3.7)$$

<sup>60</sup> Maki et al. “Remarks on the Unified Model of Elementary Particles” (1962).

<sup>61</sup> Bilenyk et al. “On Oscillations of Neutrinos with Dirac and Majorana Masses” (1980).

<sup>62</sup> Aghanim et al. “Planck 2018 results” (2020).

<sup>63</sup> Aker et al. “Improved Upper Limit on the Neutrino Mass from a Direct Kinematic Method by KATRIN” (2019).

Here, the squared mass differences  $\Delta m_{ij}^2 = m_i^2 - m_j^2$  result in phase shifts for the different mass eigenstates during propagation if their masses are different. These phase shifts eventually result in a mixing of mass eigenstates and thus in a mixing of flavor content as a function of time. This non-zero probability of observing a different neutrino flavor with respect to the one initially produced is called neutrino oscillation. Commonly, the mass differences  $\Delta m_{21}^2$  and  $\Delta m_{31}^2$  are referred to as the *solar* and *atmospheric mass splitting*, respectively, due to respective sensitivities of pioneer oscillation experiments. A current best-fit of the PMNS matrix elements<sup>64</sup> is depicted in fig. 3.1 and current best-fit results of oscillation parameters<sup>65</sup> are given in table 3.1. It is important to note that while the sign of  $\Delta m_{21}^2$  is known to be positive from matter effects (refer to section 3.2), the sign of  $\Delta m_{31}^2$  is unknown as of today. Nevertheless, a positive sign is commonly referred to as *normal* (NH) and a negative sign to *inverted mass hierarchy* (IH). In the figure and table, results for both orderings are shown. The investigations related to clarifying the neutrino mass ordering are an active field in neutrino physics and usually make use of different neutrino sources to study a particular set of mixing parameters.

Parameter	Unit	Best fit (90% CL)	
		NH	IH
$\Delta m_{21}^2$	$10^{-5} \text{ eV}^2$	$7.53 \pm 0.18$	
$ \Delta m_{32}^2 $	$10^{-3} \text{ eV}^2$	$2.45 \pm 0.03$	$2.55^{+0.03}_{-0.04}$
$\sin^2 \theta_{12}$	$10^{-1}$	$3.07^{+0.13}_{-0.12}$	
$\sin^2 \theta_{23}$	$10^{-1}$	$5.45 \pm 0.21$	$5.47 \pm 0.21$
$\sin^2 \theta_{13}$	$10^{-2}$	$2.18 \pm 0.07$	
$\delta$	$\pi$	$1.36 \pm 0.17$	

### 3.2 Matter effects

The presence of electrons and nucleons in regular matter influences neutrino oscillations as it provides a coherent forward scattering channel for neutrinos<sup>32</sup>. Already early studies by Wolfenstein<sup>66</sup> as well as Mikheyev and Smirnov<sup>67,68</sup> have shown that matter can significantly change oscillation behavior with respect to the vacuum case. While a thorough theoretical treatment<sup>e.g. 32,66–73</sup> exceeds the scope of this work, the main change is in the effective Hamiltonian where the vacuum case  $H_0$  is extended by the effective matter potential  $V$

$$H = H_0 + V, \quad \text{with} \quad V = V_e - V_{\mu,\tau} = \sqrt{2} G_F n_e \quad (3.8)$$

with the Fermi coupling constant  $G_F$  and the electron number density in the medium  $n_e$ . Note that the neutral-current contribution cancels out as it is the same for all channels and the sign of the potential flips for antineutrinos. However, this further means the eigenstates

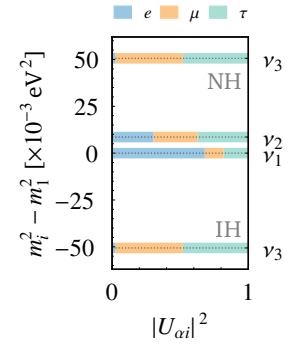


**Figure 3.1:** Neutrino mass ordering and flavor content of the mass eigenstates  $\nu_1$ ,  $\nu_2$  and  $\nu_3$ . The colors show the different neutrino flavor contributions from electron ( $e$ ), muon ( $\mu$ ) and tau ( $\tau$ ) to the mass eigenstates. Both a normal (NH) and an inverted (IH) mass hierarchy are depicted, showing  $\Delta m_{31}^2 = \pm 1$ , respectively. For details on the used data refer to the text.

<sup>64</sup> Ellis et al. “Current and future neutrino oscillation constraints on leptonic unitarity” (2020).

<sup>65</sup> Zyla et al. “Review of Particle Physics” (2020).

**Table 3.1:** Current knowledge of neutrino mixing parameters given as the 90% confidence levels for both normal (NH) and inverted (IH) hierarchies. Reference to data in the text.

<sup>66</sup> Wolfenstein “Neutrino oscillations in matter” (1978).

<sup>67</sup> Mikheyev et al. “Resonance Amplification of Oscillations in Matter and Spectroscopy of Solar Neutrinos” (1985).

<sup>68</sup> Mikheev et al. “Resonant amplification of neutrino oscillations in matter and solar neutrino spectroscopy” (1986).

<sup>69</sup> Akhmedov “Neutrino physics” (1999).

<sup>70</sup> Smirnov “The MSW effect and solar neutrinos” (2003).

<sup>71</sup> Gonzalez-Garcia et al. “Neutrino masses and mixing: Evidence and implications” (2003).

<sup>72</sup> Horoi “On the MSW neutrino mixing effects in atomic weak interactions and double beta decays” (2018).

<sup>73</sup> Mondal “Physics of Neutrino Oscillation” (2015).

in matter  $\nu_m$  – and subsequently the mixing angles in matter – are different with respect to the vacuum case. Thus, propagation is now defined by an altered evolution equation which reads in flavor basis<sup>69</sup>

$$i \frac{\partial}{\partial t} \begin{pmatrix} \nu_e \\ \nu_\mu \\ \nu_\tau \end{pmatrix} = \left[ \frac{1}{2E} U \begin{pmatrix} m_1^2 & 0 & 0 \\ 0 & m_2^2 & 0 \\ 0 & 0 & m_3^2 \end{pmatrix} U^\dagger + \begin{pmatrix} V & 0 & 0 \\ 0 & 0 & 0 \\ 0 & 0 & 0 \end{pmatrix} \right] \begin{pmatrix} \nu_e \\ \nu_\mu \\ \nu_\tau \end{pmatrix} \quad (3.9)$$

While this equation is generally treated numerically, a two-flavor approximation is sufficient to introduce some of the matter-induced effects on neutrino oscillations. Here, again making use of the assumption of neutrinos being ultra-relativistic, this reduces to<sup>69</sup>

$$i \frac{\partial}{\partial t} \begin{pmatrix} \nu_e \\ \nu_\mu \end{pmatrix} = \begin{pmatrix} -\frac{\Delta m^2}{4E} \cos 2\theta_0 + \sqrt{2} G_F n_e & \frac{\Delta m^2}{4E} \sin 2\theta_0 \\ \frac{\Delta m^2}{4E} \sin 2\theta_0 & \frac{\Delta m^2}{4E} \cos 2\theta_0 \end{pmatrix} \begin{pmatrix} \nu_e \\ \nu_\mu \end{pmatrix} \quad (3.10)$$

<sup>a</sup> Note that vacuum mixing in the two-flavor approximation is implied, that is  $\Delta m^2 \equiv m_2^2 - m_1^2$  and  $\theta_0 = \theta_{12}$

which describes mixing of  $\nu_e \leftrightarrow \nu_\mu$ <sup>a</sup> in the presence of matter. For flavor conversions  $\nu_e \leftrightarrow \nu_\tau$  this equation has the same form only adjusted with different mixing parameters. It should be noted that, while not included in this basic two-flavor approximation, in the three-flavor treatment the mixing of  $\nu_\mu \leftrightarrow \nu_\tau$  is also influenced by matter due to the non-zero mixing contributions of  $\nu_e$  in all dimensions<sup>69</sup>. Now, it is clear that the presence of matter alters the evolution equation of the neutrino flavors and thus the mixing itself. Solving eq. (3.10) with the simplest assumption of a constant matter density along the neutrino propagation path yields an effective oscillation probability<sup>69</sup>

$$P(\nu_e \rightarrow \nu_\mu) \sim \frac{\left(\frac{\Delta m^2}{4E}\right)^2 \sin^2 2\theta_0}{\left(\frac{\Delta m^2}{4E} \cos 2\theta_0 - \sqrt{2} G_F n_e\right)^2 + \left(\frac{\Delta m^2}{4E}\right)^2 \sin^2 2\theta_0} \quad (3.11)$$

with possible resonant mixing amplification when

$$\sqrt{2} G_F n_e = \frac{\Delta m^2}{2E} \cos 2\theta_0 \quad (3.12)$$

This resonance implies that mixing in matter can be large even if it is small in vacuum. It was subsequently dubbed the *Mikheyev-Smirnov-Wolfenstein (MSW) resonance* honoring the pioneers in the field of matter oscillation theory<sup>66,68</sup>.

In a more realistic setting neutrinos encounter varying matter densities along their path. Here, alterations of the vacuum oscillations are primarily driven by the the density profile of the encountered matter and are generally treated numerically. In the matter mass eigenstates basis, the off-diagonal elements of the Hamiltonian govern the transitions between different matter mass eigenstates during propagation. These off-diagonal terms depend on the density gradient and are only non-negligible if they are comparable in size to the diagonal terms<sup>32</sup>. Thus, in the special scenario where the density profile changes smoothly and slowly – as is the case, for example, in stars – no transitions between the mass eigenstates occur. This is called *adiabatic conversion* as it converts the matter mass eigenstates at neutrino

production smoothly to their respective vacuum states. However, as the density changes, so does the mixing angle and thus the flavor composition of this mass eigenstate. This so-called *MSW effect* leads to an observed deficit of electron neutrinos in the solar neutrino flux as electron neutrinos, produced in the dense core, are adiabatically transformed to a vacuum mass eigenstate which, depending on the vacuum mixing angles, only contains a certain admixture of electron flavor. Furthermore, since the sign of the potential in eq. (3.8) flips for antineutrinos, this effect can only occur for particles or antiparticles. Finally, this broken particle-antiparticle degeneracy of the MSW effect eventually allowed determination of the sign of the solar mass splitting  $\Delta m_{21}^2$  to be positive as it affects the flavor composition of neutrino and antineutrino fluxes in both solar and reactor neutrino experiments<sup>58,65,74–76</sup>. While there are other matter-induced effects on neutrino oscillations<sup>e.g. 32,77,78</sup>, due to theoretical complexity, they will be omitted here.

### 3.3 Oscillation effects in astrophysics

Experimental observations of astrophysical neutrinos are inherently altered by the presence of flavor oscillations. On the one hand, oscillatory effects can help disentangle degeneracies of mixing parameters as in the example of the MSW effect for the solar neutrino flux (section 3.2). On the other hand, they also affect, and potentially wash out, the flavor ratios of astrophysical neutrino sources making it more difficult to assess the physical processes involved in the generation and acceleration of the highest-energetic particles. Here, if neutrinos travel astronomical distances, the finite experimental resolution in energy and distance makes it impossible to target the explicit phase of the oscillatory signature. Instead, a mean effect is observed since the oscillatory terms in eq. (3.7) average on large distances due to<sup>79,80</sup>

$$\langle \sin^2 x \rangle \rightarrow \frac{1}{2} \quad \langle \sin x \rangle \rightarrow 0 \quad (3.13)$$

which smears out the initial flavor ratio at the source. Eventhough the most prominent source models – namely pion decay, muon damping and neutron decay – are assumed to show distinct flavor ratios ( $\nu_e : \nu_\mu : \nu_\tau$ ) at the source, these are altered on astronomical distances due to oscillations and yield approximately<sup>45</sup>

$$(1 : 2 : 0)_S \rightsquigarrow (1 : 1 : 1) \quad (\text{pion decay}) \quad (3.14)$$

$$(0 : 1 : 0)_S \rightsquigarrow (1 : 2 : 2) \quad (\text{muon damping}) \quad (3.15)$$

$$(1 : 0 : 0)_S \rightsquigarrow (2 : 1 : 1) \quad (\text{neutron decay}) \quad (3.16)$$

Figure 3.2 shows this effect as a function of the ratio  $L/E$  for the relative fluxes of  $\nu_\mu$  and  $\nu_\tau$  with respect to  $\nu_e$  using a current set of best-fit values and 90% confidence levels given in table 3.1; reprocessed based on<sup>20</sup>. Here, the averaging effect of oscillations on distinct initial flavor ratios is clearly visible. Further this means that – independent of the source model – typically all neutrino flavors can be detected and precision measurements of the flavor ratio are necessary to identify a distinct dominant physical process responsible for high-energy

<sup>74</sup> Eguchi et al. “First Results from KamLAND: Evidence for Reactor Antineutrino Disappearance” (2003).

<sup>75</sup> Fogli et al. “Evidence for the MSW effect” (2004).

<sup>76</sup> Agostini et al. “Comprehensive measurement of pp-chain solar neutrinos” (2018).

<sup>77</sup> Akhmedov “Neutrino oscillations in inhomogeneous matter. (In Russian)” (1988).

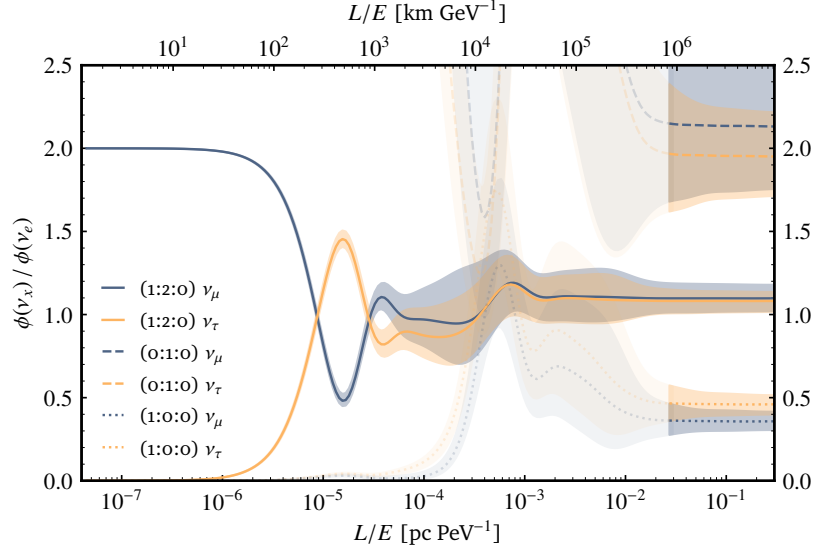
<sup>78</sup> Akhmedov “Parametric resonance of neutrino oscillations and passage of solar and atmospheric neutrinos through the earth” (1999).

<sup>79</sup> ATHAR et al. “Intrinsic and oscillated astrophysical neutrino flavor ratios revisited” (2006).

<sup>80</sup> Coenders “High-energy cosmic ray accelerators: searches with IceCube neutrinos” (2016).

neutrino emission. However, as mentioned in section 2.3.4, this is difficult for current experiments since it is challenging to differentiate flavors in astrophysical neutrino observations of large-volume detectors. A detailed description of these detection mechanisms and their respective difficulties is given in chapter 4.

**Figure 3.2:** Neutrino oscillations on astronomical distance scales. Shown are the 90% flux bands of  $\nu_\mu$  and  $\nu_\tau$  relative to the flux of  $\nu_e$  as a function of  $L/E$  given the best fit parameters in table 3.1. These flux ratios are further shown for different source model flavor ratio assumptions ( $\nu_e : \nu_\mu : \nu_\tau$ ). For visibility, all except the pion-decay source model (1 : 2 : 0) are shaded in intermediate regions and were smoothed with a Gaussian kernel to reflect finite detector resolution. For figure references and details refer to the text.



# 4

## Large-volume detectors, systematics and calibration

Neutrinos, albeit impinging on earth from various sources throughout the universe, are solely weakly interacting particles and, thus, hard to detect. This chapter first outlines detection principles for neutrinos as well as the necessary physics. Then, the goal of detecting high-energy neutrinos using large-volume neutrino telescopes is outlined using current and future detectors. Then, the chapter closes with a general description of light propagation within water- and ice-based detectors as well as related systematic effects and calibration methods.

### 4.1 Neutrino detection principles

In general, the weak nature of neutrinos makes detection inherently difficult as the interaction rates compare poorly to electromagnetic or hadronic interactions. Thus, neutrino detectors typically require large target masses to try and counteract these small detection cross sections and, most importantly, to observe significant numbers of the intended neutrino interactions. There are numerous neutrino detector types<sup>e.g.</sup><sup>81</sup> being used by past and current experiments especially concerning the measurement of low- to medium-energy neutrinos as emitted by the Sun or nuclear reactors. Here, artificial volumes of tens to hundreds of cubic metres are typically filled with appropriate material which facilitates the detection of neutrinos via, for example, radiochemical neutrino capture in the pioneering experiments *Homestake*<sup>82</sup> as well as *GALLEX*<sup>83</sup> or scintillator-based detection in experiments like *BOREXINO*<sup>84</sup> or *Double Chooz*<sup>85</sup>.

#### 4.1.1 High-energy neutrino interactions

When aiming for the detections of higher-energetic neutrinos above GeV-scales, the necessary volume increases to hundreds of cubic meters or even cubic kilometers. These high-energy experiments aim to detect neutrino-induced secondary particles via the lepton produced in a charged-current process and further secondary particles produced by inelastic scattering with the target material. The governing primary processes are the charged- and neutral-current neutrino interactions with the target material

$$\nu_\alpha + N \rightarrow \ell_\alpha + X \quad (\text{CC}) \quad (4.1)$$

$$\nu_\alpha + N \rightarrow \nu_\alpha + X \quad (\text{NC}) \quad (4.2)$$

At high energies, the cross section for CC interactions is significantly larger than for NC contributions with the cross-sectional data<sup>86</sup> of high-energy neutrino interactions shown in fig. 4.1; repro-

<sup>81</sup> Nath et al. “Detection techniques and investigation of different neutrino experiments” (2018).

<sup>82</sup> Cleveland et al. “Measurement of the Solar Electron Neutrino Flux with the Homestake Chlorine Detector” (1998).

<sup>83</sup> Hampel et al. “GALLEX solar neutrino observations: Results for GALLEX IV” (1999).

<sup>84</sup> Alimonti et al. “The Borexino detector at the Laboratori Nazionali del Gran Sasso” (2009).

<sup>85</sup> Palomares “Double-Chooz Neutrino Experiment” (2009).

<sup>86</sup> Gandhi et al. “Ultra-high-energy neutrino interactions” (1996).

<sup>87</sup> Glashow “Resonant Scattering of Antineutrinos” (1960).

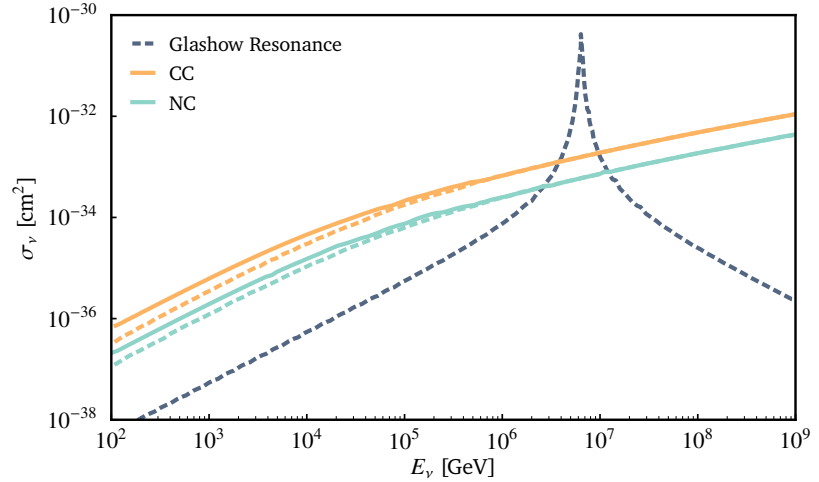
cessed based on<sup>20</sup>. The conventional CC and NC contributions are only surpassed by the *Glashow resonance* – a distinct resonant production channel involving electron antineutrinos<sup>87</sup> – at energies of around 6.3 PeV. This interaction describes the resonant production of a  $W^-$  boson via

$$\bar{\nu}_e + e^- \rightarrow W^- \rightarrow X \quad (4.3)$$

Notably, it was recently found that the first observation of the latter was most likely detected with IceCube in 2016<sup>88</sup>.

<sup>88</sup> Aartsen et al. “Detection of a particle shower at the Glashow resonance with IceCube” (2021).

**Figure 4.1:** High-energy neutrino cross sections as a function of neutrino energy. Shown are contributions of the neutral-current (NC), charged-current (CC) as well as the Glashow resonance interaction channels. Solid and dashed lines depict neutrino and antineutrino contributions, respectively. For a reference to the used data refer to the text.



<sup>89</sup> Hewett et al. “Fundamental Physics at the Intensity Frontier” (2012).

<sup>90</sup> Formaggio et al. “From eV to EeV: Neutrino cross sections across energy scales” (2012).

<sup>91</sup> Albacete et al. “Neutrino-nucleon cross section at ultrahigh energy and its astrophysical implications” (2015).

<sup>92</sup> Patrignani et al. “Review of Particle Physics” (2016).

<sup>93</sup> Cherenkov “Visible luminescence of pure liquids under the influence of  $\gamma$ -radiation” (1934).

<sup>94</sup> Frank et al. “Coherent visible radiation of fast electrons passing through matter” (1937).

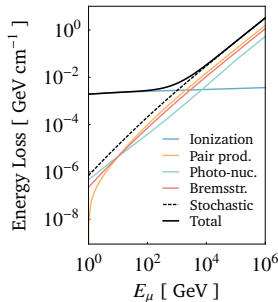


**Figure 4.2:** Muon energy loss contributions as a function of energy. Details and reference to data in the text.

However, above energies of around 20 GeV the scattering is typically deeply inelastic<sup>89–91</sup> and, as a result, the target nucleus is ripped apart and a particle shower ensues. These secondary showers – comparable to air showers in the atmosphere (fig. 2.4) – start off hadronically but eventually develop also an electromagnetic component via stochastic processes. Examples for the latter are pion decays from inelastic nuclear scattering, bremsstrahlung, ionization or pair production<sup>65</sup>. Example energy-dependent contributions for muons are shown in fig. 4.2; reprocessed based on<sup>20</sup> using data from<sup>92</sup>. Additionally, charged particles traversing the matter at high energies will emit optical Cherenkov<sup>93,94</sup> radiation which is one of the primary detection means of high-energy neutrino detectors. This is especially true for charged-current interactions as the neutrino will transfer a significant fraction of its energy to the secondary lepton<sup>12</sup>. As will be reviewed in section 4.2, this is the reason why most neutrino experiments make use of optically translucent detector media.

#### 4.1.2 Cherenkov effect

The Cherenkov effect causes radiation to be generated if charged particles traverse the detector at speeds greater than the speed of light in their medium of propagation. Then, as visualized in fig. 4.3, the resulting relaxation of electromagnetic polarization creates coherent photon wavefronts originating from the track of the particle; reprocessed based on<sup>20</sup>.

The characteristic emission angle  $\theta$  with respect to the particle path, depends on the speed of light  $c$ , the particle speed  $v$  as well as

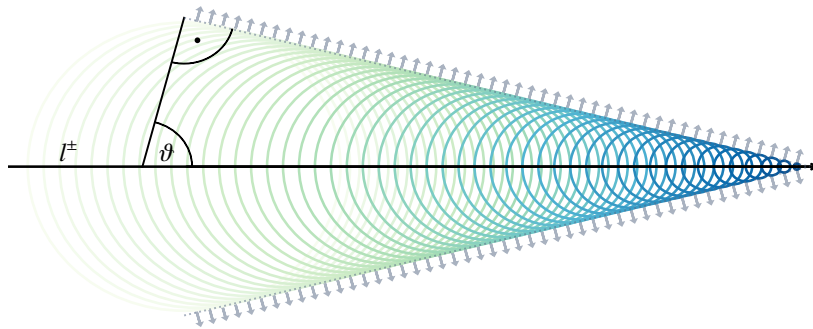


**Figure 4.3:** Illustration of the Cherenkov effect for a particle moving from left to right with superluminal speed in some medium. Shown are the electromagnetic disturbances (colored circles) as well as the resulting coherent wavefronts (dashed, arrows). For details on the effect, refer to the text.

the refractive index of the medium  $n$  and is given by

$$\cos \vartheta = \frac{1}{\beta n}, \quad \beta = \frac{v}{c} \quad (4.4)$$

For optically translucent media like water or ice with a refractive index of around  $n \approx 1.3$ , a highly relativistic particle ( $\beta \sim 1$ ) emits Cherenkov photons at an angle of around  $41^\circ$ . The photon emission can be analytically described by the Frank-Tamm formula<sup>94</sup>

$$\frac{d^2N}{dx d\lambda} = \frac{2\pi\alpha z^2}{\lambda^2} \left(1 - \frac{1}{\beta^2 n^2(\lambda)}\right) \quad (4.5)$$

which characterizes the amount of photons generated per distance and wavelength as a function of particle charge  $z$ , photon wavelength  $\lambda$ , refractive index of the medium  $n$  and fine structure constant  $\alpha$ . Due to the inverse proportionality in wavelength, the number of emitted Cherenkov photons increases towards smaller wavelengths. In water and ice, the Cherenkov emission is typically increasingly significant from 600 nm downwards at which also common optical sensors are sensitive<sup>95</sup>. As such, the detection of neutrinos via secondary particles and their subsequent emission of optical Cherenkov light is the main mechanism for high-energy neutrino observations and used in various experiments outlined in the next section. It should be noted that particle showers induced by deep-inelastic scattering processes produce various particles until the initial energy deposition is depleted. Thus, numerous charged particles in the shower will emit Cherenkov radiation but also take part in other electromagnetic processes which eventually result in photon emission. As such, while Cherenkov radiation is one critical emission contribution, a manifold of radiative processes contribute to the photonic signals of neutrino interactions at high energies<sup>96</sup>. The total amount of light deposited in the medium by such an interaction scales with the energy transfer of the primary neutrino<sup>97</sup>.

## 4.2 Large-volume neutrino experiments

Large-volume neutrino detectors make use of translucent media to detect photons emitted by neutrino-induced secondary particles. The need for large instrumented volumes is here primarily motivated by

<sup>95</sup> Katz “Cherenkov light imaging in astroparticle physics” (2020).

<sup>96</sup> Aartsen et al. “Energy reconstruction methods in the IceCube neutrino telescope” (2014).

<sup>97</sup> Rädcl et al. “Calculation of the Cherenkov light yield from electromagnetic cascades in ice with Geant4” (2013).

the steeply falling neutrino spectrum with high-energies (see section 2.3) as it significantly reduces the high-energy neutrino detection rate per target mass. Thus, the intent of detecting primary neutrinos with very high energies leads to the requirement of instrumenting large volumes of optically transmissive media.

#### 4.2.1 Location

Towards very high energies the necessary volumes are typically of the order of cubic kilometers<sup>98,99</sup>. Since artificial volumes of such sizes are simply infeasible, high-energy experiments make use of naturally existing detector media. Examples of such are lakes and the ocean as well as the Antarctic ice at the South Pole. Furthermore, these rare neutrino observations are heavily outnumbered by, and as such prone to be confused with, background from atmospheric neutrinos and muons created in air showers (see section 2.2). To provide shielding from this, high-energy neutrino detectors are located in great depths to use part of the natural medium to shield atmospheric background.

Prominent examples of currently operating experiments are the ANTARES detector<sup>100</sup> in the Mediterranean Sea, the *Baikal Gigaton Volume Detector* (GVD)<sup>101</sup> in Lake Baikal in Siberia and the IceCube Neutrino Observatory at the South Pole; the latter plays a primary role in this work and will be discussed in detail in chapter 5. In addition, the recent popularity of neutrino astronomy has sparked also further future experiments to be developed. Among these are the *Cubic Kilometre Neutrino Telescope* (KM3NeT)<sup>102</sup> in the Mediterranean Sea and the *Pacific Ocean Neutrino Experiment* (P-ONE)<sup>103</sup> in the Pacific Ocean, both targeting neutrinos of ultra-high energies.

#### 4.2.2 Detector arrangement

Generally, the layout of these detectors is a three-dimensional array of photosensors that instruments the experimental volume. By installing numerous sensors – typically photomultiplier tubes (PMTs) – the light deposition of neutrino-induced interactions can be resolved spatially and energetically by monitoring the arrival time and the amount of light received at different points within the sensor grid. A schematic view of such a layout is depicted for the IceCube detector<sup>104</sup> in fig. 4.4. Due to the necessary atmospheric shielding and the resulting depths of the instrumented volume, this grid is usually realized in the form of multiple lines of photosensors modules, so-called *strings*. These strings host photosensor modules connected by appropriate infrastructure (typically electrical or optical cables and steel wires) which are then vertically deployed to the depths required within the chosen detector volume. By installing multiple strings, the whole target volume can be instrumented with the intended sensor density. Depending on the optical parameters of the medium and desired energy threshold, the inter-string and inter-module spacing is adjusted accordingly. For very high neutrino energies above 100 GeV, these spacings are typically of the order of 100 m – 200 m and 20 m – 40 m, respectively,<sup>102,105</sup>. For lower energies, the light yield of the interaction decreases and a denser instrumentation is needed.

<sup>98</sup> Babson et al. “Cosmic-ray muons in the deep ocean” (1990).

<sup>99</sup> Gaisser et al. “Particle astrophysics with high energy neutrinos” (1995).

<sup>100</sup> Ageron et al. “ANTARES: The first undersea neutrino telescope” (2011).

<sup>101</sup> Collaboration et al. “The Baikal-GVD neutrino telescope: First results of multi-messenger studies” (2019).

<sup>102</sup> Margiotta “The KM3NeT deep-sea neutrino telescope” (2014).

<sup>103</sup> Agostini et al. “The Pacific Ocean Neutrino Experiment” (2020).

<sup>104</sup> “Evidence for High-Energy Extraterrestrial Neutrinos at the IceCube Detector” (2013).

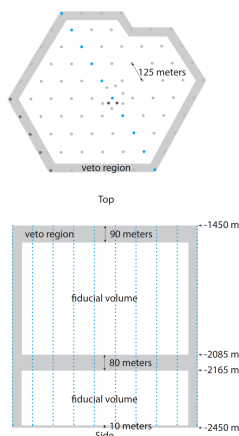


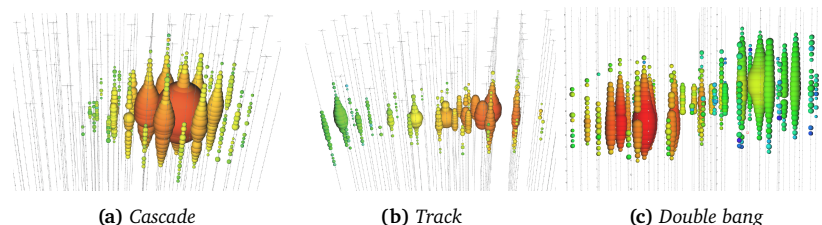
**Figure 4.4:** IceCube detector layout in top and side view. Reference to the figure in the text.

<sup>105</sup> Spiering “IceCube and KM3NeT: Lessons and relations” (2011).

### 4.2.3 Neutrino signatures

At high energies, neutrino events in large-volume experiments are typically classified as either *tracks* or *cascades*. Cascades encompass all events that produce spatially clustered depositions of light induced by hadronic or electromagnetic showers. This includes all NC as well as most  $\nu_e$  and  $\nu_\tau$  CC processes. Hadrons and electrons have short interaction lengths in matter and will directly induce an electromagnetic shower while in the latter case of a tau interaction the produced lepton will essentially decay immediately unless its energy is higher than many PeV<sup>106,107</sup>. Here, the signature is distinct with two cascades – at interaction and decay vertex, respectively – and an intermediate track, sometimes referred to as a *double bang*. A recent analysis showed first hints for this rare type of event<sup>108</sup>. However, most commonly all-flavor NC as well as  $\nu_e$  and  $\nu_\tau$  CC events will show similar shower-like detection signatures. This inherent difficulty to disentangle flavors is the major contribution to the degeneracy in the flavor ratio measurement discussed in previous sections.

Tracks on the other hand refer to high-energy muons created in  $\nu_\mu$  CC interactions which can traverse the medium for kilometers on a straight path<sup>103</sup>. Eventhough these muons can undergo stochastic energy losses, the tracks make their signature significantly distinct from cascades. A comparison of example high-energy simulations of track, cascade and double bang signatures in IceCube<sup>109</sup> is given in fig. 4.6 and shows the characteristic event views for the respective interaction types.



The long lever arm created by muon tracks also makes them ideal candidate events for neutrino astronomy as they point back to their sources at very high energies<sup>110</sup>. The angle between the incident muon neutrino and the secondary muon – also referred to as the *kinematic angle* – lies well below  $1^\circ$  at high energies<sup>20</sup>. The kinematic angle as well as the fractional energy transferred to the secondary muon as a function of primary neutrino energy are shown in fig. 4.5; reprocessed based on<sup>20</sup>. Pointing with cascades on the other hand is more difficult. With increasing energy the shower development gains intrinsic direction due to secondaries being boosted by the primary neutrino, however, this elongation is typically well below the sensor spacing of typical high-energy neutrino detectors<sup>111,112</sup>. Since this marginal timing difference has to be inferred, pointing with cascades typically results in larger angular uncertainties of more than a few degrees at high energies<sup>96</sup>.

The inverse is true for energy reconstruction. While high-energy showers deposit all of their energy in a relatively confined space, high-energy tracks are rarely fully contained in the detector and are

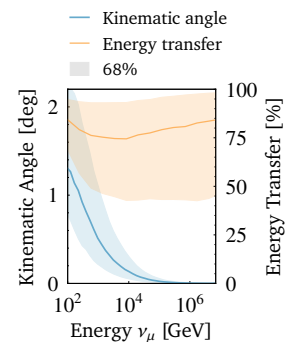


**Figure 4.5:** Kinematic angle and transferred energy of a secondary muon produced in a charged-current interaction as a function of incident neutrino energy. Reference in the text.

<sup>106</sup> Beacom et al. “Measuring flavor ratios of high-energy astrophysical neutrinos” (2003).

<sup>107</sup> Cowen “Tau neutrinos in IceCube” (2007).

<sup>108</sup> Stachurska “First Double Cascade Tau Neutrino Candidates in IceCube and a New Measurement of the Flavor Composition” (2019).

<sup>109</sup> IceCube-Masterclass “IceCube and Neutrinos” (2018).

**Figure 4.6:** Example IceCube neutrino signatures. The figures show the sensor modules (dots) with size representing detected amount of light and color its arrival time. Details and reference in the text.

<sup>110</sup> “Search for correlations between the arrival directions of IceCube neutrino events and ultrahigh-energy cosmic rays detected by the Pierre Auger Observatory and the Telescope Array” (2016).

<sup>111</sup> Stransky et al. “Reconstruction of cascade-type neutrino events in KM3NeT/ARCA” (2016).

<sup>112</sup> Aartsen et al. “Search for Sources of Astrophysical Neutrinos Using Seven Years of IceCube Cascade Events” (2019).

<sup>113</sup> Abbasi et al. “An improved method for measuring muon energy using the truncated mean of  $dE/dx$ ” (2013).

<sup>114</sup> Bradner et al. “Long base line measurements of light transmission in clear water” (1984).

<sup>115</sup> Spiering “Neutrino Detectors Under Water and Ice” (2020).

<sup>a</sup> Notably, the reciprocals are called the *scattering* and *absorption coefficients*. Typically referred to as  $b$  and  $a$ , respectively, so that it is  $\ell_{\text{abs}} = 1/a$  and  $\ell_{\text{scat}} = 1/b$

<sup>116</sup> Lambert “Photometria sive de mensura et gradibus luminis, colorum et umbrae” (1760).

<sup>117</sup> Beer “Bestimmung der Absorption des rothen Lichts in farbigen Flüssigkeiten” (1852).

<sup>118</sup> Mie “Beiträge zur Optik trüber Medien, speziell kolloidaler Metallösungen” (1908).

<sup>119</sup> Li et al. “A Discussion on the Applicable Condition of Rayleigh Scattering” (2015).

<sup>120</sup> Kirk “Multiple scattering of a photon flux: implications for the integral average cosine of the underwater light field” (1999).

<sup>121</sup> Chandrasekhar “Radiative Transfer” (2013).

<sup>122</sup> Ackermann et al. “Optical properties of deep glacial ice at the South Pole” (2006).

<sup>123</sup> Balkanov et al. “In situ measurements of optical parameters in Lake Baikal with the help of a Neutrino telescope” (1999).

<sup>124</sup> Balkanov et al. “Simultaneous measurements of water optical properties by AC9 transmissometer and ASP-15 Inherent Optical Properties Meter in Lake Baikal” (2003).

<sup>125</sup> Aguilar et al. “Transmission of light in deep sea water at the site of the ANTARES Neutrino Telescope” (2005).

<sup>126</sup> Riccobene et al. “Deep seawater inherent optical properties in the Southern Ionian Sea” (2007).

<sup>127</sup> Ackermann et al. “Optical properties of deep glacial ice at the South Pole” (2006).

<sup>128</sup> Lundberg et al. “Light tracking for glaciers and oceans: Scattering and absorption in heterogeneous media with Photonics” (2007).

further subject to stochastic energy losses which occur at random and have to be estimated<sup>96,113</sup>. Thus, energy reconstructions for showers are commonly much more precise than for tracks. In IceCube, the precision of primary neutrino energy reconstruction is typically below 10 % for cascades and 20 % – 50 % for tracks at energies above 100 GeV. However, for tracks this usually corresponds to lower limits on the primary energy<sup>96</sup>.

#### 4.2.4 Optical medium & light propagation

The prominent driver of neutrino signatures within neutrino telescopes is the optical medium. Its scattering and absorption behaviour will determine the way light from neutrino interactions will develop throughout the detector volume. In the most basic scenario, while traversing the medium photons can either be scattered and possibly change direction or get absorbed and disappear<sup>114,115</sup>. The probability of these processes along the photon path is wavelength-dependent and described using the *absorption* and *scattering lengths* –  $\ell_{\text{abs}}$  or  $\ell_a$  and  $\ell_{\text{scat}}$  or  $\ell_b$ , respectively<sup>a</sup> – characteristic for a specific medium. These parameters give an average path length after which only a fraction of  $1/e$  photons remains unaffected from the considered process and results from a generalization of the *Lambert-Beer law*<sup>116,117</sup>

$$N(d) = N_0 e^{-d/\ell_x} \quad (4.6)$$

which describes the number of photons  $N$  that remain non-absorbed (or non-scattered) after path length  $d$  given an initial emission of  $N_0$ .

While an absorbed photon simply disappears in the medium, a scattered photon generally changes direction. This directional change depends on the medium and was first discussed in the extensive electromagnetic treatment of radiation by Mie<sup>118</sup>. Scattering is characterized by the *scattering function* which describes the angular distribution of the photon after the scattering process, that is, the probability of scattering at a given angle  $\theta$ . Primarily, the exact scattering theory depends on the photon wavelength and the size of the scattering particle<sup>e.g. 119</sup>. If a photon field is scattered  $n$  times, its average scattering angle is then<sup>120</sup>  $\langle \cos \theta \rangle_n = \langle \cos \theta \rangle^n$  and in the limit of numerous scatterings, this leads to the *effective scattering length*<sup>121,122</sup>

$$\ell_b^{\text{eff}} = \frac{\ell_b}{1 - \langle \cos \theta \rangle} \quad (4.7)$$

which regularizes scattering lengths for different manifestations of the scattering function<sup>115</sup>. For typical media of Cherenkov telescopes, like water and ice, the value of  $\langle \cos \theta \rangle$  ranges between 0.8 – 0.95<sup>114,115</sup> and is thus highly forward-peaked. Furthermore, typical values of absorption and effective scattering lengths for different high-energy neutrino detector sites are summarized in table 4.1; table taken from<sup>115</sup> based on data from<sup>123–128</sup>.

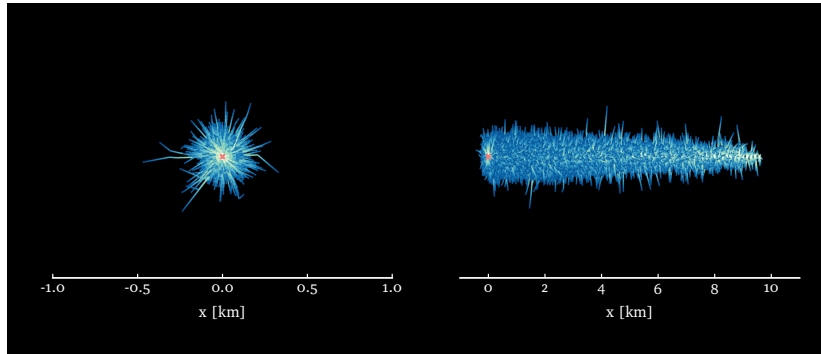
Now, absorption and scattering significantly influence the way photonic neutrino signatures develop within the detector volume. Absorption on the one hand limits the light propagation distance and thus the spacing of the sensor modules has to be adjusted so that

Depth [m]	$\ell_a$ [m]	$\ell_b^{\text{eff}}$ [m]
Lake Baikal (1 km depth)	18 – 22	150 – 250
Ocean (below 1.5 km depth)	40 – 70	200 – 300
Antarctic ice (1.5 – 2 km depth)	~ 95	~ 20
Antarctic ice (2.2 – 2.5 km depth)	> 100	30 – 40

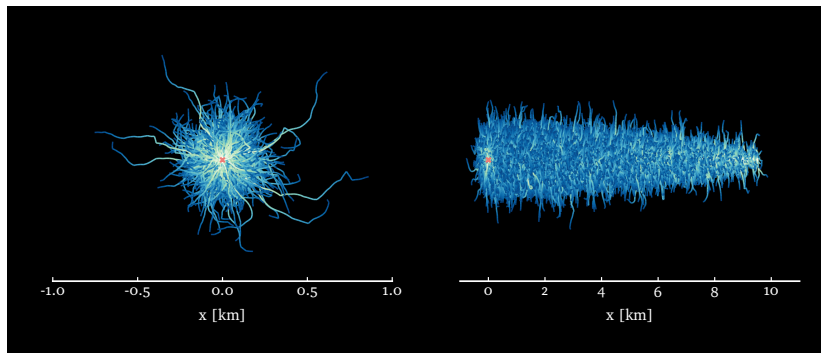
**Table 4.1:** Summary of respective wavelength-dependent maximum absorption and effective scattering lengths at various neutrino telescope sites. Reference to data in the text.

enough light from the intended interaction energies can be collected. Scattering primarily influences the timing distribution of the photon development and hence small scattering lengths obscure the raw photon signal of an interaction. Critically, this can lead to a loss of timing information of the initial light emission and can make it especially hard to differentiate between interaction types if the physical difference is related to the photon timing distribution. This is the case, for example, in distinguishing charged-current  $\nu_e$  and  $\nu_\tau$  interactions<sup>107</sup>.

The different experimental sites around the world instrument lakes, the deep sea as well as the Antarctic ice at the South Pole. Here, as per table 4.1, the site conditions are two-fold: the water-based sites experience relatively strong absorption but small scattering influence while the situation in the Antarctic ice at the South Pole is the opposite. An example comparison for a track-like and cascade-like neutrino signatures in water and ice, based on a previous study<sup>20</sup>, is given figs. 4.7a and 4.7b, respectively and highlights the significant difference of light propagation in the different media.



(a) Example photon tracks in water for cascade-like (left) and track-like (right) interactions.



(b) Example photon tracks in ice for cascade-like (left) and track-like (right) interactions.

**Figure 4.7:** Example cascade-like and track-like neutrino signatures in water (a) and ice (b). All figures show toy simulations of Cherenkov photon tracks emitted by charged particles produced at the center (red cross) with the track-like particle propagating to the right. These simulations are done assuming absorption/scattering lengths of 50/150 m and 100/20 m in water and ice, respectively. Both the cascade-like and the track-like events approximately resemble a primary neutrino energy of 30 TeV. For the photon paths color is representative of the relative time from production (white) to absorption (blue). Reference to the figure in the text.

### 4.3 Detector systematics and calibration methods

Studying particle and astroparticle physics with large-volume experiments inevitably comes with systematic uncertainties related to the involved physics processes and detector understanding. This is especially true when instrumenting cubic kilometers of optical medium with thousands of photosensors where calibration is a crucial component of successful experiment operation. Not only is the expected development of neutrino event signatures predominantly determined by the optical properties of the medium but also the understanding of the photosensors and their responses to light signals is critical in understanding these observations. Together, the knowledge of the detector volume as well as its detection units forms the baseline of calibration operations for large-volume detectors. In general, the encountered calibration tasks encompass optical medium, photosensor instrumentation, detector geometry and background all of which depend intricately on the medium as well as the specific realization of the detector in terms of layout and hardware.

#### 4.3.1 Optical medium

As outlined previously, the optical properties of the detector medium determine the evolution of neutrino signatures and as such are a primary calibration goal. The main focus here is typically absorption and scattering lengths as well as the mean scattering angle. In both water and ice, this is typically realized using some form of calibration light sources within the detector volume. Examples of such calibration tools are the optical systems of ANTARES<sup>125,129</sup>, KM<sub>3</sub>NeT<sup>130,131</sup>, GVD<sup>123,124</sup> as well as P-ONE<sup>13,132</sup> and IceCube<sup>133,134</sup> all of which make use of optical emitter-receiver systems to calibrate the respective detector medium properties. Since these detectors encompass volumes of kilometer-scales, this calibration is typically done as a function of depth. In contrast to static ice, water-based detectors further have to constantly monitor these parameters as different seasonal and tidal effects exchange the water within the detector continuously<sup>125,135</sup>.

The general principle of these calibrations is to emit light using artificial light sources within the detection volume and then use either the detector itself or designated photosensors to measure the received

<sup>129</sup> Ageron et al. “The ANTARES Optical Beacon System” (2007).

<sup>130</sup> Baret et al. “The Calibration Units of the KM<sub>3</sub>NeT neutrino telescope” (2016).

<sup>131</sup> Real et al. “Nanobeacon: A time calibration device for KM<sub>3</sub>NeT” (2019).

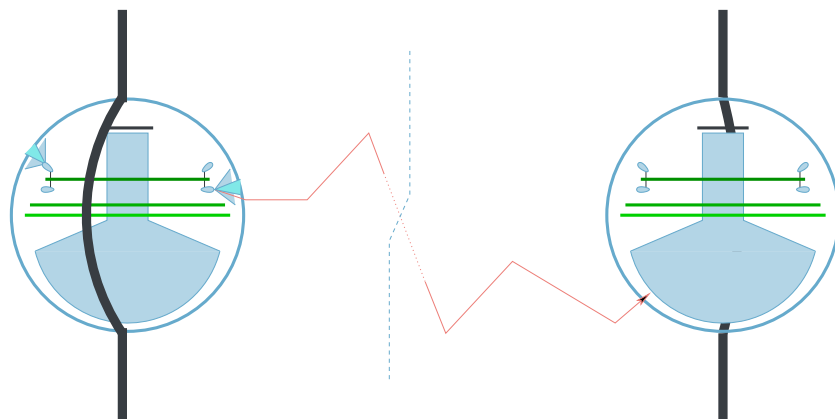
<sup>132</sup> Boehmer et al. “STRAW (STRings for Absorption length in Water): pathfinder for a neutrino telescope in the deep Pacific Ocean” (2019).

<sup>133</sup> Aartsen et al. “Measurement of South Pole ice transparency with the IceCube LED calibration system” (2013).

<sup>134</sup> Rongen “Calibration of the IceCube Neutrino Observatory” (2019).

<sup>135</sup> Riccobene et al. “Deep seawater inherent optical properties in the Southern Ionian Sea” (2007).

**Figure 4.8:** Illustration of the IceCube LED calibration system. The detection module on the left side emits calibration light pulses using integrated LEDs. The propagation of the photons (red) is governed by the optical properties of the medium until they are eventually detected by other detection modules (right). Baseline figure reference in the text.



light at different positions within the medium. An illustration<sup>133</sup> of this procedure is given in fig. 4.8 for the IceCube LED flashers integrated in the detection modules (details in chapter 5). Then, light emission simulations of the used calibration light sources with different models of the optical medium are carried out and compared to the measurements in order to find a best-fit. Since these simulations are multi-dimensional and require large-scale propagation of photons they are complex, computationally extensive and often degenerate if different systematic effects cause similar observational changes to the calibration light pulses<sup>e.g. 133</sup>. Most of these calibrations are done using integrated light sources, such as light emitting diodes (LEDs) or lasers, as a result, the knowledge of their respective properties is key in the final precision of the measurements. Lastly, since the emitted Cherenkov spectrum encompasses a wide range of wavelengths, the calibration would ideally encompass multiple wavelength points. For example, in IceCube this is interpolated by using the power-law expectation from Mie theory based on various measurements at different wavelengths<sup>122,133</sup>.

#### 4.3.2 Optical backgrounds

In addition, the detector medium can also contain various intrinsic sources of light which are not attributed to high-energy particle interactions. Instead, different medium and detector mechanisms can cause such light background to arrive at detection modules and has to be differentiated from neutrino events. Examples for such effects are radioactive decays near (or in) the detection modules<sup>136,137</sup> or bioluminescence<sup>138,139</sup>. The former is mainly caused by <sup>40</sup>K and can generate charged particles that are energetic enough to emit Cherenkov light; the latter mainly appears in water-based detectors and is attributed to various organisms which emit light, for example, when stimulated mechanically by currents<sup>140</sup>. Additionally, the most common photosensors are PMTs which have intrinsic *dark noise* that mimics single-photon signals but is caused by the photoactive material within the PMT<sup>141</sup>. However, since all of these light backgrounds are typically occurring on spatial scales much smaller than high-energy neutrino interactions, a common strategy to remove them is the requirement of correlated signals at multiple detection modules within small time windows. This is typically called *triggering* and is one of the central tasks in any large-volume neutrino telescope<sup>141,142</sup>. Furthermore, these backgrounds can also be used for calibration purposes, as is done, for example, in ANTARES<sup>136,143</sup>.

#### 4.3.3 Detection modules

In addition to data acquisition (DAQ) electronics and appropriate encapsulation for the area of operation, the photosensors pose the key part of the detection module in large-volume detectors. Due to the large scales of these experiments and the resulting potentially low light levels, the photosensors should encompass a large photoactive area sensitive to the Cherenkov spectrum (refer to section 4.1.2), good timing resolution as well as moderate cost. While there are various

<sup>136</sup> Zaborov “Coincidence analysis in ANTARES: Potassium-40 and muons” (2009).

<sup>137</sup> Unland Elorrieta “Studies on dark rates induced by radioactive decays of the multi-PMT digital optical module for future IceCube extensions” (2017).

<sup>138</sup> Collaboration et al. “The ANTARES detector: background sources and effects on detector performance” (2007).

<sup>139</sup> Meighen-Berger et al. “Bioluminescence modeling for deep sea experiments” (2021).

<sup>140</sup> Aguzzi et al. “Inertial bioluminescence rhythms at the Capo Passero (KM3NeT-Italia) site, Central Mediterranean Sea” (2017).

<sup>141</sup> Aartsen et al. “The IceCube Neutrino Observatory: Instrumentation and Online Systems” (2017).

<sup>142</sup> Bruijn “KM3NeT Readout and Triggering” (2019).

<sup>143</sup> Aguilar et al. “Time Calibration of the ANTARES Neutrino Telescope” (2011).

<sup>144</sup> Hamamatsu Photonics “*Photomultiplier Tubes – Basics and Applications*” (2007).

<sup>145</sup> Amram et al. “*The ANTARES optical module*” (2002).

<sup>146</sup> Hanson et al. “*Design and production of the IceCube digital optical module*” (2006).

<sup>147</sup> Leonora “*The Digital Optical Module of KM<sub>3</sub>NeT*” (2018).

<sup>148</sup> Abbasi et al. “*Calibration and Characterization of the IceCube Photomultiplier Tube*” (2010).

<sup>149</sup> Aartsen et al. “*In-situ calibration of the single-photoelectron charge response of the IceCube photomultiplier tubes*” (2020).

<sup>150</sup> Gomez-Gonzalez “*Calibration systems of the ANTARES neutrino telescope*” (2013).

<sup>151</sup> Kulikovskiy “*Calibration methods and tools for KM<sub>3</sub>NeT*” (2016).

<sup>152</sup> Bagley et al. “*KM<sub>3</sub>NeT: Technical Design Report for a Deep-Sea Research Infrastructure in the Mediterranean Sea Incorporating a Very Large Volume Neutrino Telescope*” (2009).

<sup>153</sup> Viola et al. “*Acoustic positioning system for KM<sub>3</sub>NeT*” (2016).

<sup>154</sup> Jonske et al. “*Trilateration-based geometry calibration of the IceCube detector*” (2019).

types of photosensors, the most prominent example in large-volume detectors is the PMT. These devices use photoactive material to produce secondary electrons which are in turn intrinsically amplified to eventually produce an electrical signal<sup>144</sup>. As they are available in sizes up to tens of inches with moderate cost, many large-volume detectors make use of PMTs in their respective detection modules, such as ANTARES<sup>145</sup>, IceCube<sup>146</sup> and also KM<sub>3</sub>NeT<sup>147</sup>. The electrical signals are then processed in complex analog front- and digitization back-ends within the module until eventually being read and stored in the experiment data center. Critical for using detected signals for physics analyses is the understanding of the photosensor as well as the DAQ electronics and related timing effects of each detection module. While details of these systems differ from experiment to experiment, all large-volume detectors ensure understanding of its detection modules, signals and absolute timing synchronization with appropriate calibration procedures<sup>123,145,148–151</sup>. Most importantly, the photon detection efficiency – which governs the probability of detecting a photon and is influenced by the PMT itself as well as the encapsulation – can cause degeneracies in the calibration procedures of the optical medium as it directly affects the measured photon flux. As such, a proper understanding of the sensor as well as the calibration light source instrumentation is absolutely crucial to disentangle the different systematic effects related to medium and detection module, respectively.

#### 4.3.4 Geometry

Lastly, the geometry of the detector is central to the reconstruction of neutrino-induced interactions. As such, geometry calibration is an important aspect of the calibration procedures in large-volume telescopes. This is especially true for water-based experiments as the geometry is constantly changing with tides and currents. Here, the geometry is constantly monitored using both optical and acoustical calibration instruments<sup>150,152</sup> which are complementary to trilaterate the detection modules to centimeter precision and as such determine the geometry continuously. The general principle is to emit optical or acoustical pulses which are then detected by the instruments with appropriate receivers; combining these detections of multiple emitters allows the reconstruction of the detector geometry. While light is detected directly with the photosensor instrumentation, detecting acoustic signals requires additional hardware, either in the detection modules or in designated additional modules within the detector volume<sup>153</sup>. In IceCube, no acoustic positioning system is implemented yet as the mostly static Antarctic ice does not require constant monitoring. However, due to heavy scattering and the resulting diffusion of initially short light pulses, the precision of the optical geometry calibration is limited to a precision of a few meters, largely based on positional data from the drill during detector installation<sup>141,154</sup>.

# 5

## The IceCube Neutrino Observatory

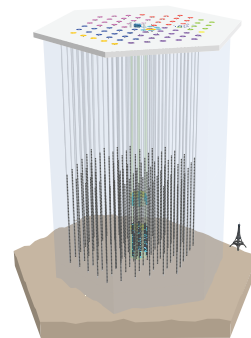
Fully operating since 2010, the IceCube Neutrino Observatory is located at the geographic South Pole and instruments around one cubic kilometer of Antarctic ice. As pictured in fig. 5.1a, the experiment hosts 86 strings, with 60 *digital optical modules* (DOMs) each, totalling over 5000 sensors distributed within the detection volume in depths of 1450 m – 2450 m beneath the surface of the Antarctic ice. In addition to the bulk detector, IceCube also contains the air shower array *IceTop* on the ice surface, a densely-instrumented low-energy region called *DeepCore* in its center and its main experiment control in the *IceCube Lab* (ICL) on top.

### 5.1 Experimental design

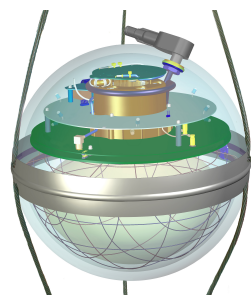
As typical for large-scale neutrino telescopes, the strings in IceCube provide the mechanical and electrical backbone of the detector and further host the sensor instrumentation. The strings themselves are load-bearing multi-stranded cables that supply power and enable communication to the DOMs as well as provide support for their mechanical mounting structure<sup>141</sup>. As shown schematically in fig. 5.1b, each of the DOMs hosts a PMT of 25 cm diameter as well as calibration and DAQ electronics that control the DOM functionality, acquire signals from the PMT and communicate with the surface station. All these components are encapsulated in a glass pressure sphere which is in turn mounted to the string. Using optical gel, the PMT is coupled to a glass pressure sphere which itself is necessary to protect its sensitive contents from the environment. As the holes for string installation are melted into the Antarctic ice, high pressures are present in the hole while it is still liquid and even more so during the refreezing process<sup>141</sup>.

Based on optical measurements of the Antarctic ice with the predecessor experiment *Antarctic Muon And Neutrino Detector Array* (AMANDA)<sup>122</sup>, the 79 bulk detection strings are installed with inter-string and inter-DOM spacing of 125 m and 17 m, respectively<sup>155</sup>. For the remaining seven strings in *DeepCore*, this is adjusted to around 42 m and 7 m, respectively, which more densely instruments a smaller volume and thus translates to better sensitivity towards lower energies<sup>156</sup>. The bulk detector is intended to observe energies upwards of 100 GeV with *DeepCore* extending down to few GeV<sup>156</sup>. The temporal reconstruction of these events is further possible due to sub-nanosecond time synchronization of the whole array with a central clock distribution system<sup>141,157</sup>.

Also calibration of the DOMs as well as the optical properties of the Antarctic ice play a primary role in the understanding of neutrino



(a) IceCube detector layout.



(b) Digital Optical Module.

**Figure 5.1:** (a) Hexagonal IceCube detector layout including strings (black) and *DeepCore* region (cyan). Eiffel Tower for scale. (b) Schematic view of an IceCube DOM with its PMT and electronics encapsulated in a glass pressure sphere. Both figures are a courtesy of the IceCube Collaboration.

<sup>155</sup> Karle “*IceCube: Construction Status and First Results*” (2009).

<sup>156</sup> Abbasi et al. “*The design and performance of IceCube DeepCore*” (2012).

<sup>157</sup> Abbasi et al. “*The IceCube data acquisition system: Signal capture, digitization, and time-stamping*” (2009).

signatures. Thus, as already shown schematically in fig. 4.8, each DOM contains twelve 405 nm LEDs that can be used to emit light pulses of adjustable intensity and width<sup>141</sup> into the ice. These pulses in turn can be detected by various surrounding modules. As a result, the signal combination of thousands of emitter and receiver pairs is the primary calibration tool in IceCube and can be used to calibrate, for example, geometry and optical properties<sup>133,134</sup>. They can be further divided into groups of six *horizontal* and six *tilted* LEDs, emitting light horizontally and around 48° upwards from the DOM equator into the ice, respectively<sup>141</sup>.

## 5.2 Systematic detector effects

In addition to statistical uncertainties related to the low rate of neutrino interactions, systematic uncertainties related to the involved physical processes – for example cross sections, fluxes or mixing parameters – as well as limited detector understanding define fundamental limits on the precision of high-energy neutrino experiments. Depending on the analysis, specifically the involved neutrino flavors and energies as well as interaction types, different physical uncertainties contribute e.g. 46,88,158. However, the understanding of the detector is generally crucial to deduce physical meaning from experimental data. In IceCube, the dominating detector systematics compose of

1. **Bulk ice** – Depth-dependent scattering and absorption coefficients of the bulk ice, anisotropy and tilt of ice layers with similar properties all determine the large-scale propagation and time evolution of photons and thus the development of light depositions within the detection volume – section 5.2.1.
2. **Hole ice** – Refrozen drill hole ice has been found to contain high concentrations of bubbles and as a result vastly different optical properties. Since the DOMs are installed within the drill holes, the optical properties of this local ice around them critically determines their response to incoming photons – section 5.2.2.
3. **DOM response** – Photon detection efficiency, angular sensitivity and linearity of the DOM response to incoming fluxes of photons is crucial in understanding the amount of detected light and thus the observed neutrino signatures – section 5.2.3.
4. **Geometry** – Knowledge of the DOM positions, their potential tilt and the cable position influences the expected photon signals of neutrino interactions and thus the precision of reconstructions – section 5.2.4.

While the geometry and bulk ice effects on neutrino detection have already been outlined in section 4.2, the formation of the so-called *hole ice* or *bubble column* is an effect solely present in IceCube. The effect itself was already known in AMANDA<sup>159</sup>, however, still remains poorly constrained as of today. During installation of IceCube, a camera of the *Sweden Camera System*, installed at one of the strings, revealed an unexpected, cloudy ice column that formed during the refreezing

<sup>158</sup> Aartsen et al. “Measurement of the multi-TeV neutrino cross section with IceCube using Earth absorption” (2017).

<sup>159</sup> Niessen “Simulated bubbles and their effect on some observables in AMANDA B4” (1998).

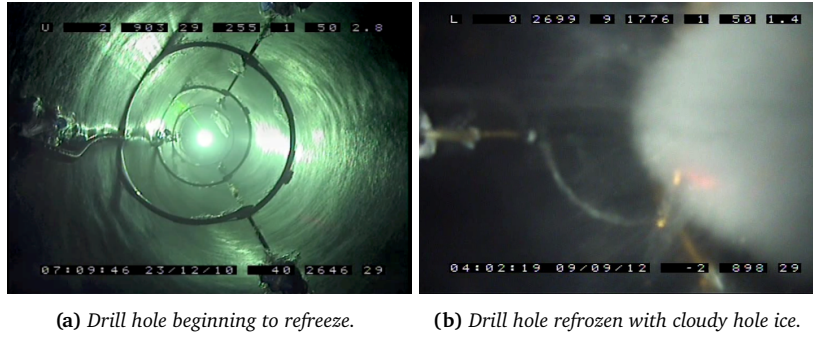


**Figure 5.2:** Sweden Camera pictures of the drill hole refreezing process during its beginning (a) and after being completely refrozen (b). While the hole looks clear initially, a cloudy bubble column forms in the hole after it has frozen completely. Figure reference in the text.

period<sup>160</sup>, with a camera view of this formation<sup>160</sup> is depicted in fig. 5.2. Lastly, the understanding of the DOM response to incident photons is the final requirement in order to correctly translate the measured photon signal to the one incident on the DOM. While this partly also includes the correct understanding of the bubble column, it is primarily related to the PMT photon detection efficiency and signal response, the DAQ electronics processing the PMT output and also the light detection and transmission characteristics of the PMT as well as DOM glass and optical gel, respectively.

### 5.2.1 Bulk ice

Optical parameters of the Antarctic bulk ice within the IceCube detection volume have been found to be primarily driven by dust concentrations within the ice<sup>122,161,162</sup>. These measurements were further confirmed by Antarctica ice core samples<sup>163</sup> and dust logger measurements<sup>164</sup> which are in accordance with LED calibrations of the IceCube bulk ice<sup>122,133,134</sup> assuming Mie theory<sup>118</sup>. Scattering is dominated by impurities and effective scattering angles of around  $\langle \cos \theta \rangle \approx 0.95$ <sup>133,134,162</sup>, thus strongly forward-peaked. Generally, the bulk ice within IceCube shows absorption and effective scattering lengths between 50 – 125 m and 15 – 40 m, respectively, and becomes clearer with depth. One exception is the *dust layer* between depths of approximately 1950 m – 2100 m where a large dust concentration significantly lowers the ice transparency. The uncertainty on the bulk ice parameters is estimated to be about 10 %<sup>133</sup>.

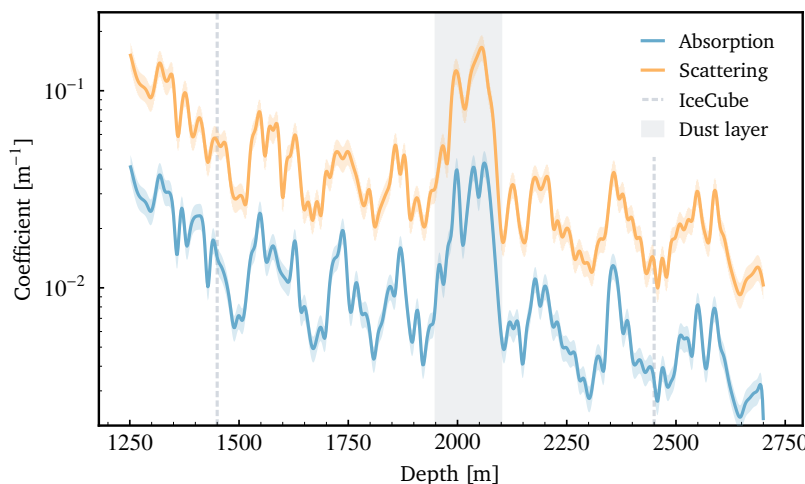


**Figure 5.3:** IceCube bulk ice optical properties as a function of depth. The figure shows the 10% bands for both absorption (blue) and scattering (orange) coefficients as a function of depth within IceCube. Also shown are the dust layer and the instrumented volume edges. Data courtesy of the IceCube Collaboration.

In addition to the optical parameters, the layers of the bulk ice with similar dust properties are further showing tilt or relief<sup>133</sup> and the bulk ice volume in general shows anisotropy<sup>165,166</sup>. While the former simply means the ice layers with similar dust properties are not well aligned, the latter describes a direction-dependent photon propagation variation which appears to be intrinsic to the optical properties of the Antarctic ice<sup>134</sup>. As discussed later in section 6.2, both of these effects need to be taken into account for simulating light sources and photon propagation within the detector.

### 5.2.2 Hole ice

The cloudy bubble column of ice forming within the drill holes of IceCube (see fig. 5.2) is one of the major detector effects which remains poorly understood. This column of ice is showing vastly different optical properties with respect to the bulk ice<sup>167</sup>. Its formation process is believed to be caused by residual air bubbles and impurities in the water which accumulate towards the center of the hole while it refreezes<sup>134</sup>. Since its discovery, various approaches have taken on the task of calibrating the hole ice properties, for example, via LED flashers<sup>134,167,168</sup> or muons<sup>169,170</sup>. Two general approaches towards hole ice calibration are prominently used: direct local simulation of the bubble column using photon tracking<sup>171</sup> and large-scale simulations with modified DOM polar angular acceptance curves<sup>134</sup>. While the angular acceptance of the DOM has been calibrated in the lab<sup>134,172</sup>, it can be skewed by a cloudy column of strongly-scattering hole ice. If hole ice is not simulated directly, it is typically modeled by modifying the DOM angular acceptance function, a collection of which is shown in fig. 5.4 for different fit results<sup>134,168,173</sup>; reprocessed based on<sup>134</sup>. Generally, hole ice is expected to reduce the forward acceptance – as photons incident head-on to the PMT can be scattered away – and increase the backward acceptance – as photons incident from behind the PMT have a chance to be scattered towards the photocathode. Since this model description might be DOM-dependent its local study is an active topic within IceCube.

<sup>165</sup> Chirkin “Evidence of optical anisotropy of the South Pole ice” (2013).

<sup>166</sup> Chirkin et al. “Light diffusion in birefringent polycrystals and the IceCube ice anisotropy” (2019).

<sup>167</sup> Rongen, Martin “Measuring the optical properties of IceCube drill holes” (2016).

<sup>168</sup> Chirkin “Fitting the hole ice angular sensitivity model with the all-string flasher data” (2015).

<sup>169</sup> Olbrechts “On the Angular Sensitivity of Optical Modules in the Ice” (2001).

<sup>170</sup> Gerhardt “Effects of Hole Ice on Hit Time” (2009).

<sup>171</sup> Fiedlschuster “The Effect of Hole Ice on the Propagation and Detection of Light in IceCube” (2019).

<sup>172</sup> Tosi et al. “Calibrating the photon detection efficiency in IceCube” (2015).

<sup>173</sup> Karle et al. “Hole Ice Studies with YAG data.” (1998).

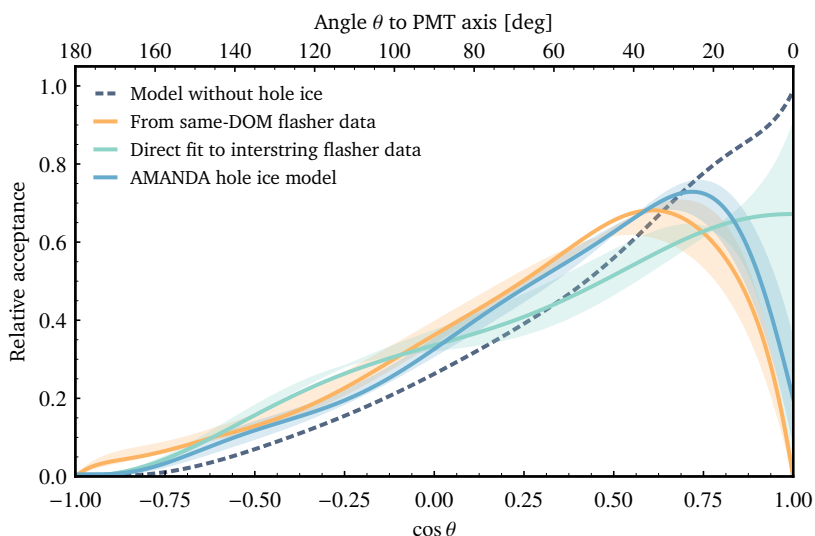


**Figure 5.4:** IceCube angular acceptance models for different calibration procedures as a function of incident angle with respect to the PMT axis. Photons incident with  $\theta = 0^\circ$  and  $180^\circ$  arrive head-on to and from behind the PMT, respectively. Figure reference and details in the text.

In addition to the polar modification, hole ice can be off-center with respect to the PMT and hence also modify the azimuthal acceptance of the DOM<sup>134</sup>. However, both of these effects are only now becoming more and more constrained<sup>174</sup> and are thus an active calibration topic within IceCube. The most prominent model is the *unified hole-ice parameterization*<sup>175</sup> which was done within IceCube in order to homogenize the different angular acceptance models used throughout different analyses.

### 5.2.3 DOM response

Responses of the DOMs to incident photons of specific wavelengths depend on the optical parameters of the DOM, the intrinsic PMT response as well as the read-out electronics. First, light has to pass the glass pressure sphere as well as the optical gel used for coupling the PMT which initially shapes the transmission of different wavelengths depending on the material parameters. Then, the PMT quantum efficiency determines the probability to detect these photons and its intrinsic electrical characteristics determine the pulse output charge and time profile. Lastly, the read-out electronics determine the shape and sampling of the digitized recording of this pulse.

The wavelength acceptance of the DOM ranges from around 350 nm – 600 nm which is primarily determined by the transmittance of the glass pressure sphere, the optical gel and the PMT quantum efficiency<sup>148</sup>. While the actual PMT quantum efficiency at 400 nm is around 25 %<sup>148</sup>, the nominal photon detection efficiency of the whole DOM is about 10 % including all material and electrical characteristics of the read-out chain<sup>133</sup>. In addition, DeepCore DOMs are equipped with enhanced PMTs showing higher quantum efficiencies of around 34 %<sup>141</sup>. Also, linearity of the PMTs plays a primary role if large photon fluxes are expected, for example, in the vicinity of high-energy events or flashing calibration light sources. DOMs with large signals are commonly classified as *bright* and typically have to be excluded from analyses but would have the potential to significantly boost the reconstruction precision<sup>176</sup>. As such, an in-situ verification of the DOM linearities would be beneficial for reconstructions, however, is limited by the current LED intensity calibration precision of around 20 – 30 %<sup>134</sup>. In addition, yearly re-calibrations of the DOMs are carried out via in-situ procedures<sup>149</sup> in order to account for potential aging effects of the PMT and subsequent electronics.

### 5.2.4 Geometry

The geometry determination of the IceCube detector was done in two stages: first the drill and survey data of the string installation process was used to setup a geometry baseline and then a dedicated LED flasher campaign was carried out to refine and correct the initial measurement<sup>141</sup>. While the first stage used inertial measurements of the drill head, the second stage used calibration LEDs within the DOMs and trilateration algorithms to deduce the string z position as a function of depth with an accuracy of around 20–30 cm<sup>141</sup>. As shown in fig. 5.5 this proved to be consistent with drill data in the shallow

<sup>174</sup> Chirkin “A calibration study of local ice and optical sensor properties in IceCube” (2021).

<sup>175</sup> Eller “Unified angular acceptance model” (2019).

<sup>176</sup> Yuan “Improvement in IceCube event reconstructions” (2018).

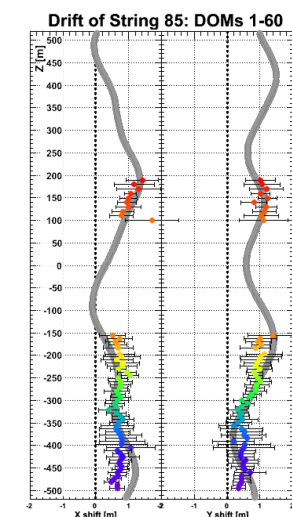


**Figure 5.5:** IceCube geometry calibration using trilateration algorithms of DOM flasher LEDs on string 85 of DeepCore and compared to drill data (gray band). Details and figure reference in the text.

<sup>177</sup> Sheremata “DeepCore DOM Profiles with the Trilateration Algorithm” (2013).

ice, however, decreased in agreement with depth <sup>177</sup>. The latter effect is most likely attributed to the integral accumulation of errors within drill sensor data <sup>134</sup>. In addition to the raw positioning of the DOMs, also the calibration of their respective cable positions and potential tilt of the DOM itself need to be understood. At the moment, all of these calibrations are based on LED flasher data <sup>174</sup>.

### 5.3 IceCube extensions

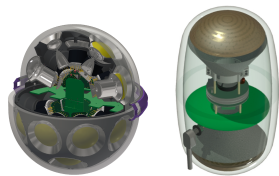
With the IceCube detector in operation for over ten years and the field of neutrino astronomy on the rise, possibilities to extend the IceCube capabilities have been investigated within recent years. Two science goals towards extending the IceCube experiment are commonly discussed: increasing the IceCube fiducial volume for high-energy neutrino astronomy <sup>178,179</sup> and installation of an additional sub-detector denser than DeepCore in order to compete in the sector of neutrino oscillation and mixing <sup>180,181</sup>. These projects are now typically referred to as *IceCube-Gen2* which, however, is more commonly associated with the neutrino astronomy extension whereas the low-energy installation is called the *IceCube Upgrade* since it will be installed within the next few years and as such is the first phase of the second-generation IceCube experiment.

<sup>178</sup> Aartsen et al. “IceCube-Gen2: A Vision for the Future of Neutrino Astronomy in Antarctica” (2014).

<sup>179</sup> Aartsen et al. “IceCube-Gen2: The Window to the Extreme Universe” (2020).

<sup>180</sup> Aartsen et al. “Letter of Intent: The Precision IceCube Next Generation Upgrade (PINGU)” (2014).

<sup>181</sup> Ishihara “The IceCube Upgrade – Design and Science Goals” (2019).



(a) Multit-PMT Optical Module. (b) D-Egg Optical Module.

**Figure 5.6:** IceCube Upgrade photosensors. Figure reference in the text.

#### 5.3.1 IceCube Upgrade

The IceCube Upgrade is the first phase of the IceCube-Gen2 experiment extension and will instrument a dense region within DeepCore with an additional set of seven strings. These strings will host a total of around 700 new photosensor modules, densely spaced along the strings with an inter-string and inter-module spacing of around 20 m and 3 m, respectively, with a general layout shown in fig. 5.7.

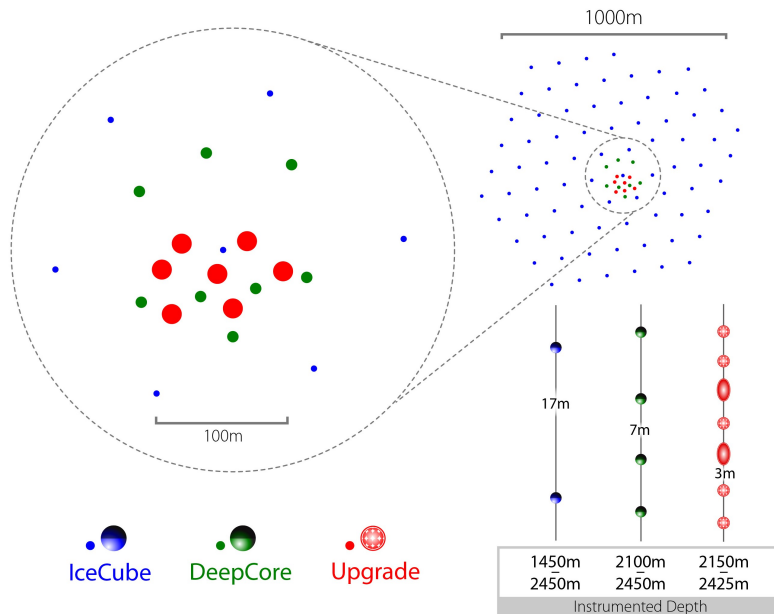
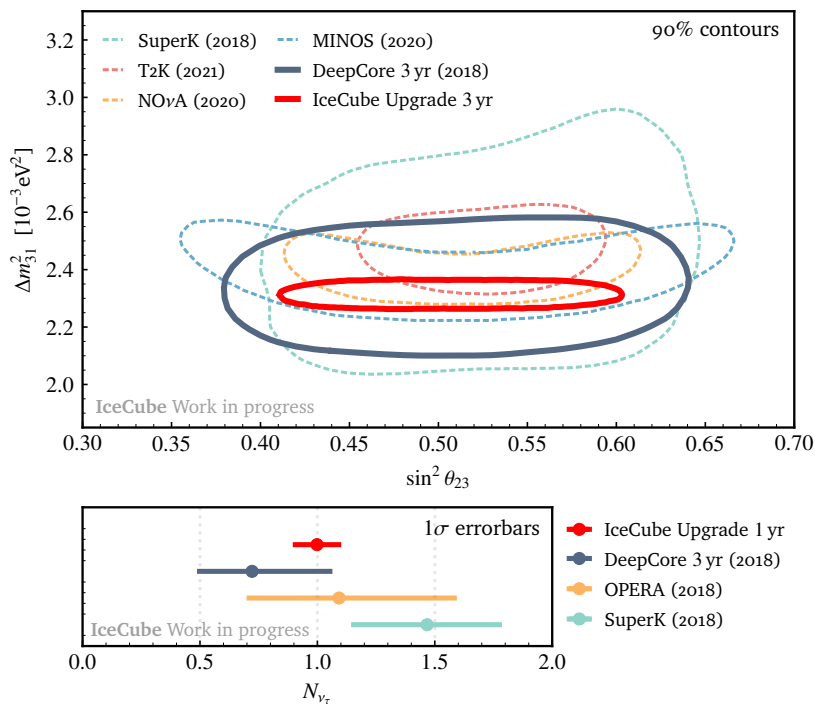


**Figure 5.7:** IceCube Upgrade layout overview showing its positioning within DeepCore as well as the dense inter-module spacing optimized for low-energy neutrino detection. Figure courtesy of the IceCube Collaboration.

The scope of the Upgrade is the extension of IceCube towards lower energies<sup>181</sup>, however, also the possibilities to deploy more, new and versatile calibration instrumentation will be used to tackle the dominating systematic effects of IceCube. As seen in fig. 5.6<sup>182</sup>, the new photosensor modules primarily compose of the *multi-PMT Digital Optical Module* (mDOM)<sup>183</sup> as well as the *Dual optical sensors in an Ellipsoid Glass for Gen2* (D-Egg)<sup>184</sup>. However, also an updated version of the DOM<sup>185</sup> as well as more experimental photosensors modules will be deployed. The latter are *research and development* (R&D) modules which primarily aim for potential applications within IceCube-Gen2 or the investigation of physics beyond the Standard Model. The new calibration devices encompass camera systems<sup>186</sup>, acoustic positioning systems<sup>187</sup> as well as novel calibration light sources<sup>188,189</sup>. Among the latter is the *Precision Optical Calibration Module* (POCAM) which is the topic of this work and will be discussed from chapter 6 on.

In terms of oscillation and mixing, the Upgrade is expected significantly improve the sensitivity of DeepCore and be competitive to current leading neutrino mixing experiments<sup>181</sup>. This is mainly due to increased detection rates for low-energy neutrinos as well as their subsequent photon signals using a large and more densely-instrumented detection volume with high-efficiency photodetection modules<sup>181</sup>. Here, the increased number of detected photons from the interactions yields improved reconstruction precision for low-energy events, specifically in the differentiation of flavors<sup>96,190</sup>. A comparison of current experimental limits<sup>46,191–196</sup> on the tau normalization  $n_\tau$ , the mixing angle  $\theta_{23}$  as well as the mass squared difference  $\Delta m_{31}^2$  is shown in the common fashion of oscillation experiments in fig. 5.8; reprocessed based on<sup>181</sup>. Here, the competitive expectation of oscillation measurements with the IceCube Upgrade is evident.



<sup>182</sup> Aartsen et al. “The IceCube Neutrino Observatory - Contributions to ICRC 2017 Part VI: IceCube-Gen2, the Next Generation Neutrino Observatory” (2017).

<sup>183</sup> Classen et al. “A multi-PMT Optical Module for the IceCube Upgrade” (2019).

<sup>184</sup> Shimizu et al. “Overview and performance of the D-Egg optical sensor for IceCube-Gen2” (2018).

<sup>185</sup> Sandstrom et al. “Digital optical module design for PINGU” (2014).

<sup>186</sup> Kang et al. “The camera system for the IceCube Upgrade” (2019).

<sup>187</sup> Heinen et al. “An Acoustic Calibration System for the IceCube Upgrade” (2021).

<sup>188</sup> Knuckles “Pencil Beam Overview” (2020).

<sup>189</sup> Fruck et al. “The POCAM as self-calibrating light source for the IceCube Upgrade” (2020).

<sup>190</sup> Eller et al. “Low Energy Event Reconstruction in IceCube/DeepCore” (work in progress).

<sup>191</sup> Aartsen et al. “Measurement of Atmospheric Neutrino Oscillations at 6–56 GeV with IceCube DeepCore” (2018).

<sup>192</sup> Li et al. “Measurement of the tau neutrino cross section in atmospheric neutrino oscillations with Super-Kamiokande” (2018).

<sup>193</sup> Agafonova et al. “Final Results of the OPERA Experiment on  $\nu_\tau$  Appearance in the CNGS Neutrino Beam” (2018).

<sup>194</sup> T2K Collaboration et al. “Improved constraints on neutrino mixing from the T2K experiment with  $3.13 \times 10^{21}$  protons on target” (2021).

<sup>195</sup> Himmel “New Oscillation Results from the NOvA Experiment” (2020).

<sup>196</sup> Whitehead “Neutrino Oscillations with MINOS and MINOS+” (2016).

**Figure 5.8:** Experimental sensitivities on mixing angle  $\theta_{23}$  and mass-squared difference  $\Delta m_{32}^2$  (top) as well as tau normalization (bottom) for selected experiments along with the IceCube Upgrade. Reference to the used data in the text.

### 5.3.2 IceCube-Gen2

IceCube observations of an astrophysical neutrino flux<sup>3</sup> as well as a first potential neutrino point source<sup>1,2</sup> triggered deeper investigations related to the requirements for improving the prospects of neutrino astronomy. The baseline plan for such extensions generally encompasses an increased fiducial volume in order to boost the detection rates of the highest-energetic neutrinos as well as larger possible lever arms for neutrino-induced muon tracks to provide better angular resolution e.g. <sup>103,179,197</sup>. For IceCube Gen2, the idea is to install a more sparsely instrumented array covering approximately ten times the fiducial volume of the current IceCube detector. This sparse spacing is possible due to the high transparency of the Antarctic ice. In addition to the in-ice array, the surface would host a large air-shower array as well as an even larger radio array extending the capabilities of the current IceTop detector, operating complementary to the in-ice array to probe the highest neutrino energies as well as cosmic rays and finally also provide needed air-shower veto capabilities<sup>179,197</sup>. The foreseen detector plans are visualized fig. 5.9 and show the Gen2 array extensions in addition to the current IceCube detector.

<sup>197</sup> Aartsen et al. “Neutrino astronomy with the next generation IceCube Neutrino Observatory” (2019).

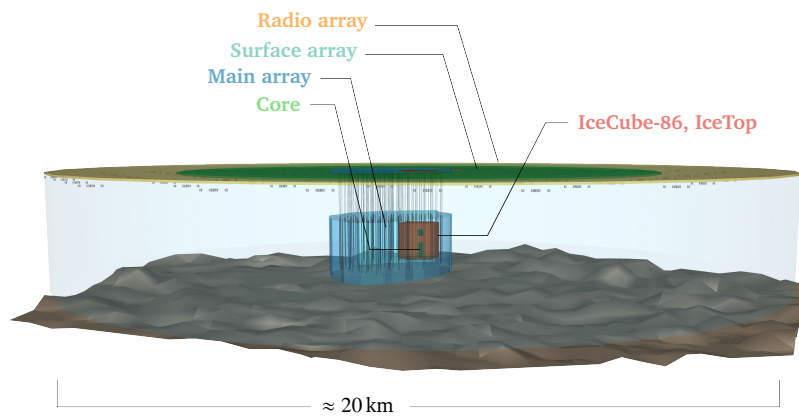


**Figure 5.9:** IceCube-Gen2 array extensions including the radio, surface and main array as well as the dense core for low-energy physics. The existing IceCube detector is also shown within the main array. Figure courtesy of the IceCube Collaboration and slightly adjusted.

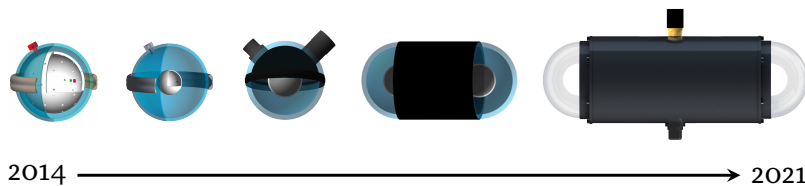
# 6

## Precision Optical Calibration Module: simulation and sensitivity estimates

With LED flashers limited in resolving the remaining systematic effects in IceCube, the realization of the IceCube Upgrade will enable the development of new and complementary calibration modules. With the Upgrade planned to be realized until the South Pole season of 2022/23, the project of developing the *Precision Optical Calibration Module* (POCAM)<sup>198</sup> was the main task of this work with a total 21 POCAMs planned to be installed in the Upgrade volume. Before reviewing the development of the hardware design in chapter 7, this chapter summarizes the device concept and then discusses simulation studies and machine learning techniques in order to quantify expected improvements of systematic uncertainties in IceCube. The chapter will eventually close with a physics-specific study of how the reduction of systematic uncertainties would translate into sensitivities of oscillation parameters within IceCube low-energy studies.

### 6.1 Instrument concept

Two problems of the existing IceCube LED flashers are their intensity fluctuations as well as pointing accuracy<sup>134</sup>. These systematic effects limit the achievable calibration precision and, thus, the investigation of a self-monitoring light source was initiated<sup>199–201</sup>. The idea of the POCAM is to install well-understood isotropic light sources within the IceCube detection volume which self-monitor their emission intensity. Hence, they remove the limiting capabilities of LED flashers as their characteristics are inherently independent from the detector signals. The POCAM development has been ongoing since 2014 and previous device iterations have already been installed in the GVD detector in Lake Baikal<sup>202</sup> as well as in the *Strings for Absorption Length in Water* (STRAW) experiment in the Pacific Ocean<sup>13,132</sup>. Over the course of these instrument installments, the device knowledge and calibration precision have continuously increased. A timeline of the device design progress is depicted in fig. 6.1; reprocessed based on<sup>13</sup>.



<sup>198</sup> Henningsen et al. “A self-monitoring precision calibration light source for large-volume neutrino telescopes” (2020).

<sup>199</sup> Jurkovič et al. “A Precision Optical Calibration Module (POCAM) for IceCube-Gen2” (2016).

<sup>200</sup> Veenkamp “A Precision Optical Calibration Module for IceCube-Gen2” (2016).

<sup>201</sup> Ackermann et al. “The IceCube Neutrino Observatory” (2017).

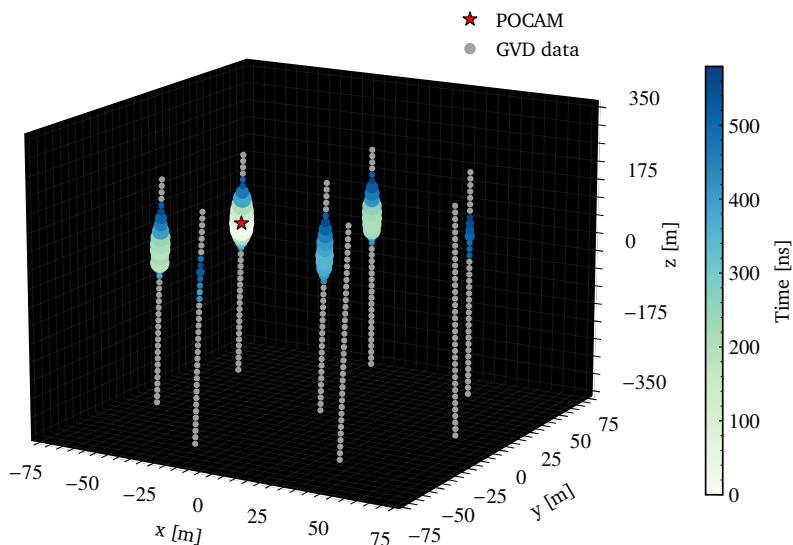
<sup>202</sup> Holzapfel “Testing the Precision Optical Calibration Modules in the Gigaton-Volume-Detector” (2018).

**Figure 6.1:** POCAM instrument timeline running from first studies (left) to the current device design (right). Figure reference in the text.

While the detailed device design and development is described in chapter 7, it is here sufficient to think of the POCAM as an isotropic light source emitting light pulses of  $10^5 - 10^{10}$  photons and widths of

2 ns – 50 ns and selectable wavelengths of 350 nm – 520 nm. An example event view of a POCAM flashing in the GVD cluster is depicted in fig. 6.2.

**Figure 6.2:** Example mean POCAM light signals observed at different detection modules within a GVD cluster. The dots show detection modules with their size representative of the logarithmic detected charge and their color representative of the light pulse peak arrival time. The position of the POCAM is indicated with a red star and this first instrument version emitted around  $10^9$  photons. Data courtesy of the GVD Collaboration.



The emitted number of photons of every pulse is monitored *in-situ*, that is, within the device itself and as such provides a detector-independent measure of the absolute intensity scale. This self-monitoring, together with the device calibration prior to deployment, provides precision information of the absolute number of emitted photons of each light pulse. In addition to the orientation-independent emission, the POCAM provides a reference light source able to tackle systematic effects within large-volume detectors. In total, the current plan is to install 21 of these instruments within the IceCube Upgrade.

## 6.2 Photon tracking simulation

Large-scale simulations of particles with thousands of detecting photosensors can readily cause extensive computational efforts. Tracking of particles over large propagation distances in IceCube is nowadays done using *graphics processing units* (GPUs)<sup>203</sup> where parallelizing multiple individual photon tracks speeds up the simulation significantly compared to central processing units (CPUs).

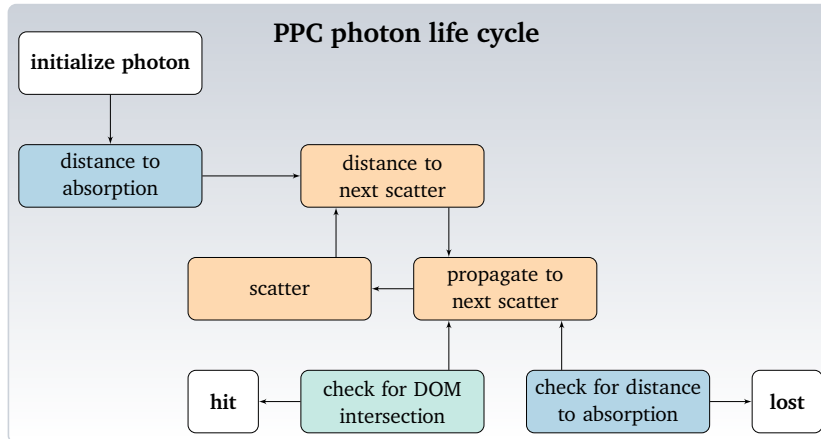
### 6.2.1 PPC: photon propagation code

One such framework is the *photon propagation code* (PPC)<sup>204</sup> which uses Monte-Carlo (MC) sampling to simulate photons propagating through the Antarctic ice by tracking scattering centers and resulting directional change as well as absorption and detection at different DOMs. The probabilities for scattering, absorption and detection are determined by the optical properties of the bulk ice volume, the hole ice description as well as the DOM photon acceptance function. For light emission PPC allows to simulate single and multiple LEDs as well as custom emission profiles, for example, isotropic or beamed. Here, the possibility to implement custom emission profiles enables

<sup>203</sup> Chirkin “Photon tracking with GPUs in IceCube” (2013).

<sup>204</sup> Chirkin “Photon Propagation Code” (2021).

studies of future calibration light sources. Upon initialization of a photon, it is propagated through the optical volume and can get scattered, absorbed or detected all of which is tracked individually for each photon within PPC. To imitate detector hardware and material properties, PPC uses downsampling based on the photon incident angle on the PMT, its wavelength acceptance curve and DOM efficiency to mimic the existing hardware and its transmission characteristics as well as the angular acceptance model. A general work flow of the simulation concept is shown in fig. 6.3; reprocessed based on <sup>205</sup>.



<sup>205</sup> Chirkin “Photon Propagation with GPUs in IceCube” (2014).

**Figure 6.3:** Flow chart of a photon life cycle simulated with PPC. Once the photon is initialized, scattering processes are tracked until the photon is either absorbed or hits a DOM. Figure referene in the text.

As for the optical parameters, the detection volume is typically divided into layers of similar optical properties as shown in fig. 5.3. Commonly, these ice layers are chosen to be 10 m in height and as such around 100 horizontal layers describe the detection volume of IceCube. In addition to the implementation of absorption and scattering coefficients as well as anisotropy, these ice layers follow the parametrization of the Antarctic relief<sup>133</sup> in order to account for the tilt of the layers with respect to each other. As for scattering, it is implemented in PPC by two analytical approximations of the Mie scattering function via the Henyey-Greenstein (HG)<sup>206</sup> and Simplified-Liu (SL)<sup>207</sup> scattering parametrizations described as

$$p(\cos \theta) = \frac{1}{2} \frac{1 - g^2}{(1 + g^2 - 2g \cos \theta)^{3/2}} \quad (\text{HG}) \quad (6.1)$$

$$p(\cos \theta) \propto (1 + \cos \theta)^\alpha, \quad \text{with } \alpha = \frac{2g}{1 - g} \quad (\text{SL}) \quad (6.2)$$

respectively. In both cases, the functions are described solely by the average scattering angle  $g = \langle \cos \theta \rangle$ . In addition to  $g$ , the ice model fits are carried out approximating the scattering function in the Antarctic ice with a superposition of both parametrizations via the fractional parameter  $f_{\text{SL}}$  as

$$p(\cos \theta) = (1 - f_{\text{SL}}) \cdot \text{HG}(\cos \theta) + f_{\text{SL}} \cdot \text{SL}(\cos \theta) \quad (6.3)$$

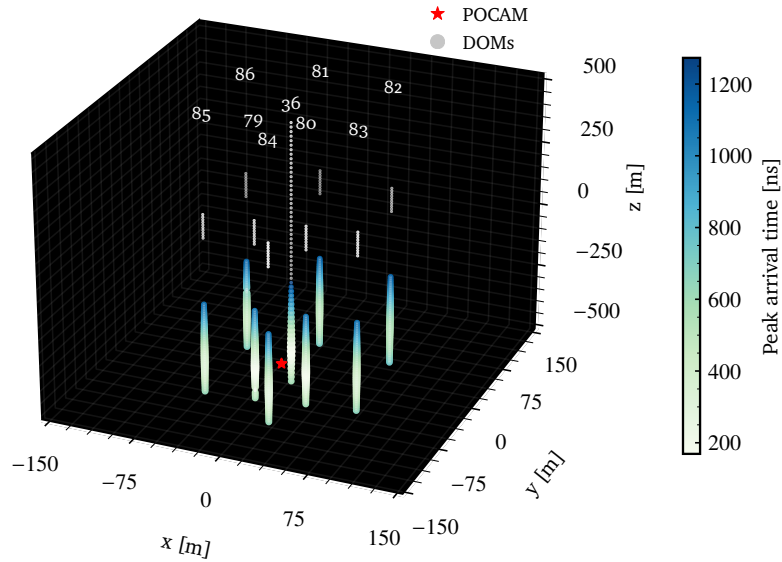
To speed up simulations further, PPC allows to configure a *DOM oversizing* parameter which allows inflation of the DOM size. Oversizing the DOMs typically only results in a small timing bias<sup>134</sup> and

<sup>206</sup> Henyey et al. “Diffuse radiation in the Galaxy.” (1941).

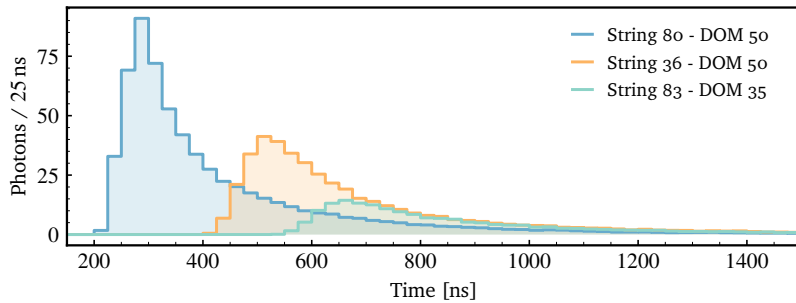
<sup>207</sup> Liu “A new phase function approximating to Mie scattering for radiative transport equations” (1994).

is thus a common strategy to increase simulation speed. All simulations described in the following use the PPC software chain with a DOM oversizing factor of 16 to simulate emission, propagation and detection of photons in the IceCube detector. An example event view of flashing an isotropic light source within the IceCube detection volume is shown in fig. 6.4 together with particular DOM response curves given as the histogram of detected photons as a function of time.

**Figure 6.4:** Example PPC simulation output of an isotropic light source within the IceCube volume. The figure shows both the 3-dimensional event display of the light detection (top) with size representative of detected charge and color arrival time as well as individual DOM response histograms (bottom) of detected photons as a function of time for three different emitters. In the top figure, the grid shows the simulated volume encompassing DeepCore (strings 79 to 86) as well as string 36 of the bulk IceCube array. The simulated POCAM position in the Upgrade is marked with a red star and, in this particular example, emits around  $1 \times 10^9$  photons.



(a) Simulated event view of an isotropic light flash within IceCube at one of the Upgrade strings.



(b) Simulated charge histograms recorded by three different sensor positions within the array.

### 6.2.2 Upgrade deployment baseline

For the Upgrade, a baseline deployment plan for all calibration devices has been laid out and the scope of these simulation studies was to verify whether the targetted calibration goals could be achieved with it. Positioning of the Upgrade strings as well as the vertical instrumentation plans are shown in the top and bottom figure of fig. 6.5, respectively. Here, the dense instrumentation of the Upgrade within the DeepCore volume as well as the distribution of POCAMs is visible. While more than 20 POCAMs will be installed within the Upgrade, due to the complexity and required computational effort of IceCube simulation studies, the focus of this work lies on the seven POCAMs located in the physics volume. The latter is the clearest ice between

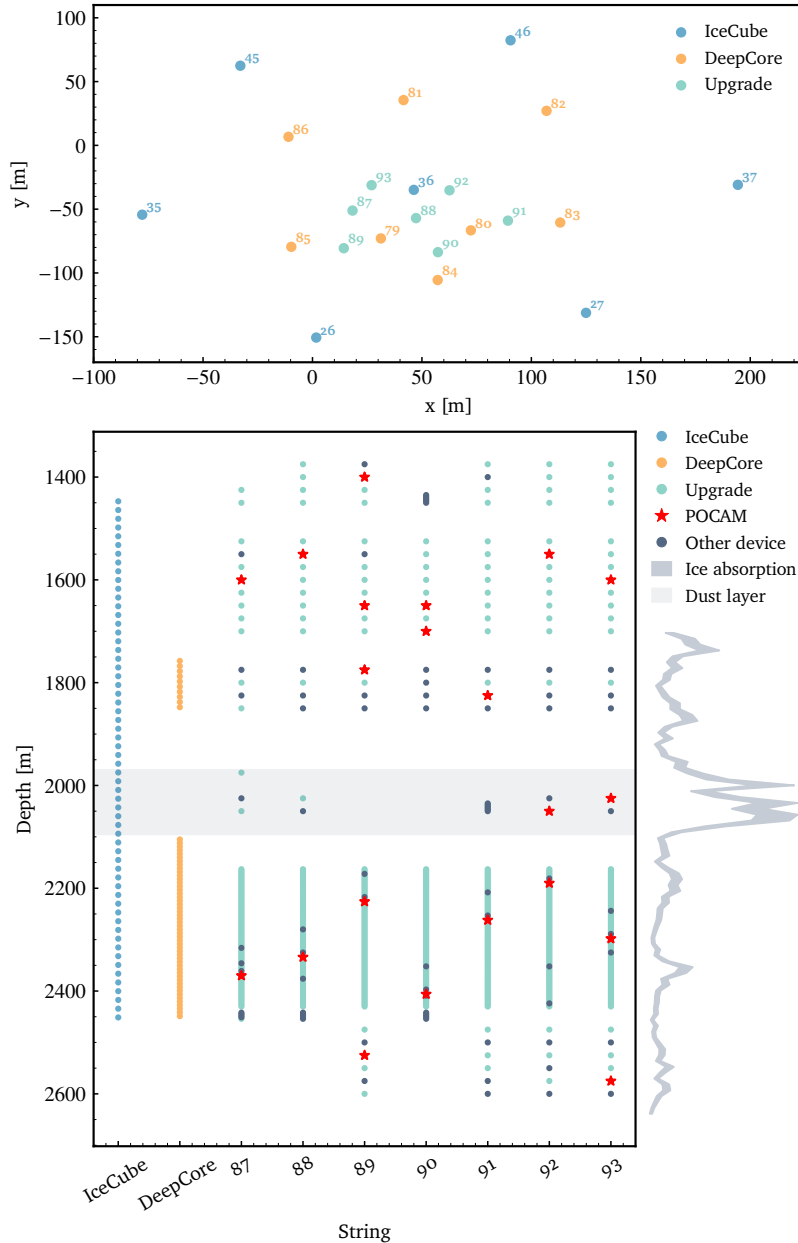


**Figure 6.5:** *IceCube Upgrade baseline layout in birds-eye (top) and vertical (bottom) view. Both figures show the existing IceCube detector (blue) as well as DeepCore (orange) in addition to the new Upgrade string design plan. The bottom plot further shows the positions Upgrade photosensors (green) as well as POCAM positions (red star) and other special devices planned for the Upgrade (dark blue). On the side of the bottom figure the ice absorption coefficient is further shown qualitatively. Data courtesy of the IceCube Collaboration.*

approximately 2100 m – 2450 m. The calibration sensitivity study of this sub-section of POCAMs aims to provide a proof-of-principle that this calibration instrument can significantly contribute to the improvement of systematics in the IceCube detector. The considered POCAM instrument positions are further detailed in table 6.1. To further simplify the situation, only DOMs within DeepCore as well as string 36 are considered for this study, totalling around 540 DOMs. To estimate even more conservative results, the Upgrade photosensors are not included.

### 6.2.3 Parameter space

With all the systematics detailed in chapter 5, this study aims to find calibration sensitivities for the systematics of bulk ice absorption and scattering, DOM efficiency and hole ice parameters. Additional pa-

**Table 6.1:** POCAM positions and depths within the physics volume considered for proof-of-principle simulation studies.

POCAM	String	DOM	Depth [m]
1	87	84	2370
2	88	72	2334
3	89	38	2226
4	90	100	2406
5	91	50	2262
6	92	28	2190
7	93	64	2298

parameters, for example ice anisotropy or the average scattering angle, can be readily added to the general analysis work flow, however, are not part of this first study.

In order to check these systematic effects, a simulation work flow has to be set up which is able to produce simulations based on different systematic parameter sets. The range of different systematic parameters depends mostly on their uncertainty from previous studies. Among these, bulk absorption and scattering are among the less ambiguous systematics and are, as already outlined in chapter 5, commonly denoted with a 10 % systematic uncertainty on their absolute values. Since dust loggers and ice fits have shown similar results for the relative layer-to-layer variations of the ice model, these relative layer relations will be adapted and only a global scaling of the parameters will be performed in the range of their uncertainties. For DOM efficiency one has to differentiate between relative and absolute DOM efficiency. Relative DOM efficiencies describe the DOM-to-DOM variations and also can be obtained from flasher fits<sup>134</sup>. Thus, these relative variations will also be adapted here and only global scaling of the absolute DOM efficiency is applied within the simulation. Lastly, the hole ice within IceCube and as such all currently possible hole ice models are considered. The general parameter ranges are summarized in table 6.2.

**Table 6.2:** Systematic parameter ranges in the POCAM simulation study. Given for each parameter is its absolute interval as well as its mean and the considered distribution for potential interval sampling. Data provided by the IceCube Collaboration.

Parameter	Mean	Range	Distribution
Bulk ice, absorption	1.0	[0.4, 1.6]	Normal
Bulk ice, scattering	1.0	[0.4, 1.6]	Normal
DOM efficiency	1.0	[0.4, 1.6]	Normal
Hole ice, $p_0$	0	[-1.0, 1.0]	Uniform
Hole ice, $p_1$	0.05	[-0.1, 0.2]	Uniform

While the DOM efficiency linearly scales the number of detected photons, the remaining parameters directly influence the detected charge responses for different DOMs. A collection of these effects is given in fig. 6.6 for a particular emitter-receiver pair.

In this case, each parameter affects the shape and normalization of the recorded charge histogram and the coherent change in all DOMs

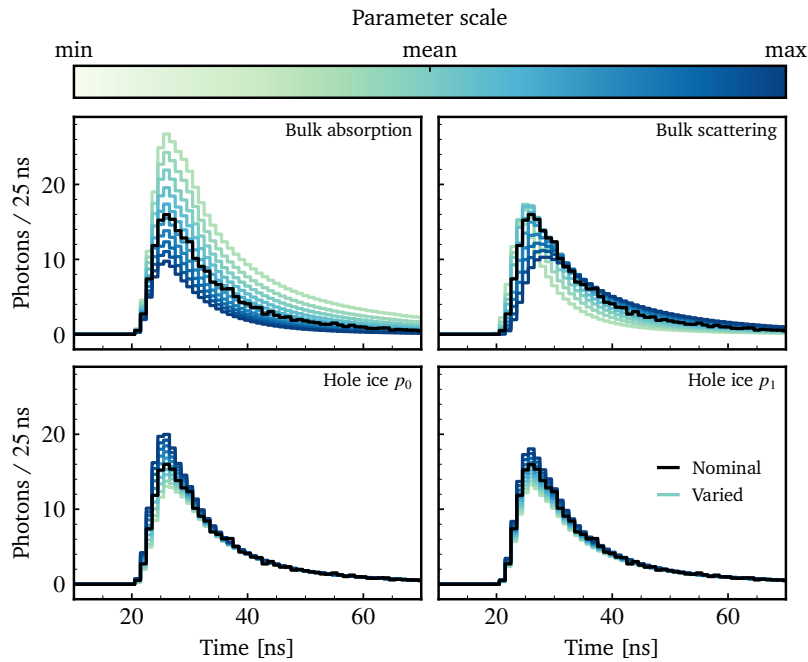


**Figure 6.6:** Systematic parameter effects on an example DOM response histogram for bulk ice absorption and scattering as well as the unified hole ice parameters. The colorbar indicates the scaling of the parameter relative to its respective mean and interval range. While the effects of the bulk ice variation are significant, the hole variation causes only subtle changes to the profile of this particular DOM.

throughout different systematic parameter configurations eventually allows determination of a best-fitting set of parameters via statistical methods explained later in section 6.4. While the bulk ice variation causes significant changes to the response histograms, changes of the hole ice are more subtle and only the measurement of different emitter positions can help disentangle its properties for a particular receiver.

### 6.3 Machine learning approximation

With the goal of this study being to investigate sensitivities in a five-dimensional systematic parameter space, computational effort has to be considered. With a single simulation of one flashing DOM emitting  $N = 100$  flashes of  $1 \times 10^9$  photons each and DOM oversizing of 16 running around 1-2 hours, grid scanning of the whole parameter space in reasonable granularity is not feasible. And since an analytical approximation with sufficient precision does not exist<sup>134</sup>, we will make use of machine learning. Instead of carrying out countless simulations, we sample the parameter space sparsely and use a neural network to interpolate between simulated grid points.

#### 6.3.1 Neural network basics

Neural networks (NNs) are structures of interconnected nodes. This smallest unit of each neural network is mathematically described by

$$y = f\left(\sum_i^N w_i x_i + b\right) \quad (6.4)$$

where the inputs  $x_i$  and the weights  $w_i$  together with a bias term  $b$  and a non-linear activation function  $f$  result in the output  $y$  given  $N$

<sup>208</sup> Rosenblatt “The perceptron: a probabilistic model for information storage and organization in the brain.” (1958).

<sup>209</sup> Kronmueller “Application of Deep Neural Networks on Event Type Classification in IceCube” (2018).

<sup>210</sup> Shukla “Designing Your Neural Networks” (2019).

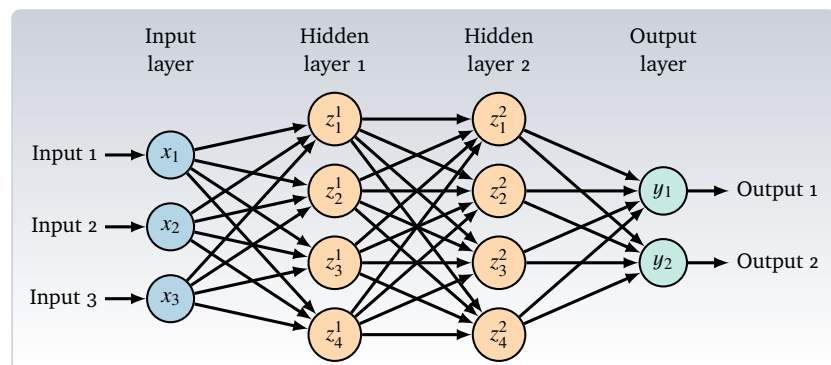
<sup>211</sup> Agarap “Deep Learning using Rectified Linear Units (ReLU)” (2018).

input values. Such a node is commonly referred to as a *Rosenblatt Perceptron*<sup>208</sup>. Given some input, the strength (that is the weight  $w_i$ ) of these connections between different nodes together with the used activation function determines the output of the network. While various activation functions exist e.g. <sup>209,210</sup>, a common starting point for any application is the *Rectified Linear Unit (ReLU)*<sup>211</sup> which simply maps negative values to zero and otherwise returns the input. The network itself is then built from various layers each of which contains some number of nodes. In its simplest form, a neural net is structured as follows

1. **Input layer** – This layer depends on the format of the input data that should be given to the network. It can be, for example, pixels of an image or a vector of parameters.
2. **Hidden layer** – Multiple of these layers can be used between input and output layers. The contained nodes provide the functionality to describe the output given the input by means of weighting their interconnections.
3. **Output layer** – This layer depends on the format of the expected output that should be returned by the network. This can be, for example, probabilities of classes or arbitrary output data.

Each of the nodes in each of the layers is interconnected to nodes of the previous and the following layer in a way that depends on the layer type. Different layer types exist e.g. <sup>209,210</sup> and the way of structuring them is often the result of empirical experimentation in order to find an architecture that describes the data of a given application suitably<sup>210</sup>. In the simplest case of a fully-connected network pictured in fig. 6.7, each node is connected to all nodes of the previous and all nodes of the following layer.

**Figure 6.7:** Schematic view of a fully-connected deep neural network with input, output and two hidden layers. In a fully-connected network each of the nodes is connected to all nodes of the previous and all nodes of the following layer. Graphic adapted from M. Völk (September 2021, [https://github.com/mvoelk/nn\\_graphics](https://github.com/mvoelk/nn_graphics))



Once the network architecture is set up, the last step is training the network on a dataset. For this, one training and one validation dataset are necessary. While the former is used to train the network, the latter is used to validate the trained network output. The training process now iteratively adjusts the connection weights between the layers so that the the training input describes the training output more and more accurately. This is done by trying to minimize the *loss  $L$*  of the network – which describes the quality of the network prediction given the known truth from the dataset – following its

gradient and iteratively updating the model weights  $\theta_i$ . A *gradient-descent algorithm*<sup>212</sup> adjusts the weights based on the learning rate  $\alpha$  and can be described via<sup>209</sup>

$$\theta_{t+1} = \theta_t - \alpha \frac{dL}{d\theta_t} \quad (6.5)$$

Here, again various loss functions exist and their selection depends on the application<sup>209,210</sup>.

Finally, training success depends on the network architecture, the quality and size of the training dataset as well as the training time and intrinsic training configuration all of which are usually adjusted empirically until the neural net performs as expected or required for a specific application. It should be noted that improper architecture or training configuration can result in overtraining, that is, the NN learning artificial features only present in the training dataset. This can be avoided by adjusting the learning rate as well as introducing batch normalization or dropout layers within the net which regulate the training during optimization so that artificial feature extraction is reduced<sup>209,210,213</sup>.

### 6.3.2 Network architecture

In our case, the network is supposed to approximate DOM response histograms given a specific vector of input parameters. Our inputs must minimally contain the flasher and receiver positional information within the detector as well as the systematic parameter configuration but we can also include additional information which might be useful when training the net. Thus, we will make use of the following input vector

$$\vec{v}_{\text{input}} = \begin{pmatrix} \text{String index}_{\text{emitter}} \\ \text{DOM index}_{\text{emitter}} \\ \text{String}_{\text{receiver}} \\ \text{DOM}_{\text{receiver}} \\ \text{Distance}_{\text{emitter/receiver}} \\ \text{Polar angle}_{\text{emitter/receiver}} \\ \text{Bulk ice absorption} \\ \text{Bulk ice scattering} \\ \text{DOM efficiency} \\ \text{Hole ice, } p_0 \\ \text{Hole ice, } p_1 \end{pmatrix} = \begin{pmatrix} S_e \\ D_e \\ S_r \\ D_r \\ d \\ \theta \\ a \\ b \\ \epsilon \\ p_0 \\ p_1 \end{pmatrix} \quad (6.6)$$

defining the parameters of emitter and receiver positions as well as their relative distance and polar angle in addition to the systematic parameters. It should be noted that ice anisotropy would show as an azimuthal effect in the simulation, thus, upon its implementation in the systematic variation, the azimuthal angle of the emitter/receiver pair should be included in the training.

The neural net response of such an input vector should return the

<sup>212</sup> Ruder “An overview of gradient descent optimization algorithms” (2017).

<sup>213</sup> Srivastava et al. “Dropout: A Simple Way to Prevent Neural Networks from Overfitting” (2014).

DOM response histograms for the given input configuration, that is

$$\text{DOM response histograms} = \text{NN}(\vec{v}_{\text{input}}) \quad (6.7)$$

In terms of architecture, several NN structures have been tested and the best-performing one is given in table 6.3. Here, the NN is composed of an input, an output and seven hidden layers with the number of nodes increasing towards the center layer and decreasing towards the edge layers. Additionally we have included batch normalization layers at each hidden layer stage to reduce overfitting. While the shape of the input layer is determined by eq. (6.6), the output layer shape depends on the number of desired histogram bins  $N_{\text{bins}}$  which the net should predict. The softplus activation of the output layer finally only allows non-negative values as we expect histogram bins to have non-negative entry counts only.

**Table 6.3:** Neural network architecture for predicting DOM response histograms. Given is the layer structure of the neural net including number of nodes, activation function and whether batch normalization was used.

Layer	Nodes	Activation	Batch normalization
Input	11	-	-
Hidden 1	64	ReLU	yes
Hidden 2	128	ReLU	yes
Hidden 3	256	ReLU	yes
Hidden 4	512	ReLU	yes
Hidden 5	256	ReLU	yes
Hidden 6	128	ReLU	yes
Hidden 7	64	ReLU	yes
Output	$N_{\text{bins}}$	Softplus	-

### 6.3.3 Multi-dimensional parameter sampling

The input dataset required for training the NN needs to contain simulated DOM response histograms of various emitter/receiver combinations as well as systematic parameter variations. As such, its dimensionality scales with

$$\dim(\text{dataset}) \sim N_{\text{emitter}} \times N_{\text{receiver}} \times N_{\text{sys}} \quad (6.8)$$

As mentioned previously, we limit ourselves to the physics volume of IceCube and only look at the eight DeepCore strings in addition to string 36 totaling  $N_{\text{receiver}} = 540$  DOMs. With the number of POCAMs within the physics volume of the IceCube Upgrade being seven, the remaining determining factor for the number of simulations is the systematic variation size  $N_{\text{sys}}$ . Now, to sample the parameter space, one could use common randomizing tools of multi-dimensional problems in Python<sup>214</sup>, for example, NumPy<sup>215</sup> or SciPy<sup>216</sup>. While such tools are readily available, in our case the  $n$ -dimensional quasi-random number sequence  $R_n$  developed by Roberts<sup>217</sup> has some advantages, especially at small sample sizes. Using a generalized Golden Ratio<sup>218</sup>,

<sup>214</sup> Van Rossum et al. “Python reference manual” (1995).

<sup>215</sup> Harris et al. “Array programming with NumPy” (2020).

<sup>216</sup> Virtanen et al. “SciPy 1.0: Fundamental Algorithms for Scientific Computing in Python” (2020).

<sup>217</sup> Roberts “The Unreasonable Effectiveness of Quasirandom Sequences” (2018).

<sup>218</sup> Krcadinac “A new generalization of the golden ratio” (2006).

the infinite  $R_n$  sequence constructs a multi-dimensional sequence of quasi-random numbers that samples the parameter space without overhead and with low discrepancy. For  $d$  dimensions and  $N$  samples it is defined as<sup>217</sup>

$$\vec{t}_n = \{n\vec{\alpha}\}, \quad n = 1, 2, 3, \dots, N \quad (6.9)$$

$$\text{where } \vec{\alpha} = (1/\Phi_d^0, \dots, 1/\Phi_d^d) \quad (6.10)$$

$$\text{and } \Phi_d \text{ is the unique positive root of } x^{d+1} = x + 1 \quad (6.11)$$

Furthermore, if it becomes evident that some initially-chosen number of samples was insufficient to achieve the required precision, the grid can simply be extended by including more points of the sequence. A two-dimensional example of this sequence is shown in fig. 6.8 in comparison to the implementation of pseudo-random numbers in NumPy. Here, the benefits of the  $R_n$  sequence at small numbers of samples  $N \sim \mathcal{O}(100)$ , especially with regard to overhead and sampling density, are evident.

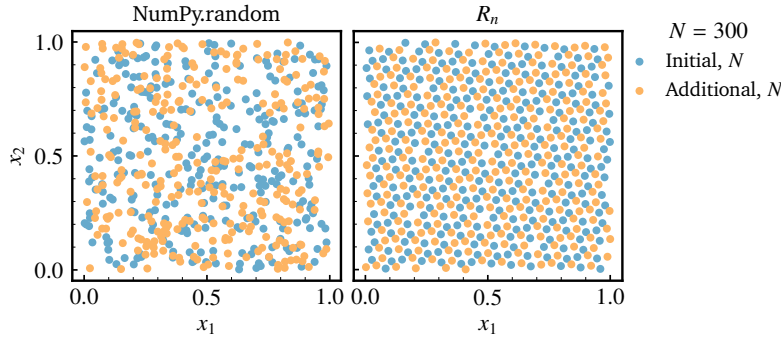


**Figure 6.8:** Comparison of NumPy.random and the  $R_n$  sequence of quasi-random numbers in the two-dimensional ( $n = 2$ ) unit interval. The figures show the sampling of initial  $N = 300$  points (blue) and an additional  $N = 300$  points (orange). It is evident that the  $R_2$  sequence produces essentially no overhead while more uniformly sampling the parameter space when a small number of points is used.

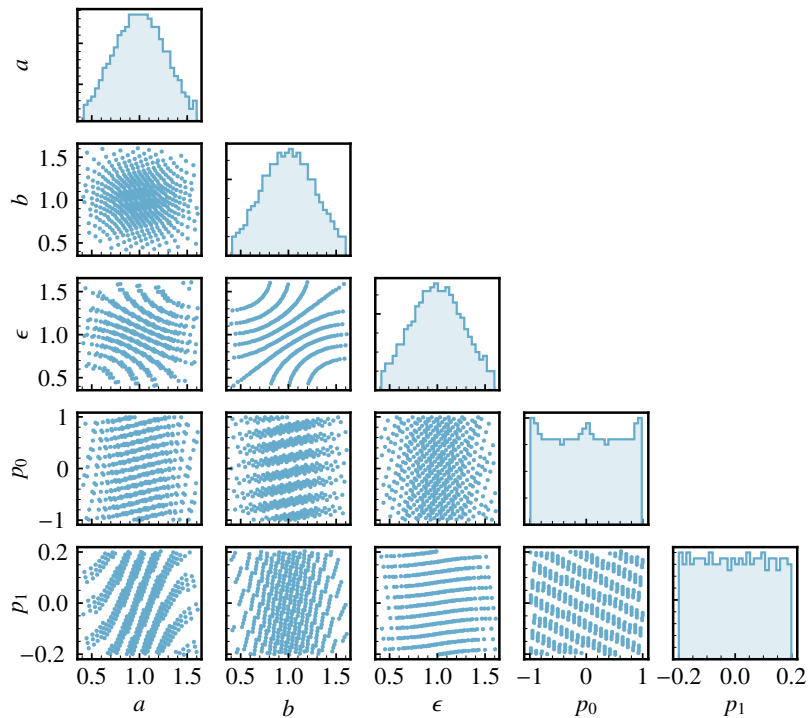
Once a unit-interval sample of the systematic parameter space is generated, we can further transform the space based on prior constraints to each of the dimensions. Such priors can constrain parameter ranges as well as distributions and make sense if other means – for example other analyses of systematic effects within IceCube – have already provided knowledge of these parameters. That being said, we impose the priors given in table 6.2 on the parameters in the generated unit-interval sample<sup>a</sup> and the resulting parameter distribution within the five-dimensional systematic space is pictured example in fig. 6.9 for a systematic set of size  $N_{\text{sys}} = 500$ . Also here it is evident that the  $R_n$  sequence samples the parameter space without creating significant overhead which is essential when simulation time and resources are limiting factors.

#### 6.3.4 Dataset generation and training

In the scope of this study, the two datasets given in table 6.4 have been simulated: the first contains the cumulative emission of all six horizontal flasher LEDs for ten different DOMs distributed throughout the physics volume, the second one contains the isotropic emission of seven virtual POCAMs at their baseline positions within the IceCube Upgrade. Systematic variations for both sets were 1000 and 2000 points, respectively, mostly limited by the computational time of the

<sup>a</sup> Note that for Gaussian priors this is done by applying the inverse of the cumulative Normal distribution function to the sample; for unit intervals this is done by a simple substitution of the interval edges.

**Figure 6.9:** Five-dimensional systematic parameter sampling using the quasi-random sequence  $R_n$  ( $n = 5$ ) for a sample size of  $N = 500$  samples. Shown here are the relative parameter sampling points in their respective two-dimensional projections (off-diagonal) as well as the general one-dimensional parameter distributions (diagonal) resulting from prior constraints on the unit-interval sampling points. While Normal priors are assumed for absorption ( $a$ ), scattering ( $b$ ) and DOM efficiency scales ( $\epsilon$ ), the hole ice parameters ( $p_0, p_1$ ) are uniformly constrained only on their respective expected ranges.



respective simulations and the resulting dataset size. Notably, as the POCAM dataset is solely based on simulation, its binning can be chosen freely at this point. While the POCAM dataset should be used for estimating potential calibration improvements after its installation, the flasher dataset is used in section 6.4.3 to verify the applicability of the analysis chain on actual experimental flasher data of IceCube. For the flasher data, on the other hand, the binning was pre-determined by the available experimental data to be 25 ns. table 6.4 also contains light pulse characteristics within the specific simulations. For the flasher dataset those result predominantly from the settings used in the LED flasher calibration runs from IceCube, for the POCAM these correspond to its expected characteristics.

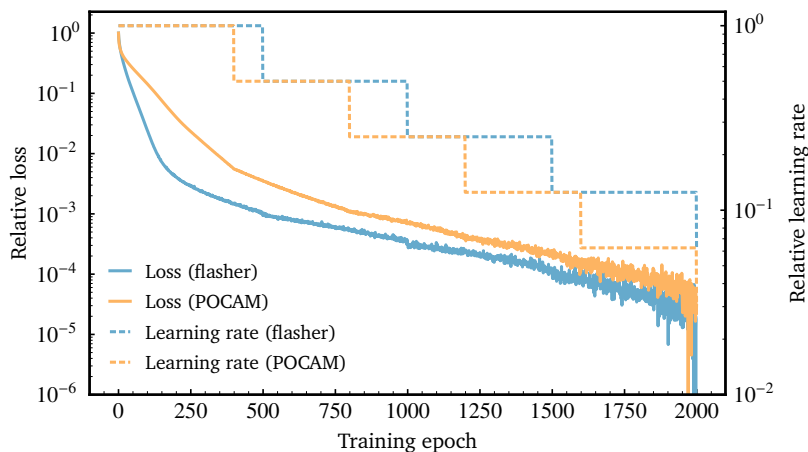
**Table 6.4:** Dataset generation properties for neural net training. The table shows both generated datasets and their generation configurations in terms of emitter and receiver statistics as well as emission characteristics of the light pulses. For the flashers the latter were set to match an experimental dataset, for the POCAM they are based on expected performance.

Parameter	Dataset	
	Flasher	POCAM
Emission	Six horizontal DOM LEDs (cumulative)	Isotropic
Flashers	10	7
DOMs		540
Systematic samples	1000	2000
Pulses / flasher		100
Photons / pulse		$1 \times 10^9$
Pulse width [ns]	70	5
Wavelength [nm]		405
Simulations	10 000	14 000

In order to setup and train a neural network able to predict DOM response histograms using a given dataset, we make use of the *TensorFlow package*<sup>219</sup> for Python. Here, the network architecture described in table 6.3 is readily setup and can be trained on a given dataset. Since we are dealing with histogram bins, the loss function in our case is best described by a probabilistic Poisson-type loss of expected prediction  $\hat{y}$  and true value  $y$  via<sup>220</sup>

$$L = \frac{1}{N} \sum_i^N (\hat{y}_i - y_i \log \hat{y}_i) \quad (6.12)$$

which directly describes the nature of our data (number of hits in a bin) and further accounts for relative contributions to the loss depending on bin entry counts. We then further use the *Adam minimization algorithm*<sup>221</sup> to minimize the loss function during training of the network. This minimizer is an advanced version of the basic gradient-descent algorithm and tends to work well also when starting parameters are chosen suboptimally<sup>210</sup>. Furthermore, experimentation showed that starting with a large learning rate and iteratively decreasing it stepwise works best since weight changes iteratively increase in precision during optimization. Once proper training configurations are found, a neural net is trained for both datasets and for an amount of epochs that results in convergence. For both datasets, the training configuration was setup with an initial learning rate of  $10^{-6}$  and stepwise decreasing it by a factor of 1/2 after every a few hundred epochs totalling a training time of 3000 epochs and using the corresponding binning of the dataset. The result of this training procedure for both datasets is shown in fig. 6.10 where both the relative loss of the networks as well as the learning rate adjustments are drawn.



<sup>219</sup> Abadi et al. “TensorFlow: Large-Scale Machine Learning on Heterogeneous Systems” (2015).

<sup>220</sup> Fallah et al. “Nonlinear Poisson regression using neural networks: A simulation study” (2009).

<sup>221</sup> Kingma et al. “Adam: A Method for Stochastic Optimization” (2017).

**Figure 6.10:** Relative loss and learning rate for an example network training process using the flasher dataset. Shown are the relative loss of the network (blue) and the step-wise adjusted learning rate (orange) as a function of the training epoch.

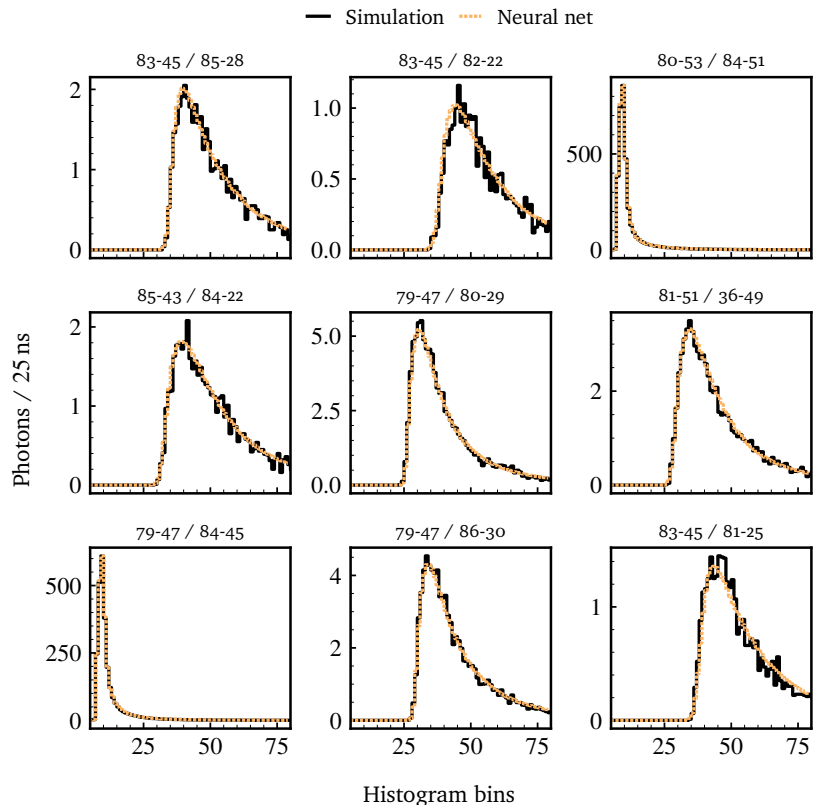
As for the learning configuration, these numbers were found after experimenting with different training configurations until proper convergence without significant overtraining was found. Since the datasets are similar in size and general shape, both neural nets showed similar convergence behaviour with this configuration. The resulting shape of the loss function further gives us reasonable confidence that the learning parameters were chosen properly and the

network did not overtrain significantly since the loss curve does not flatten out for the majority of the training time. The latter would result in weight adjustments fixing on specific data patterns which we want to avoid. As for the binning, the flasher dataset was only available in 25 ns binning so the neural net was trained in the same binning configuration. For the POCAM dataset, the analysis is based on simulation and so the binning was chosen to increase exponentially. More details on the binning of both datasets are discussed in section 6.4.3 and section 6.4.4, respectively.

### 6.3.5 DOM histogram predictions

Finally, once the networks are trained on the datasets, they can be used for DOM response histogram predictions given variable systematic parameter configurations. An example selection of emitter/receiver predictions using the flasher dataset is given in fig. 6.11. Here, it is evident that the neural net performs well across a large range of bin counts from DOMs that see very faint light to DOMs that are close to the emitter. However, the figure also shows that there are occasionally slight discrepancies in bin counts which are most likely attributed to limited training time and the complexity of the dataset.

**Figure 6.11:** Example neural net DOM response histogram predictions for given emitter/receiver position combinations. The figure shows simulated (blue) and predicted (orange) data for nine distinct combinations of emitter/receiver positions within the detection volume for a given set of systematic parameters. The neural net is able to predict the DOM responses over a large dynamic range of photon statistics.



Nevertheless, the general accuracy of the net to reproduce the expected DOM response histograms given some systematic configuration seems reasonable. To further examine the interpolation of systematic parameters, the neural net scaling of the five different systematic parameters is shown in fig. 6.12 for an example DOM with

reasonable photon statistics. First and foremost, the DOM efficiency is a simple linear scaling of the bin counts which the net reproduces to sufficient precision given the bin statistics in this particular case. Also the scaling of the bulk and hole ice parameters resembles the one found with simulation (refer to fig. 6.6). Thus, we can preliminarily conclude the net performs the necessary interpolation of our systematic parameters for a given emitter/receiver position.

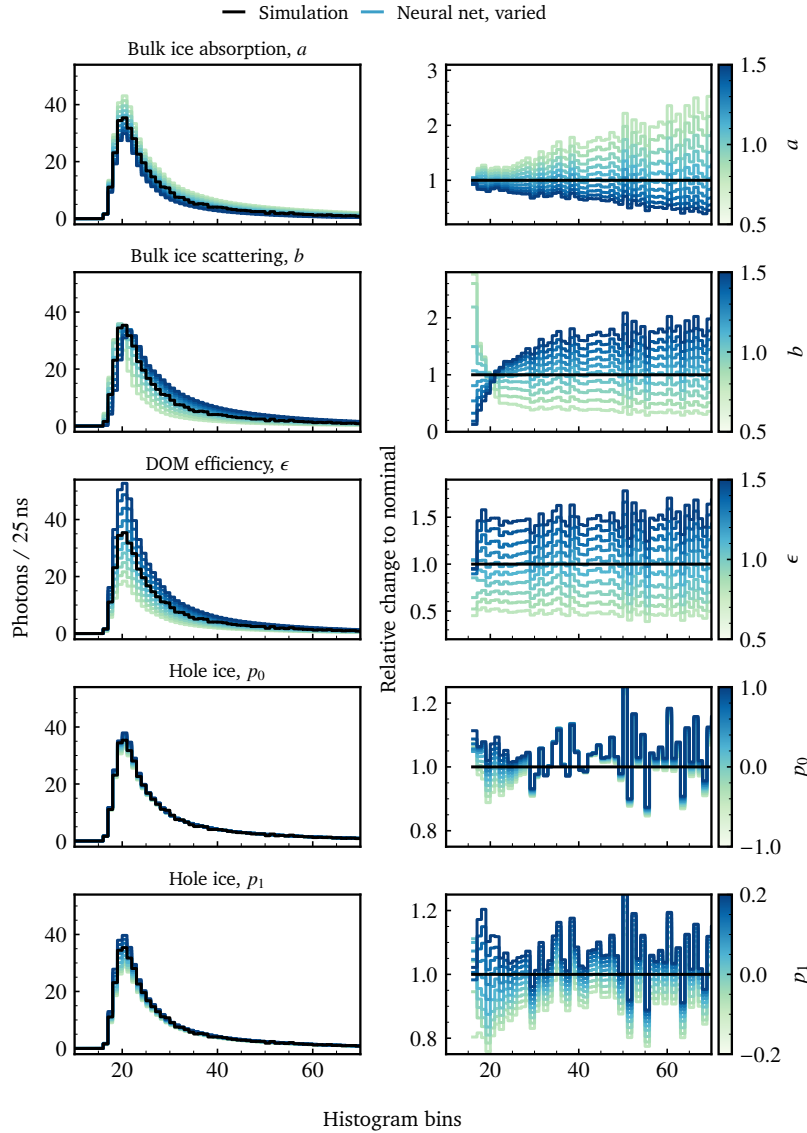
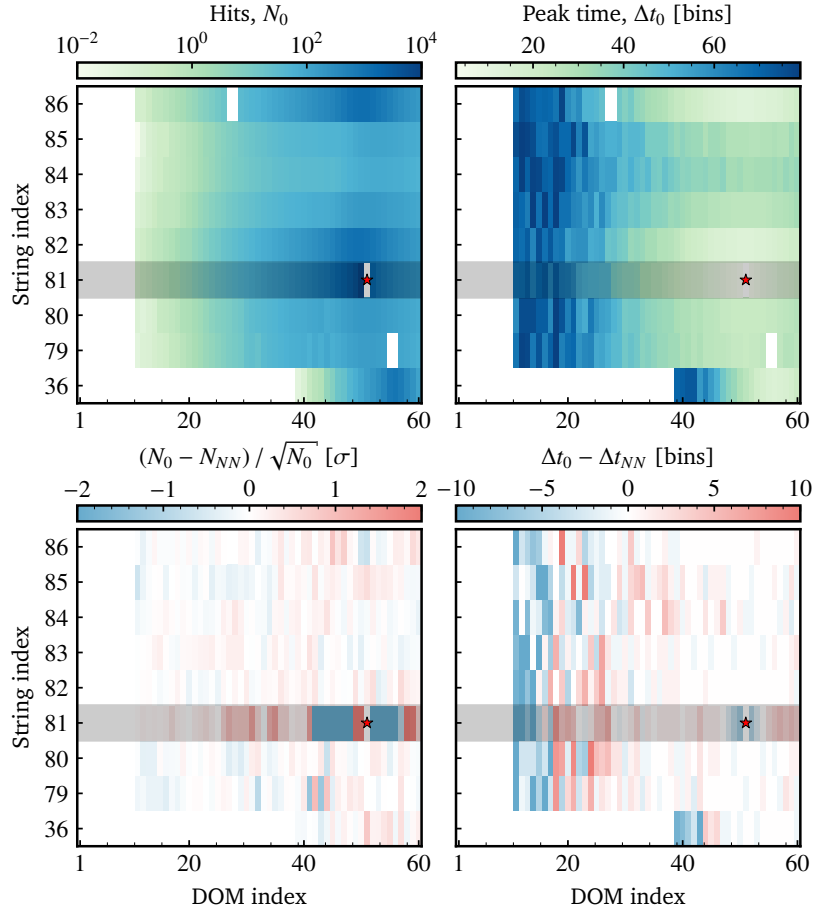


**Figure 6.12:** Systematic parameter scaling of a particular emitter/receiver pair as predicted using the neural network trained on the flasher dataset. The left figure columns show the raw DOM response histograms for both the simulated emission (black) as well as the varied systematic parameters (colored).

Now, the comparison shown in fig. 6.12 needs to be expanded to include the whole array of sensors used in order to make sure the net performs throughout the volume. For this, we reduce the data to two quantities, total hits and peak time, and draw the relative comparison between a simulated dataset and the neural net prediction. An example of this is shown in fig. 6.13 and verifies that the neural net indeed performs well throughout most of the detector volume given that statistics at the receiver are sufficient. However, it is also evident that the net fails to predict properly on the string where the flasher is located. After investigation, this seems to be an issue for any flasher position and is related to the zenith angle training pa-

parameter as it is zero for all DOMs on a particular string. Thus, all intra-string receivers and their data are subsequently excluded from any further analysis which is not an issue as enough receivers remain and the same is also done in existing IceCube flasher analyses<sup>133,134</sup>. As the POCAMs were placed on Upgrade strings, this problem is mitigated in their respective neural net as it is trained solely on data of existing strings and hence does not suffer the zenith problem. The detailed Python implementation of the training procedure is given in appendix A.

**Figure 6.13:** Comparison of detector signal for a simulated event of the flasher dataset and the corresponding neural net prediction. The figure shows simulated total hits  $N_0$  (top left) and simulated peak time of the light pulse  $\Delta t_0$  (top right) as well as the relative difference to the neural net prediction to total hits (bottom left) and peak time (bottom right) as a function of string and DOM index. The color scales for the hit and the peak time difference show the deviation of the neural net prediction in units of standard deviation and time bins, respectively. All figures indicate the example flasher position (red star) as well as the inter-string region (grey band) which will not be used in subsequent analyses. The occasional missing data points correspond to DOMs which were marked malfunctional in the geometry file.



Finally, in order to reflect limited hardware resolution capabilities of IceCube as well as the neural net zenith problem, selected cuts are applied to the dataset prior to analysis. In addition to removing DOMs that are on the same string of the flashing one, data bins are only taken into account when showing significant entries ( $n > 10$ ) but remain below saturation limit of the PMTs given the particular binning (32 hits/ns).

## 6.4 Data analysis methods

Before we can verify the interpolation of the neural net on experimental data, we need to confirm that it actually performs well enough to re-fit simulated data. This can be done by preparing a procedure for analyzing and fitting a set of pseudo-data – which was generated on some combination of systematic parameters – using the neural

net. If the net performs well throughout the detector and across the multi-dimensional parameter space, it should be able to re-fit the configuration of systematic parameters used to generate the set of pseudo-data. Furthermore, using the net within such an analysis gives direct feedback on its achievable precision.

#### 6.4.1 Poisson-binned likelihood histogram comparison

When dealing with counting data it is common to use a Poisson-likelihood approach e.g. <sup>222,223</sup>. This is valid since the counts in each bin are described by a Poisson distribution <sup>224</sup>, that is, the probability to observe  $k$  events given an expected count  $\gamma$  via

$$p(k|\gamma) = \frac{\gamma^k}{k!} e^{-\gamma} \quad (6.13)$$

Now, the comparison of (pseudo-) data to a model can be done by using this Poisson probability to describe the chance of observing a particular bin count  $k$  given the bin expectation  $\gamma$ . This is typically applied to all bins and the resulting likelihood, that is, the product of all relevant bins  $i$ , is described by

$$\mathcal{L}(\{k_i\}|\{\gamma_i\}) = \prod_i p_i(k_i|\gamma_i) \quad (6.14)$$

and gives a measure for the match of the data given a particular model expectation. The better the expectation and data match, the larger this likelihood. For numerical reasons, minimization of the negative logarithmic likelihood (LLH) is often easier as it reduces the product to a sum

$$-\log \mathcal{L}(\{k_i\}|\{\gamma_i\}) = \sum_i \log p_i(k_i|\gamma_i) \quad (6.15)$$

$$= \sum_i (\gamma_i - k_i \log \gamma_i) \quad (6.16)$$

where, in the last line, we have omitted model-independent terms as they only contribute constant factors <sup>223</sup>. However, several approximations to this cost function exist and the usage as well as potential bias introduction depends on the application <sup>223</sup>.

#### 6.4.2 Sampling posterior distributions

We want to estimate the set of model parameters – that is,  $a$ ,  $b$ ,  $\epsilon$ ,  $p_0$  and  $p_1$  – which best describes the DOM response histograms for some (pseudo-) data at hand. Here, the simulation is replaced with the trained neural net.

While there are several minimization procedures, the potential existence of various nuisance parameters – such as individual flasher intensity scales – as well as the interest in the posterior sensitivities prompted the use of a Bayesian *Markov chain Monte Carlo* (MCMC) approach e.g. <sup>225</sup>. Here, several walkers are spawned throughout the parameter space following prior distributions and, guided by randomization algorithms, explore the posterior distributions within all dimensions given some quality measure, that is, in our case, the binned

<sup>222</sup> Chirkin “Likelihood description for comparing data with simulation of limited statistics” (2013).

<sup>223</sup> Fowler “Maximum-Likelihood Fits to Histograms for Improved Parameter Estimation” (2014).

<sup>224</sup> Poisson “Recherches sur la probabilité des jugements en matière criminelle et en matière civile” (1837).

<sup>225</sup> Brooks et al. “Handbook of Markov Chain Monte Carlo” (2011).

<sup>226</sup> Bayes “An essay towards solving a problem in the doctrine of chances” (1763).

likelihood. While the prior distributions may contain any a priori knowledge about the parameters, the posterior distribution results from the Bayes theorem<sup>226</sup>

$$P(H|D) = \frac{P(D|H)P(H)}{P(D)} \quad (6.17)$$

where the hypothesis  $H$  and experimental data  $D$  are used to determine the posterior probability  $P(H|D)$  of some hypothesis given the data based on the prior probability of the hypothesis  $P(H)$  and the likelihood  $P(D|H)$  of observing  $D$  given  $H$ . The denominator is equal for all hypotheses and thus does not contribute in distinguishing relative differences.

<sup>227</sup> Foreman-Mackey et al. “emcee: The MCMC Hammer” (2013).

Using the Python implementation of *emcee*<sup>227</sup>, we are then able to sample the posterior distribution space using the likelihood definition in eq. (6.16) and directly obtain a measure of the precision of the technique as well as the performance of the neural net. One Python implementation of this method for this particular study is added in appendix B. In addition, priors can be imposed on the parameters which can be used to implement prior knowledge into the sampling procedure. However, in the flasher cases, flat priors are assumed throughout, that is, no prior knowledge on the parameters is imposed.

To verify that the neural net prediction and the analysis chain are eventually able to distinguish between the different systematic dimensions, the first test is to fit pseudo-data. Here, a particular set of systematic parameters is simulated and the neural net as well as the likelihood description are used to determine a fit to this data. The first step of the expectation/data comparison is to decide whether or not the individual flasher intensities should be fit. While the former works well if the light source characteristics are known to some precision and stable, it reduces in precision once the light emission characteristics are poorly understood on an absolute level. If that is the case, one circumvention is to force the expectation to match the charge of the data and thus removing absolute intensity as well as DOM efficiency  $\epsilon$  from the fit. This is done by renormalizing the expectation via

$$\text{expectation}_{\text{norm}} = \text{expectation} \times \frac{\max(\text{data})}{\max(\text{expectation}_{\text{nominal}})} \quad (6.18)$$

with the nominal expectation from the current best-fit parameters in IceCube. While this introduces a slight bias towards the nominal model, it ensures that the remaining parameters of hole and bulk ice determine the light pulse shapes and relative bin counts but the uncertain flasher intensity effect on the response curves is significantly reduced. For the pseudo-data set, the posterior sampling of the fit using the renormalized expectation is shown in fig. 6.14 with the results tabulated in table 6.5. From these results it is clear that the neural net performs well and we are able to re-fit the systematic parameters of the pseudo-dataset with sub-percent precision.

### 6.4.3 Verification using experimental IceCube LED data

Once verified using the pseudo-data, the analysis chain can further be applied to the experimental IceCube LED dataset. Here, again, we

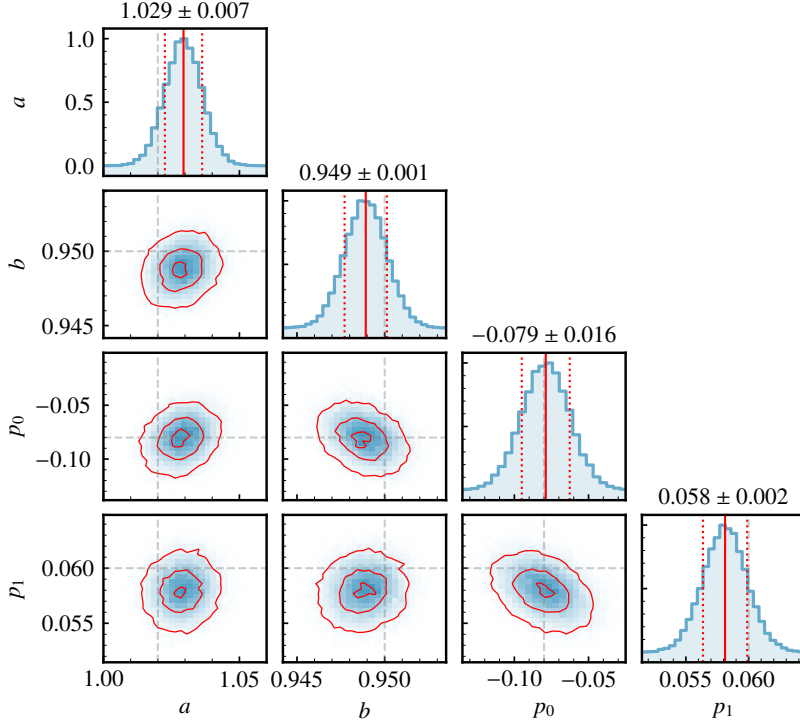


**Figure 6.14:** Pseudo-data fit results using the neural net and MCMC sampling. The plot shows the posterior parameter distributions of the MCMC random walk sampling in one-dimensional (diagonal) and two-dimensional (off-diagonal) projections. The best-fit results are indicated above the diagonal entries with mean and  $1\sigma$  indicated with a line and dashed lines, respectively. The off-diagonal distributions contain contours corresponding to normalized distribution levels of 0.1, 0.5 and 0.9. All figures show the true systematic parameters of the pseudo-data as grey dashed lines.

Parameter	True	Best-fit	Total error
Bulk ice, $a$	1.02	$1.029 \pm 0.007$	0.012
Bulk ice, $b$	0.95	$0.949 \pm 0.001$	0.002
Hole ice, $p_0$	-0.08	$-0.079 \pm 0.016$	0.016
Hole ice, $p_1$	0.06	$-0.058 \pm 0.002$	0.003

**Table 6.5:** Systematic parameter fit results of the flasher pseudo-data using the neural net and MCMC sampling. The table shows the injected truth of the pseudo-data, best-fit and total error of the fit procedure for the ice parameters. The latter is the quadratic sum of the fit standard deviation and its mean deviation from the true value.

make no use of priors as we do not want to impose any knowledge on any of the systematic parameters. Furthermore, the fit is carried out twice: once with no constraints on the likelihood and once normalized per-DOM by averaging the likelihood over all used flashers and receivers. The latter more conservatively captures the effect of global variations in the systematic parameters on individual DOMs. However, in both cases, time jitter is emulated by randomly shifting the relative bin position of model and data by one bin, that is, 25 ns. While that is extreme, it also adds to the conservativeness of the fit.

The MCMC sampling results for the per-DOM average likelihood approach are shown in fig. 6.15 and results for both approaches are tabulated in table 6.6. From this it is evident that the procedures are able to handle experimental data and the best-fit results are within the expected uncertainty of the nominal depth-dependent IceCube fits of around 10% as well as the flat hole ice ranges. It should be noted that, while the given uncertainties appear to be relatively small in the unconstrained likelihood case, the model is significantly simplified by removing absolute intensity-dependence via the normalization in eq. (6.18) and thus prone to over-estimate the fitting parameter precision. However, the more conservative result in this case, the per-DOM average likelihood, captures gives reasonable confidence that the fit

procedure is sound. In general, the analysis shows to be compatible with simulated and experimental data and the precise knowledge of the POCAM emission intensity in subsequent studies should allow to estimate expected improvements.

**Figure 6.15:** Systematic parameter fit results of the flasher dataset using the neural net and MCMC sampling and the per-DOM average likelihood approach. The plot shows the posterior parameter distributions of the MCMC random walk sampling in one-dimensional (diagonal) and two-dimensional (off-diagonal) projections. The best-fit results are indicated above the diagonal entries with mean and  $1\sigma$  indicated with a line and dashed lines, respectively. The off-diagonal distributions contain contours corresponding to normalized distribution levels of 0.1, 0.5 and 0.9.

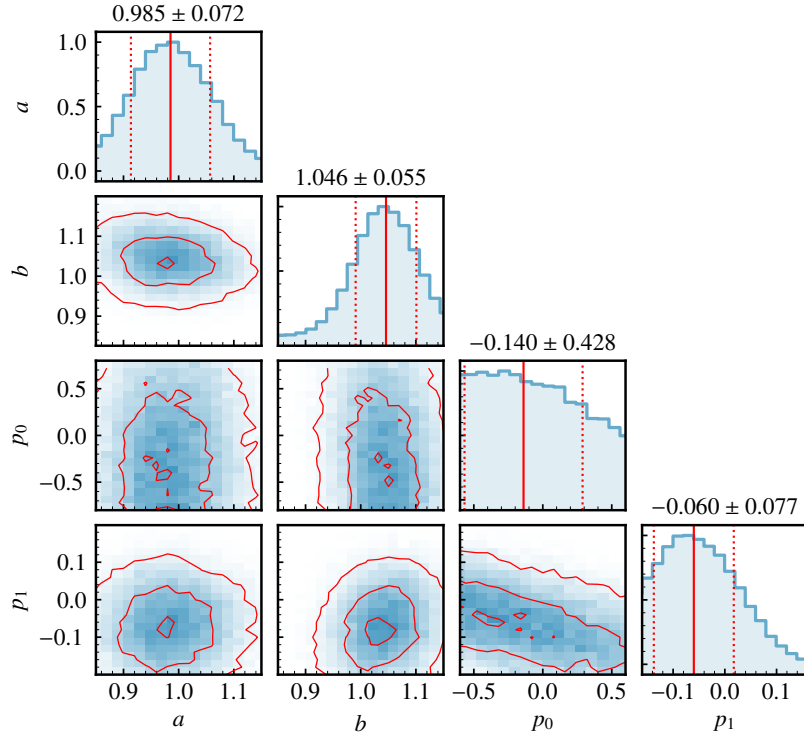


**Table 6.6:** Systematic parameter fit results of the flasher dataset using the neural net and MCMC sampling. The table shows the best-fit as well as the nominal IceCube values for the ice parameters resulting from the unconstrained global and the per-DOM average likelihood fits.

Parameter	Nominal	Best-fit global	Best-fit per-DOM
Bulk ice, $a$	$1.0 \pm 0.1$	$0.988 \pm 0.024$	$0.985 \pm 0.072$
Bulk ice, $b$	$1.0 \pm 0.1$	$1.048 \pm 0.018$	$1.046 \pm 0.055$
Hole ice, $p_0$	$-0.27^{+0.57}_{-0.23}$	$-0.312 \pm 0.252$	$-0.140 \pm 0.428$
Hole ice, $p_1$	$-0.042^{+0.092}_{-0.058}$	$-0.046 \pm 0.037$	$-0.060 \pm 0.077$

#### 6.4.4 Improvement of low-energy sensitivities in IceCube

After verifying the integrity of the fitting procedure on both simulated and experimental data, the next step is now to estimate potential improvements using the POCAMs and their well-calibrated emission profiles. For this, the normalization eq. (6.18) is removed and individual flasher intensity scaling parameters are introduced in the MCMC sampling. These scales receive priors related to the POCAM intensity calibration precision which is around 4% as is derived later in chapter 7. This also enables fitting the DOM efficiency in addition to the ice parameters and as such it is also included in the sampling.

For seven POCAMs distributed within the physics volume of IceCube and emitting nominal intensities of around  $10^9$  photons in a sharp 5 ns pulse the fit results are shown in fig. 6.16. The figure

clearly shows the precision that can be reached with well-calibrated light sources. The results, tabulated in table 6.7, show that percentage precision is achievable on bulk ice parameters as well as DOM efficiency and that also hole ice can globally be constrained more stringently than it is now. That is especially important to potential improvements on existing physics analyses.

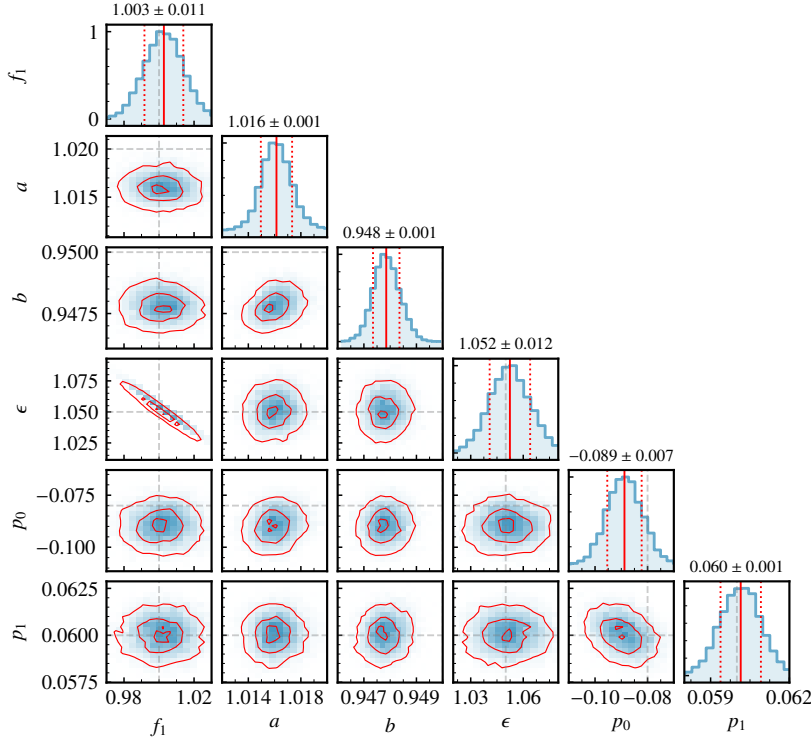


**Figure 6.16:** Systematic parameter fit results of the POCAM dataset using the neural net and MCMC sampling. The plot shows the posterior parameter distributions of the MCMC random walk sampling in one-dimensional (diagonal) and two-dimensional (off-diagonal) projections. The best-fit results are indicated above the diagonal entries with mean and  $1\sigma$  indicated with a line and dashed lines, respectively. The off-diagonal distributions contain contours corresponding to normalized distribution levels of 0.1, 0.5 and 0.9. All figures show the true systematic parameters of the pseudo-data as grey dashed lines. Note that here also the emission intensity of all seven POCAMs was fitted individually even though only one of them ( $f_1$ ) is explicitly drawn here.

Parameter	True	Best-fit	Total error
Bulk ice, $a$	1.02	$1.016 \pm 0.001$	0.004
Bulk ice, $b$	0.95	$0.948 \pm 0.001$	0.002
Efficiency, $\epsilon$	1.05	$1.052 \pm 0.012$	0.012
Hole ice, $p_0$	-0.08	$-0.089 \pm 0.007$	0.011
Hole ice, $p_1$	0.06	$0.060 \pm 0.001$	0.001

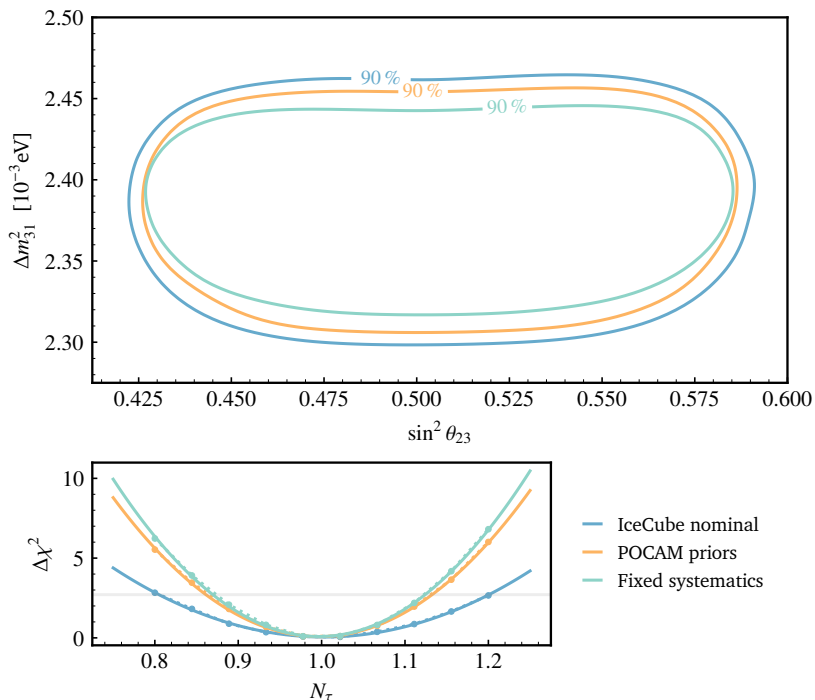
We can now use these priors as potential improvements of the systematic parameters within IceCube and check how their reduction influences low-energy analyses. For this, we use the latest high-statistics simulation sample which extends the latest published oscillation analysis<sup>46,191,228</sup> to eight years of simulated data and utilizes an improved selection. This next-generation analysis is currently under development in IceCube. We then run it once with nominal and once with POCAM-modified priors in order to check the resulting sensitivities on different physics parameters. Here, the focus lies on tau normalization as well as the oscillation parameters  $\sin^2 \theta_{23}$  and  $\Delta m_{31}^2$  and re-running the analysis chain for different priors results in the contours shown in fig. 6.17. The general take-away is that the POCAM improvements have the potential to significantly boost

**Table 6.7:** Systematic parameter fit results of the POCAM pseudo-data using the neural net and MCMC sampling. The table shows the injected truth of the pseudo-data, best-fit and total error of the fit procedure for the ice parameters. The latter is the quadratic sum of the fit standard deviation and its mean deviation from the true value.

<sup>228</sup> Aartsen et al. “Development of an analysis to probe the neutrino mass ordering with atmospheric neutrinos using three years of IceCube DeepCore data” (2020).

low-energy sensitivities. All parameters of interest show significant improvements on the POCAM-modified priors with respect to the nominal case. With respect to the nominal case the 90 % confidence levels for  $\sin^2 \theta_{23}$ ,  $\Delta m_{31}^2$  and tau normalization improve by around 5 %, 10 % and 31 %, respectively. That means, the POCAM as a well-calibrated light source has the potential to significantly impact the estimation of the mixing parameters of neutrinos with IceCube. This all will be further improved once the IceCube Upgrade will be also installed. We also expect, but need to be validated with further dedicated studies, that similar studies can be carried out in the future to check if also high-energy point-source and diffuse flux analyses can benefit from the POCAM application.

**Figure 6.17:** Low-energy sensitivities depending on different systematic prior assumptions for  $\sin^2 \theta_{23}$  and  $\Delta m_{31}^2$  (top) and tau normalization (bottom). The top contours show the 90% confidence levels for nominal, POCAM-improved and fixed systematics and clearly state the potential improvement using the POCAM. The bottom plot shows the fit procedure  $\Delta\chi^2$  as a function of tau normalization and the 90 % level of the one-dimensional  $\Delta\chi^2$  distribution. In all parameter dimensions, the POCAM priors significantly improve the sensitivity of the study with respect to the physics parameters of interest.



## 6.5 POCAM emission and hole ice simulation

Another smaller study was the development of a detailed instrument simulation. This simulation is embedded in the *Geometry and Tracking* (GEANT4) framework<sup>229</sup> and makes use of individual photon tracking to simulate and optimize the POCAM emission profile. An example snapshot of a visualized simulation is shown in fig. 6.18 and highlights the detail to which the optical properties of the various POCAM components are simulated.

Here, the light emission of an LED is simulated within the POCAM integrating sphere which in turn makes the light pulse isotropic. This emission can further be selected to include the POCAM housing, the glass pressure hemisphere as well as internal components and potential coating. While the optimization procedure of these various optical quantities only becomes relevant in the hardware part (chapter 7), this simulation additionally includes the possibility to vary the surrounding medium and even to include a simplified hole ice.

<sup>229</sup> Agostinelli et al. “*Geant4 – a simulation toolkit*” (2003).

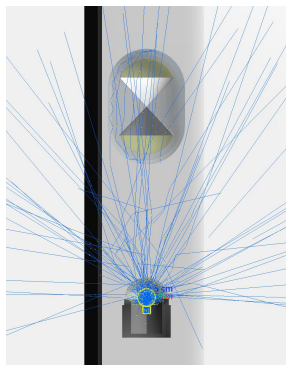


**Figure 6.19:** Direct hole ice simulation setup with POCAM (bottom), D-Egg (top) and main cable (left).

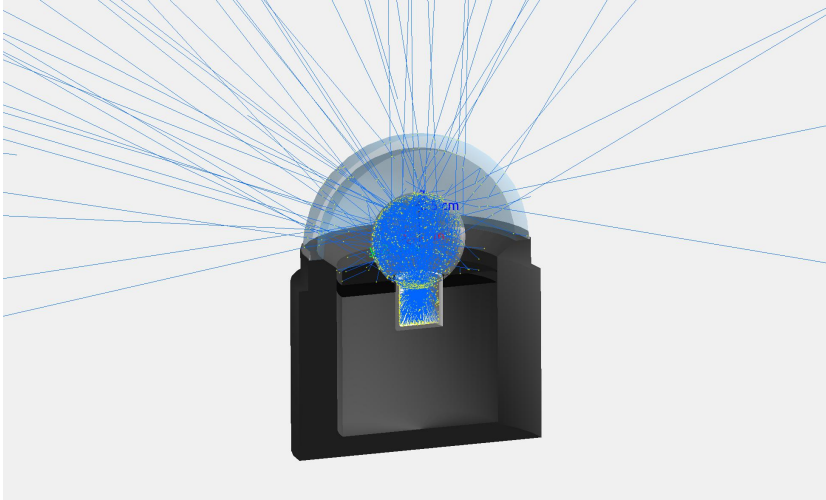


**Figure 6.18:** POCAM GEANT4 emission simulation including housing, glass pressure hemisphere, integrating sphere, internal mounting components and coating. The photons emitted in the integrating sphere are diffused and eventually exit to the outside.

As the inclusion of hole ice is possible, a study was carried out to check whether hole ice properties could be inferred from neighboring instruments. In this study, the POCAM was placed 3 m below of a simplified D-Egg module and both were placed in a hole ice column; as pictured schematically in fig. 6.19. Then, the D-Egg detected photons at its upper and lower PMTs which were then binned in time and compared to pseudo-data with the likelihood definition of eq. (6.16). Doing so, it was possible to scan two of the primary hole ice parameters: size and scattering length. Due to the cylindrical symmetry, this setup has no access to a potential offset angle of the hole ice with respect to the drillhole, however, using an mDOM with multiple azimuthal PMT directions should also allow to tackle this parameter.

Carrying out a simple grid scan in the two dimensions of hole ice size and scattering length results in the likelihood landscape shown in fig. 6.20. Here, it is evident that constraining the hole ice parameters is possible in such a simplified scenario. However, more detailed studies within this framework are planned prior to POCAM deployment – especially looking towards including mDOMs with multiple PMTs – that should be able to more stringently constrain realistic hole ice parameters and even allow investigating azimuthal effects.

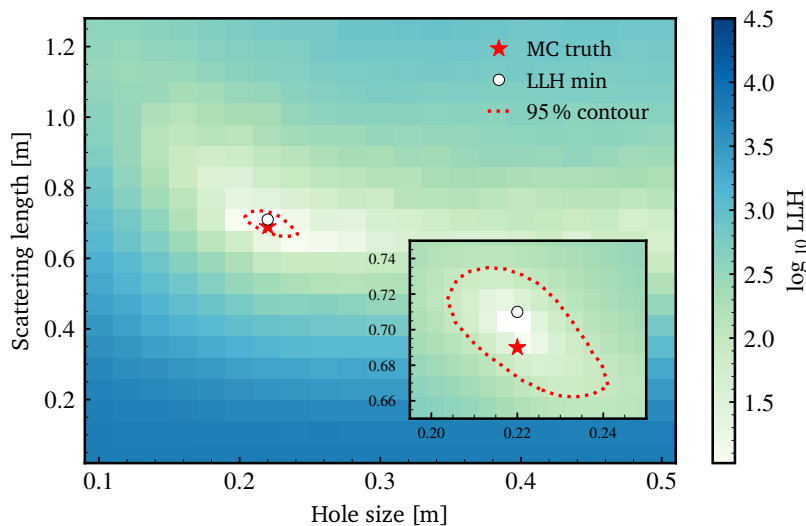


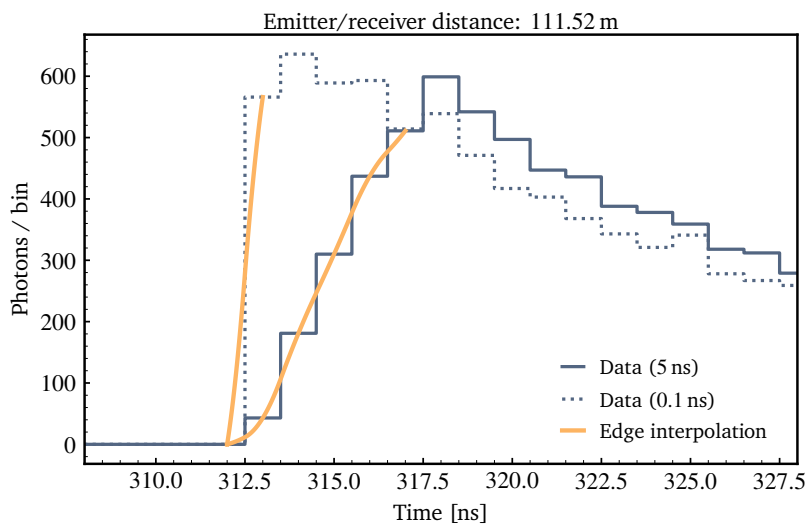
**Figure 6.20:** Direct hole ice parameter fit using pseudo-data in the GEANT4 simulation framework of the POCAM. The figure shows the logarithmic log-likelihood (LLH) profile in the dimensions of hole ice size and scattering length together with the Monte-Carlo truth, the LLH minimum and the 95% contour. In addition an interpolated, zoomed view of the fit region is shown within the small figure on the bottom right.

## 6.6 Optical geometry calibration in water

When doing optical geometry calibration, the main task of the light source is to provide a light pulse that is sharp in time and intense enough to illuminate a significant fraction of the detector. The detected rising edge of the pulse at different sensors in combination with synchronization of the detector then gives means to trilaterate the detector geometry in-situ. As water-based detectors are constantly subjected to currents, this continuous geometry calibration is critical. Thus, also the potential optical geometry calibration in water with the POCAM in water-based telescopes like KM<sub>3</sub>NeT or P-ONE was studied. For this, we make use of the large-scale simulation framework developed for the IceCube sensitivity study and replace the optical properties of ice with those of water. Then, we simulate and check what calibration precision would be possible and how it is affected by the timing performance of the optical light source.

As for the simulation, we produce a set of nominal optical water properties with absorption and scattering lengths of 33 m and 150 m, respectively as well as sets with marginally scaled values. These sets are then produced for light pulse widths of 0.1 ns and 5 ns in order to capture how this affects the timing information. Then, we interpolate the rising edges of the pulses arriving at each DOM and use quantiles of 0 %, 10 %, 50 % and 90 % to observe the loss of timing information with increasing charge threshold. Here, 0 % refers to the first bin with photon hits. Example interpolations are shown in fig. 6.21 for the same emitter/receiver pair and highlights the importance of time-narrow pulses for geometry calibrations.

**Figure 6.21:** Rising edges of calibration light pulses in water at 0.1 ns and 5 ns. The figure shows the simulated data for the two pulse widths including interpolated rising edges used for later analysis.



Now, before calculating distances it is important to define the speed with which light propagates through the medium. As we are observing light pulses of finite width, the group velocity  $v_g = c/n_g$  determines the propagation velocity of the pulse envelope. A priori the precise group refractive index  $n_g$  is unknown and has to be inferred from data. To do so, we assume that close receivers on the same string see direct light in the first bin with non-zero counts. Then, assuming the intra-string module distance is known to good precision, we use

their timing information to infer  $v_g$  by averaging the arrival times of all  $N$  receivers within some critical distance to the emitter on that string to find the group velocity via

$$v_g = \frac{d_{\text{crit}}}{t_0} \quad \text{with} \quad t_0 = \frac{1}{N} \sum_i^N t_{i,0} \quad (6.19)$$

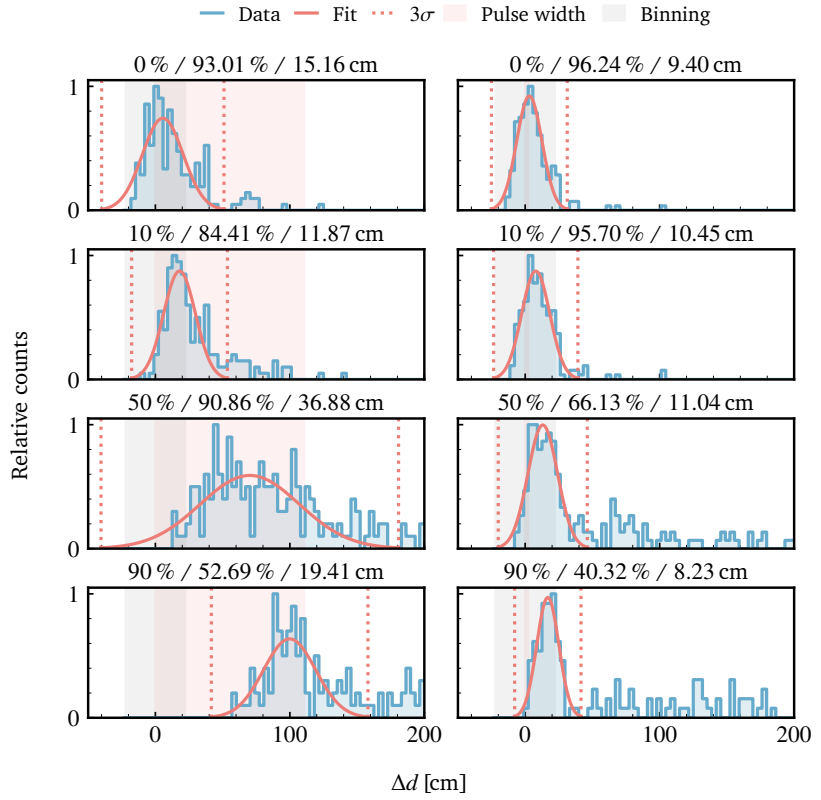
with the arrival time used as the first non-zero bin  $t_{i,0}$  of DOM  $i$ . While the critical distance will typically depend on the medium properties, in our nominal case using  $d_{\text{crit}} = 30$  m results in the reasonable precision of

$$\left| 1 - \frac{v_g}{v_{g,\text{sim}}} \right| = \begin{cases} 6.7 \times 10^{-4}, & 5 \text{ ns} \\ 6.2 \times 10^{-5}, & 0.1 \text{ ns} \end{cases} \quad (6.20)$$

when compared to the group velocity of the simulation and thus can be inferred from data without significant loss of precision. Then, upon using the pulses at each DOM and the group velocity one can infer the distance of emitter to receiver as  $d = v_g t$ .

Histogramming the differences of these calibrated to the true distances results in fig. 6.22. Here, fitting Normal distributions to the bulk of the sensor arrival times results in an approximate precision achievable with these two pulse widths and depends also on the used quantile. While the quality of calibration tends to deteriorate for large quantiles, small quantiles achieve geometry calibration precision below 10 cm even with pulses of 5 ns width. As expected, it appears that the 1 ns binning actually contributes significantly to the geometry calibration uncertainty using the 0.1 ns pulse. This, however, is reasonable as it reflects a conservative estimate on typical large-scale structure synchronization precision. Summarizing, the POCAM can be used to calibrate water-based detector geometries given that the emission time profile is sharp and well understood in addition to a sufficiently precise detector synchronization.

**Figure 6.22:** Water geometry calibration study using POCAMs in the framework developed for the Upgrade studies. The plots show the histogrammed differences between calibrated distance and true distance for pulse widths of 5 ns (left column) and 0.1 ns (right column). All figures additionally show Normal distribution fits and carry a title with information about the used charge quantile, the number of DOMs within a range of  $\pm 3\sigma$  as well as the fit standard deviation.



# 7

## POCAM development for the IceCube Upgrade

The general idea of the POCAM is to provide isotropic, self-monitored, nanosecond light pulses as a reference for large-scale neutrino telescopes. And, as already outlined in section 6.1, the first prototypes – POCAMv1 and POCAMv2 – were installed in the GVD (Lake Baikal, Siberia)<sup>202</sup> and STRAW (Pacific Ocean, ONC)<sup>13,132</sup> detectors, respectively. Here, they were able to provide a functional proof of principle and even contribute to measurements and calibration of the respective detectors. Installation photographs of both experiment applications are given in figs. 7.1 and 7.2.

This chapter describes the final device iteration development for the IceCube Upgrade. That means, the design of the device has been overhauled and made ready for an application in the IceCube Upgrade experiment at the South Pole. I lead the first description of this development as published in the Journal of Instrumentation in 2020 as “A self-monitoring precision calibration light source for large-volume neutrino telescopes”<sup>198</sup>. This chapter will follow the general structure of this publication.

### 7.1 Instrument overview

The initial design idea of the POCAM was to provide a spherical module similar to a DOM<sup>200</sup>. However, after several student-based studies regarding potential POCAM developments, it became evident that such a module would not be able to merge the idea of isotropic emission and sufficient space for electronics and connectors. Thus, the design in fig. 7.3 emerged which combines two hemispheres for emission with a cylindrical component to house electronics and mount connectors. On detector scales, the small hemisphere separation is insignificant and the instrument will effectively act as a point source.

The POCAM in general consists of a multitude of components which can be roughly divided into the following subgroups

1. **Pressure housing** – Enable vacuum seal during installation in great depths of water or ice under potentially extreme conditions. Furthermore hosts penetrator for electrical connection to the detector infrastructure and vacuum port for pressure compensation and nitrogen flushing.
2. **Optical components** – Two diffusing integrating sphere to make light pulses isotropic and coated components to precisely control the emission pattern of each hemisphere.
3. **Analog electronics** – Circuitry for the generation of nanosecond light pulses and operating sensors for self-monitoring.



Figure 7.1: POCAMv1 during installation at the GVD telescope in Siberia with the author in the back. Credit J. Thompson.



Figure 7.2: POCAMv2 installed at one of the STRAW strings in the Pacific at a depth of 2.6 km. Credit Ocean Networks Canada.

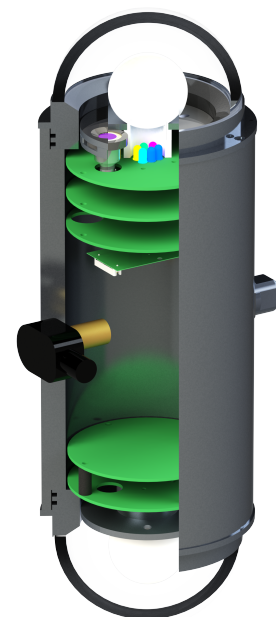
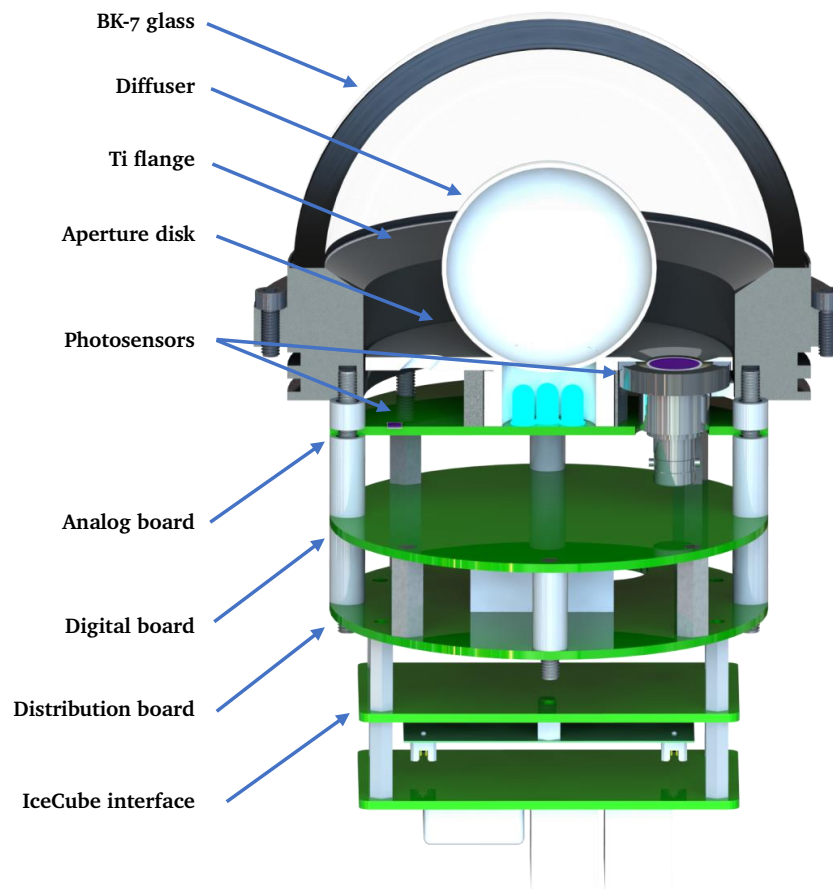


Figure 7.3: POCAM instrument design in full view.

4. **Digital / interface electronics** – Controls the instrument components, enables integration into the detector DAQ as well as synchronization protocols and distributes external signals to both hemispheres. In addition to internal digital boards, distribution and DAQ integration is handled by a central distribution board as well as an IceCube interface board.

All of the components are mounted to the two flanges with an example assembly given in fig. 7.4; reprocessed based on<sup>198</sup>. Here it is evident that the space requirement for electronics justifies the cylindrical adaptation to the initially spherical POCAM idea.

**Figure 7.4:** POCAM flange layout and assembly including all sub-components. For details on the latter or the figure reference refer to the text.



## 7.2 Requirements for in-ice installation

In order to deploy instruments into the IceCube detector at the South Pole, the devices have to experimentally justify their application and at the same time need to be able to withstand the present environmental conditions. While the former has been thoroughly outlined for the POCAM in chapter 6, the latter now becomes relevant for the hardware development.

### 7.2.1 Environmental requirements

Most prominently, an installation at the South Pole to depths of up to 2.6 km requires the housing to withstand temperatures as low as

–50 °C and pressures up to 260 bar without loss of housing integrity. During refreezing of the drill holes, pressures can further spike<sup>141</sup> and generally a conservative pressure rating of around 680 bar is required. The temperature requirement further translates to electrical and optical components all of which can not lose functionality at low temperature. Additionally, optical components need to have most of the internal humidity removed as any residual water might freeze out on critical surfaces and disturb the otherwise known optical instrument behaviour. Lastly, the device should be able to handle vibrations and needs to be small enough so that it fits in the drill hole and manageable enough so it can be mounted to the string by ground personnel by hand.

### 7.2.2 *Electro-digital requirements*

Power at the South Pole is sparse and so the supply of thousands of instruments needs to be managed carefully. All devices for the Upgrade are given a baseline voltage of 96 V providing each device with the relevant power for all of the device functionality.

Additionally, all devices need to speak to the IceCube DAQ system using its inherent protocol. Here, a special form of serial communication is modulated to the DC power supply wire-pair connected to each device<sup>141</sup>. As the whole detector works on that protocol, it is required for additional devices to adhere to it as well. Furthermore, synchronization is also managed via this wire-pair and, thus, the closer each device resembles a DOM within the experimental DAQ, the more straightforward its integration into the data stream and the detector synchronization.

Lastly, the devices should be designed as redundant as possible in order to avoid single points of failure after installation. That means predominantly that the device should function as expected at all times. And while that can never be guaranteed completely, the design of the device can be adapted in a way that common points of problems can be equipped with backup solutions.

### 7.2.3 *Optical requirements*

The POCAM is supposed to emit isotropic light pulses of nanosecond duration in order to be able to calibrate photomultipliers or similar detectors. For this, in addition to the isotropy of the emitted light, the pulse widths should be in the range of 1 ns – 50 ns and intensities of  $1 \times 10^6$  photons –  $1 \times 10^{10}$  photons per pulse in order to be able to calibrate several distance scales and various different systematic parameters. The spectral range of emission should further be focussed around 405 nm as it is the current IceCube default wavelength but other emitters in the range of 350 nm – 530 nm should be included in every POCAM in order to verify the existing wavelength-dependent power-law behavior. Lastly, the self-monitoring sensors should be able to monitor pulses over the whole dynamic range of intensities by complementary sensor technologies and adjusted analog readouts.

### 7.3 Measurement setups

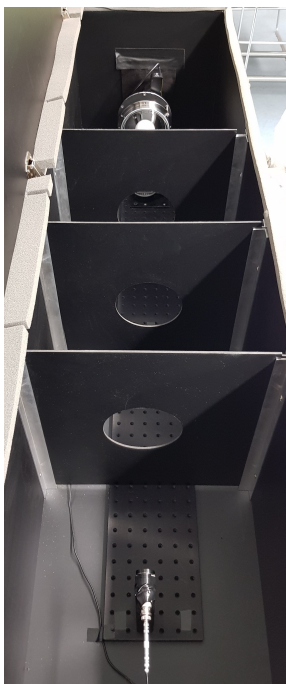


**Figure 7.5:** POCAM angular calibration setup installed within the TUM laboratory.

<sup>230</sup> Marshall “NIST Calibration Services Users Guide 1998 Edition” (1998).

All subsequent studies of different POCAM components typically require the measurement of one or several observables. As such, we first introduce the experimental measurement setups which were developed for this reason. All subsequent results which use experimental data are obtained from one or multiple of these calibration setups.

#### 7.3.1 Emission profile

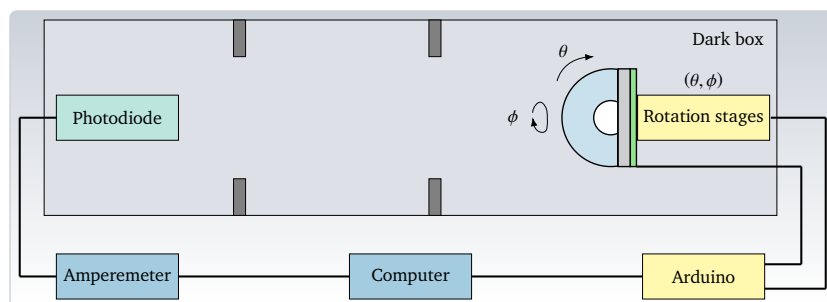
The first setup that was developed targets the emission profile of one POCAM hemisphere. As the emission is supposed to be isotropic, the knowledge of how the current design and material parameters translate into the actual emission profile is crucial. When speaking of emission profile, we mean the relative light intensity variation  $I(\theta, \phi)$  with polar angle  $\theta$  and azimuthal angle  $\phi$ , that is

$$I(\theta, \phi) = I_0 \cdot f_1(\theta, \phi) \quad (7.1)$$

and by measuring the emission profile for a variety of angle combinations, we can characterize the function  $f_1(\theta, \phi)$  for every flange/diffuser assembly and hence calibrate the emission intensity as a function of emission direction. Furthermore, putting this together with the developed simulation framework (refer to section 6.5), we can use the in-air measurements of the emission profile to match it with simulation and then optimize material parameters and, most importantly, translate the results to an outer medium of water or ice. The absolute intensity scale  $I_0$  is then calibrated at the very end of the calibration chain by means of a precise NIST-calibrated <sup>230</sup> photodiode.

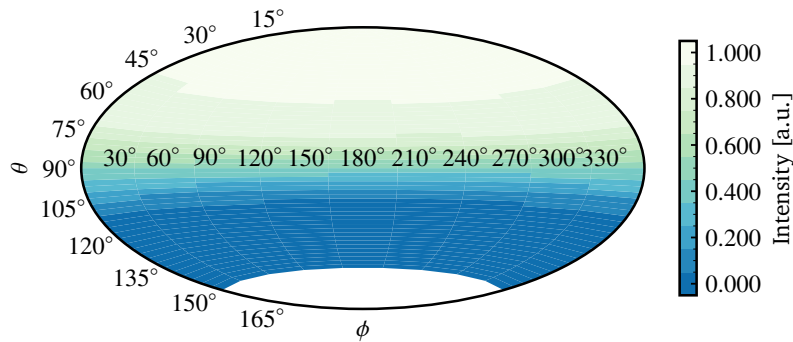
The setup itself is relatively simple as it makes use of only three active components: two rotation stages, a photodiode as well as an illumination board. The stages are mounted together in a way that allows rotation of a POCAM hemisphere around two axes and hence any pair of  $(\theta, \phi)$ . The photodiode is mounted in a distance of about 1 m from the hemisphere and measures light emitted from the POCAM illumination board with a solid angle of around  $0.3^\circ$  in both dimensions. This board hosts the same emitter matrix as the POCAM analog boards, however, in switchable continuous mode. Furthermore, intermediate light baffles reduce stray light so that only intensity fluctuations from POCAM-based components are recorded. The whole experimental setup is pictured schematically in fig. 7.6.

**Figure 7.6:** POCAM rotation calibration setup for characterizing hemispherical emission profiles. The setup consists of a two-axis rotation stage to which the flange is mounted, a POCAM illumination board and the measuring photodiode. Additionally, peripheral electronics for control and data acquisition are located outside the dark box.

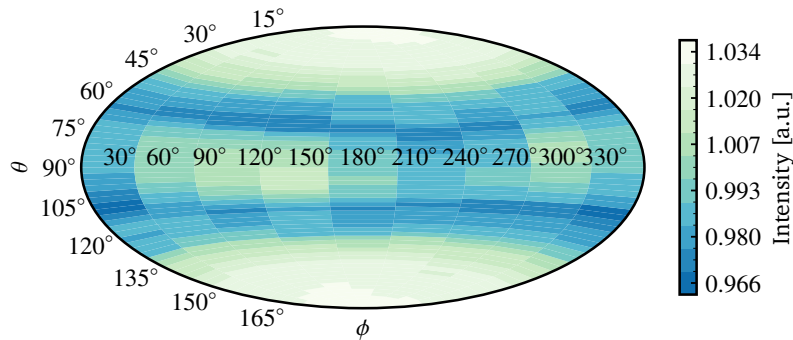


As mentioned, this setup further allows to swap the conventional photodiode for a NIST-calibrated one in order to perform absolute

intensity calibration at the very end of the calibration procedure. Using this setup, a measurement of a flange emission profile is possible with some desired angular granularity. One example measurement is shown in fig. 7.7 and shows the two-dimensional in-air intensity scan in azimuthal and polar angle with angular steps of  $40^\circ$  and  $2.5^\circ$ , respectively; reprocessed based on <sup>198</sup>.



(a) Singular hemisphere emission profile calibration.



(b) Virtual total POCAM emission profile.

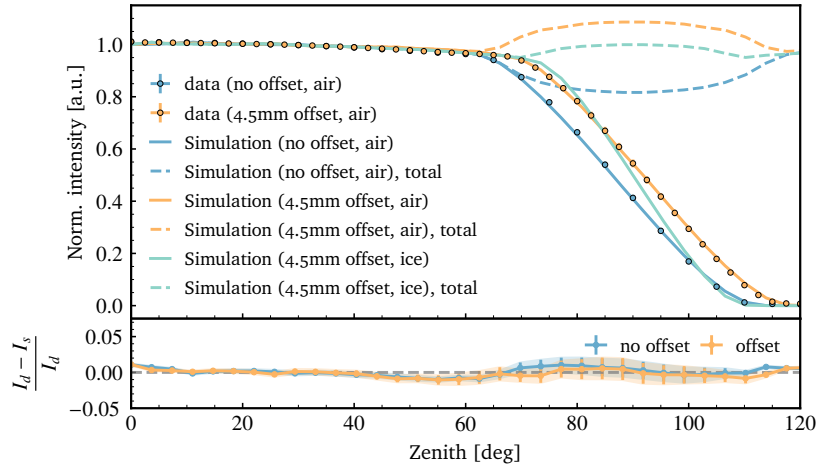
**Figure 7.7:** Singular (a) and virtual total (b) POCAM emission profile measurements from the calibration setup with relative intensity indicated by color. The virtual POCAM is artificially created by summing the single hemisphere measurement with a mirrored and randomly rotated version of itself. Figure reference in the text.

Furthermore, due to the availability of the simulation framework, the measured emission profile data can be matched with simulations as shown by example in fig. 7.8; reprocessed based on <sup>198</sup>. On the one hand this allows translation into different optical media and the study of subsequent emission profile changes. On the other hand it also enables to study component parameters, geometry and design by investigating their effect on the emission profile. The latter further enables optimization of the geometry and optical properties of the used components to achieve the highest possible grade of isotropy in the application medium. Details on these studies will be given on a per-component basis throughout section 7.4.

### 7.3.2 Light pulse properties

The second setup for calibration of the POCAM is the light pulse or flasher characterization setup. The general goal of this experimental setup is to characterize light pulse properties, like relative intensity, time profile and spectrum, as a function of internal configuration parameters and temperature. Here, the configuration parameters include internal settings as, for example, applied bias voltages to the analog circuits or, if applicable, pulse width parameters. This char-

**Figure 7.8:** Mean polar emission profile of a POCAM hemisphere and calibration data averaged over all azimuthal measurements. The figure shows experimental data (dots) as well as GEANT4 simulation results for the same setup (lines) in addition to a data/sim ratio (bottom). The data is shown for both a nominal diffuser position and one offset from the flange equator. Additionally, the simulation for an outer medium of ice is shown which highlights the expected change in the critical region around the hemisphere equator. Figure reference in the text.



acterization now defines the secondary relative calibration function as

$$I(t, \lambda, T, \vec{p}) = I_0 \cdot f_2(t, \lambda, T, \vec{p}) \quad (7.2)$$

which defines the relative light pulse output as a function of time  $t$ , emitter  $\lambda$ , temperature  $T$  and configuration parameters  $\vec{p}$ . Also here, the absolute scale  $I_0$  is the same as given in eq. (7.1) and determined via absolute calibration at the end of the characterization procedure.

In order to characterize all these properties, the setup consists of a dark box which hosts all sensor instrumentation and a remote-controllable freezer in which the POCAM hemisphere electronics can be installed. The sensors include the previously-explained Hamamatsu S2281-01 photodiodes (PDs) connected to a picoammeter and a small Hamamatsu R1925A PMT connected to a digital oscilloscope for intensity calibration. For time profile characterization we make use of the avalanche photodiode (APD) ID100 from ID Quantique with a time resolution of around 40 ps connected to a high-precision TDC. The light intensity from the fiber for the APD is further controlled by a neutral density filter wheel – with an attenuation of up to  $1 \times 10^5$  – to ensure predominantly single-photon hits. This is necessary so that the measured time profile is sampled correctly and not skewed by multi-photon hits. Finally, to measure the spectrum we use the serial-controllable Hamamatsu spectrometer C12880MA. Each of these sensors is supported with peripheral electronics that either enable or help control the measurement as shown in figs. 7.9 and 7.10. The fully-assembled POCAM stack, including optical components, is installed in a stainless steel frame within the freezer in order to allow coupling to optical fibers and a quartz rod which act as light guides towards the sensors.

Here, since temperatures far below  $0^\circ\text{C}$  need to be calibrated and temperature-induced optical coupling changes are expected, a reference light source is used to couple light to a reference sensor as well as the diffusing sphere of the POCAM stack. Since the fiber coupling is realized in the same way both times, monitoring the relative changes in the reference output allows temperature-induced coupling change correction. This is shown in figs. 7.11 and 7.12. The measure-

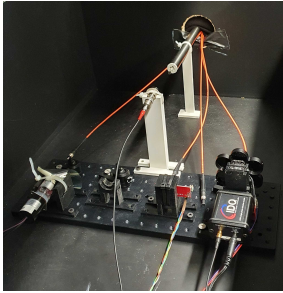


**Figure 7.9:** POCAM light pulse characterization setup.

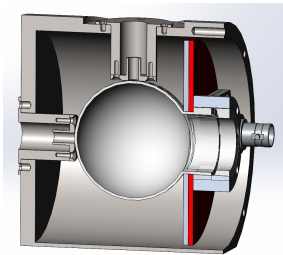


**Figure 7.11:** Fiber termination concept for the freezer of the pulser characterization setup.

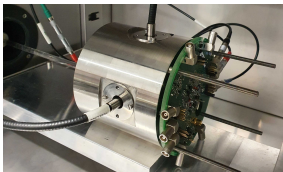


**Figure 7.12:** Fiber termination in the freezer of the pulser characterization setup.

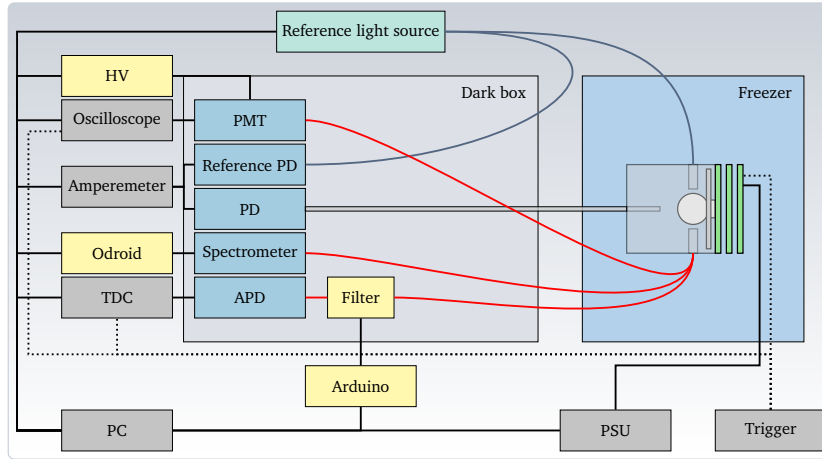


**Figure 7.10:** POCAM light pulse calibration setup for characterizing light pulse properties. The setup consists of a dark box with sensors for pulse characterization as well as a controllable freezer in which the POCAM electronics are installed. The sensors located in the dark box calibrate light pulses guided from the POCAM emitters via optical fibers (red). A reference light source and sensor monitor temperature changes of the optical system via the same fiber coupling (blue). For details on the components refer to the text.

ment principles for all sensors at each temperature and configuration parameter point are summarized as follows:

**Intensity** The intensity measurement is the most comprehensive. Depending on the light yield of the pulses, the PMT and the photodiode are used complementarily. While the PMT is more sensitive to low light levels, the PD is used for the larger pulser intensities. In order to have complementary measurements of both sensors, the quartz rod is used to increase the absolute light yield of the pulses on the PD. This allows it to measure also relatively faint pulses. After measuring the light intensity with the PD, the pulsing is switched off and the reference light source is switched on and, after warming up, the photocurrent of the reference PD is measured. The latter is then compared to its initial value at room temperature, where nominal coupling is assumed, and so temperature-dependent coupling changes on the fibers and the quartz rod can be corrected for. An example output of such a calibration is given in fig. 7.13; reprocessed based on <sup>198</sup>.

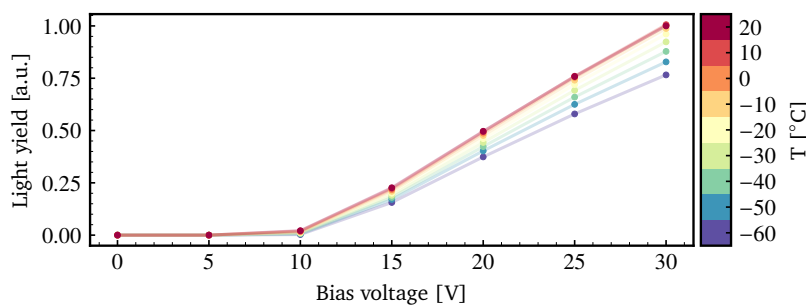


**Figure 7.13:** Example light yield calibration as a function of temperature using the photodiode. Figure reference in the text.

For the PMT the intensity is given by the integrated mean total charge of the measured pulses. For the PDs we measure dark current with all sources of light switched off and total current with light pulser or reference switched on. The mean photocurrent induced in the PD by either the light pulser or the reference source is then

$$I_{\text{photo}}(T) = I_{\text{total}}(T) - I_{\text{dark}}(T) \quad (7.3)$$

and we can correct both PD and PMT intensity measures via the

correction

$$I_{\text{photo}}^{\text{corr}}(T) = I_{\text{photo}}(T) \cdot \frac{I_{\text{photo}}^{\text{ref}}(T = T_{\text{nominal}})}{I_{\text{photo}}^{\text{ref}}(T)} \quad (7.4)$$

that effectively removes temperature-dependent coupling changes within the optical system at temperature  $T$  using the measurement at room temperature  $T_{\text{nominal}}$  where nominal coupling is assumed.

**Time profile** The time profile of the light pulse is measured using time-correlated single-photon counting. Here, the light pulse coming from the fan-out fiber towards the APD is attenuated using the neutral density filter wheel. This controls the occupancy  $\eta$  – that is the fraction of detected pulses given the number of triggered pulses – and makes sure that predominantly single photons are recorded. Only then the true time profile shape is sampled and remains unskewed by multi-photon hits. With an occupancy of less than 10 % we achieve basically pure single-photon hits as can be verified using Poisson statistics by calculating the single-photon ( $k \leq 1$ ) probability

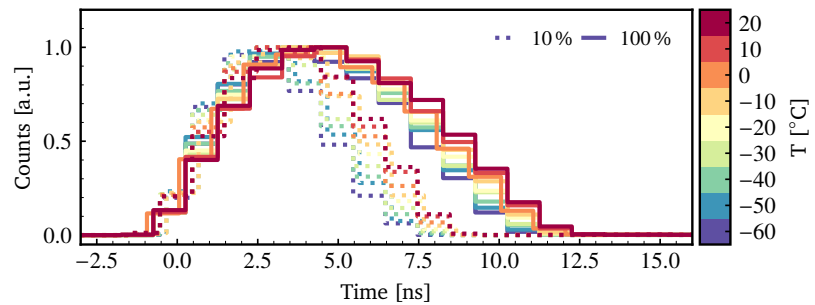
$$P(k \leq 1 | \eta) = P(0 | \eta) + P(1 | \eta) \quad (7.5)$$

$$= \exp(-\eta) \cdot (1 + \eta) \quad (7.6)$$

$$\rightarrow P(k \leq 1 | \eta)|_{\eta=0.1} = 0.995 \quad (7.7)$$

Finally, the TDC records the relative arrival times of the photons respect to the trigger pulse and the resulting histogram depicts the probability of detecting a photon a certain time after the trigger, that is, the light pulse time profile. An example output of such a calibration is given in fig. 7.14.

**Figure 7.14:** Example time profile calibration as a function of temperature for 10% and 100% relative emission intensity.



**Spectrum** The used mini-spectrometer has a fiber adapter to which one of the fan-out fibers is attached. It is further plugged to a small custom circuit board and read out via serial protocol with the help of a small single-chip computer. When measuring the spectrum, the spectrometer integrates incoming pulses for some amount of time and outputs the measured counts of its different spectral bins. The integration time is hereby adjusted iteratively until no saturation in any of the bins is observed. An example output of such a calibration is given in fig. 7.15 and shows the measured wavelength distribution of an example flasher as a function of temperature.

Once this integration time is found, a dark spectrum is recorded with all light sources switched off and a total spectrum with the

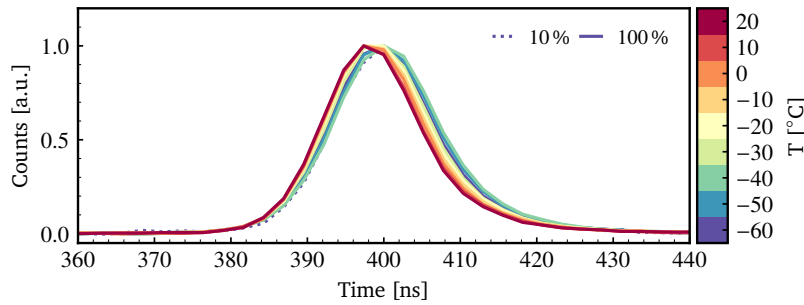


**Figure 7.15:** Example spectrum calibration as a function of temperature.

pulsar switched on. Similarly to eq. (7.3), the subtraction of these two spectra – that is their bin counts – eventually produces the pure photo spectrum induced by the pulser and removes ambient influences on the spectrometer. This is especially important since the spectrometer measurement is affected strongly by temperature variations of its internal sensor and could skew the measured wavelength distribution.

### 7.3.3 Orientation

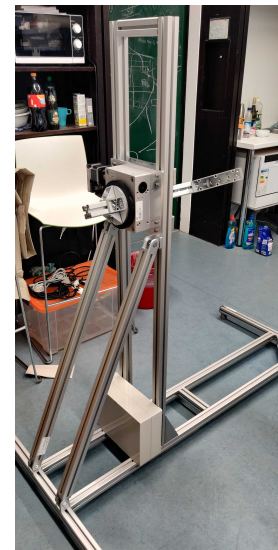
In order to monitor the POCAM orientation via integrated accelerometers and magnetic field sensors (refer to section 7.6), we developed an orientation station to rotate the whole instrument. The station picture in fig. 7.16 shows a stainless steel frame with mounting capabilities for the POCAM and a heavy-duty rotation stage. The latter is necessary as the POCAM can be rotated not only around its center of gravity but also around the center of one of its flanges which requires larger rotational force. Furthermore, the whole setup can be turned to a horizontal position so that the POCAM can be placed and rotated in an existing water pool.

The conventional center of gravity rotation can be used to calibrate the integrated sensors for orientation and tilt. The off-center rotation around the flange center and the possibility to to turn the setup and rotate the whole instrument horizontally allow testing in a water pool. This is especially important to measure the emission profile in water similarly to the emission profile characterization and verify that the simulation is able to correctly predict the effects by an optical medium change.

For the tilt calibration the setup will rotate the POCAM and the integrated accelerometer is read out at each position. The correlation of the measured gravitational acceleration and the angle with respect to the nominal vertical position allows relating the accelerometer data to the instrument tilt. Similarly, rotating the instrument while reading the magnetic field sensor and the known position within the Earth magnetic field allow to measure the azimuthal orientation of the POCAM to some precision. At the time of writing this thesis the setup was not yet fully functional and so no experimental data was available. However, the setup itself will be finalized in the coming months to be ready when production of the instruments starts.



(a) Concept design.



(b) Current development status.

**Figure 7.16:** POCAM orientation calibration setup concept (a) and current development status (b) for characterizing instrument orientation. Image courtesy of L. Geilen.

## 7.4 Mechanical and optical design

The mechanical and optical design of the POCAM critically determines its emission pattern and its experimental applicability within different environments and as such needs to be studied in detail.

### 7.4.1 Instrument housing



**Figure 7.17:** POCAM housing with one attached flange and visible vacuum port (right) and the penetrator (left) including its cable tail.

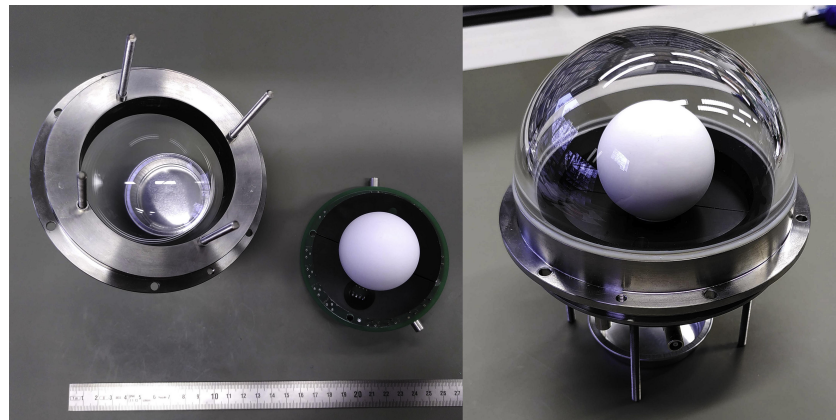
<sup>231</sup> “Schott N-BK7” (2014).

<sup>232</sup> 3M “Scotch-Weld DP 460” (2003).

The instrument housing is designed by *Nautilus Marine Service GmbH* in Germany and is made mainly from titanium. It consists of a cylindrical component hosting the penetrator and the vacuum port as well as a flange with a glass hemisphere on each end of the cylinder with a total length of around 40 cm. Here, the glass hemisphere is made from optically enhanced borosilicate glass BK-7<sup>231</sup> in order to provide undisturbed light emission. The glass hemisphere is glued to the titanium flange using temperature-rated epoxy<sup>232</sup> and the flange itself is screwed to the cylindrical housing part, sealing it with O-rings. Nautilus pressure-rated this housing to withstand up to 1500 bar, more details on the stress tests are discussed in section 7.4.4. A photograph of the housing including flanges is shown in figs. 7.17 and 7.18.

The flange design itself is intricate as it directly influences the emission profile of the device and is responsible for sealing the housing. Since the integrating sphere is of finite size, any protruding edges from epoxy or metal will directly impact the polar emission profile. As such, together with Nautilus, the gluing procedure was iteratively optimized until the created disturbance was minimal while maintaining structural integrity of the assembly. The final design and its epoxy edge is shown in fig. 7.18; reprocessed based on<sup>198</sup>.

**Figure 7.18:** POCAM flange design and optical component fitting. The left picture shows a prototype optical component stack on an analog board, the right side shows the assembled prototype flange. Figure reference in the text.



Furthermore, the inside surface of the flange is coated to reduce reflections which would otherwise skew the emission profile. The used coating is Aektar MagicBlack<sup>233</sup> which shows a reflectance of less than 1% over a wavelength range of 0.01  $\mu\text{m}$  – 1  $\mu\text{m}$  and as such is applicable within a wide spectral range.

Lastly, the housing hosts two penetrators: a vacuum port and an electrical connector provided by the IceCube Upgrade. The former is used to evacuate the housing and simplify pressure equalization when closing and opening the housing. Furthermore it allows flushing the housing with nitrogen in order to remove humidity. The electrical penetrator is provided by the Upgrade experiment and provides the

<sup>233</sup> Aektar - Advanced Coatings “MagicBlack” (2020).

wire pairs connected to the electronics which enable communication and power supply to the device.

#### 7.4.2 Diffusing sphere

One primary aspect of the POCAM is its intrinsically isotropic emission. Initially, the idea in early POCAM studies<sup>200</sup> was to realize this using a sphere made of *Lambertian* or *diffusely-reflecting* material<sup>234</sup>. Optically speaking, that means light is scattered homogeneously in all directions so that observing the intensity of some illuminated surface area  $A$  at an angle  $\theta$  scales as

$$I(\theta) \sim A \cos(\theta) \quad (7.8)$$

Then, according to integrating sphere theory<sup>13,235</sup>, homogeneous illumination of the internal sphere surface is achieved if ideal Lambertian reflectance of the material and ideal sphere geometry are realized.

While several ideas for potential sphere geometries were investigated in earlier studies, the current design realizes this isotropy using a semi-transparent two-component integrating sphere made of *polytetrafluorethylen* (PTFE) or *teflon* as seen in fig. 7.19; reprocessed based on<sup>13</sup>. The design of the sphere foresees the main sphere body with a diameter of around 50 cm and a plug which complements the sphere. With teflon being close to a Lambertian emitter, photons are reflected isotropically of the surface at each scatter and so, in theory, the inner surface of the sphere should roughly be homogeneously illuminated. Then, due to being semi-transparent, this homogeneous illumination should be transferred to the outside and result in isotropic light emission from the sphere surface. The plug plays the crucial role of pre-diffusing the initial emitter pulse before light enters the sphere body and reduces the impact of the initial light emission direction.

Previous device iterations v1 and v2 were using diffusing spheres from conventional teflon, however, this new device design makes use of *optical teflon*<sup>236</sup>. As is visualized in fig. 7.20, optical teflon significantly increases the isotropical characteristics of the light integration and emission. Furthermore, this material is specifically produced for optical applications and as such shows less impurities which could cause further deviations in the emission pattern.

The last detail in the integrating sphere design is to account for the equator edge. Simulations show and measurements verify that placing the diffusing sphere center slightly offset with respect to the flange center can counteract some of the intensity drop caused by the flange edge around the equator (refer to fig. 7.8). As such, the integrating sphere is moved slightly upwards from the flange equator which results in some level of counteraction of the intensity drop around the equator edge. The final offset is based on simulation in order to achieve the most homogeneous emission profile in ice.

#### 7.4.3 Aperture disk

An additional component within the POCAM hemisphere assembly is the aperture disk or *shadow mount*. This two-component disk from stainless steel provides a flat and homogeneous surface towards the

<sup>234</sup> Koppal “Lambertian Reflectance” (2014).

<sup>235</sup> Labsphere “Integrating Sphere Theory and Applications” (2017).

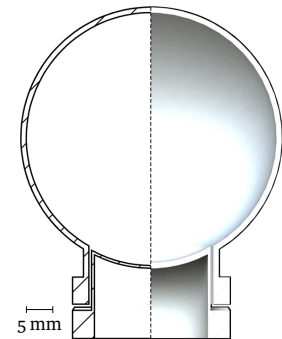


**Figure 7.19:** POCAM diffusing sphere design with main sphere body and plug. The left half of the figure shows the reference drawing, the right half a rendered view of the sphere. Figure reference in the text.

<sup>236</sup> Berghof Fluoroplastic Technology GmbH “Optical PTFE - The reference for light” (2019).

**Figure 7.20:** Conventional and optical teflon emission profile comparison for the POCAM diffusing sphere. The data points show emission profile measurements of a prototype POCAM flange using diffusing spheres from different materials but the same geometry; the lines show the interpolated (solid) and virtual total (dashed) POCAM emission. The optical PTFE version shows significantly more stable emission towards the equator region.

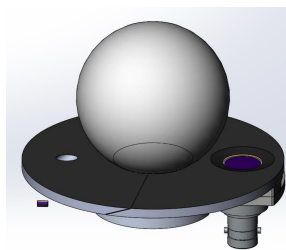
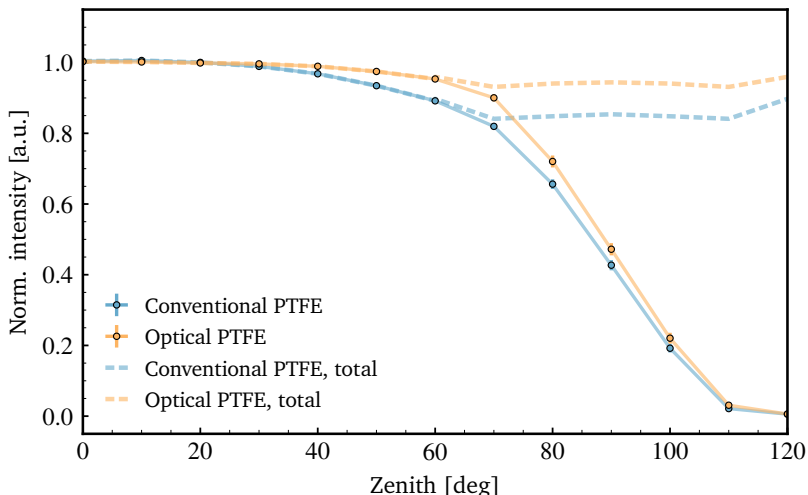


**Figure 7.21:** POCAM aperture disk, diffusing sphere and sensors in CAD view.

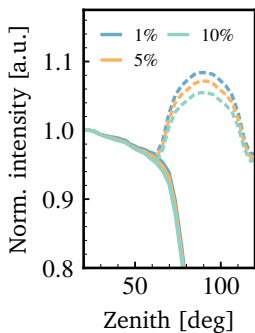


**Figure 7.22:** Simulated aperture disk reflectivity effect on the emission profile for three different reflectivity values.

internal components, fixes the diffusing sphere to its position and can be used to mount the self-monitoring sensors while additionally providing their respective solid angles. The disk is realized as the two-part design shown in fig. 7.21 and combines around the neck of the diffusing sphere.

For coating, as visible in fig. 7.18, the aperture disks are treated with the same anti-reflective material as the flange, namely *Acktar MagicBlack* coating. Since reflections off of the surface of this disk would directly skew the emission profile towards forward direction, coating of its surface is critical. As simulations in fig. 7.22 show, already a reflectivity of 5 % would affect the emission profile. For this reason, the MagicBlack coating was chosen since a 1 % reflectivity was sufficient to achieve the least skewage of the emission profile and homogeneous surface reflectivity properties.

As for mechanical mounting, since the diffusing sphere is made from teflon and temperatures of around  $-50\text{ }^{\circ}\text{C}$  to  $-40\text{ }^{\circ}\text{C}$  are expected at the South Pole, shrinkage of the sphere would cause it to loosen within the aperture disk mounting. Instead, the diffusing sphere is artificially designed so that proper fitting into the aperture mounting is achieved at  $-60\text{ }^{\circ}\text{C}$ . For mounting, the spheres are cooled down, mounted to the aperture disks and left to warm up which ensures proper fitting also at low temperature. Tests of this procedure have confirmed that the sphere can be fit at temperatures of  $-50\text{ }^{\circ}\text{C}$  and remains stable also once warmed up to room temperature.

#### 7.4.4 Stress testing

In order to verify the POCAM applicability in South Pole conditions, the requirements listed in section 7.2 need to be verified by means of stress testing. The latter includes temperature and pressure as well as vibrational and shock testing.

**Temperature** While the application in Siberia within the GVD telescope already subjected a POCAM prototype housing to temperatures of around  $-30\text{ }^{\circ}\text{C}$ , temperature testing of all POCAM components is systematically carried out two-fold: mechanically and electrically. For

the electrical tests, section 7.3 already summarizes the setup and measurement technique that makes sure all electrical components work as expected in all relevant temperature conditions. For the mechanical testing, the housing is first temperature-shocked ten times by being put to a freezer at  $-80^{\circ}\text{C}$  for a full day, taken out to room temperature and immediately being subjected to mechanical stress applied manually. Here, especially the glass domes with the epoxy are tested for mechanical stability. As this stress test cycle was completed without any problems, the second test is subjecting a sealed POCAM with an internal pressure sensor to  $-40^{\circ}\text{C}$  for five weeks. This test should spot potential vacuum leakage problems caused by temperatures or the housing design in general. However, also here, the pressure remained stable and the tests were declared successful with the POCAM temperature-rated for Antarctica. Pictures of the POCAM housing during the tests are given in figs. 7.23 and 7.24 and show the housing in both environments.



Figure 7.23: POCAM housing shortly after being taken out of the freezer at  $-80^{\circ}\text{C}$ . Photo courtesy by C. Spannfellner.



Figure 7.24: POCAM housing during temperature test.

**Pressure** In addition to the successful operation of POCAMs in Lake Baikal (1000 m depth) and the STRAW experiment (2600 m depth), the housing needs to be verified to the expected pressures occurring in the refreezing process of the IceCube drill holes. Thus, the housing was subjected to a dedicated pressure test at the Nautilus facility where it was cycled between 1 bar to 700 bar for a period of 14 hours. Also here, the housing did not show any signs of structural damage nor sealing problems. A photograph of the housing after the test cycle is given in fig. 7.25.



Figure 7.25: POCAM housing after Nautilus pressure test. Photo courtesy of Nautilus Marine Service GmbH.

**Vibration and shocks** Finally, as the instruments will travel a significant distance to the South Pole and then will be manually installed to the strings, vibrations and shocks can not endanger system integrity. As such, the whole instrument is subjected to a vibration and shock test according to the ISO norm 13628-6 at a local test facility. Also here, the tests showed no significant resonance peaks and no structural damage to the instrument and as such were declared successful.

Concluding and passing all of these tests, the POCAM instrument and its housing fulfill all necessary environmental requirements for transit to and application in the conditions present in Antarctica.

## 7.5 Light pulsing and self-monitoring

With the mechanical and optical components of the POCAM described, we now discuss the analog board of the POCAM. This board hosts primarily the light emitters and respective pulse drivers as well as the self-monitoring sensors. In addition, we will discuss the temperature dependence of all constituents.

### 7.5.1 Pulse drivers

The POCAM makes use of two distinct pulse drivers: the Kapustinsky LED pulse driver<sup>132,237</sup> and the newly-added LD-type driver based on industrial applications<sup>238</sup>. Schematics for both driver circuits are given in figs. 7.26 and 7.28.

**Kapustinsky driver** The Kapustinsky driver schematic is shown in fig. 7.26; reprocessed based on<sup>198</sup>. Its working principle relies on two fast transistors, a capacitor, an inductance, and negative bias voltage of up to  $-32$  V. The latter charges the capacitor  $C$  and upon opening the transistor path with the rising edge of a trigger pulse the capacitor discharges through the LED making it emit light. However, the pulse is artificially cut short by the inductance  $L$  as part of the discharge current passing through counteracts the initial flow. The output pulse shape of this circuit can be tuned by adjusting the parameters ( $L$ ,  $C$ ) and the maximum frequency via the protection resistor  $R$  since it charges  $C$  via the bias voltage. Furthermore, for most LEDs, the emitted intensity scales linearly with the applied bias voltage as it directly controls the available discharge current in the capacitor.

For the sake of defining the proper ( $L$ ,  $C$ ) configuration, we decided to pursue two distinct driver configurations: a fast and a default one. While the latter uses the configuration also used in the STRAW experiment, the former is supposed to provide much shorter pulses for calibrating potential systematics on short-distance scales which might be time-sensitive. For testing we make use of the best-performing STRAW LED at 405 nm namely the *XRL-400-5E*<sup>239</sup>. Then, the nominal configuration foresees an ( $L$ ,  $C$ ) configuration of (22 nH, 1.2 nF) at 4 – 8 ns FWHM while the fast configuration uses (22 nH, 150 pF) which lowers the total intensity output but significantly decreases the pulse width to 1 – 2 ns FWHM. However, these values are highly dependent on the selected emitter. Example pulse shapes for both configurations are given in fig. 7.30; reprocessed based on<sup>198</sup>.

<sup>237</sup> Kapustinsky et al. “A fast timing light pulser for scintillation detectors” (1985).

<sup>238</sup> EPC “Development Board EPC9126/EPC9126HC Quick Start Guide” (2019).

<sup>239</sup> Roithner LaserTechnik GmbH “XRL-400-5E” (2010).

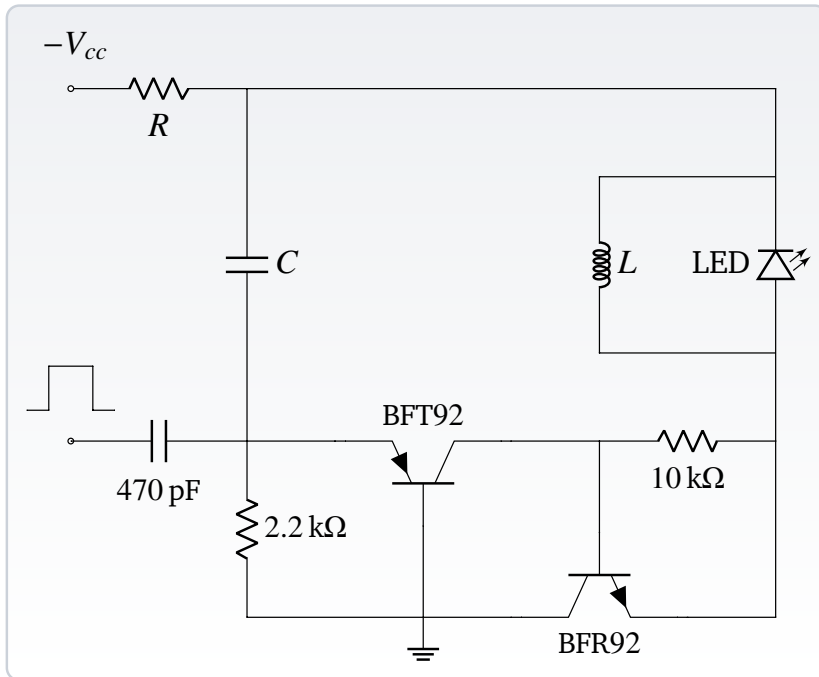


**Figure 7.26:** Kapustinsky pulse driver schematic. The Kapustinsky circuit operates on negative bias voltage and discharges the capacitor  $C$  through the LED and the inductance  $L$  upon opening the transistor path with the rising edge of a trigger pulse. The inductance will subsequently counteract the current flow and cut the pulse short, removing a potentially long emission tail and creating nanosecond pulses. Figure reference in the text.

Since the IceCube application demands redundancy wherever possible and the flashers are the primary part of POCAM-related calibration studies, the used Kapustinsky driver is slightly modified. By usage of diodes, the fast and the nominal Kapustinsky configuration are connected to the same LED. By enabling one or the other bias voltage path via logic-controlled transistors (refer to section 7.6) control of the used configuration is possible. This allows the usage of two Kapustinsky configurations on one emitter pad and allows to include multiple emitters with both Kapustinsky configurations. The circuit schematic realization of this setup is further shown in fig. 7.27; reprocessed based on <sup>240</sup>. Here, the two distinct diode paths towards the same LED are visible. This is also the reason that both the default and the fast Kapustinsky share the same inductivity  $L$  and the capacitors were chosen appropriately in order to cover the targetted intensities and pulse widths. Finally, to negate any unwanted left-over charge in the capacitors, discharge resistors  $R_{dis}$  make sure that unused capacitors discharge via the created ground connection prior to flashing.

<sup>240</sup> Spannfellner “Development of pathfinder missions and instruments for the Pacific Ocean Neutrino Experiment” (2020).

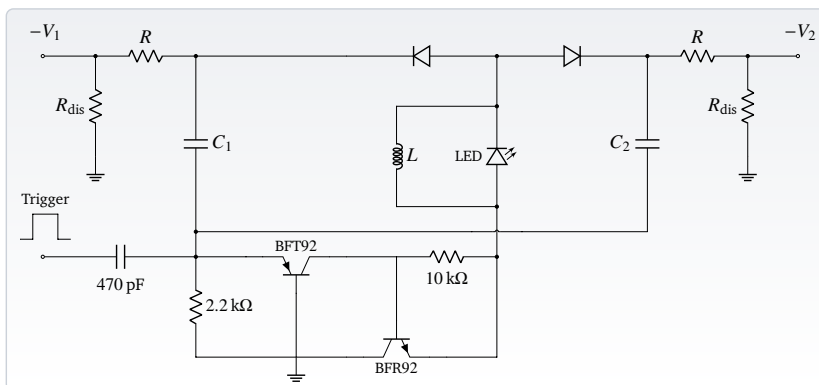
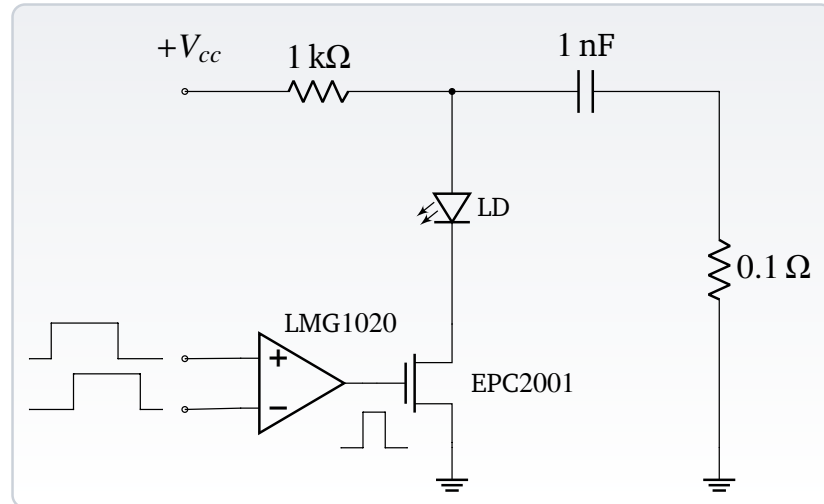


**Figure 7.27:** Dual-Kapustinsky configuration for one POCAM emitter. The schematic shows the two diode-decoupled paths of different capacitors to the same emitter which allow using the same emitter with different pulse configurations ( $L, C$ ) by means of logically selecting which capacitor to charge. Figure reference in the text with special gratitude to C. Spannfellner.

**LD-type driver** For the LD-type driver we make use of existing technology for pulsing infrared laser diodes<sup>238</sup> and adapt it to the emitters in the spectral range of the POCAM. The schematic in fig. 7.28 shows the general working principle of the circuit; reprocessed based on<sup>198</sup>.

**Figure 7.28:** LD-type pulse driver schematic. The LD-type driver operates on positive bias voltage and charges a capacitor bank which can be discharged via the ultra-fast switching components LMG1020 and the GaNFET EPC2001C delivering nanosecond pulses of up to kilowatts of per-pulse power. Figure reference in the text.



This circuit operates on positive bias voltage of up to 32 V and charges a capacitor bank. Then, the ultra-fast switching components LMG1020 and a subsequent *gallium-nitride field-effect transistor* (GaNFET) EPC2001C enable creating high-power trigger pulses of sub-nanosecond length which discharge through the emitters. Since LEDs and LDs in the optical range are usually prone to over-current we limit the bias voltage for protection reasons to 30 V. However, due to the large available currents, this allows driving laser diodes in addition to LEDs and thus much larger intensities at small to moderate pulse widths and offers increased spectral possibilities. Furthermore, the LMG1020 allows dynamically scaling the driver pulse length by means of logically combining phase-shifted enable and disable trigger inputs. This is especially useful for our application as it allows us to increase or decrease the trigger pulse depending on the required pulses for a specific systematic parameter study.

Also for the LD-type driver we require the flasher circuitry to be designed as fail-safe as possible. As the flowing currents through the sensitive GaNFET devices can be large, we decided to double the LMG1020 and EPC2001C paths and have all emitters connected to both discharge paths but each with their own capacitor bank. However, the development of these circuits is complex as it required testing and selecting suitable components that effectively do not alter the flashing behavior of the circuit. Thus, similarly to the Kapustinsky, we make use of transistors and diodes to switch between emitters via the enabled bias voltage path and logic signals to select the discharge path. In case one of the discharge paths stops working, we can then pursue with the secondary one without impacting functionality of the connected emitters. The circuit schematic for this setup is shown in fig. 7.29; reprocessed based on<sup>240</sup>.

Generally, with the LD-type driver, pulse width FWHMs of a few to tens of nanoseconds are possible at intensities typically ranging

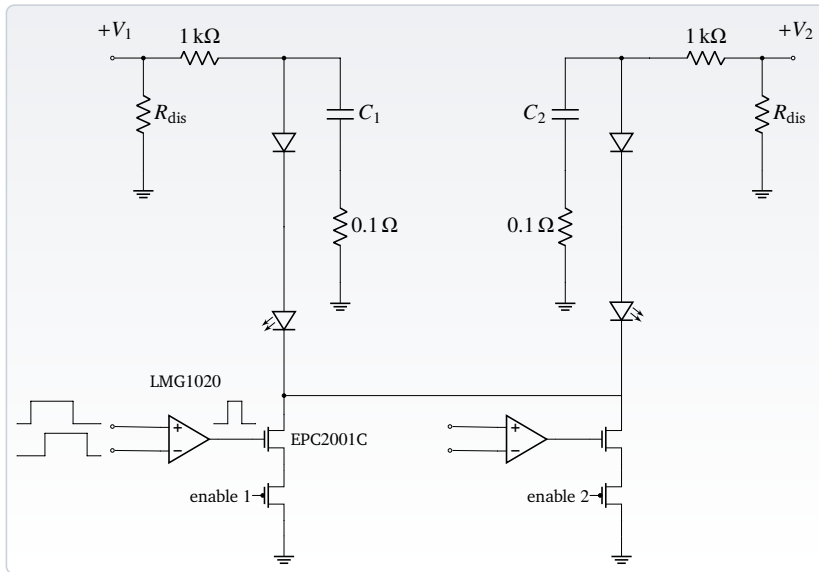
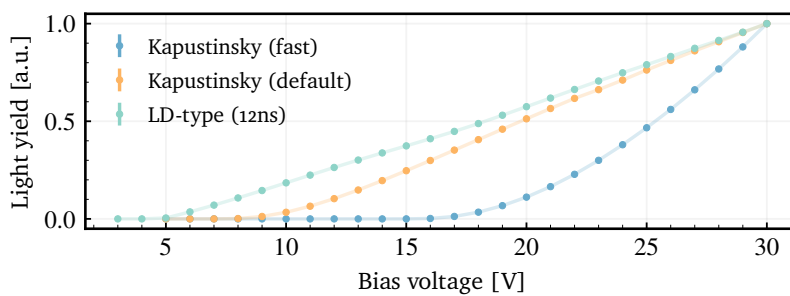
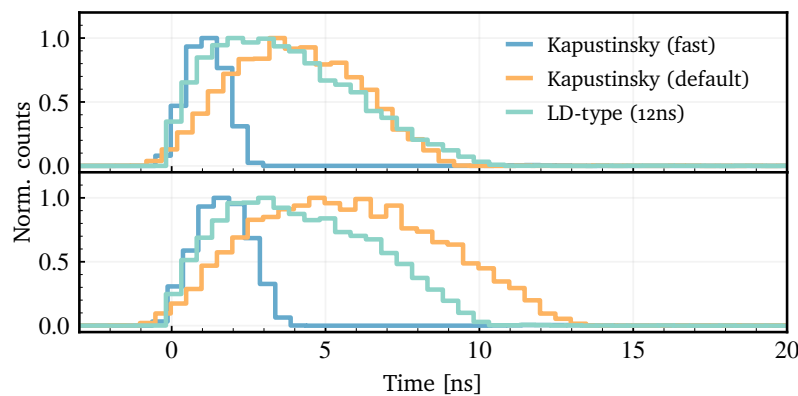


**Figure 7.29:** Dual-discharge LD-type pulse driver schematic. The dual-discharge LD-type driver can switch between emitters by selecting which capacitor bank to charge and between discharge paths by means of the trigger channel. Figure reference in the text with special gratitude to C. Spannfellner.

from  $10^7 - 10^{12}$  photons per pulse. Example pulse shapes are also shown in fig. 7.30; reprocessed based on <sup>198</sup>.



(a) Example intensity scaling of the three light pulse drivers.



(b) Example time profiles of the three light pulse drivers.

**Figure 7.30:** Example intensity scaling (a) and time profile pulse shapes (b) from all used driver circuits for the nominal 405 nm LED. The time profiles are recorded at 10 % (top) and 100 % (bottom) intensity configuration; the LD-type driver was configured to produce a 12 ns pulse. Figure reference in the text.

### 7.5.2 Light emitters

With the pulse driver circuits identified, the emitters can be tested and selected. For the purpose of this work more than 60 LEDs and LDs in a spectral range of 300 nm – 600 nm were tested for their dynamic intensity range and time profile in order to identify the most promising candidates to be deployed within the POCAM. Due to the

limited space within the diffusing sphere plug, the LED/LD matrix can host at most 6 emitters of which we decided to equip two slots with the dual-configuration Kapustinsky driver and the remaining four with the dual-discharge LD-type driver. The schematical emitter layout is shown in fig. 7.31; reprocessed based on <sup>198</sup>.

**Figure 7.31:** POCAM emitter and pulse driver layout on an analog board. The graphic shows the six emitter types all of which can be driven by two distinct pulse drivers. Figure reference in the text.

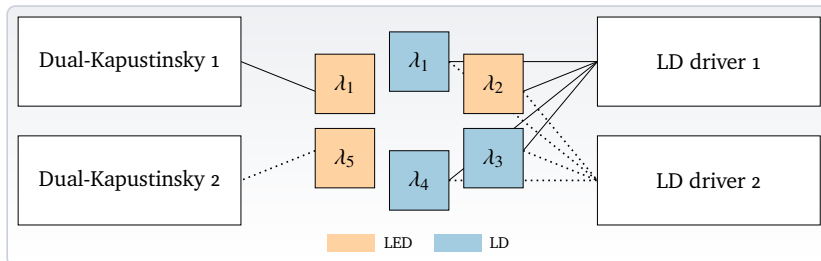
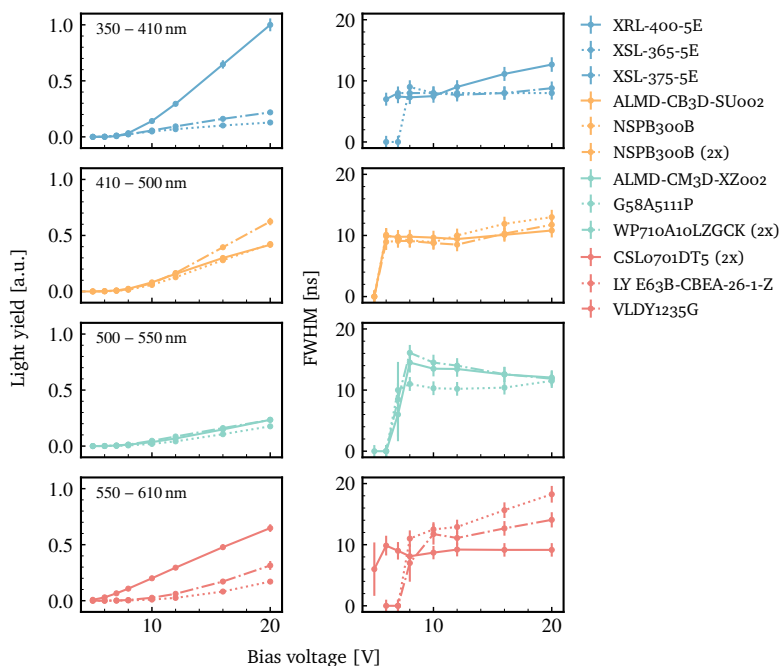


**Figure 7.32:** POCAM emitter matrix.

**Figure 7.33:** Example emitter selection process for a set of tested LEDs. The figure shows the measured intensity (left) and pulse FWHM (right) variation with bias voltage for an example sub-set of tested LEDs. The intensity scale is further normalized to the nominal 405 nm LED and wavelength-corrected. Figure reference in the text.



For the case of LEDs, previous work <sup>13,198,240</sup> had already provided an intricate selection of emitters. For LDs, numerous devices and vendors were ordered and tested. Each emitter was judged base on achieved maximal intensity, dynamic intensity range and pulse width behavior with intensity. The final selection of emitters is summarized in table 7.1 and taken from <sup>198</sup>. Furthermore, we have not selected any emitter for the IceCube Upgrade POCAM in the wavelength range 550 nm – 610 nm as IceCube physics impact is expected largest at

smaller Cherenkov wavelengths. Instead, the sampling of this spectral range is increased by adding a UV LED. Here it should be noted that this LED is selected to be driven by the LD-type driver as tests show that the relatively high current requirements for UV LEDs, in order to produce significant light output, can be provided by this driver.

Emitter	Vendor	Wavelength [nm]	Type
XSL-365-5E	Roithner Lasertechnik	$365 \pm 8$	LED
XRL-400-5E	Roithner Lasertechnik	$405 \pm 8$	LED
RLT405500MG	Roithner Lasertechnik	$405 \pm 5$	LD
PL-TB450B	Laser Components	$450 \pm 10$	LD
NSPB300B	Nichia Corporation	$465 \pm 7$	LED
PLT5_520_B1-3	OSRAM	$520 \pm 10$	LD

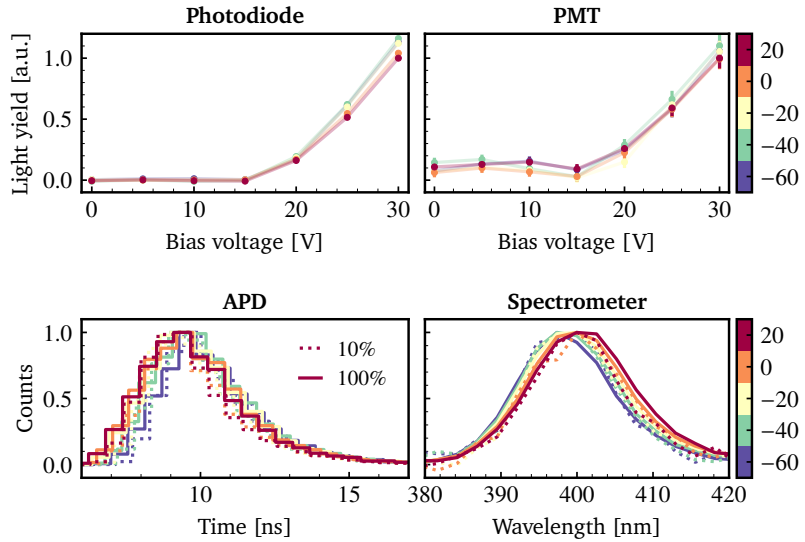
**Table 7.1:** POCAM emitter selection results. All LD-type emitters are driven in the selectable dual-discharge configuration; all Kapustinsky-driven emitters can be operated in dual-mode, that is a fast and a default configuration.

For all chosen emitters, the summarized light pulse behavior is shown in figs. 7.34 and 7.35 for the nominal wavelength of 405 nm LEDs and in the appendix in figs. D.1 to D.4 for all remaining emitters. All these plots show example calibration of intensity, time profile and spectrum behavior as a function of bias voltage and temperature. The general selection process results are summarized in the following with all per-pulse photon intensities given with an estimated 10 % systematic uncertainty <sup>a</sup>:

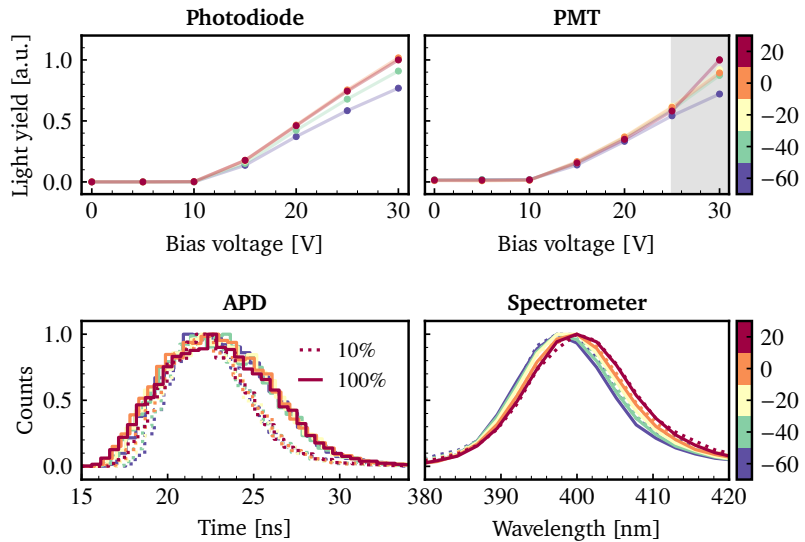
- **365 nm** – The selection of UV LEDs has proven very complicated. Not only are UV emitters very expensive but tests with the Kapustinsky drivers showed very poor results in terms of absolute light intensity. However, the larger current requirements for these emitters can be provided by the LD-type driver while maintaining reasonable pulse widths. After testing several emitters, the selected ones are relatively cost-efficient while providing good performance with intensities reaching  $1 \times 10^{10}$  photons per pulse. The resulting pulser performance using the LD-type driver at 12 ns pulse width is shown in fig. D.1.
- **405 nm (LED)** – For the nominal wavelength of 405 nm we find that the STRAW LED also performs well with the updated Kapustinsky drivers and offers pulse FWHMs of 3 – 8 ns and intensities ranging from  $1 \times 10^7$  –  $4 \times 10^9$  photons per pulse, both depending on the used Kapustinsky configuration. The selection process was quick in this case as the LEDs had been previously selected for the STRAW experiment. The resulting pulser performances are summarized in fig. 7.34 and show both the fast and default Kapustinsky configuration.

<sup>a</sup> These specific per-pulse intensities have been measured with a conventional and not the NIST-calibrated photodiode and as such are subject to larger systematic uncertainties.

**Figure 7.34:** Summary plot of the Kapustinsky 405 nm emitter selected for the POCAM in the IceCube Upgrade. The figure shows pulser behavior for the fast (a) and the default (b) Kapustinsky configuration via the photodiode (top left) as well as the PMT (top right), the time profile variation as measured by the APD (bottom left) and the spectrum variation as measured by the spectrometer (bottom right) as a function of temperature and bias voltage. Both the spectrum and the time profile are given for around 10% (dotted) and 100% (solid) intensity, respectively. The grey band in the PMT plot shows a region of expected non-linearity of the sensor.



(a) Pulser performance of the fast Kapustinsky driver for the selected 405 nm emitter.



(b) Pulser performance of the default Kapustinsky driver for the selected 405 nm emitter.

- 405 nm (LD)** – For the LD, the selection process involved testing several emitters from different vendors using the LD-type driver. The selected LD makes use of the controllable pulse widths and the pulses show no significant tails at greatly increased absolute brightness with respect to the Kapustinsky driver of up to  $2 \times 10^{11}$  photons per pulse. As for selection, the selected LDs have quickly shown to be the most promising candidates during testing and thus selection did not prove difficult. The pulser performance is summarized in fig. 7.35 and shows the emitter behavior for a selected pulse width of 12 ns.
- 450 nm** – The selection of this emitter has proven difficult as only few LDs were available on the market for testing. Furthermore, available diodes show long pulse tails even when used with the ultra-fast LD-type driver. As such, the best candidate emitter was selected, however, shows a distinct double-peak

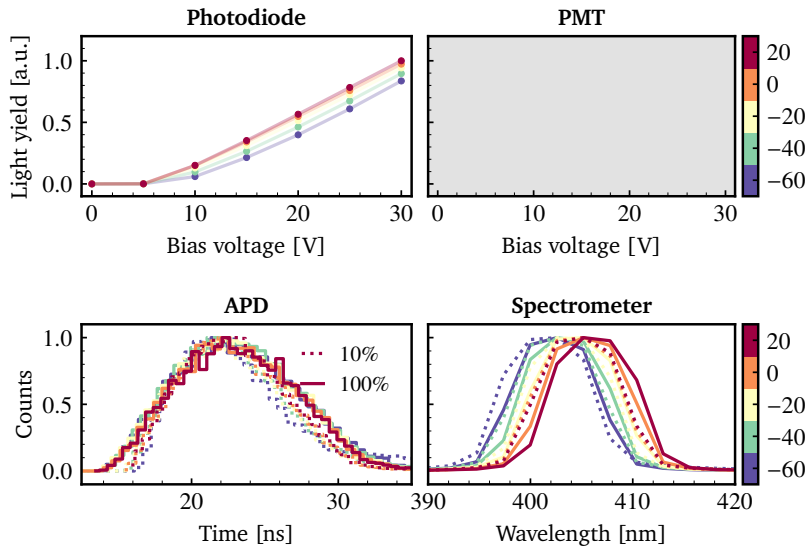


**Figure 7.35:** Summary plot of the LD-type 405 nm emitter selected for the POCAM in the IceCube Upgrade. The figure shows the intensity variation as measured by the photodiode (top left) as well as the PMT (top right), the time profile variation as measured by the APD (bottom left) and the spectrum variation as measured by the spectrometer (bottom right) as a function of temperature and bias voltage. Both the spectrum and the time profile are given for around 10% (dotted) and 100% (solid) intensity, respectively. Due to its large intensity, no PMT data was recorded for this emitter.

time profile which might negatively impact calibration precision. Nevertheless, with an intensity of up to  $1 \times 10^{11}$  photons per pulse long-distance calibration might still be possible to significant precision. The pulser performance is shown in fig. D.2 with a configured LD-type driver pulse width of 13 ns.

- **465 nm** – The blue emitters are also re-used from application in the STRAW experiment and hence have known to work well with the Kapustinsky driver. The pulser performance test shown in fig. D.3 also confirms that the performance remains with the updated Kapustinsky schematics and for both the fast and default configuration. The emitter shows pulse widths of 6 – 12 ns pulse width FWHMs with intensities ranging from  $1 \times 10^7$  –  $3 \times 10^9$  photons per pulse.
- **520 nm** – The most difficult selection process presents itself for green emitters. Here, a significant number of tested samples show long pulse tails independent of the pulse driver configuration. Eventually we selected the best-performing emitter candidate eventhough pulser performance was suboptimal. With optimistic FWHMs of larger than 20 ns at intensities up to  $3 \times 10^{10}$  photons per pulse the pulser performs worse than the other selections. The results of the pulse performance tests are shown in fig. D.4 and highlight the aforementioned time profile effects. However, long-distance calibration procedures can still work on a precision level.

### 7.5.3 Self-monitoring sensors

With the light emitter section completed, the remaining open topic on the analog board is self-monitoring. These sensors are included to provide in-situ information of the pulse intensity and starting time to reduce missing for the existing IceCube calibration LEDs. As the POCAM pulse drivers cover a large dynamic range of almost five orders of magnitude in intensity, the self-monitoring photosensors need to be

able to cover the whole range of emitted light pulse intensities. Since this is difficult to achieve with a single type of sensor, the analog board hosts two distinct ones: a photodiode and a *Silicon photomultiplier* (SiPM).

While the photodiode is able to cover the medium- to high-intensity pulses with good signal-to-noise ratio (SNR), the SiPM is able to record the very faint pulses down to, in principle, single photon level. In the best case, both sensor front-ends are adjusted in a way that there is an intermediate region where both sensors are able to monitor the light pulses and as such further provide cross-check possibilities.



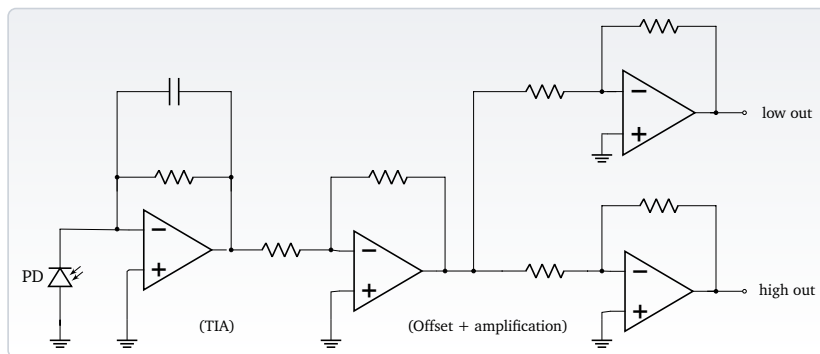
**Figure 7.36:** Hamamatsu S2281-01 photodiode. Image reference in the text.

<sup>241</sup> Hamamatsu “Si photodiodes - S2281 series” (2015).

**Photodiode** For the photodiode we make use of the model S2281-01 manufactured by Hamamatsu as shown in fig. 7.36; taken from <sup>241</sup>. This device provides a photoactive area of 100 mm<sup>2</sup> and shows low dark current<sup>241</sup> which makes it one of the more stable photodiodes on the market. Furthermore it comes in a sturdy metal package including a connector that allows simple mounting and connection as well as some environmental protection. This photodiode is mounted to the aperture disk as shown in fig. 7.21 and a dedicated connection scheme is used to electrically connect the analog board to the provided photodiode connector.

On the analog board the photocurrent by the photodiode is fed through a chain of amplifier stages in order to produce an output signal that is eventually sampled by an *analog-to-digital converter* (ADC). The general readout scheme was predominately developed by C. Spannfellner in the scope of his thesis and can be found in appendix C.3 with a simplified version pictured in fig. 7.37; reprocessed based on <sup>198,240</sup>.

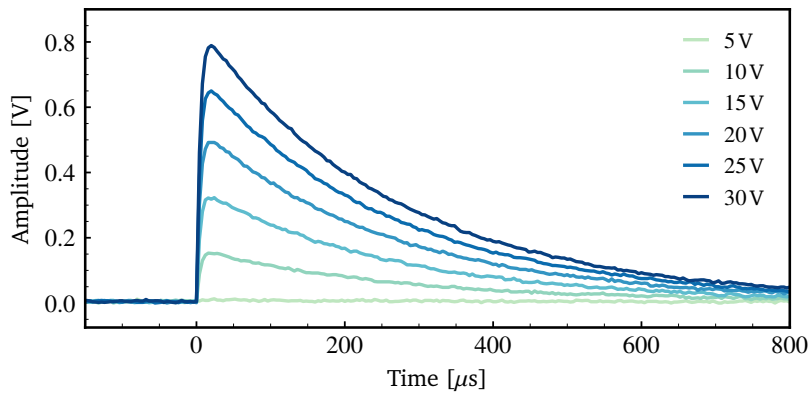
**Figure 7.37:** Simplified view of the photodiode readout chain schematics including amplifier stages. Figure reference in the text and special gratitude to C. Spannfellner.



For the signal chain, first the photocurrent is fed via cable to a *transimpedance amplifier* (TIA) that integrates the current and provides a voltage signal. The amplitude of this signal is proportional to the light intensity and is subsequently fed to a first amplifier that enables offset adjustment and first stage amplification of the signal. The signal is then split into two distinct secondary amplifiers that provide low- and high-gain amplifications, respectively, before being fed to the ADC. These distinct paths enable a larger dynamic range coverage of the signal due to limited amplifier output voltages as well as ADC input voltage range.

Testing the first version of this readout required several iterations and careful component choices in order to arrive at a stable output

signal baseline which could be used for further optimizations. An example output signal of both gain stages when flashing the LD-type driver using the 405 nm emitter is given in fig. 7.38; reprocessed based on <sup>242</sup>.



<sup>242</sup> Pertl “Development and characterization of IceCube Upgrade calibration instrumentation” (2021).

**Figure 7.38:** Example photodiode readout output pulses for the high-gain channel of the readout for the 405 nm emitter using the LD-type driver. Figure reference in the text.

During optimization of the readout chain it was required to adapt the gain of the amplifiers to match both the required ADC input voltage range (refer to section 7.6) and the dynamic range expected from the different flashers in combination with the spectral response of the photodiode. The latter is lowest in the UV and monotonically increases towards larger wavelengths <sup>241</sup>. The adjusted signal output for all emitters is finally shown in fig. 7.39; reprocessed based on <sup>242</sup>.

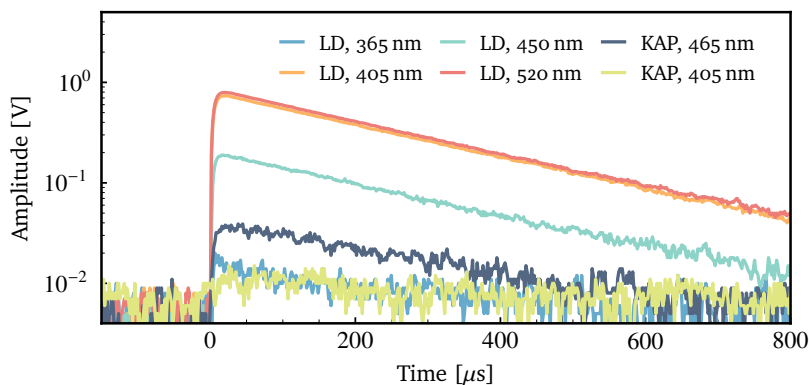


**Figure 7.39:** Photodiode readout output pulses for all emitters. The plot shows output pulses of the photodiode for all emitters at their respective highest intensity. Figure reference in the text.

<sup>243</sup> Gruber et al. “Over saturation behavior of SiPMs at high photon exposure” (2014).

<sup>244</sup> Kotera et al. “Describing the response of saturated SiPMs” (2015).

<sup>245</sup> Ketek “SiPM - Silicon Photomultiplier PM3315-WB-Co” (2019).

**Silicon photomultiplier** A SiPM is a pixelated photosensor meant for detection of photons in low-light environments. Due to its limited number of pixels, its dynamic range is inherently limited. However, while the SiPM is intended for single-photon detection applications, its saturating response to larger light fluxes is investigated thoroughly in literature <sup>243,244</sup> and can also be used for moderate light fluxes if appropriate signal descriptions are used. For the POCAM we want to self-monitor also the faint pulse intensities and for this make use of a Ketek PM3315-WB model which has a photoactive area of 9 mm<sup>2</sup> pixelated into 38 800 microcells. The sensor is shown in fig. 7.40; taken from <sup>245</sup>. The SiPM is supplied with a positive bias voltage and soldered directly to the analog board as well as additionally fixed using a drop of epoxy.

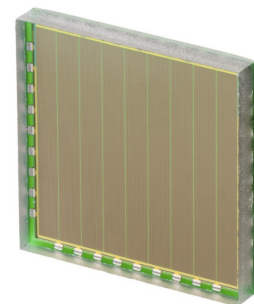
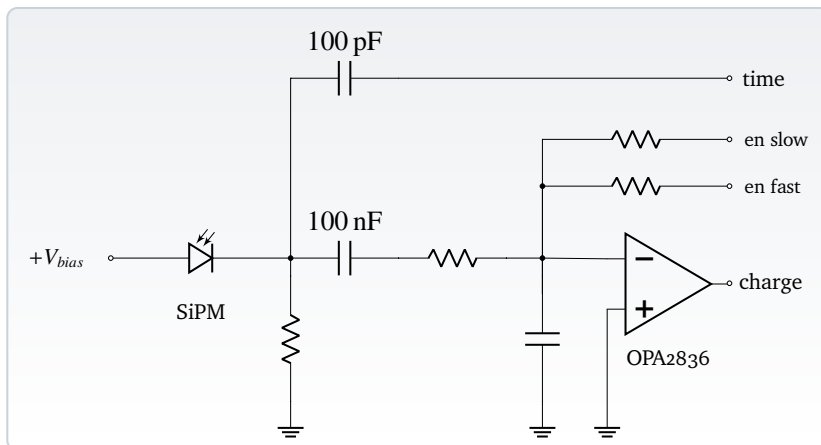


**Figure 7.40:** Ketek SiPM PM3315-WB. Image reference in the text.

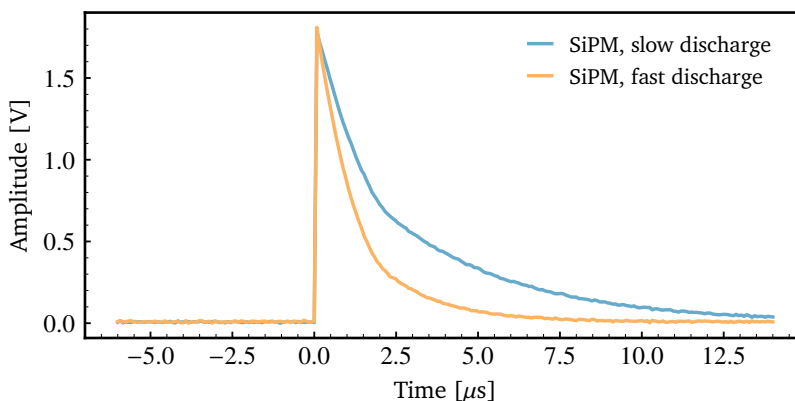
A simplified version of the SiPM readout is pictured in fig. 7.41 with detailed schematics given in appendix C.4; figure reprocessed based on<sup>198</sup>. Generally, the signal is split in two paths: 1 % of the signal goes into the timing path, 99 % of the signal are fed into the charge path. The timing path makes use of a fast transistor to provide a precise description of the rising edge of the pulse which is finally fed to one channel of the *time-to-digital converter* (TDC). This provides internal reference timing for the pulse on-set time and can be compared to external experiment clocks or synchronization signals. The charge path uses the signal to charge a capacitor which in turn is discharged, amplified and also fed to the TDC. By controlling the discharge decay constant  $RC$  of the capacitor  $C$  via the used discharge resistor  $R$  and recording the *time-over-threshold* (ToT) of the signal via the TDC allows reconstructing the initial charge. Two resistors can be used for discharging in fast or slow manner. This is implemented in order to cover also here a larger dynamic range since discharging small charges faster retains precision if the initial pulse is faint.

**Figure 7.41:** Simplified SiPM readout schematic showing both the timing and the charge paths. The latter are controlled by the enabled discharge resistor in either fast or slow mode. Figure reference in the text and special gratitude to C. Spannfellner.



Example pulses of the charge paths are given in fig. 7.42 and show the amplified pulses in both of the two distinct capacitor discharge channels; reprocessed based on<sup>242</sup>. Including the fast time pulse, all of these channels are fed to the TDC. For the time path the TDC samples the on-set time while for the charge paths the TDC samples the ToT which relates to the total charge.

**Figure 7.42:** Example SiPM readout output pulses for the timing and the charge paths using the 405 nm emitter and the default Kapustinsky driver. Figure reference in the text.



**Dynamic range coverage** With the self-monitoring sensors in place, the question remains how these sensors cover the large dynamic range of POCAM emission intensities. For this, we monitor the response curves of both the photodiode and the SiPM and extract the intensity information. For the photodiode this is the sampled maximum amplitude of the amplified TIA signals in the low- and high-gain path, for the SiPM this is the ToT of the sampled fast and slow capacitor discharge curves. Setting up a POCAM hemisphere and flashing the different emitters with the respective pulse drivers allows extracting the self-monitoring sensor information. Then, using a nearby reference photodiode monitor, we can plot the sensor intensity measure with respect to the total POCAM emission intensity. The plot using all emitters is shown in fig. 7.43 and highlights the importance of both sensors as it clearly shows the complementary behavior of photodiode and SiPM for high and low intensities, respectively; figure reprocessed based on <sup>198</sup>. Furthermore, the intermediate region can be monitored using both sensors and as such allows cross-checks even after deployment of the instrument.

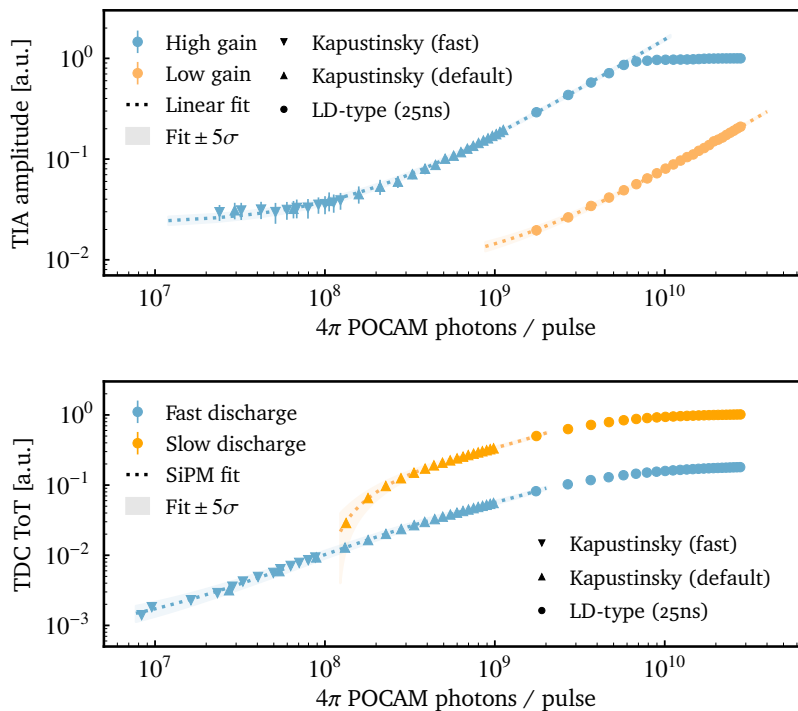


**Figure 7.43:** Dynamic range coverage of both self-monitoring sensors for the in-situ intensity monitoring of the POCAM. The plots show the ADC-sampled photodiode signals (top) as well as the TDC-sampled time-over-threshold for the SiPM charge path. For both sensors, the distinct readout channels are shown separately. Figure reference in the text.

## 7.6 Digital and interface electronics

The last remaining component of the POCAM electronics are the digital and interface electronics. Generally, the layout in fig. 7.4 shows the following components necessary for controlling the device and interfacing it to the IceCube Upgrade detector

- **Digital board** – Installed in each hemisphere and interfaces directly to the analog board as well as the interface board.
- **Interface board** – Installed once per instrument and interfaces

to the digital boards as well as the IceCube interface board.

- **IceCube interface board** – Installed once per instrument and interfaces to the IceCube detector communication and synchronization streams.

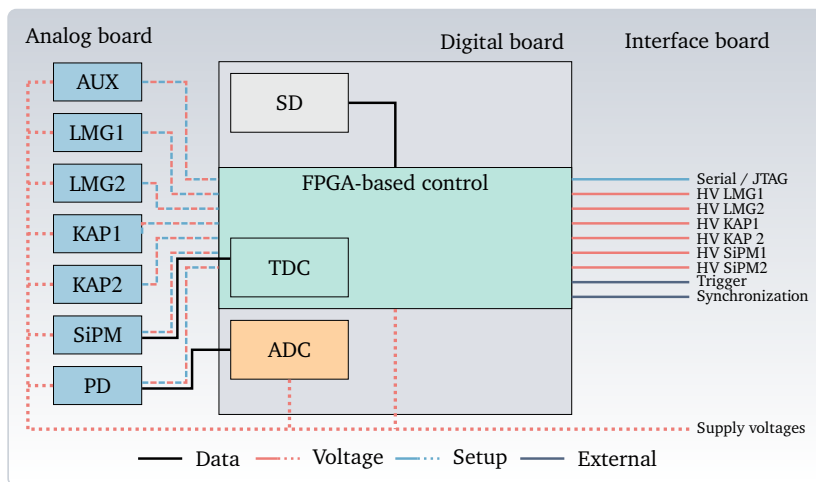
The interplay between these boards eventually enables all POCAM functionality as well as connection to the IceCube detector DAQ and synchronization. These boards were developed by senior scientist M. Boehmer in close collaboration with the author.

### 7.6.1 Digital board

The digital board (DB) is the primary control board for a hemisphere and interfaces directly to the analog board (AB) as well as the interface board (IB). Thus, each hemisphere hosts one such board.

The board itself hosts a central *field-programmable gate array* (FPGA) which is responsible for controlling all sub-devices on the board. The latter includes a variety of switching components, the ADC and FPGA-internal TDC responsible for reading the self-monitoring sensors and a variety of ambient sensors as well as voltage and current monitors in order to stay in check with the system state at all times. The central functionality of the DB is the configuration of the analog board. That includes configuring light pulser settings – for example emitter selection as well as configuration of the dual-Kapustinsky or the LD-type discharge path – as well as SiPM discharge configuration and switching of related voltages. Additionally, the board hosts a heavy-duty SD-card for temporary storage of self-monitoring data. A flowchart of the board functionality and central components is given in fig. 7.44 and shows the main devices located on the DB as well as its connections to subsequent boards.

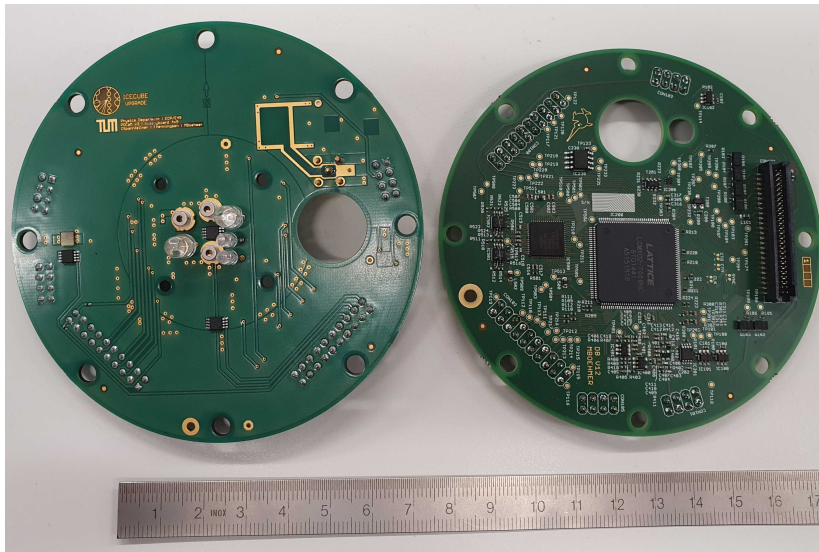
**Figure 7.44:** Flowchart of the digital board functionality and key components. The flowchart shows the digital board with its central components and how they connect to the analog and interface boards. For details on the figure, refer to the text.



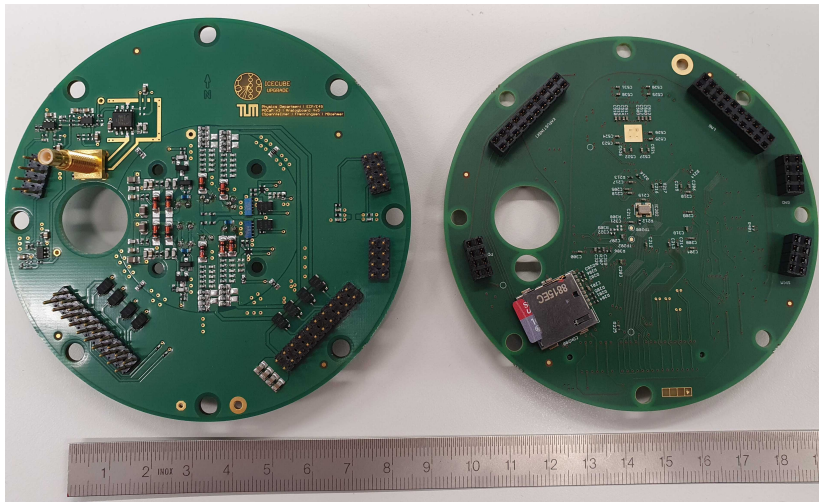
All signals from the interface board are distributed to the used components on AB and DB of both hemispheres. In particular this includes baseline voltage supplies for components as well as necessary voltages for light pulse drivers and self-monitoring sensors. From the analog board side, the DB hosts and controls optical switches to handle pulse driver configuration, including voltage and discharge selection for the LD-type driver as well as fast/default selection for

the Kapustinsky driver. Furthermore it uses the same switches to handle the SiPM fast/slow discharge selection.

The FPGA runs on the same clock as the main microcontroller on the IceCube interface board (refer to section 7.6.3). In addition to provided trigger and synchronization pulses, this allows to make use of synchronous timing within each of the POCAM hemispheres, mainly for the FPGA but also for subsequent time-sensitive components like the TDC. However, a backup oscillator is in place so that, in case the external clock fails for any reason, the instrument can proceed to function. Both the analog and digital board are shown together in fig. 7.45.



(a) Top view



(b) Bottom view

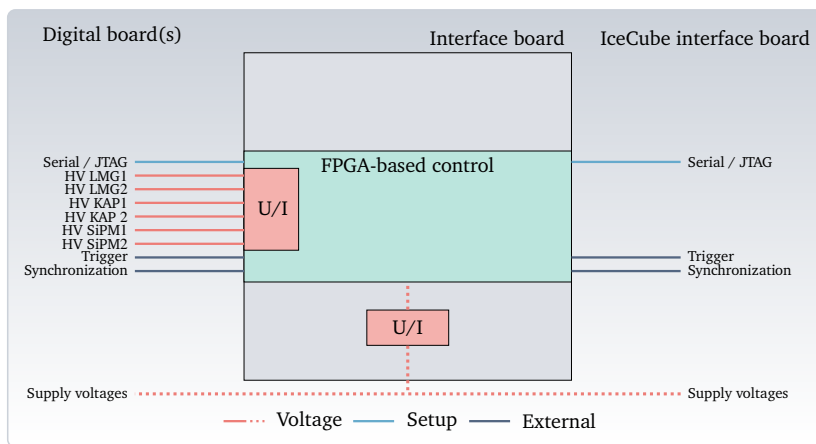
Figure 7.45: POCAM analog (left) and digital board (right) in top and bottom view.

### 7.6.2 Interface board

The subsequent board to the digital board is the interface board (IB). The IB is installed only once per instrument and interfaces to both digital boards via multi-strand teflon cables. It also hosts an FPGA and generates all voltages required throughout the instrument. In

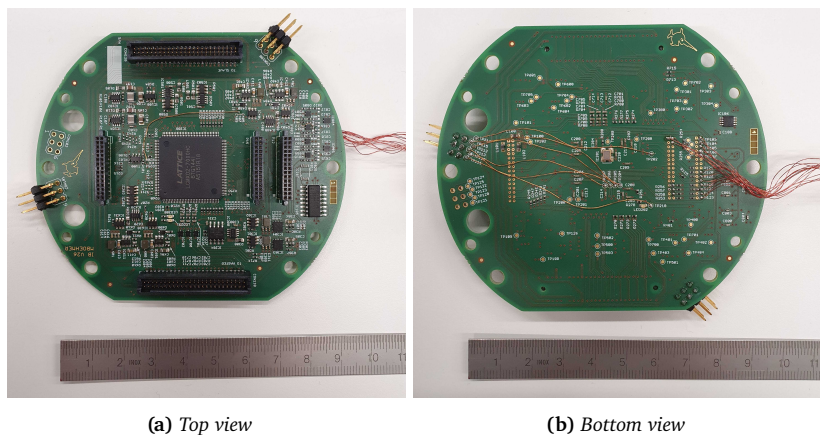
addition to the necessary supply voltages of 1.8 V, 3.3 V and 5 V this includes the voltages for the light pulse drivers as well as the SiPM. All of these voltage generation circuits are included twice in the design and are switchable by optical transistors controlled by the central FPGA on each of the DBs. This redundancy allows recovery from potential, however unexpected, malfunctions within the voltage generation components. Since these voltage generators need to provide all functionality to subsequent components, potential damages can be circumvented by having a copied fallback voltage generator in place that can replace a damaged one. The general work flow of the IB is pictured in fig. 7.46.

**Figure 7.46:** Flowchart of the interface board functionality and key components. The flowchart shows the interface board with its central components and how they connect to the digital and IceCube interface boards. For details on the figure, refer to the text.



In addition to voltages, the IB also hosts the central trigger distribution system as it receives the external triggers and synchronization pulses from the IceCube interface board (refer to section 7.6.3). These triggers are used to send out centralized and synchronous triggers to either or both of the hemisphere DBs, depending on the flashing configuration. The DBs then set up the pulser configuration according to the user specification and will use subsequent trigger pulses to initiate synchronous flashing. While the boards are designed completely symmetrically there might be differences in the flashing on nanosecond scales, however, the SiPM pulse time information channel will allow precise reconstruction of the light pulse time on-set of both hemispheres for data analysis. The board is pictured in fig. 7.47.

**Figure 7.47:** POCAM interface board in top and bottom view. The attached wires allow observing signals of interest on this prototype board while developing its firmware.



(a) Top view

(b) Bottom view

### 7.6.3 IceCube interface board

Finally, the last board interfacing to the IB is the IceCube interface board (IIB). This board stack comprises of three boards and is developed by the IceCube collaboration and is used within all devices which are not DOMs in order to provide a homogenized interface to the IceCube detector. In addition to the *IceCube communications module* (ICM)<sup>246</sup>, the stack consists of one board dealing with power conversion from the IceCube wire pair to the supply voltages of all subsequent devices and one board hosting the main Icecube Upgrade microcontroller (MCU) including auxiliary sensors. The latter include accelerometers and magnetic field sensors for orientation and tilt of the instrument. The ICM connects to the MCU-hosting board of the IIB and provides the necessary hard- and firmware to disentangle the IceCube communication and time synchronization signals modulated on the wire pair DC bias voltage<sup>141</sup>. It further allows to integrate the module within the IceCube synchronization stream. The stack of controller and power board as well as ICM is pictured in fig. 7.48.

<sup>246</sup> Nagai et al. “*Electronics Development for the New Photo-Detectors (PDOM and D-Egg) for IceCube-Upgrade*” (2019).

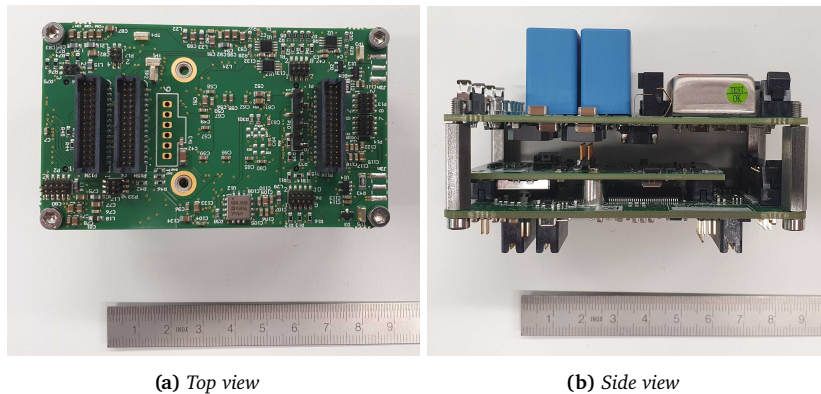


**Figure 7.48:** IceCube interface board stack in top (left) and side (right) view. The latter shows the power board on top, the controller board on the bottom and the ICM in between the two other boards.

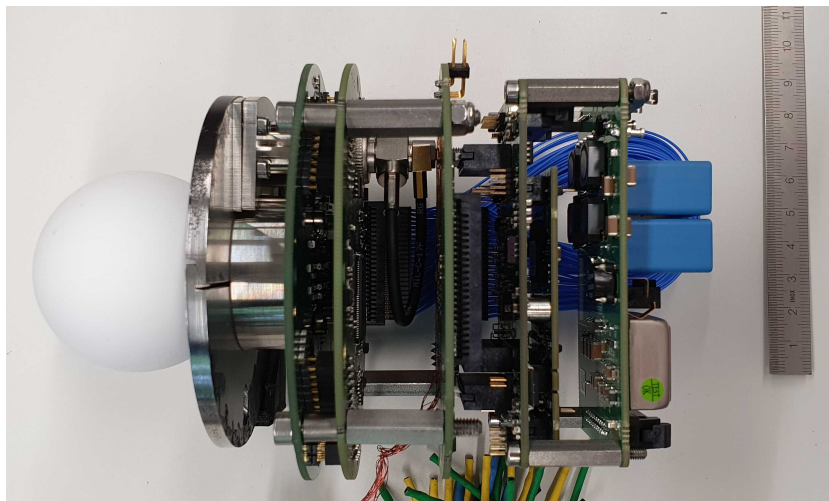
As for the POCAM, the only relevant capabilities of the IIB are its communication interfaces, the provided clock, trigger and synchronization signals as well as provided baseline voltages. All FPGAs on IB and DB can be programmed via the serial or JTAG interface provided by the main MCU on the IIB which allows to update internal POCAM firmware even after instrument deployment. All of these communications are distributed first to the IB and then to either or both of the hemispheres. That means the firmware of all internal FPGAs on IB and DBs can be upgraded after deployment.

The software development for the IIB is centralized within the IceCube Upgrade and each special device is identified via a dedicated jumper configuration on the IIB and its respective software is loaded upon powering on and initializing the instrument. All subsequent instrument controls can then be handled via the IceCube DAQ. A fully assembled POCAM stack including two hemisphere AB/DB stacks is pictured in fig. 7.49.

## 7.7 Calibration procedures

Finally, with all POCAM components in place, each instrument needs to be calibrated to below 5% precision. For this we make use of the

**Figure 7.49:** Fully-assembled POCAM stack including analog and digital board stacks for both hemispheres as well as internal and IceCube interface boards.



calibration setups discussed in section 7.3 and define the following calibration chain

1. **Relative flasher characterization** – Each of the POCAM stacks will undergo flasher characterization in the freezer. Here, relative temperature and configuration parameter dependence on the light pulses will be characterized.
2. **Relative emission profile characterization** – Each of the hemispheres will undergo emission profile characterization where the individual flange, diffusing sphere and shadow mounting properties are mapped.
3. **Absolute intensity calibration** – Each fully-assembled hemisphere will then be placed within the emission profile setup and a NIST-calibrated photodiode is used to estimate its total light output to high precision.
4. **Orientation calibration** – Each assembled instrument is finally subjected to the orientation setup. By this, the accelerometer as well as magnetic field sensors are calibrated to later estimate instrument tilt and orientation.
5. **In-water emission profile verification** – A few instruments will finally be subjected to in-water tests of the emission profile as the previous characterization is done in air and translated to ice using simulations. This test should verify the general applicability of this simulation-based adjustment.

For each calibration step we summarize the preliminary granularity for all measurements in table 7.2. These measurement points combine reasonable calibration times with a precision of below 5 % for the relevant gradients in temperature and configuration parameters. For each of the flasher characterization setup parameters all light pulse characteristics will be calibrated, totaling in a per-hemisphere calibration time span of up to 36 hours.

Now, since the POCAM is supposed to work on a precision level for calibration purposes, relevant systematics of all calibrations need to be considered to estimate the final calibration error on its light

Parameter	Range	Step	Unit
Temperature	[−60, 20]	10	°C
Bias voltage, drivers	[0, 30]	5	V
Bias voltage, SiPM	[28, 32]	2	V
Pulse width, LD-type	[5, 55]	10	ns
Emission profile, azimuthal	[0, 360]	60	deg
Emission profile, polar	[0, 130]	10	deg

**Table 7.2:** POCAM calibration measurement granularity for all calibration parameters.

pulsing characteristics. An extended list of systematics is given in table 7.3; reprocessed based on<sup>198</sup>. Summarizing this table we can estimate the total uncertainty on the absolute POCAM light yield, the knowledge about its spectrum and the time profile conservatively to 3.7%, 1 nm and 0.2 ns, respectively. The total isotropy  $1\sigma$  range achieved with our flange geometry is around  $\pm 3.5\%$  over the whole angular range and around  $\pm 1.5\%$  for the undisturbed polar emission region of  $\theta \in [0^\circ, 60^\circ]$ . But since this emission profile is well mapped, it can be plugged directly into simulation.

Systematic effect	Estimated impact
Temperature-dependent fiber coupling	2.0 %
Room temperature fluctuation	0.1 %
Internal temperature readout drift	$\leq 1.0\%$
Rotational angular uncertainties	0.4 %
Picoammeter drift / calibration	1.0 %
Self-monitoring sensor aging	$< 1.0\%$
Point source approximation	$< 1.0\%$
Flashing frequency stability	$< 1.0\%$
NIST calibration	$\leq 0.7\%$
Simulation mismatch	$\leq 2.5\%$
Spectral calibration filter width	1.0 nm
TDC time calibration	0.2 ns
<b>Spectrum</b>	<b>1.0 nm</b>
<b>Time profile</b>	<b>0.2 ns</b>
<b>Relative light yield</b>	<b>2.6 %</b>
<b>Absolute light yield</b>	<b>3.7 %</b>

**Table 7.3:** POCAM calibration setup systematics and final calibration precision on light pulse properties. Figure reference in the text.

## 7.8 *Instrument assembly and production*

While only in preparation at the time of writing this thesis, instrument mass production is planned to proceed over the next months. In the scope of this preparation, electronics assembly, testing, calibration, mechanical assembly and eventual instrument sealing was tested and optimized. The general principle of instrument assembly is outlined by the following steps

1. **Electronics assembly and testing** – Prior to assembly with optical components, the electronic stack is connected to a test backend and a basic verification test script runs through its major functionality verifying correct behavior.
2. **Emission profile characterization** – Diffusing sphere, aperture disk and flange are mounted in the emission profile measurement setup and characterized. This can be done in parallel to the prior electronics verification step.
3. **Internal stack assembly** – Once electronics and optical components are verified to operate as expected, the internal stack is assembled. This assembly works independently of the flange via distinct mounting procedures: while the stack is assembled using threaded spacers, additional holes allow sliding it to threaded bars installed at the flanges and hence allow relatively simple mounting.
4. **Flasher characterization** – The internal stack is then mounted to the flasher characterization setup and all light pulsers and emitters are calibrated with respect to temperature and configuration parameters.
5. **Flange assembly** – Once the stack has been fully characterized, it is mounted to the thoroughly-cleaned flange via the aforementioned threaded bars.
6. **Absolute calibration** – The fully assembled hemispheres are installed in the emission profile characterization setup and absolutely calibrated in terms of light output using the NIST-calibrated photodiode.
7. **Nitrogen flushing** – After all calibrations, one flange is mounted to the cylindrical part of the housing and fixed using screws. The remaining flange is left loose and the instrument is placed in a nitrogen atmosphere within a glovebox.
8. **Instrument sealing** – After drying in the glovebox for around two weeks, the instrument is closed, evacuated to around 100 mbar and closed completely. After no significant pressure changes within two weeks, the instrument is considered ready for deployment and prepared for shipment to the South Pole.

All of these steps are outlined in more detail in the following sections including images of the whole process.

### 7.8.1 Electronics assembly and testing

One electronics stack comprises of two ABs, two DBs, one IB and one IIB. The IIB stack is connected to the IB via three connectors on the center of the board. Each AB/DB combination is connected via pin-header connectors and eventually connected to the IB using the multi-strand teflon cable. An example of such a test setup is shown in fig. 7.50.

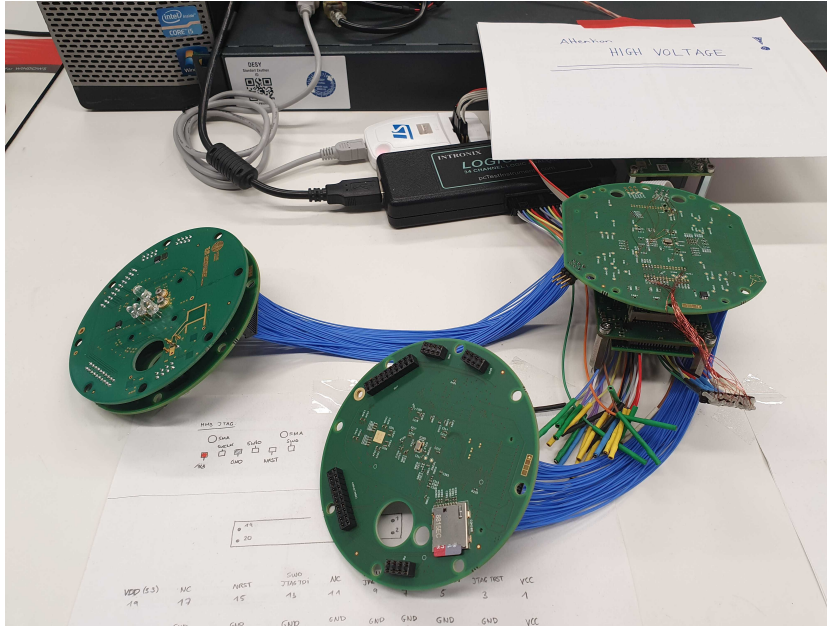


**Figure 7.50:** POCAM electronic stack testing with IB, IIB, two DBs and one AB for a prototype setup. The FH is visible in the background including several diagnostic and communication tools.

For testing purposes the stack is then connected to a *field-hub* (FH) which emulates the IceCube DAQ interface and provides IceCube-like communication and synchronization. The FH was provided by the electronics department of the *Deutsches Elektronen-Synchrotron* (DESY) and is able to connect two devices via wire pairs that resemble the IceCube interface. The wire pair provides 95 V of supply voltage and the communication and synchronization signals which are modulated on the DC voltage supply. Then, a simple test script runs through all the basic functionalities of the IB and DB and returns a report of failed and successful tests. Based on these results, the board is either accepted or returned for further investigation.

### 7.8.2 Internal stack assembly

Once the electronics have passed basic functionality the stack can be assembled. For this, the AB is equipped with diffusing sphere and aperture disk including internal sensors and the photodiode cable is connected to the amplifier chain input. Then, the AB/DB stacks are coupled using screws and threaded spacers and then eventually fixed using nuts. The same goes for the IB/IIB stack, also here the electronically-connected stack is fixed using screws and threaded spacers. The IB/IIB stack is finally attached to one of the AB/DB stacks via threaded spacers and fixed using nuts. The whole setup is shown example in fig. 7.49 for the AB/DB stack that hosts the IB/IIB stack.

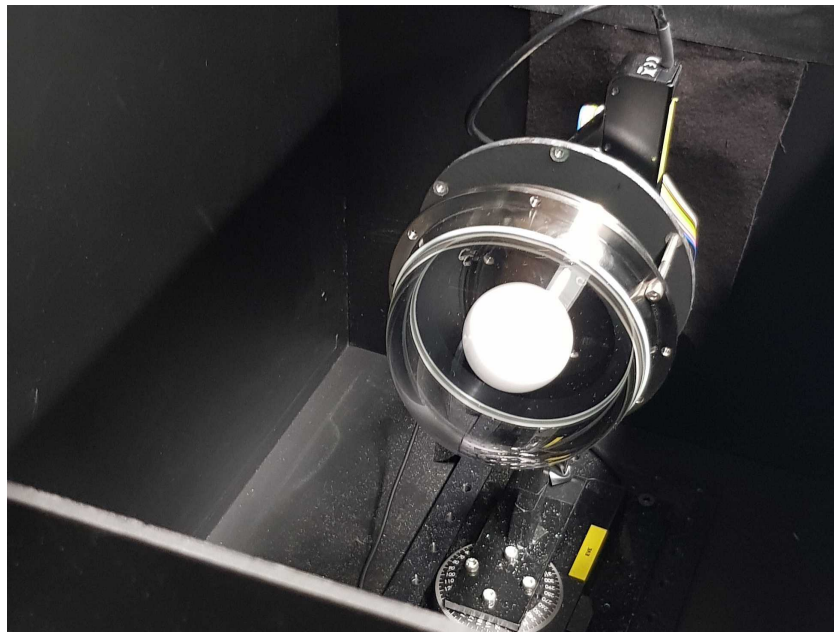
### 7.8.3 Flasher characterization

Once a stack is tested, fully assembled and equipped with optical components it can be calibrated in the flasher characterization setup. For this, it is mounted within the freezer setup and a whole temperature and configuration parameter scan is performed, that is, at different temperatures and configuration settings all light pulser properties are measured. This measurement usually takes around a full day to complete as at every temperature step the setup has to adjust itself to the ambient temperature first before measurements can continue. The output of this is a calibration file that clearly identifies to the measured stack identification credentials and can be used for later processing. The installation is further shown in fig. 7.12 for a prototype analog board.

### 7.8.4 Emission profile characterization

While the electronics are assembled and tested, optical components can already be calibrated in the emission profile setup. For this, a flange, a diffusing sphere and a shadow mounting are selected as a set and mounted to the illumination board of the emission profile setup. This board hosts the same LED/LD matrix as every POCAM but in DC-mode for brighter illumination and better signal-to-noise ratio for the monitoring photodiode. One such example setup is shown fig. 7.51.

**Figure 7.51:** POCAM flange installed to the rotation stages in the emission profile characterization setup.



Then, the flange assembly is mounted to the rotation stages and the measurement is started. Upon finishing after a few hours, a calibration file is stored which hosts the relative emission profile, clearly identified with the identification credentials of the set and can be used for later processing as well.

### 7.8.5 Flange assembly

Once the electronics stack and the optical components have been calibrated, the flange can be fully assembled. For this, four threaded bars are installed in the threads present in the flange and the board stack can slide on them using designated mounting holes in the circuit boards. However, first the flange and the glass are thoroughly cleaned and o-rings are installed. Then, the appropriate optical component set is merged with the electronics stack and eventually installed on the threaded bars in the flange, fixed with nuts. An example assembly of this is shown in fig. 7.52.



**Figure 7.52:** POCAM stack assembly with the AB/DB/IB/IIB stack attached to the flange and the secondary AB/DB stack not connected to its flange here.

### 7.8.6 Absolute calibration

For absolutely calibrating the relative intensity scales of previous measurements the assembled flanges are mounted to the relative emission profile setup and the photodiode is exchanged with a NIST-calibrated one. Then, the absolute measurement of different light emitter configurations allows estimating the total light output to high precision. This is done for all flanges and also stored in an identifiable calibration file.

### 7.8.7 Nitrogen flushing and sealing

Prior to fully closing the instrument it needs to be flushed with nitrogen in order to remove leftover humidity. For this, the flange hosting the IB/IIB stack is connected to the wire pair from the penetrator and screwed to the cylindrical housing. The second flange remains unscrewed and the setup is moved to a glovebox where a pure nitrogen atmosphere is present. Here the unscrewed flanged is opened but remains electrically connected via the multi-strand teflon cables and the whole instrument is left there for two weeks to dry. An example of this is shown in fig. 7.53.

**Figure 7.53:** *POCAM instrument prior to sealing and final assembly in the glovebox.*



After that the second flange is also screwed to the housing and the instrument is evacuated to around 200 mbar in order to provide under pressure and thus providing some sealing for the housing from the inside. The instrument is then electrically tested for basic functionality one last time before being declared ready for shipment.

The IceCube detector at the South Pole and its astroparticle and physics results drive the field of neutrino astronomy sparking new ideas all around the world to extend the neutrino sky coverage. Its low-energy extension and re-calibration using the IceCube Upgrade will further improve its possible physics observations and extend its capabilities. This will potentially provide unprecedented precision on some of the mixing parameters of neutrinos via oscillation measurements. In this thesis, the development and physics impact of a calibration light source for the IceCube Upgrade with potential applications in all large-volume telescopes is presented. The *Precision Optical Calibration Module* (POCAM) is aimed to be an isotropic, self-monitoring, nanosecond calibration light source able to provide detector-independent reference light pulses which can be used to tackle existing detector systematics to percentage precision. The main focus of this thesis is divided in two parts: a simulation effort to study the potential POCAM-induced improvements for low-energy oscillation analyses in IceCube and the hardware development of the device itself for the IceCube Upgrade.

The presented simulation study makes use of machine learning techniques to interpolate and speed up the multi-dimensional simulation effort necessary to study calibration light sources within IceCube. The used neural net is able to estimate the response of DOMs given a light source position within the detector and the systematic parameter set of interest. By providing the net with a sample of systematic parameter variations it can eventually interpolate between the sets and provide fast, precise DOM response approximations without the need of simulation. This technique is then further investigated on simulated pseudo-data sets aiming to fit back the used systematic parameters. Using a Poisson-binned likelihood approach and the trained neural net, this fit returns the input systematics to sub-percent precision. In a second step, experimental data of DOM flashers is fit using the same technique only adjusted for the fact that no absolute light intensity information can be included. Also here, the fit results in IceCube bulk and hole ice parameters within the expected range and to below 10 % precision. Then, the study is used on an artificial set of POCAM pseudo-data within the Upgrade detector and provides preliminary calibration estimates of around 1 – 3 % on the bulk ice properties and DOM efficiency as well as more stringent constraints on the hole ice parameters than what is possible with current means. Finally, plugging these new potential POCAM priors to an existing IceCube oscillation analysis shows improvements of 8 – 30 % on the oscillation parameters  $\Delta m_{31}^2$ ,  $\sin^2 \theta_{23}$  and  $n_\tau$  with respect to the current systematic priors. The simulation chapter closes with

short stand-alone studies on the local effects of the refrozen hole ice using the POCAM GEANT4 simulation framework to tackle hole ice parameters as well as potential optical geometry calibrations in water.

The hardware development section of this thesis encompasses the whole process of designing, developing, producing and calibrating 30 POCAMs for the IceCube Upgrade. After summarizing existing efforts of the POCAM instrument, the detailed function of all instrument components are discussed. Most importantly, this includes the revised flasher circuits for light pulsing. In addition to the proven and reliable Kapustinsky drivers, these now include a laserdiode driver which significantly increases possible light pulse intensities of the instrument. This extends the dynamic range of the POCAM to  $10^6 - 10^{11}$  photons per pulse over wavelengths of 365, 405, 450, 465 and 520 nm. Special focus was put on redundancy so that each flasher has a backup channel so that flashing is still possible in case the primary one fails. The revised self-monitoring circuitry uses a photodiode and a silicon photomultiplier and allows to monitor light pulse intensities and timing information in-situ to high precision. This is made possible via multiple gain channels within the sensor readouts which allows for both sensors to monitor complementary within the dynamic range of the emitted light intensities. The work conducted on the analog boards hosting flasher and sensor circuitry, digital boards hosting FPGAs and auxiliary components necessary for instrument control, and an interface board which connects to the IceCube Upgrade interface electronics, profitted significantly from the support of Michael Boehmer (TUM head of the electronics division) and Christian Spann-fellner (colleague within the research group). Via the interface board the instrument can be installed to virtually any large-volume telescope given that appropriate interface electronics are available for including the instrument to the telescope DAQ. Finally, the absolute hemispherical light yield is precisely calibrated in terms of configuration parameters as well as ambient temperature with a remaining systematic uncertainty of around 3.7 %. This is made possible via two calibration setups that were developed to calibrate the pulser properties in terms of relative intensity, spectrum and time profile as well as hemispherical emission profile. The absolute calibration of all these measurements is finally done using a NIST-calibrated photodiode and provides the absolute light yield per solid angle of each device as a function of configuration parameters of the pulsers as well as ambient temperature.

In summary, the presented device investigation and development provides exciting physical grounds for a precision calibration light source to improve the IceCube detector. The instrument hardware includes mechanical, electrical and optical aspects all of which were optimized in view of their IceCube application. In addition, streamlined assembly and calibration procedures are made possible by dedicated experimental setups which allow efficient production and precise calibration of all produced instruments. Here, a newly developed instrument shows increased dynamic range with respect to previous device iterations in intensity and spectral properties as well as fail-safe redundancy modifications and increased precision in the self-

monitoring sensors. The instrument production and calibration of all 30 devices for the Upgrade will be the main task for the coming months in view of planned instrument shipments to the South Pole.





```
1 import os
2 import sys
3
4 import time
5 import copy
6 import joblib
7 import pickle
8 import tables
9 import numpy as np
10 import importlib
11 import matplotlib.pyplot as plt
12
13 import tensorflow as tf
14 from tensorflow.python.client import device_lib
15 from sklearn.model_selection import train_test_split
16
17 import pandas as pd
18
19 #####
20 ## user input
21 #####
22 # get input directory
23 direc = sys.argv[1]
24 paramfile = os.path.join(direc, 'out_params.npy')
25
26 # training config
27 decay_steps = int(sys.argv[2]) # training depth decay
28 epochs = int(sys.argv[3]) # epochs per training instance
29 batch_size = int(sys.argv[4]) # batch size: bigger model --> smaller
30
31 # define outname for model
32 nn_outname = sys.argv[5] # model save name
33
34 # use re-binned data
35 rebin = True if sys.argv[6] == 'True' else False
36
37 # use fractional data
38 frac = True if sys.argv[7] == 'True' else False
39
40 # use specific number of bins
41 binlim = True if sys.argv[8] == 'True' else False
42 n_bins_inp = int(sys.argv[9]) if binlim else None
43
44 #####
45 ## read-in and setup data
46 #####
47 # whether rebinned data should be used
48 if rebin:
49     out_data = os.path.join(direc, 'out_df-data-sim-rebin.pkl')
50 elif frac:
51     out_data = os.path.join(direc, 'out_df-data-sim-frac.pkl')
52 else:
53     out_data = os.path.join(direc, 'out_df-data-sim.pkl')
54 # read input file
55 print('Loading data...')
56 df = joblib.load(out_data)
57 print('... done!\n')
58 print('Dataset size:', df.shape)
59
60 # read params/data/user/fhenningsen/deeppcore_data/binned_5d-nn-n-0-1500/nn_training/nn
61 # -training_cyc-10_ep-1000.tf.out
62 params = np.load(paramfile, allow_pickle=True, encoding='latin1').item()
63
64 # get number of bins
65 n_data = params['n_bins_new']
66 if rebin or frac:
67     n_data = n_data + len([df.columns.get_loc("x%i" %i) for i in range(5000) if "x%i"
68 %i in df.columns])
69 if binlim:
70     n_data = n_bins_inp
71
72 # inputs and outputs for the NN
73 t_columns = ['flasher_string', 'flasher_om', 'string', 'om', 'dist', 'zenith', 'abs',
74 'sca', 'domeff', 'p0', 'p1']
75 x_columns = df.columns[:n_data]
76 print('Training parameters: %s\n' %(t_columns))
77 print('Data bins: %s\n' %(n_data))
78
79 # generate train and test data
80 # remove buggy OMs (same string, same om, etc)
81 print('Applying DOM cuts...')
```

```

79 m1 = (df['valid'] == True) & (df['zenith'] > 0) & (df['zenith'] < np.pi) & (df['dist']
80 > 0)
81 m2 = (np.sum(df[x_columns], axis=1) > 0) && (np.sum(df[x_columns], axis=1) < 60e3) #
      qmin, qmax
82 m = m1 & m2
83 x = df.loc[m][x_columns].values
84 t = df.loc[m][t_columns].values
85 x_train, x_test, t_train, t_test = train_test_split(x, t, test_size=0.2, random_state
      =42)
86 print('... done!')
87 print('Masked dataset size:', df.loc[m].shape, '\n')
88 #####
89 ### setup NN
90 #####
91 print('Setting up training...')
92 # identify gpus
93 def get_available_gpus():
94     local_device_protos = device_lib.list_local_devices()
95     return [x.name for x in local_device_protos if x.device_type == 'GPU']
96 print('Devices found: %s' %(', '.join(get_available_gpus() ) ) )
97
98 # use multiple gpus
99 # checkout https://keras.io/guides/distributed_training/
100 strategy = tf.distribute.MirroredStrategy()
101 print('Number of devices in scope: {}'.format(strategy.num_replicas_in_sync))
102
103 # define net
104 # check: https://www.tensorflow.org/tutorials/keras/overfit_and_underfit?hl=zh-tw#
      add_weight_regularization
105 regularizer = None #tf.keras.regularizers.l2(0.001)
106 activation = 'relu'
107 with strategy.scope():
108     inputs = tf.keras.Input(shape=(t_train.shape[1],))
109
110     h = tf.keras.layers.Dense(64, activation=activation, kernel_regularizer=
      regularizer)(inputs)
111     h = tf.keras.layers.BatchNormalization()(h)
112
113     h = tf.keras.layers.Dense(128, activation=activation, kernel_regularizer=
      regularizer)(h)
114     h = tf.keras.layers.BatchNormalization()(h)
115
116     h = tf.keras.layers.Dense(256, activation=activation, kernel_regularizer=
      regularizer)(h)
117     h = tf.keras.layers.BatchNormalization()(h)
118
119     h = tf.keras.layers.Dense(512, activation=activation, kernel_regularizer=
      regularizer)(h)
120     h = tf.keras.layers.BatchNormalization()(h)
121
122     h = tf.keras.layers.Dense(256, activation=activation)(h)
123     h = tf.keras.layers.BatchNormalization()(h)
124
125     h = tf.keras.layers.Dense(128, activation=activation, kernel_regularizer=
      regularizer)(h)
126     h = tf.keras.layers.BatchNormalization()(h)
127
128     h = tf.keras.layers.Dense(64, activation=activation, kernel_regularizer=
      regularizer)(h)
129     h = tf.keras.layers.BatchNormalization()(h)
130
131     outputs = tf.keras.layers.Dense(x_train.shape[1], activation='softplus')(h)
132
133     model = tf.keras.Model(inputs=inputs, outputs=outputs)
134     print(model.summary())
135
136     initial_learning_rate = 1e-5
137
138     # piecewise constant
139     def step_decay(epoch):
140         drop = 0.5
141         epochs_drop = decay_steps
142         lrate = initial_learning_rate * np.power(drop, np.floor((1+epoch)/epochs_drop)
      )
143         return lrate
144     lr_schedule = tf.keras.callbacks.LearningRateScheduler(step_decay)
145
146     # early stopping
147     early_stop = tf.keras.callbacks.EarlyStopping(monitor='val_loss',
148                                                  mode='min',
149                                                  verbose=1,
150                                                  patience=min([100, decay_steps]))
151
152     # callbacks
153     callbacks = [lr_schedule, early_stop]
154
155     # optimizer
156     optimizer = tf.keras.optimizers.Adam()
157
158     # compile
159     model.compile(loss='poisson', optimizer=optimizer)
160     print('... done!\n')
161
162     #####
163     ### train
164     #####
165     print('Training...')
166     hist = model.fit(t_train, x_train,

```

```
167     epochs=epochs,
168     validation_data=(t_test, x_test),
169     batch_size=batch_size,
170     callbacks=callbacks,
171     verbose=1)
172 print('... done!\n')
173
174 #####
175 ## save
176 #####
177 print('Saving outputs...')
178 # save model
179 model.save(nn_outname)
180
181 # save history
182 assets_extra = '%s/assets.extra' %(nn_outname)
183 if not os.path.exists(assets_extra):
184     print('Creating output directory in {}'.format(assets_extra))
185     os.makedirs(assets_extra)
186 np.save('%s/history.npy' %(assets_extra), hist.history)
187 print('... done!\n')
```



# B

## MCMC implementation

```
1 # system
2 import gc
3 import os
4 import sys
5 import time
6 import copy
7 import importlib
8
9 # allow plot saving in detached screen
10 import matplotlib
11 matplotlib.use('Agg')
12
13 # usual
14 import joblib
15 import pickle
16 import tables
17 import numpy as np
18 import pandas as pd
19 import matplotlib.pyplot as plt
20 from scipy.optimize import minimize
21
22 # nn and mcmc
23 os.environ["CUDA_VISIBLE_DEVICES"]="0"
24 import emcee
25 import corner
26 import llh_main
27 import tensorflow as tf
28
29 #####
30 ### user parameters
31 #####
32 argv = sys.argv
33
34 # user inputs
35 direc = argv[1]
36 nn_dir = argv[2]
37 out_dir = argv[3]
38
39 # mcmc config
40 nwalkers = int(argv[4])
41 nburn = int(argv[5])
42 nrun = int(argv[6])
43 nthin = int(argv[7])
44
45 # run config
46 b_perdom_avg = True if argv[8] == 'True' else False
47 b_flasher = True if argv[9] == 'True' else False
48 b_flasher_gauss = True if argv[10] == 'True' else False
49
50 # optional bin limit
51 b_binlim = True if argv[11] == 'True' else False
52 n_bin = int(argv[12])
53
54 # identifier for files
55 ident = 'global-renorm-walk-%i_burn-%i_run-%i_thin-%i_seed-truth_usingflasher-%s' %(
56     nwalkers, nburn, nrun, nthin, b_flasher)
57
58 # charge cut [photons/bin]
59 q_min = 10
60 q_max = 2000
61
62 #####
63 ### read-in model and truth
64 #####
65 # input files
66 print('Loading data ...')
67 params = np.load(os.path.join(direc, 'out_params.npy'), allow_pickle=True,
68     encoding='latin1').item()
69 data_f = joblib.load(os.path.join(direc, 'out_df-data-sim.pkl'))
70 if b_flasher:
71     truth_f = joblib.load(os.path.join(direc, 'out_df-data-flasher.pkl'))
72     print('\t-- using experimental flasher data')
73 else:
74     truth_f = joblib.load(os.path.join(direc, 'out_df-truth.pkl'))
75     print('\t-- using simulated data')
76 print('done.\n')
77
78 # get meta
79 print('Initializing parameters...')
80 grid = params['grid']
81 flashers = params['flashers']
82 stringoms = params['oms']
```

```

81 zeniths = params['zenith']
82 distances = params['distance']
83 n_data = params['n_bins_new']
84 n_flasher = len(flashers)
85 n_oms = len(stringoms)
86 n_grid = len(grid)
87
88 # take care of optional bin limitations
89 n_data_actual = len([data_f.columns.get_loc("x%i" %i) for i in range(5000) if "x%i" %i
90 in data_f.columns])
91 if n_data != n_data_actual:
92     print('Found mismatch in bin shapes!')
93     if n_data > n_data_actual:
94         n_data = n_data_actual
95 if b_binlim:
96     if n_data > n_bin:
97         n_data = n_bin
98 # get truth
99 truth_bins = truth_f.values[:, :n_data]
100 truth_vals = [params['truth_%s' %i] for i in ['abs', 'sca', 'p0', 'p1']]
101 truth_vals_poc = truth_vals
102
103 # define pocam intensity uncertainty
104 delta_pocam = 0.041
105
106 # access data files
107 data_columns = ['x%i' %i for i in range(n_data)]
108 grid_columns = ['abs', 'sca', 'p0', 'p1']
109
110 # print status
111 print('\t-- parameter keys:', [i for i in params.keys()], '\n')
112 print('\t-- truth shape:', truth_f.shape)
113 print('\t-- truth nn input values (pocam):', [i for i in truth_vals_poc])
114 print('\t-- truth bins shape:', truth_bins.shape)
115 print('\t-- data bins used:', n_data)
116
117 print('\t-- POCAM error: %.2f %%\n' %(delta_pocam*100))
118 print('done.\n')
119
120 #####
121 ### prepare nn input grid
122 #####
123 print('Preparing NN input grid...')
124 # model dimensions
125 ndim = 5 # abs, sca, domeff, p0, p1
126
127 # vectorize
128 flashes_i = np.zeros(( n_flasher, 2 ))
129 flashes = np.zeros(( n_oms * n_flasher, 3 ))
130 scales = np.ones(( n_oms * n_flasher, n_data ))
131 geo = np.zeros(( n_oms * n_flasher, 4 ))
132 nn_in = np.zeros(( n_oms * n_flasher, ndim + 6 )) # 6 from [ps, po, s, o, dist, zen
133 ]
134
135 cntnr = 0
136 for pi, p in enumerate(flashers):
137     poc = p
138     # get key
139     ps, po = [int(i) for i in poc.split('-')]
140     # put to array
141     flashes_i[pi] = [ps, po]
142     for so in stringoms:
143         # get key
144         s, o = [int(i) for i in so.split('-')]
145         key = '%s-%s-%s' %(poc, s, o)
146         # put to array
147         flashes[cntnr] = [pi, ps, po]
148         geo[cntnr] = [ps, po, s, o]
149         # increment
150         cntnr += 1
151
152 # put together
153 base = np.hstack([geo, np.expand_dims(distances, axis=1), np.expand_dims(zeniths, axis
154 =1)])
155
156 # fill into input grid
157 nn_in[:, :6] = base
158
159 print('done.\n')
160 #####
161 ### prepare nn
162 #####
163 print('Loading NN...')
164 nn = tf.keras.models.load_model(nn_dir)
165 print('done.\n')
166
167 #####
168 ### prepare mcmc likelihoods
169 #####
170 print('Preparing likelihoods...')
171 # parameter limits
172 b_abso_0, b_abso_1 = 0.80, 1.20
173 b_sca_0, b_sca_1 = 0.80, 1.20
174 b_p0_0, b_p0_1 = -0.80, 0.80
175 b_p1_0, b_p1_1 = -0.20, 0.20
176
177 # parameter priors

```

```

177 def flat_prior(d, a, b):
178     if (a < d < b):
179         return 0
180     else:
181         return -np.inf
182
183 def gaussian_prior(d, mu, sigma):
184     return ((d - mu)/sigma)**2
185
186 # global POCAM prior
187 def log_prior_global(theta):
188     # initial prior
189     lp = 0.
190     # get mcmc state vector
191     abso, sca, p0, p1 = theta
192     # first evaluate uniform priors
193     b_abso = (b_abso_0 <= abso <= b_abso_1)
194     b_sca = (b_sca_0 <= sca <= b_sca_1)
195     b_p0 = (b_p0_0 <= p0 <= b_p0_1)
196     b_p1 = (b_p1_0 <= p1 <= b_p1_1)
197     if not (b_abso and b_sca and b_p0 and b_p1):
198         return -np.inf
199     else:
200         return lp
201
202 # global llh with modified domeff/scale usage
203 def log_llh_global(theta):
204     # get prior
205     lp = log_prior_global(theta)
206     if not np.isfinite(lp):
207         return -np.inf
208     # put mcmc point to nn input vector
209     _abs, _sca, _p0, _p1 = theta
210     nn_in[:,6+0] = _abs
211     nn_in[:,6+1] = _sca
212     nn_in[:,6+2] = 1.0
213     nn_in[:,6+3] = _p0
214     nn_in[:,6+4] = _p1
215     # prepare llh
216     llh_total = 0
217     for i in range(n_flasher):
218         # get flasher
219         fs, fo = flashes_i[i]
220         # get selection
221         m_flgsh = (flashes[:,1] == fs) & (flashes[:,2] == fo) & (nn_in[:,2] != fs)
222         # get data
223         data = copy.deepcopy(truth_bins[m_flgsh])
224         # get nn prediction
225         model = nn.predict(nn_in[m_flgsh])
226         # mask invalid entries
227         q_min = 10
228         q_max = 2000
229         m1 = (data >= q_min) #& (model >= q_min)
230         m2 = (data <= q_max) #& (model <= q_min)
231         m = m1 & m2
232         data[~m] = np.nan
233         model[~m] = np.nan
234         # remove model zeros to avoid divergence
235         model += 1e-8
236         # renormalize total charge
237         weight = np.nansum(data) / np.nansum(model)
238         model = model * weight
239         #print('%i, %.2f, %.2f, %.2f' % (i, weight, np.nanmin(model), np.nanmin(data)))
240         # calculate llh
241         llh_i = llh_main.llh(model, data,
242                             scale_pocam=1.0,
243                             chi2modpen=False,
244                             logpoiss=False,
245                             )
246         llh_sum = np.nansum(llh_i)
247         llh_total += llh_sum
248     # return
249     return lp + 0.5 * llh_total
250
251 initial = [1,1,0,0]
252 initial2 = [0.8,1,0,0]
253 initial3 = [1,1,-0.27,-0.042]
254 log_llh = log_llh_global
255
256 llh_test = log_llh(initial)
257 print('\t-- LLH test ([1,1,0,0]): %.3e' % llh_test)
258
259 llh_test = log_llh(initial2)
260 print('\t-- LLH test ([0.8,1,0,0]): %.3e' % llh_test)
261
262 llh_test = log_llh(initial3)
263 print('\t-- LLH test ([1,1,-0.27,-0.042]): %.3e' % llh_test)
264
265 llh_truth = log_llh(truth_vals_poc)
266 print('\t-- LLH test (%s): %.3e\n' % (truth_vals_poc, llh_truth))
267 print('done.\n')
268
269 #####
270 ### mcmc seeding
271 #####
272 # select starting point
273 print('Setting MCMC seed...')
274 p0_abs = np.random.uniform(b_abso_0, b_abso_1, size=(nwalkers, 1))
275 p0_sca = np.random.uniform(b_sca_0, b_sca_1, size=(nwalkers, 1))

```

```

276 p0_p0 = np.random.uniform(b_p0_0, b_p0_1, size=(nwalkers, 1))
277 p0_p1 = np.random.uniform(b_p1_0, b_p1_1, size=(nwalkers, 1))
278 p0 = np.hstack([p0_abs, p0_sca, p0_p0, p0_p1])
279 print(p0.shape)
280 for i in range(nwalkers):
281     print('\t-- seed: %s' %(np.round(p0[i], 2)))
282     print('\t-- updated LLH test (seed %i): %.3f\n' %(i, log_llh(p0[i])))
283 print('done.\n')
284
285 #####
286 ### mcmc global
287 #####
288 print('Running MCMC...')
289 print('\t-- config (burn, run, thin): %i, %i, %i' %(nburn, nrun, nthin))
290 # run burn-in
291 sampler = emcee.EnsembleSampler(nwalkers, p0.shape[1], log_llh)
292 state = sampler.run_mcmc(p0, nburn, progress=True)
293
294 # reset sampler
295 sampler.reset()
296
297 # run production mcmc
298 sampler.run_mcmc(state, nrun, progress=True)
299 print('done.\n')
300
301 #####
302 ### save output
303 #####
304 print('Saving outputs...')
305 # store samples
306 samples = sampler.get_chain(discard=nburn, thin=nthin, flat=False)
307 np.save(os.path.join(out_dir, 'mcmc-samples_%s.npy' %(ident)), samples)
308 flat_samples = sampler.get_chain(discard=nburn, thin=nthin, flat=True)
309 np.save(os.path.join(out_dir, 'mcmc-samples_%s-flat.npy' %(ident)), flat_samples)
310
311 #####
312 ### save plots
313 #####
314 # walker chains
315 fig, axes = plt.subplots(ndim-1, figsize=(10, 7), sharex=True)
316 labels = ['a', 'b', 'p0', 'p1']
317 for i in range(ndim-1):
318     ax = axes[i]
319     ax.plot(samples[:, :, i], "k", alpha=0.3)
320     ax.set_xlim(0, len(samples))
321     ax.set_ylabel(labels[i])
322     ax.yaxis.set_label_coords(-0.1, 0.5)
323 axes[-1].set_xlabel("step number")
324 fig.savefig(os.path.join(out_dir, 'walker-chains_%s.pdf' %(ident)))
325
326 # corner plot
327 fig = corner.corner(flat_samples, labels=labels, truths=truth_vals_updated,
328                   quantiles=[0.16, 0.5, 0.84], show_titles=True)
329 fig.savefig(os.path.join(out_dir, 'corner_%s.pdf' %(ident)))
330 print('done.')

```

# C

## Schematics

### C.1 Dual-Kapustinsky driver

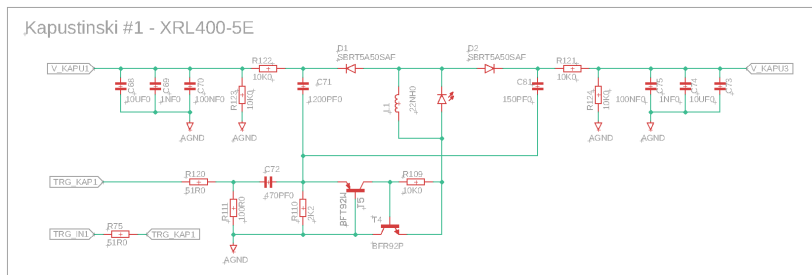


Figure C.1: Dual-Kapustinsky driver schematics.



### C.3 Photodiode readout

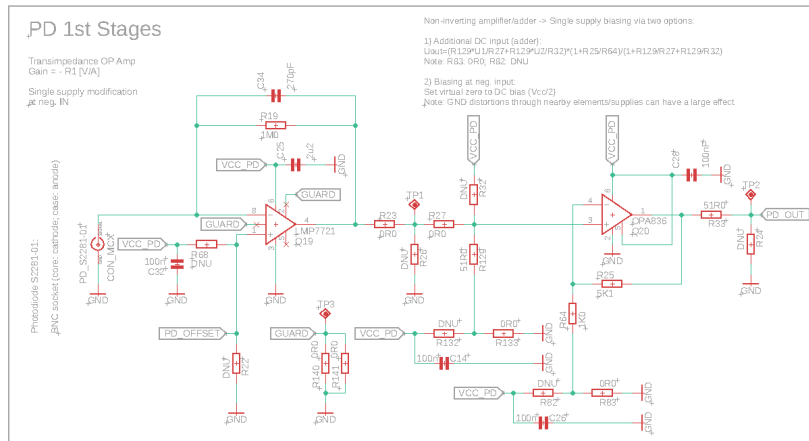


Figure C.3: Photodiode readout schematics, first stage.

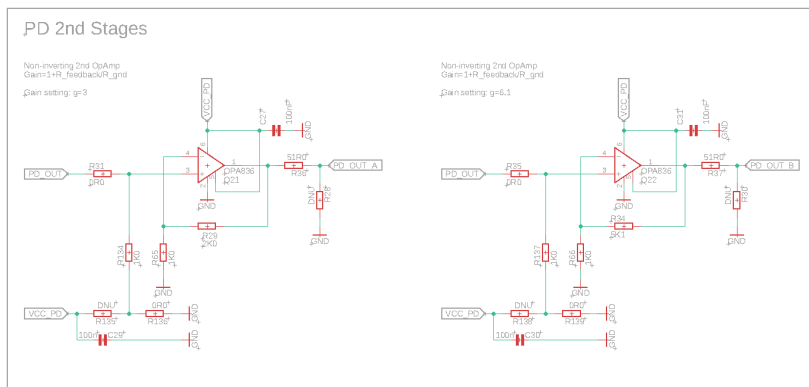
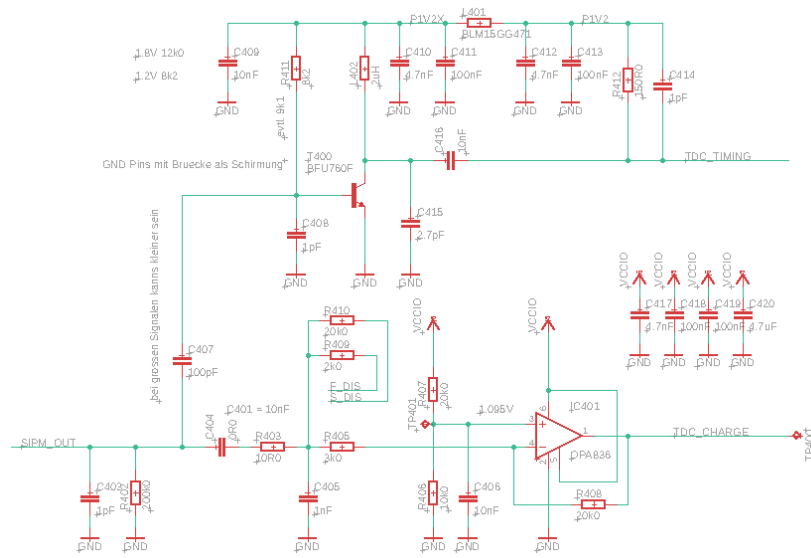


Figure C.4: Photodiode readout schematics, second stage.

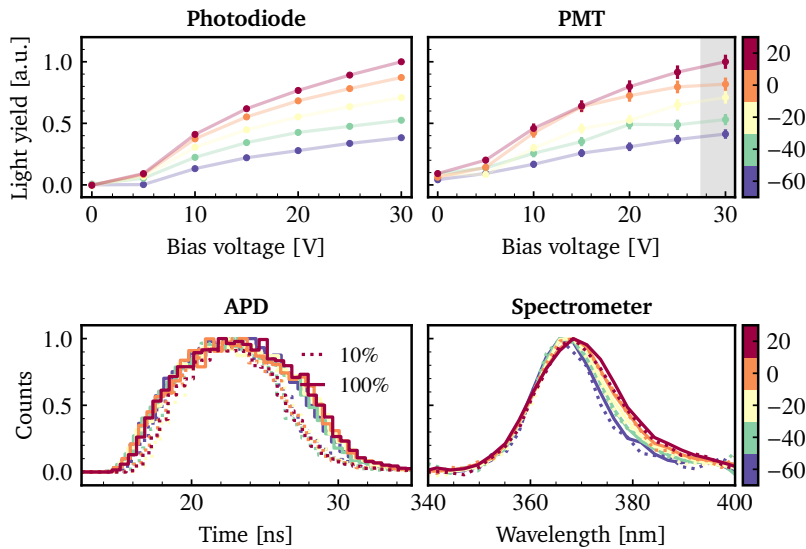
## C.4 Silicon photomultiplier readout

Figure C.5: SiPM readout schematics.



# D

## LED measurements



**Figure D.1:** Summary plot of the LD-type 365 nm emitter selected for the POCAM in the IceCube Upgrade. The figure shows the intensity variation as measured by the photodiode (top left) as well as the PMT (top right), the time profile variation as measured by the APD (bottom left) and the spectrum variation as measured by the spectrometer (bottom right) as a function of temperature and bias voltage. Both the spectrum and the time profile are given for around 10% (dotted) and 100% (solid) intensity, respectively. The grey band in the PMT plot shows a region of expected non-linearity of the sensor.

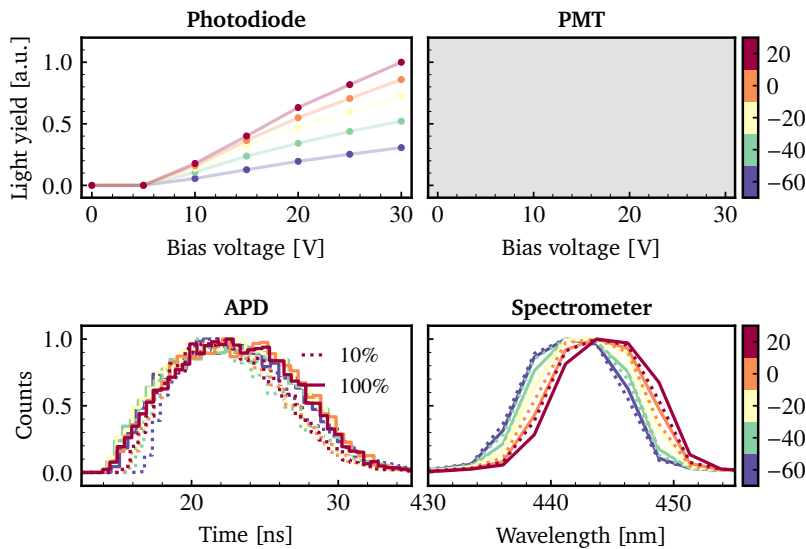
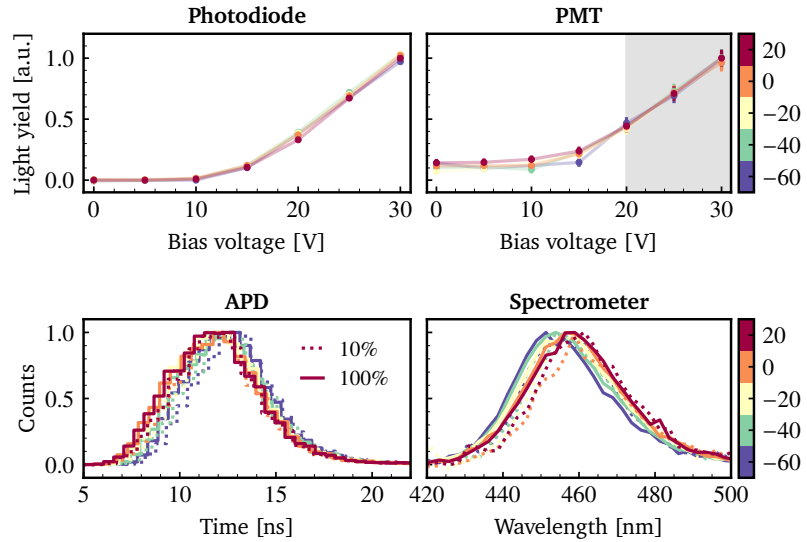
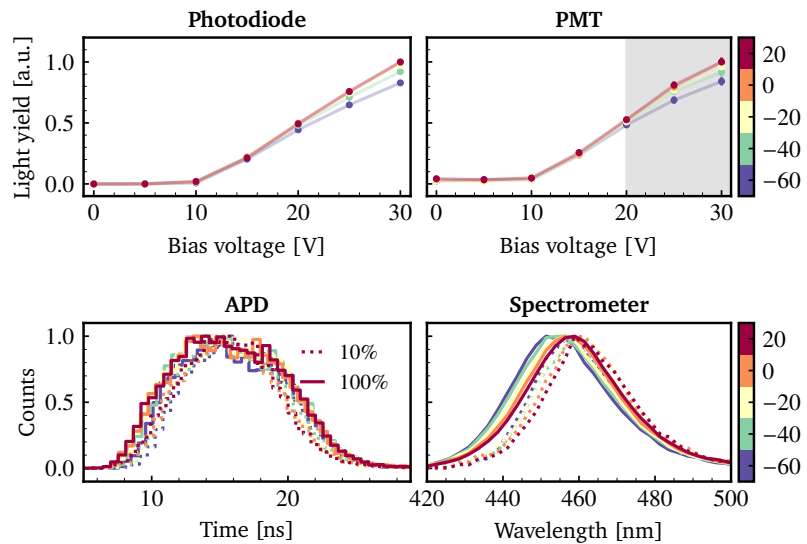


**Figure D.2:** Summary plot of the LD-type 450 nm emitter selected for the POCAM in the IceCube Upgrade. The figure shows the intensity variation as measured by the photodiode (top left) as well as the PMT (top right), the time profile variation as measured by the APD (bottom left) and the spectrum variation as measured by the spectrometer (bottom right) as a function of temperature and bias voltage. Both the spectrum and the time profile are given for around 10% (dotted) and 100% (solid) intensity, respectively. The grey band in the PMT plot shows a region of expected non-linearity of the sensor.

**Figure D.3:** Summary plot of the Kapustinsky 465 nm emitter selected for the POCAM in the IceCube Upgrade. The figure shows pulser behavior for the fast (a) and the default (b) Kapustinsky configuration via the photodiode (top left) as well as the PMT (top right), the time profile variation as measured by the APD (bottom left) and the spectrum variation as measured by the spectrometer (bottom right) as a function of temperature and bias voltage. Both the spectrum and the time profile are given for around 10% (dotted) and 100% (solid) intensity, respectively. The grey band in the PMT plot shows a region of expected non-linearity of the sensor.

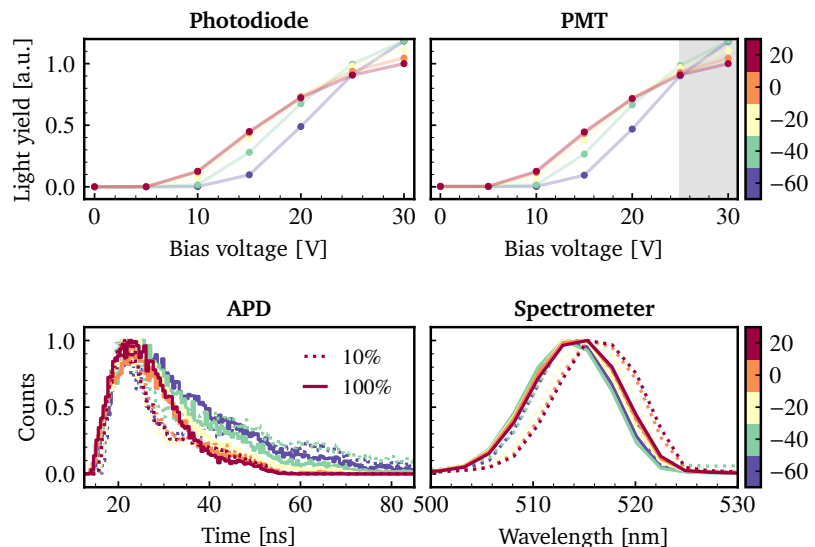


(a) Pulser performance of the fast Kapustinsky driver for the selected 465 nm emitter.



(b) Pulser performance of the default Kapustinsky driver for the selected 465 nm emitter.

**Figure D.4:** Summary plot of the LD-type 520 nm emitter selected for the POCAM in the IceCube Upgrade. The figure shows the intensity variation as measured by the photodiode (top left) as well as the PMT (top right), the time profile variation as measured by the APD (bottom left) and the spectrum variation as measured by the spectrometer (bottom right) as a function of temperature and bias voltage. Both the spectrum and the time profile are given for around 10% (dotted) and 100% (solid) intensity, respectively. The grey band in the PMT plot shows a region of expected non-linearity of the sensor.



## List of Figures

---

2.1	Multi-messenger astronomy . . . . .	3
2.2	Cosmic ray spectrum and distinct features . . . . .	5
2.3	Hillas plot showing high-energy cosmic accelerator conditions and resulting maximum particle energies. . . . .	6
2.4	Illustration of an air shower induced by a primary cosmic ray . . . . .	7
2.5	Neutrino flux models of various astrophysical origins as a function of energy including selected high-energy experimental results. . . . .	8
2.6	Flavor ratio measurement for high-energy astrophysical neutrinos by IceCube including different source models . . . . .	10
3.1	Neutrino mass ordering and flavor content . . . . .	15
3.2	Neutrino oscillations on astronomical distance scales. . . . .	18
4.2	Muon energy loss contributions. . . . .	20
4.1	High-energy neutrino cross sections. . . . .	20
4.3	Illustration of the Cherenkov effect. . . . .	21
4.4	IceCube detector layout . . . . .	22
4.5	Kinematic angle (left axis) and transferred energy (right axis) of a secondary muon produced in a charged-current interaction as a function of incident neutrino energy. . . . .	23
4.6	Example IceCube neutrino detector signatures. . . . .	23
4.7	Example cascade-like and track-like neutrino signatures in water and ice. . . . .	25
4.8	Illustration of the IceCube LED calibration system. . . . .	26
5.1	IceCube detector . . . . .	29
5.2	Sweden Camera pictures of the drill hole refreezing process. . . . .	31
5.3	IceCube bulk ice optical properties as a function of depth. . . . .	31
5.4	IceCube angular acceptance models. . . . .	32
5.5	IceCube geometry calibration used flasher LEDs. . . . .	33
5.6	IceCube Upgrade photosensors. . . . .	34
5.7	IceCube Upgrade layout overview. . . . .	34
5.8	Experimental sensitivities on tau normalization $n_\tau$ , mixing angle $\theta_{23}$ as well as the mass difference $\Delta m_{32}^2$ . . . . .	35
5.9	IceCube-Gen2 array extensions. . . . .	36
6.1	POCAM instrument timeline. . . . .	37
6.2	Example mean POCAM light signals observed at different detection modules within a GVD cluster. . . . .	38
6.3	Flow chart of a photon life cycle simulated with PPC. . . . .	39

6.4	Example PPC simulation output of an isotropic light source within the IceCube volume. . . . .	40
6.5	IceCube Upgrade baseline layout. . . . .	41
6.6	Systematic parameter effects on DOM response histograms. . . . .	43
6.7	Schematic view of a fully-connected deep neural network. . . . .	44
6.8	Comparison of NumPy.random and the $R_n$ sequence of quasi-random numbers in two dimensions. . . . .	47
6.9	Five-dimensional systematic parameter sampling using the quasi-random sequence $R_n$ . . . . .	48
6.10	Loss and learning rate for an example network training process. . . . .	49
6.11	Example neural net DOM response histogram predictions. . . . .	50
6.12	Systematic parameter scaling as predicted using a trained neural network. . . . .	51
6.13	Comparison of detector signal for a simulated event of the flasher dataset and the corresponding neural net prediction. . . . .	52
6.14	Pseudo-data fit results . . . . .	55
6.15	Systematic parameter fit results of the experimental flasher dataset. . . . .	56
6.16	Systematic parameter fit results of the POCAM dataset. . . . .	57
6.19	Direct hole ice simulation setup. . . . .	58
6.17	Low-energy sensitivities depending on different systematic prior assumptions. . . . .	58
6.18	POCAM GEANT4 emission simulation. . . . .	59
6.20	Direct hole ice parameter fit using pseudo-data. . . . .	59
6.21	Rising edges of calibration light pulses in water. . . . .	60
6.22	Water geometry calibration study using POCAMs. . . . .	62
7.1	POCAMv1 during installation at the GVD telescope. . . . .	63
7.2	POCAMv2 installed at one of the STRAW strings. . . . .	63
7.3	POCAM instrument design in full view. . . . .	63
7.4	POCAM flange layout. . . . .	64
7.5	POCAM angular calibration setup. . . . .	66
7.6	POCAM rotation calibration setup. . . . .	66
7.7	Singular and virtual total POCAM emission profile. . . . .	67
7.8	Mean polar emission profile of a POCAM hemisphere and calibration data. . . . .	68
7.9	POCAM light pulse characterization setup. . . . .	68
7.11	Fiber termination concept for the freezer of the pulser characterization setup. . . . .	68
7.12	Fiber termination in the freezer of the pulser characterization setup. . . . .	68
7.10	POCAM light pulse calibration setup. . . . .	69
7.13	Example light yield calibration. . . . .	69
7.14	Example time profile calibration. . . . .	70
7.15	Example spectrum calibration. . . . .	71
7.16	POCAM orientation calibration setup concept. . . . .	71
7.17	POCAM housing with one attached flange. . . . .	72

7.18	POCAM flange design and optical component fitting. . . . .	72
7.19	POCAM diffusing sphere design. . . . .	73
7.20	Conventional and optical teflon emission profile comparison for the POCAM diffusing sphere. . . . .	74
7.21	POCAM aperture disk, diffusing sphere and sensors in CAD view. . . . .	74
7.22	Simulated aperture disk reflectivity effect. . . . .	74
7.23	POCAM housing after being taken out of the freezer at $-80^{\circ}\text{C}$ . . . . .	75
7.24	POCAM housing during temperature test. . . . .	75
7.25	POCAM housing after Nautilus pressure test. . . . .	75
7.26	Kapustinsky pulse driver schematic. . . . .	77
7.27	Dual-Kapustinsky configuration for one POCAM emitter. . . . .	77
7.28	LD-type pulse driver schematic. . . . .	78
7.29	Dual-discharge LD-type pulse driver schematic. . . . .	79
7.30	Example intensity scaling and time profile pulse shapes from all used driver circuits for the nominal 405 nm LED. . . . .	79
7.32	POCAM emitter matrix. . . . .	80
7.31	POCAM emitter and pulse driver layout. . . . .	80
7.33	Example emitter selection process. . . . .	80
7.34	Summary plot of the Kapustinsky 405 nm emitter selected for the POCAM in the IceCube Upgrade. . . . .	82
7.35	Summary plot of the LD-type 405 nm emitter selected for the POCAM in the IceCube Upgrade. . . . .	83
7.36	Hamamatsu S2281-01 photodiode. . . . .	84
7.37	Schematical view of the photodiode readout chain. . . . .	84
7.40	Ketek SiPM PM3315-WB. . . . .	85
7.38	Example photodiode readout output pulses. . . . .	85
7.39	Photodiode readout output pulses for all emitters. . . . .	85
7.41	Simplified SiPM readout schematic. . . . .	86
7.42	Example SiPM readout output pulses. . . . .	86
7.43	Dynamic range coverage of both self-monitoring sensors. . . . .	87
7.44	Flowchart of the digital board functionality and components. . . . .	88
7.45	POCAM analog and digital board in top and bottom view. . . . .	89
7.46	Flowchart of the interface board functionality and components. . . . .	90
7.47	POCAM interface board in top and bottom view. . . . .	90
7.48	IceCube interface board stack in top and side view. . . . .	91
7.49	Fully-assembled POCAM stack including analog and digital board stack for one hemisphere as well as internal and IceCube interface boards. . . . .	92
7.50	POCAM electronic stack testing. . . . .	95
7.51	POCAM flange installed to the rotation stages in the emission profile characterization setup. . . . .	96
7.52	POCAM stack assembly with the major stack attached to the flange. . . . .	97
7.53	POCAM instrument prior to sealing and final assembly in the glovebox. . . . .	98
C.1	Dual-Kapustinsky driver schematics. . . . .	111

C.2	LD-type driver schematics. . . . .	112
C.3	Photodiode readout schematics, first stage. . . . .	113
C.4	Photodiode readout schematics, second stage. . . . .	113
C.5	SiPM readout schematics. . . . .	114
D.1	Summary plot of the LD-type 365 nm emitter selected for the POCAM in the IceCube Upgrade. . . . .	115
D.2	Summary plot of the LD-type 450 nm emitter selected for the POCAM in the IceCube Upgrade. . . . .	115
D.3	Summary plot of the Kapustinsky 465 nm emitter se- lected for the POCAM in the IceCube Upgrade. . . . .	116
D.4	Summary plot of the LD-type 520 nm emitter selected for the POCAM in the IceCube Upgrade. . . . .	116

## List of Tables

---

3.1	Current knowledge of neutrino mixing parameters. . .	15
4.1	Summary of scattering and absorption lengths at various neutrino telescope sites. . . . .	25
6.1	POCAM positions and depths within the physics volume.	42
6.2	Systematic parameter ranges in the POCAM simulation study. . . . .	42
6.3	Neural network architecture for predicting DOM response histograms. . . . .	46
6.4	Dataset generation properties for neural net training. .	48
6.5	Systematic parameter fit results of the flasher pseudo-data. . . . .	55
6.6	Systematic parameter fit results of the flasher dataset.	56
6.7	Systematic parameter fit results of the POCAM pseudo-data. . . . .	57
7.1	POCAM emitter selection. . . . .	81
7.2	POCAM calibration measurement granularity. . . . .	93
7.3	POCAM calibration setup systematics. . . . .	93



## Bibliography

---

- [1] The IceCube Collaboration. “Neutrino emission from the direction of the blazar TXS 0506+056 prior to the IceCube-170922A alert”. In: *Science* 361.6398 (2018). Ed. by M. Aartsen et al., pp. 147–151. URL: <http://science.sciencemag.org/content/361/6398/147>.
- [2] The IceCube Collaboration. “Multimessenger observations of a flaring blazar coincident with high-energy neutrino IceCube-170922A”. In: *Science* 361.6398 (2018). Ed. by M. Aartsen et al. URL: <http://science.sciencemag.org/content/361/6398/eaat1378>.
- [3] M. G. Aartsen et al. “Evidence for High-Energy Extraterrestrial Neutrinos at the IceCube Detector”. In: *Science* 342 (2013), p. 1242856.
- [4] A. Aab et al. “Combined fit of spectrum and composition data as measured by the Pierre Auger Observatory”. In: *Journal of Cosmology and Astroparticle Physics* 2017.04 (Apr. 2017), pp. 038–038. URL: <https://doi.org/10.1088/1475-7516/2017/04/038>.
- [5] P Sommers et al. “Cosmic ray astronomy”. In: *New Journal of Physics* 11.5 (May 2009), p. 055004. URL: <http://dx.doi.org/10.1088/1367-2630/11/5/055004>.
- [6] Luis A. Anchordoqui et al. “Cosmic neutrino pevatrons: A brand new pathway to astronomy, astrophysics, and particle physics”. In: *Journal of High Energy Astrophysics* 1-2 (2014), pp. 1–30. URL: <https://www.sciencedirect.com/science/article/pii/S2214404814000020>.
- [7] Sandip Pakvasa. “Neutrino Flavor Goniometry by High Energy Astrophysical Beams”. In: *Modern Physics Letters A* 23.17n20 (June 2008), pp. 1313–1324. URL: <http://dx.doi.org/10.1142/S0217732308027680>.
- [8] Luis A. Anchordoqui et al. “Neutrinos as a diagnostic of high energy astrophysical processes”. In: *Physics Letters B* 621.1-2 (Aug. 2005), pp. 18–21. URL: <http://dx.doi.org/10.1016/j.physletb.2005.06.056>.
- [9] B. P. Abbott et al. “GW170817: Observation of Gravitational Waves from a Binary Neutron Star Inspiral”. In: *Phys. Rev. Lett.* 119.16 (2017), p. 161101.
- [10] Victor Hess. “Über Beobachtungen der durchdringenden Strahlung bei sieben Freiballonfahrten”. In: *Phys. Z.* 13 (1912), pp. 1084–1091.
- [11] A A Watson. “High-energy cosmic rays and the Greisen-Zatsepin-Kuz’min effect”. In: *Rept. Prog. Phys.* 77 (2014), p. 036901.

- [12] Gaisser, T., Engel, R. and Resconi, E. *Cosmic Rays and Particle Physics*. 2nd ed. Cambridge University Press, 2016.
- [13] Felix Henningsen. “Optical Characterization of the Deep Pacific Ocean: Development of an Optical Sensor Array for a Future Neutrino Telescope”. MA thesis. Munich, Tech. U., July 2019.
- [14] M. Spurio. *Particles and Astrophysics: A Multi-Messenger Approach*. Astronomy and Astrophysics Library. Springer International Publishing, 2017. URL: <https://books.google.de/books?id=u8rgAQAACAAJ>.
- [15] A. M. Hillas. “The Origin of Ultra-High-Energy Cosmic Rays”. In: *Annual Review of Astronomy and Astrophysics* 22.1 (1984), pp. 425–444. URL: <https://doi.org/10.1146/annurev.aa.22.090184.002233>.
- [16] Kenneth Greisen. “End to the Cosmic-Ray Spectrum?” In: *Phys. Rev. Lett.* 16 (17 Apr. 1966), pp. 748–750. URL: <https://link.aps.org/doi/10.1103/PhysRevLett.16.748>.
- [17] G. T. Zatsepin et al. “Upper limit of the spectrum of cosmic rays”. In: *JETP Lett.* 4 (1966), pp. 78–80.
- [18] A. M. Hillas. “The Effect of Intergalactic Propagation on the Energy Spectrum of Cosmic Ray Nuclei Above  $10^{15}$ -eV”. In: *14th International Cosmic Ray Conference*. 1975, pp. 717–722.
- [19] V. S. Berezinsky et al. “Metagalactic Nuclei of Ultrahigh-Energies”. In: *14th International Cosmic Ray Conference*. 1975, pp. 711–716.
- [20] Matthias Huber. “Multi-Messenger correlation study of Fermi-LAT blazars and high-energy neutrinos observed in IceCube”. PhD thesis. Munich, Tech. U., 2020.
- [21] A M Galper et al. “The PAMELA experiment: a decade of Cosmic Ray Physics in space”. In: *Journal of Physics: Conference Series* 798 (Jan. 2017), p. 012033. URL: <https://doi.org/10.1088/1742-6596/798/1/012033>.
- [22] Tokonatsu Yamamoto. “The first scientific results from the pierre auger observatory”. In: *AIP Conf. Proc.* 842.1 (2006). Ed. by Peter D. Barnes et al., pp. 1016–1018.
- [23] Kai Martens. “The Telescope Array and its Low Energy Extension”. In: *Nuclear Physics B - Proceedings Supplements* 165 (2007). Proceedings of the Cosmic Ray International Seminars, pp. 33–36. URL: <https://www.sciencedirect.com/science/article/pii/S0920563206008395>.
- [24] A. Fedynitch et al. “Calculation of conventional and prompt lepton fluxes at very high energy”. In: *EPJ Web Conf.* 99 (2015), p. 08001.
- [25] Thomas K. Gaisser. “Atmospheric Neutrinos”. In: (Oct. 2019).
- [26] Thomas K. Gaisser. “Spectrum of cosmic-ray nucleons, kaon production, and the atmospheric muon charge ratio”. In: *Astropart. Phys.* 35 (2012), pp. 801–806.

- [27] K. Daum et al. “Determination of the atmospheric neutrino spectra with the Fréjus detector”. In: *Zeitschrift für Physik C Particles and Fields* 66.3 (Sept. 1995), pp. 417–428. URL: <https://doi.org/10.1007/BF01556368>.
- [28] The ANTARES Collaboration et al. “Measurement of the atmospheric  $\nu_\mu$  energy spectrum from 100 GeV to 200 TeV with the ANTARES telescope”. In: 73 (Aug. 2013).
- [29] M. G. Aartsen et al. “Development of a General Analysis and Unfolding Scheme and its Application to Measure the Energy Spectrum of Atmospheric Neutrinos with IceCube”. In: *Eur. Phys. J. C* 75.3 (2015), p. 116.
- [30] A Faessler et al. “Search for the Cosmic Neutrino Background”. In: *Journal of Physics: Conference Series* 580 (Feb. 2015), p. 012040. URL: <https://doi.org/10.1088/1742-6596/580/1/012040>.
- [31] Brent Follin et al. “First Detection of the Acoustic Oscillation Phase Shift Expected from the Cosmic Neutrino Background”. In: *Physical Review Letters* 115.9 (Aug. 2015). URL: <http://dx.doi.org/10.1103/PhysRevLett.115.091301>.
- [32] C. Giunti et al. *Fundamentals of Neutrino Physics and Astrophysics*. Oxford University Press, UK, 2007.
- [33] Q. R. Ahmad et al. “Measurement of the rate of  $\nu_e + d \rightarrow p + p + e^-$  interactions produced by  $^8\text{B}$  solar neutrinos at the Sudbury Neutrino Observatory”. In: *Phys. Rev. Lett.* 87 (2001), p. 071301.
- [34] Edoardo Vitagliano et al. “Grand unified neutrino spectrum at Earth: Sources and spectral components”. In: *Reviews of Modern Physics* 92.4 (Dec. 2020). URL: <http://dx.doi.org/10.1103/RevModPhys.92.045006>.
- [35] Edoardo Vitagliano et al. *Solar neutrinos at keV energies: thermal flux*. 2017.
- [36] H. Th. Janka. “Neutrino Emission from Supernovae”. In: (2017).
- [37] Bernhard Müller. “Hydrodynamics of core-collapse supernovae and their progenitors”. In: *Living Reviews in Computational Astrophysics* 6.1 (June 2020). URL: <http://dx.doi.org/10.1007/s41115-020-0008-5>.
- [38] Irene Tamborra et al. “High-resolution supernova neutrino spectra represented by a simple fit”. In: *Phys. Rev. D* 86 (2012), p. 125031.
- [39] R. M. Bionta et al. “Observation of a neutrino burst in coincidence with supernova 1987A in the Large Magellanic Cloud”. In: *Phys. Rev. Lett.* 58 (14 Apr. 1987), pp. 1494–1496. URL: <https://link.aps.org/doi/10.1103/PhysRevLett.58.1494>.
- [40] E. N. Alekseev et al. “Possible Detection of a Neutrino Signal on 23 February 1987 at the Baksan Underground Scintillation Telescope of the Institute of Nuclear Research”. In: *JETP Lett.* 45 (1987). Ed. by J. Tran Thanh Van, pp. 589–592.

- [41] K. Hirata et al. “Observation of a Neutrino Burst from the Supernova SN 1987a”. In: *Phys. Rev. Lett.* 58 (1987). Ed. by K. C. Wali, pp. 1490–1493.
- [42] Daniel Kresse et al. *Stellar Collapse Diversity and the Diffuse Supernova Neutrino Background*. 2020.
- [43] John G Learned et al. “Detecting  $\nu_\tau$  oscillations at PeV energies”. In: *Astroparticle Physics* 3.3 (May 1995), pp. 267–274. URL: [http://dx.doi.org/10.1016/0927-6505\(94\)00043-3](http://dx.doi.org/10.1016/0927-6505(94)00043-3).
- [44] Tamar Kashti et al. “Astrophysical Neutrinos: Flavor Ratios Depend on Energy”. In: *Physical Review Letters* 95.18 (Oct. 2005). URL: <http://dx.doi.org/10.1103/PhysRevLett.95.181101>.
- [45] Andrea Palladino. “The flavor composition of astrophysical neutrinos after 8 years of IceCube: an indication of neutron decay scenario?” In: *The European Physical Journal C* 79.6 (June 2019). URL: <http://dx.doi.org/10.1140/epjc/s10052-019-7018-7>.
- [46] M. G. Aartsen et al. “Measurements using the inelasticity distribution of multi-TeV neutrino interactions in IceCube”. In: *Physical Review D* 99.3 (Feb. 2019). URL: <http://dx.doi.org/10.1103/PhysRevD.99.032004>.
- [47] Marc Harper et al. “python-ternary: Ternary Plots in Python”. In: *Zenodo* 10.5281/zenodo.594435 (2021). URL: <https://github.com/marcharper/python-ternary>.
- [48] Joeran Stettner. *Measurement of the Diffuse Astrophysical Muon-Neutrino Spectrum with Ten Years of IceCube Data*. 2019.
- [49] M. G. Aartsen et al. “Characteristics of the Diffuse Astrophysical Electron and Tau Neutrino Flux with Six Years of IceCube High Energy Cascade Data”. In: *Physical Review Letters* 125.12 (Sept. 2020). URL: <http://dx.doi.org/10.1103/PhysRevLett.125.121104>.
- [50] R. Abbasi et al. “The IceCube high-energy starting event sample: Description and flux characterization with 7.5 years of data”. In: (Nov. 2020).
- [51] Klaes Møller et al. “Cosmogenic neutrinos through the GRAND lens unveil the nature of cosmic accelerators”. In: *Journal of Cosmology and Astroparticle Physics* 2019.05 (May 2019), pp. 047–047. URL: <http://dx.doi.org/10.1088/1475-7516/2019/05/047>.
- [52] Markus Ahlers et al. “Minimal cosmogenic neutrinos”. In: *Physical Review D* 86.8 (Oct. 2012). URL: <http://dx.doi.org/10.1103/PhysRevD.86.083010>.
- [53] Markus Ahlers. “High-energy Cosmogenic Neutrinos”. In: *Physics Procedia* 61 (2015). 13th International Conference on Topics in Astroparticle and Underground Physics, TAUP 2013, pp. 392–398. URL: <https://www.sciencedirect.com/science/article/pii/S1875389214006932>.

- [54] Lee Yacobi et al. “Implication of the Non-detection of gzk Neutrinos”. In: *Astrophys. J.* 823.2 (2016), p. 89.
- [55] M. G. Aartsen et al. “Differential limit on the extremely-high-energy cosmic neutrino flux in the presence of astrophysical background from nine years of IceCube data”. In: *Physical Review D* 98.6 (Sept. 2018). URL: <http://dx.doi.org/10.1103/PhysRevD.98.062003>.
- [56] B. Pontecorvo. “Inverse beta processes and nonconservation of lepton charge”. In: *Zh. Eksp. Teor. Fiz.* 34 (1957), p. 247.
- [57] Y. Fukuda et al. “Evidence for Oscillation of Atmospheric Neutrinos”. In: *Physical Review Letters* 81.8 (Aug. 1998), pp. 1562–1567. URL: <http://dx.doi.org/10.1103/PhysRevLett.81.1562>.
- [58] Q. R. Ahmad et al. “Direct Evidence for Neutrino Flavor Transformation from Neutral-Current Interactions in the Sudbury Neutrino Observatory”. In: *Phys. Rev. Lett.* 89 (1 June 2002), p. 011301. URL: <https://link.aps.org/doi/10.1103/PhysRevLett.89.011301>.
- [59] S.M. Bilenky et al. “Phenomenology of neutrino oscillations”. In: *Progress in Particle and Nuclear Physics* 43 (Jan. 1999), pp. 1–86. URL: [http://dx.doi.org/10.1016/S0146-6410\(99\)00092-7](http://dx.doi.org/10.1016/S0146-6410(99)00092-7).
- [60] Z. Maki et al. “Remarks on the Unified Model of Elementary Particles”. In: *Progress of Theoretical Physics* 28 (Nov. 1962), pp. 870–880.
- [61] Samoil M. Bilenky et al. “On Oscillations of Neutrinos with Dirac and Majorana Masses”. In: *Phys. Lett. B* 94 (1980), pp. 495–498.
- [62] N. Aghanim et al. “Planck 2018 results”. In: *Astronomy & Astrophysics* 641 (Sept. 2020), A6. URL: <http://dx.doi.org/10.1051/0004-6361/201833910>.
- [63] M. Aker et al. “Improved Upper Limit on the Neutrino Mass from a Direct Kinematic Method by KATRIN”. In: *Physical Review Letters* 123.22 (Nov. 2019). URL: <http://dx.doi.org/10.1103/PhysRevLett.123.221802>.
- [64] Sebastian A. R. Ellis et al. “Current and future neutrino oscillation constraints on leptonic unitarity”. In: *Journal of High Energy Physics* 2020.12 (Dec. 2020). URL: [http://dx.doi.org/10.1007/JHEP12\(2020\)068](http://dx.doi.org/10.1007/JHEP12(2020)068).
- [65] P A Zyla et al. “Review of Particle Physics”. In: *Progress of Theoretical and Experimental Physics* 2020.8 (Aug. 2020). 083C01. URL: <https://doi.org/10.1093/ptep/ptaa104>.
- [66] L. Wolfenstein. “Neutrino oscillations in matter”. In: *Phys. Rev. D* 17 (9 May 1978), pp. 2369–2374. URL: <https://link.aps.org/doi/10.1103/PhysRevD.17.2369>.
- [67] S. P. Mikheyev et al. “Resonance Amplification of Oscillations in Matter and Spectroscopy of Solar Neutrinos”. In: *Sov. J. Nucl. Phys.* 42 (1985), pp. 913–917.

- [68] S. P. Mikheev et al. “Resonant amplification of neutrino oscillations in matter and solar neutrino spectroscopy”. In: *Nuovo Cim. C* 9 (1986), pp. 17–26.
- [69] E. K. Akhmedov. “Neutrino physics”. In: *Proceedings, Summer School in Particle Physics: Trieste, Italy, June 21-July 9, 1999*. 1999, pp. 103–164.
- [70] A. Yu. Smirnov. “The MSW effect and solar neutrinos”. In: *Neutrino telescopes. Proceedings, 10th International Workshop, Venice, Italy, March 11-14, 2003. Vol. 1+2*. 2003, pp. 23–43.
- [71] M. C. Gonzalez-Garcia et al. “Neutrino masses and mixing: Evidence and implications”. In: *Rev. Mod. Phys.* 75 (2003), pp. 345–402.
- [72] M. Horoi. “On the MSW neutrino mixing effects in atomic weak interactions and double beta decays”. In: (2018).
- [73] S. Mondal. “Physics of Neutrino Oscillation”. In: *ArXiv e-prints* (Nov. 2015).
- [74] K. Eguchi et al. “First Results from KamLAND: Evidence for Reactor Antineutrino Disappearance”. In: *Phys. Rev. Lett.* 90 (2 Jan. 2003), p. 021802. URL: <https://link.aps.org/doi/10.1103/PhysRevLett.90.021802>.
- [75] Gianluigi Fogli et al. “Evidence for the MSW effect”. In: *New J. Phys.* 6 (2004), p. 139.
- [76] M. Agostini et al. “Comprehensive measurement of  $pp$ -chain solar neutrinos”. In: *Nature* 562.7728 (2018), pp. 505–510.
- [77] Evgeny K. Akhmedov. “Neutrino oscillations in inhomogeneous matter. (In Russian)”. In: *Sov. J. Nucl. Phys.* 47 (1988), pp. 301–302.
- [78] Evgeny K. Akhmedov. “Parametric resonance of neutrino oscillations and passage of solar and atmospheric neutrinos through the earth”. In: *Nucl. Phys.* B538 (1999), pp. 25–51.
- [79] H. ATHAR et al. “Intrinsic and oscillated astrophysical neutrino flavor ratios revisited”. In: *Modern Physics Letters A* 21.13 (Apr. 2006), pp. 1049–1065. URL: <http://dx.doi.org/10.1142/S021773230602038X>.
- [80] Stefan Coenders. “High-energy cosmic ray accelerators: searches with IceCube neutrinos”. Dissertation. München: Technische Universität München, 2016.
- [81] Ankur Nath et al. *Detection techniques and investigation of different neutrino experiments*. 2018.
- [82] Bruce T. Cleveland et al. “Measurement of the Solar Electron Neutrino Flux with the Homestake Chlorine Detector”. In: *The Astrophysical Journal* 496.1 (Mar. 1998), pp. 505–526. URL: <https://doi.org/10.1086/305343>.
- [83] W. Hampel et al. “GALLEX solar neutrino observations: Results for GALLEX IV”. In: *Phys. Lett. B* 447 (1999), pp. 127–133.

- [84] G. Alimonti et al. “The Borexino detector at the Laboratori Nazionali del Gran Sasso”. In: *Nuclear Instruments and Methods in Physics Research Section A: Accelerators, Spectrometers, Detectors and Associated Equipment* 600.3 (Mar. 2009), pp. 568–593. URL: <http://dx.doi.org/10.1016/j.nima.2008.11.076>.
- [85] Carmen Palomares. “Double-Chooz Neutrino Experiment”. In: *PoS EPS-HEP2009* (2009), p. 275.
- [86] Raj Gandhi et al. “Ultrahigh-energy neutrino interactions”. In: *Astroparticle Physics* 5.2 (1996), pp. 81–110. URL: <https://www.sciencedirect.com/science/article/pii/0927650596000084>.
- [87] Sheldon L. Glashow. “Resonant Scattering of Antineutrinos”. In: *Phys. Rev.* 118 (1 Apr. 1960), pp. 316–317. URL: <https://link.aps.org/doi/10.1103/PhysRev.118.316>.
- [88] M. G. Aartsen et al. “Detection of a particle shower at the Glashow resonance with IceCube”. In: *Nature* 591.7849 (Mar. 2021), pp. 220–224. URL: <https://doi.org/10.1038/s41586-021-03256-1>.
- [89] J. L. Hewett et al. *Fundamental Physics at the Intensity Frontier*. 2012.
- [90] J. A. Formaggio et al. “From eV to EeV: Neutrino cross sections across energy scales”. In: *Reviews of Modern Physics* 84.3 (Sept. 2012), pp. 1307–1341. URL: <http://dx.doi.org/10.1103/RevModPhys.84.1307>.
- [91] Javier L. Albacete et al. “Neutrino-nucleon cross section at ultrahigh energy and its astrophysical implications”. In: *Physical Review D* 92.1 (July 2015). URL: <http://dx.doi.org/10.1103/PhysRevD.92.014027>.
- [92] C. Patrignani et al. “Review of Particle Physics”. In: *Chin. Phys.* C40.10 (2016), p. 100001.
- [93] P. A. Cherenkov. “Visible luminescence of pure liquids under the influence of  $\gamma$ -radiation”. In: *Dokl. Akad. Nauk SSSR* 2.8 (1934), pp. 451–454.
- [94] I. M. Frank et al. “Coherent visible radiation of fast electrons passing through matter”. In: *Compt. Rend. Acad. Sci. URSS* 14.3 (1937), pp. 109–114.
- [95] U.F. Katz. “Cherenkov light imaging in astroparticle physics”. In: *Nuclear Instruments and Methods in Physics Research Section A: Accelerators, Spectrometers, Detectors and Associated Equipment* 952 (Feb. 2020), p. 161654. URL: <http://dx.doi.org/10.1016/j.nima.2018.11.113>.
- [96] M G Aartsen et al. “Energy reconstruction methods in the IceCube neutrino telescope”. In: *Journal of Instrumentation* 9.03 (Mar. 2014), P03009–P03009. URL: <http://dx.doi.org/10.1088/1748-0221/9/03/P03009>.
- [97] Leif Rädcl et al. “Calculation of the Cherenkov light yield from electromagnetic cascades in ice with Geant4”. In: *Astroparticle*

- Physics* 44 (Apr. 2013), pp. 102–113. URL: <http://dx.doi.org/10.1016/j.astropartphys.2013.01.015>.
- [98] J. Babson et al. “Cosmic-ray muons in the deep ocean”. In: *Phys. Rev. D* 42 (11 Dec. 1990), pp. 3613–3620. URL: <https://link.aps.org/doi/10.1103/PhysRevD.42.3613>.
- [99] Thomas K. Gaisser et al. “Particle astrophysics with high energy neutrinos”. In: *Physics Reports* 258.3 (July 1995), pp. 173–236. URL: [http://dx.doi.org/10.1016/0370-1573\(95\)00003-Y](http://dx.doi.org/10.1016/0370-1573(95)00003-Y).
- [100] M. Ageron et al. “ANTARES: The first undersea neutrino telescope”. In: *Nuclear Instruments and Methods in Physics Research Section A: Accelerators, Spectrometers, Detectors and Associated Equipment* 656.1 (Nov. 2011), pp. 11–38. URL: <http://dx.doi.org/10.1016/j.nima.2011.06.103>.
- [101] GVD Collaboration et al. *The Baikal-GVD neutrino telescope: First results of multi-messenger studies*. 2019.
- [102] Annarita Margiotta. “The KM3NeT deep-sea neutrino telescope”. In: *Nucl. Instrum. Meth.* A766 (2014), pp. 83–87.
- [103] Matteo Agostini et al. “The Pacific Ocean Neutrino Experiment”. In: *Nature Astronomy* 4.10 (Sept. 2020), pp. 913–915. URL: <http://dx.doi.org/10.1038/s41550-020-1182-4>.
- [104] “Evidence for High-Energy Extraterrestrial Neutrinos at the IceCube Detector”. In: *Science* 342.6161 (Nov. 2013), pp. 1242856–1242856. URL: <http://dx.doi.org/10.1126/science.1242856>.
- [105] Christian Spiering. “IceCube and KM3NeT: Lessons and relations”. In: *Nuclear Instruments and Methods in Physics Research Section A: Accelerators, Spectrometers, Detectors and Associated Equipment* 626-627 (Jan. 2011), S48–S52. URL: <http://dx.doi.org/10.1016/j.nima.2010.06.056>.
- [106] John F. Beacom et al. “Measuring flavor ratios of high-energy astrophysical neutrinos”. In: *Phys. Rev. D* 68 (2003). [Erratum: *Phys.Rev.D* 72, 019901 (2005)], p. 093005.
- [107] D. F. Cowen. “Tau neutrinos in IceCube”. In: *J. Phys. Conf. Ser.* 60 (2007). Ed. by Francis Halzen et al., pp. 227–230.
- [108] Juliana Stachurska. *First Double Cascade Tau Neutrino Candidates in IceCube and a New Measurement of the Flavor Composition*. 2019.
- [109] IceCube-Masterclass. *IceCube and Neutrinos*. <https://masterclass.icecube.wisc.edu/de/learn-ger/neutrionachweis-mit-icecube>. [Online; accessed 31<sup>st</sup> of May, 2018]. 2018.
- [110] “Search for correlations between the arrival directions of IceCube neutrino events and ultrahigh-energy cosmic rays detected by the Pierre Auger Observatory and the Telescope Array”. In: *Journal of Cosmology and Astroparticle Physics* 2016.01 (Jan. 2016), pp. 037–037. URL: <http://dx.doi.org/10.1088/1475-7516/2016/01/037>.
- [111] Dominik Stransky et al. “Reconstruction of cascade-type neutrino events in KM3NeT/ARCA”. In: *PoS ICRC2015* (2016), p. 1108.

- [112] M. G. Aartsen et al. “Search for Sources of Astrophysical Neutrinos Using Seven Years of IceCube Cascade Events”. In: *The Astrophysical Journal* 886.1 (Nov. 2019), p. 12. URL: <http://dx.doi.org/10.3847/1538-4357/ab4ae2>.
- [113] R. Abbasi et al. “An improved method for measuring muon energy using the truncated mean of  $dE/dx$ ”. In: *Nucl. Instrum. Meth. A* 703 (2013), pp. 190–198.
- [114] Hugh Bradner et al. “Long base line measurements of light transmission in clear water”. In: *Appl. Opt.* 23.7 (Apr. 1984), pp. 1009–1012. URL: <http://ao.osa.org/abstract.cfm?URI=ao-23-7-1009>.
- [115] Christian Spiering. “Neutrino Detectors Under Water and Ice”. In: *Particle Physics Reference Library: Volume 2: Detectors for Particles and Radiation*. Ed. by Christian W. Fabjan et al. Cham: Springer International Publishing, 2020, pp. 785–822. URL: [https://doi.org/10.1007/978-3-030-35318-6\\_17](https://doi.org/10.1007/978-3-030-35318-6_17).
- [116] J.H. Lambert. *Photometria sive de mensura et gradibus luminis, colorum et umbrae*. Nineteenth Century Collections Online (NCCO): Photography: The World through the Lens. sumptibus vidvae E. Klett, typis C.P. Detleffsen, 1760. URL: <https://books.google.de/books?id=JdkTAAAAQAAJ>.
- [117] Beer. “Bestimmung der Absorption des rothen Lichts in farbigen Flüssigkeiten”. In: *Annalen der Physik* 162.5 (1852), pp. 78–88. URL: <https://onlinelibrary.wiley.com/doi/abs/10.1002/andp.18521620505>.
- [118] Gustav Mie. “Beiträge zur Optik trüber Medien, speziell kolloidaler Metallösungen”. In: *Annalen der Physik* 330.3 (Jan. 1908), pp. 377–445.
- [119] Nan Li et al. “A Discussion on the Applicable Condition of Rayleigh Scattering”. In: *International Journal of Remote Sensing Applications* 5 (Jan. 2015), p. 62.
- [120] John T. O. Kirk. “Multiple scattering of a photon flux: implications for the integral average cosine of the underwater light field”. In: *Appl. Opt.* 38.15 (May 1999), pp. 3134–3140. URL: <http://ao.osa.org/abstract.cfm?URI=ao-38-15-3134>.
- [121] S. Chandrasekhar. *Radiative Transfer*. Dover Books on Physics. Dover Publications, 2013. URL: <https://books.google.de/books?id=1YHCAGAAQBAJ>.
- [122] M. Ackermann et al. “Optical properties of deep glacial ice at the South Pole”. In: 111, D13203 (July 2006), p. D13203.
- [123] Vasilij Balkanov et al. “In situ measurements of optical parameters in Lake Baikal with the help of a Neutrino telescope”. In: *Appl. Opt.* 38.33 (Nov. 1999), pp. 6818–6825. URL: <http://ao.osa.org/abstract.cfm?URI=ao-38-33-6818>.
- [124] V. Balkanov et al. “Simultaneous measurements of water optical properties by AC9 transmissometer and ASP-15 Inherent Optical Properties Meter in Lake Baikal”. In: *Nucl. Instrum. Meth. A* 298 (2003), pp. 231–239.

- [125] J. A. Aguilar et al. “Transmission of light in deep sea water at the site of the ANTARES Neutrino Telescope”. In: *Astropart. Phys.* 23 (2005), pp. 131–155.
- [126] G. Riccobene et al. “Deep seawater inherent optical properties in the Southern Ionian Sea”. In: *Astropart. Phys.* 27 (2007), pp. 1–9.
- [127] M. Ackermann et al. “Optical properties of deep glacial ice at the South Pole”. In: *J. Geophys. Res.* 111.D13 (2006), p. D13203.
- [128] Johan Lundberg et al. “Light tracking for glaciers and oceans: Scattering and absorption in heterogeneous media with Photonics”. In: *Nucl. Instrum. Meth. A* 581 (2007), pp. 619–631.
- [129] M. Ageron et al. “The ANTARES Optical Beacon System”. In: *Nucl. Instrum. Meth. A* 578 (2007), pp. 498–509.
- [130] B. Baret et al. “The Calibration Units of the KM<sub>3</sub>NeT neutrino telescope”. In: *EPJ Web Conf.* 116 (2016). Ed. by A. Capone et al., p. 06006.
- [131] Diego Real et al. “Nanobeacon: A time calibration device for KM<sub>3</sub>NeT”. In: *EPJ Web of Conferences* 207 (Jan. 2019), p. 07002.
- [132] M. Boehmer et al. “STRAW (STRings for Absorption length in Water): pathfinder for a neutrino telescope in the deep Pacific Ocean”. In: *JINST* 14.02 (2019), P02013.
- [133] M. G. Aartsen et al. “Measurement of South Pole ice transparency with the IceCube LED calibration system”. In: *Nucl. Instrum. Meth. A* 711 (2013), pp. 73–89.
- [134] Martin Rongen. “Calibration of the IceCube Neutrino Observatory”. Other thesis. Nov. 2019.
- [135] G. Riccobene et al. “Deep seawater inherent optical properties in the Southern Ionian Sea”. In: *Astroparticle Physics* 27.1 (2007), pp. 1–9. URL: <https://www.sciencedirect.com/science/article/pii/S092765050600123X>.
- [136] D. Zaborov. “Coincidence analysis in ANTARES: Potassium-40 and muons”. In: *Phys. Atom. Nucl.* 72 (2009). Ed. by Jean-Marie Frère et al., pp. 1537–1542.
- [137] M. A. Unland Elorrieta. “Studies on dark rates induced by radioactive decays of the multi-PMT digital optical module for future IceCube extensions”. Master’s Thesis. University of Münster, 2017.
- [138] ANTARES Collaboration et al. *The ANTARES detector: background sources and effects on detector performance*. 2007.
- [139] Stephan Meighen-Berger et al. *Bioluminescence modeling for deep sea experiments*. 2021.
- [140] Jacopo Aguzzi et al. “Inertial bioluminescence rhythms at the Capo Passero (KM<sub>3</sub>NeT-Italia) site, Central Mediterranean Sea”. In: *Scientific Reports* 7 (Mar. 2017), p. 44938.

- [141] M. G. Aartsen et al. “The IceCube Neutrino Observatory: Instrumentation and Online Systems”. In: *JINST* 12.03 (2017), P03012.
- [142] Ronald Bruijn. “KM<sub>3</sub>NeT Readout and Triggering”. In: *EPJ Web Conf.* 207 (2019). Ed. by C. Spiering, p. 06007.
- [143] J. A. Aguilar et al. “Time Calibration of the ANTARES Neutrino Telescope”. In: *Astropart. Phys.* 34 (2011), pp. 539–549.
- [144] K.K. Hamamatsu Photonics. *Photomultiplier Tubes – Basics and Applications*. Rev. 3a. Hamamatsu Photonics K.K. Aug. 2007.
- [145] P. Amram et al. “The ANTARES optical module”. In: *Nucl. Instrum. Meth. A* 484 (2002), pp. 369–383.
- [146] K. Hanson et al. “Design and production of the IceCube digital optical module”. In: *Nuclear Instruments and Methods in Physics Research Section A: Accelerators, Spectrometers, Detectors and Associated Equipment* 567.1 (2006). Proceedings of the 4th International Conference on New Developments in Photodetection, pp. 214–217. URL: <https://www.sciencedirect.com/science/article/pii/S016890020600920X>.
- [147] E Leonora. “The Digital Optical Module of KM<sub>3</sub>NeT”. In: *Journal of Physics: Conference Series* 1056 (July 2018), p. 012031.
- [148] R. Abbasi et al. “Calibration and Characterization of the IceCube Photomultiplier Tube”. In: *Nucl. Instrum. Meth. A* 618 (2010), pp. 139–152.
- [149] M. G. Aartsen et al. “In-situ calibration of the single-photoelectron charge response of the IceCube photomultiplier tubes”. In: *JINST* 15.06 (2020), p. 06.
- [150] J.P. Gomez-Gonzalez. “Calibration systems of the ANTARES neutrino telescope”. In: *Nuclear Instruments and Methods in Physics Research Section A: Accelerators, Spectrometers, Detectors and Associated Equipment* 725 (2013). VLVvT 11, Erlangen, Germany, 12 - 14 October, 2011, pp. 199–202. URL: <https://www.sciencedirect.com/science/article/pii/S0168900212015136>.
- [151] Vladimir Kulikovskiy. “Calibration methods and tools for KM<sub>3</sub>NeT”. In: *EPJ Web Conf.* 116 (2016). Ed. by A. Capone et al., p. 06003.
- [152] P. Bagley et al. “KM<sub>3</sub>NeT: Technical Design Report for a Deep-Sea Research Infrastructure in the Mediterranean Sea Incorporating a Very Large Volume Neutrino Telescope”. In: (2009).
- [153] Salvatore Viola et al. “Acoustic positioning system for KM<sub>3</sub>NeT”. In: *PoS ICRC2015* (2016), p. 1169.
- [154] Frederic Jonske et al. “Trilateration-based geometry calibration of the IceCube detector”. In: *Verhandlungen der Deutschen Physikalischen Gesellschaft Aache2019issue* (2019). INSTRUMENTATION RELATED TO NUCLEAR SCIENCE AND TECHNOLOGY, p. 1.
- [155] Albrecht Karle. “IceCube: Construction Status and First Results”. In: *Nucl. Instrum. Meth. A* 604 (2009), S46–S52.

- [156] R. Abbasi et al. “The design and performance of IceCube DeepCore”. In: *Astroparticle Physics* 35.10 (May 2012), pp. 615–624. URL: <http://dx.doi.org/10.1016/j.astropartphys.2012.01.004>.
- [157] R. Abbasi et al. “The IceCube data acquisition system: Signal capture, digitization, and timestamping”. In: *Nuclear Instruments and Methods in Physics Research Section A: Accelerators, Spectrometers, Detectors and Associated Equipment* 601.3 (Apr. 2009), pp. 294–316. URL: <http://dx.doi.org/10.1016/j.nima.2009.01.001>.
- [158] M. G. Aartsen et al. “Measurement of the multi-TeV neutrino cross section with IceCube using Earth absorption”. In: *Nature* 551 (2017), pp. 596–600.
- [159] P. Niessen. *Simulated bubbles and their effect on some observables in AMANDA B4*. IceCube internal report, Nov. 1998. URL: <https://internal-apps.icecube.wisc.edu/reports/amanda/data/19981101-niessen-bubbles.pdf>.
- [160] P. O. Hulth. *Results from the IceCube video camera system at 2455 meters ice depth*. Very Large Volume Neutrino Telescope (VLVNT) Conference. Aug. 2013. URL: <https://indico.fysik.su.se/event/3930/contributions/4803/contribution.pdf>.
- [161] Per Askebjør et al. “Optical properties of deep ice at the South Pole: Absorption”. In: 36 (July 1997), pp. 4168–80.
- [162] P Buford Price et al. “Optical properties of deep ice at the South Pole: Scattering”. In: 36 (July 1997), pp. 4181–94.
- [163] Sérgio H. Faria et al. “The microstructure of polar ice. Part I: Highlights from ice core research”. In: *Journal of Structural Geology* 61 (2014). Microdynamics of Ice, pp. 2–20. URL: <https://www.sciencedirect.com/science/article/pii/S0191814113001740>.
- [164] Ryan Bay et al. “South Pole paleowind from automated synthesis of ice core records”. In: *J. Geophys. Res* 115 (July 2010).
- [165] Dmitry Chirkin. “Evidence of optical anisotropy of the South Pole ice”. In: *33rd International Cosmic Ray Conference*. 2013.
- [166] Dmitry Chirkin et al. *Light diffusion in birefringent polycrystals and the IceCube ice anisotropy*. 2019.
- [167] Rongen, Martin. “Measuring the optical properties of IceCube drill holes”. In: *EPJ Web of Conferences* 116 (2016), p. 06011. URL: <https://doi.org/10.1051/epjconf/201611606011>.
- [168] D. Chirkin. *Fitting the hole ice angular sensitivity model with the all-string flasher data*. 2015. URL: <https://events.icecube.wisc.edu/event/69/contributions/4325/attachments/3558/3902/holeice.pdf>.
- [169] P. Olbrechts. *On the Angular Sensitivity of Optical Modules in the Ice*. AMANDA internal report, Jan. 2001. URL: <https://internal-apps.icecube.wisc.edu/reports/amanda/data/20010102-updn.pdf>.
- [170] L. Gerhardt. *Effects of Hole Ice on Hit Time*. Technical report Lawrence Berkeley National Laboratory, Apr. 2009. URL:

- <https://internal-apps.icecube.wisc.edu/reports/amanda/data/20010102-updn.pdf>.
- [171] Sebastian Fiedlschuster. *The Effect of Hole Ice on the Propagation and Detection of Light in IceCube*. 2019.
- [172] Delia Tosi et al. *Calibrating the photon detection efficiency in IceCube*. 2015.
- [173] A. Karle et al. *Hole Ice Studies with YAG data*. AMANDA internal report, Sept. 1998. URL: <http://icecube.berkeley.edu/kurt/interstring/hole-ice/yak.html>.
- [174] D. Chirkin. *A calibration study of local ice and optical sensor properties in IceCube*. July 2021. URL: <https://indico.desy.de/event/27991/contributions/100005/>.
- [175] P. Eller. *Unified angular acceptance model*. June 2019. URL: <https://drive.google.com/file/d/1NmfWXGqbj5Eh5NrQ7azfK62Yu6Fzn5To/view>.
- [176] T. Yuan. *Improvement in IceCube event reconstructions*. Apr. 2018. URL: <https://absuploads.aps.org/presentation.cfm?pid=14171>.
- [177] C. Sheremata. *DeepCore DOM Profiles with the Trilateration Algorithm*. 2013. URL: <https://docushare.icecube.wisc.edu/dsweb/Get/Document-65566/Presentation-OverallInformation.pdf>.
- [178] M. G. Aartsen et al. “IceCube-Gen2: A Vision for the Future of Neutrino Astronomy in Antarctica”. In: (2014).
- [179] M. G. Aartsen et al. *IceCube-Gen2: The Window to the Extreme Universe*. 2020.
- [180] M. G. Aartsen et al. “Letter of Intent: The Precision IceCube Next Generation Upgrade (PINGU)”. In: (2014).
- [181] Aya Ishihara. *The IceCube Upgrade – Design and Science Goals*. 2019.
- [182] M. G. Aartsen et al. *The IceCube Neutrino Observatory - Contributions to ICRC 2017 Part VI: IceCube-Gen2, the Next Generation Neutrino Observatory*. 2017.
- [183] Lew Classen et al. *A multi-PMT Optical Module for the IceCube Upgrade*. 2019.
- [184] Satoshi Shimizu et al. “Overview and performance of the D-Egg optical sensor for IceCube-Gen2”. In: *PoS ICRC2017* (2018), p. 1051.
- [185] Perry Sandstrom et al. “Digital optical module design for PINGU”. In: *AIP Conference Proceedings* 1630.1 (2014), pp. 180–183. URL: <https://aip.scitation.org/doi/abs/10.1063/1.4902801>.
- [186] Woosik Kang et al. *The camera system for the IceCube Upgrade*. 2019.
- [187] Dirk Heinen et al. “An Acoustic Calibration System for the IceCube Upgrade”. In: *PoS ICRC2019* (2021), p. 1030.

- [188] J. Knuckles. *Pencil Beam Overview*. Private communication. IceCube internal review, Dec. 2020.
- [189] Christian Fruck et al. “The POCAM as self-calibrating light source for the IceCube Upgrade”. In: *PoS ICRC2019* (2020), p. 908.
- [190] P. Eller et al. “Low Energy Event Reconstruction in IceCube / DeepCore”. private communication. work in progress.
- [191] M. G. Aartsen et al. “Measurement of Atmospheric Neutrino Oscillations at 6–56 GeV with IceCube DeepCore”. In: *Physical Review Letters* 120.7 (Feb. 2018). URL: <http://dx.doi.org/10.1103/PhysRevLett.120.071801>.
- [192] Z. Li et al. “Measurement of the tau neutrino cross section in atmospheric neutrino oscillations with Super-Kamiokande”. In: *Phys. Rev. D* 98.5 (2018), p. 052006.
- [193] N. Agafonova et al. “Final Results of the OPERA Experiment on  $\nu_\tau$  Appearance in the CNGS Neutrino Beam”. In: *Phys. Rev. Lett.* 120 (21 May 2018), p. 211801. URL: <https://link.aps.org/doi/10.1103/PhysRevLett.120.211801>.
- [194] The T2K Collaboration et al. *Improved constraints on neutrino mixing from the T2K experiment with  $3.13 \times 10^{21}$  protons on target*. 2021.
- [195] Alex Himmel. *New Oscillation Results from the NOvA Experiment*. July 2020. URL: <https://doi.org/10.5281/zenodo.3959581>.
- [196] Leigh H. Whitehead. “Neutrino Oscillations with MINOS and MINOS+”. In: *Nucl. Phys. B* 908 (2016), pp. 130–150.
- [197] M.G. Aartsen et al. *Neutrino astronomy with the next generation IceCube Neutrino Observatory*. 2019.
- [198] F. Henningsen et al. “A self-monitoring precision calibration light source for large-volume neutrino telescopes”. In: *Journal of Instrumentation* 15.07 (July 2020), P07031–P07031. URL: <http://dx.doi.org/10.1088/1748-0221/15/07/P07031>.
- [199] M. Jurkovič et al. “A Precision Optical Calibration Module (POCAM) for IceCube-Gen2”. In: *EPJ Web Conf.* 116 (2016), p. 06001.
- [200] J. Veenkamp. “A Precision Optical Calibration Module for IceCube-Gen2”. Master’s Thesis. Technical University Munich, 2016.
- [201] M. Ackermann et al. “The IceCube Neutrino Observatory”. In: *Proceedings, 35th International Cosmic Ray Conference (ICRC 2017): Bexco, Busan, Korea, July 12-20, 2017*. 2017. URL: <http://inspirehep.net/record/1628389/files/arXiv:1710.01207.pdf>.
- [202] K. Holzapfel. “Testing the Precision Optical Calibration Modules in the Gigaton-Volume-Detector”. Master’s Thesis. Technical University Munich, 2018.
- [203] Dmitry Chirkin. “Photon tracking with GPUs in IceCube”. In: *Nucl. Instrum. Meth. A* 725 (2013). Ed. by G. Anton et al., pp. 141–143.

- [204] D. Chirkin. *Photon Propagation Code*. 2021. URL: <https://user-web.icecube.wisc.edu/~dima/work/WISC/ppc/> (visited on 05/05/2021).
- [205] D. Chirkin. *Photon Propagation with GPUs in IceCube*. DESY – Proc. of GPUHEP, 2014, pp. 217–220.
- [206] L. G. Henyey et al. “Diffuse radiation in the Galaxy.” In: *APJ* 93 (Jan. 1941), pp. 70–83.
- [207] Pingyu Liu. “A new phase function approximating to Mie scattering for radiative transport equations”. In: *Physics in Medicine and Biology* 39.6 (June 1994), pp. 1025–1036. URL: <https://doi.org/10.1088/0031-9155/39/6/008>.
- [208] F. Rosenblatt. “The perceptron: a probabilistic model for information storage and organization in the brain.” In: *Psychological review* 65 6 (1958), pp. 386–408.
- [209] Maximilian Kronmueller. “Application of Deep Neural Networks on Event Type Classification in IceCube”. MA thesis. Munich, Tech. U., Dec. 2018.
- [210] Lavanya Shukla. *Designing Your Neural Networks*. <https://www.kdnuggets.com/2019/11/designing-neural-networks.html>. [Online; accessed 14<sup>th</sup> of May, 2021]. 2019.
- [211] Abien Fred Agarap. *Deep Learning using Rectified Linear Units (ReLU)*. cite arxiv:1803.08375Comment: 7 pages, 11 figures, 9 tables. 2018. URL: <http://arxiv.org/abs/1803.08375>.
- [212] Sebastian Ruder. *An overview of gradient descent optimization algorithms*. 2017.
- [213] Nitish Srivastava et al. “Dropout: A Simple Way to Prevent Neural Networks from Overfitting”. In: *Journal of Machine Learning Research* 15.56 (2014), pp. 1929–1958. URL: <http://jmlr.org/papers/v15/srivastava14a.html>.
- [214] Guido Van Rossum et al. *Python reference manual*. Centrum voor Wiskunde en Informatica Amsterdam, 1995.
- [215] Charles R. Harris et al. “Array programming with NumPy”. In: *Nature* 585.7825 (Sept. 2020), pp. 357–362. URL: <https://doi.org/10.1038/s41586-020-2649-2>.
- [216] Pauli Virtanen et al. “SciPy 1.0: Fundamental Algorithms for Scientific Computing in Python”. In: *Nature Methods* 17 (2020), pp. 261–272.
- [217] Martin Roberts. *The Unreasonable Effectiveness of Quasirandom Sequences*. <http://extremelearning.com.au/unreasonable-effectiveness-of-quasirandom-sequences/>. (created 2018; updated 2020) [Online; accessed 13<sup>th</sup> of May, 2021]. 2018.
- [218] Vedran Krcadinac. “A new generalization of the golden ratio”. In: *The Fibonacci Quarterly* 44 (Nov. 2006).
- [219] M. Abadi et al. *TensorFlow: Large-Scale Machine Learning on Heterogeneous Systems*. Software available from tensorflow.org. 2015. URL: <http://tensorflow.org/>.

- [220] Nader Fallah et al. “Nonlinear Poisson regression using neural networks: A simulation study”. In: *Neural Computing and Applications* 18 (Nov. 2009), pp. 939–943.
- [221] Diederik P. Kingma et al. *Adam: A Method for Stochastic Optimization*. 2017.
- [222] Dmitry Chirkin. *Likelihood description for comparing data with simulation of limited statistics*. 2013.
- [223] J. W. Fowler. “Maximum-Likelihood Fits to Histograms for Improved Parameter Estimation”. In: *Journal of Low Temperature Physics* 176.3-4 (Feb. 2014), pp. 414–420. URL: <http://dx.doi.org/10.1007/s10909-014-1098-4>.
- [224] S. -D. Poisson. *Recherches sur la probabilité des jugements en matière criminelle et en matière civile*. 1837.
- [225] Steve Brooks et al. *Handbook of Markov Chain Monte Carlo*. CRC press, 2011.
- [226] T. Bayes. “An essay towards solving a problem in the doctrine of chances”. In: *Phil. Trans. of the Royal Soc. of London* 53 (1763), pp. 370–418.
- [227] Daniel Foreman-Mackey et al. “emcee: The MCMC Hammer”. In: 125.925 (Mar. 2013), p. 306.
- [228] M. G. Aartsen et al. “Development of an analysis to probe the neutrino mass ordering with atmospheric neutrinos using three years of IceCube DeepCore data”. In: *Eur. Phys. J. C* 80.1 (2020), p. 9.
- [229] S. Agostinelli et al. “Geant4 – a simulation toolkit”. In: *Nuclear Instruments and Methods in Physics Research Section A: Accelerators, Spectrometers, Detectors and Associated Equipment* 506.3 (2003), pp. 250–303. URL: <https://www.sciencedirect.com/science/article/pii/S0168900203013688>.
- [230] J Marshall. *NIST Calibration Services Users Guide 1998 Edition*. en. 1998-01-01 1998.
- [231] Schott N-BK7. 517642.251. Schott. Jan. 2014.
- [232] 3M. *Scotch-Weld DP 460*. Rev. February. 2003.
- [233] The Acktar - Advanced Coatings. *MagicBlack*. <https://www.acm-coatings.de/produkt/magic-black/>. [Online; accessed 21<sup>st</sup> of January, 2020]. 2020.
- [234] Sanjeev J. Koppal. “Lambertian Reflectance”. In: *Computer Vision: A Reference Guide*. Ed. by Katsushi Ikeuchi. Boston, MA: Springer US, 2014, pp. 441–443. URL: [https://doi.org/10.1007/978-0-387-31439-6\\_534](https://doi.org/10.1007/978-0-387-31439-6_534).
- [235] The Labsphere. *Integrating Sphere Theory and Applications*. Tech. rep. Labsphere, 2017.
- [236] The Berghof Fluoroplastic Technology GmbH. *Optical PTFE - The reference for light*. 2019.
- [237] J.S. Kapustinsky et al. “A fast timing light pulser for scintillation detectors”. In: *Nuclear Instruments and Methods in*

*Physics Research Section A: Accelerators, Spectrometers, Detectors and Associated Equipment* 241.2 (1985), pp. 612–613.  
URL: <http://www.sciencedirect.com/science/article/pii/S0168900285906229>.

- [238] EPC. *Development Board EPC9126/EPC9126HC Quick Start Guide*. EPC2212/EPC2001C - 100 V High Current Pulsed Laser Diode Driver. Rev. 3.0. 2019.
- [239] The Roithner LaserTechnik GmbH. *XRL-400-5E*. Sept. 2010.
- [240] C. Spannfellner. “Development of pathfinder missions and instruments for the Pacific Ocean Neutrino Experiment”. Master’s Thesis. Technical University Munich, 2020.
- [241] Hamamatsu. *Si photodiodes - S2281 series*. Rev. October. 2015.
- [242] T. Pertl. “Development and characterization of IceCube Upgrade calibration instrumentation”. Master’s Thesis. Technical University Munich, 2021.
- [243] L. Gruber et al. “Over saturation behavior of SiPMs at high photon exposure”. In: *Nucl. Instrum. Meth.* A737 (2014), pp. 11–18.
- [244] Katsushige Kotera et al. “Describing the response of saturated SiPMs”. In: (2015).
- [245] Ketek. *SiPM - Silicon Photomultiplier PM3315-WB-Co*. Rev. 2019-C. 2019.
- [246] Ryo Nagai et al. “Electronics Development for the New Photo-Detectors (PDOM and D-Egg) for IceCube-Upgrade”. In: *HAWC Contributions to the 36th International Cosmic Ray Conference (ICRC2019)*. 2019.